DEMYSTIFYING LARGE UNIT-CELLED INTERMETALLIC CRYSTALS

A Dissertation

Presented to the Faculty of the Graduate School

of Cornell University

in Partial Fulfillment of the Requirements for the Degree of

Doctor of Philosophy

by

Robert Forman Berger

August 2009

DEMYSTIFYING LARGE UNIT-CELLED INTERMETALLIC CRYSTALS

Robert Forman Berger, Ph.D.

Cornell University 2009

This thesis represents an effort to understand the factors that drive large unit-celled intermetallic crystal structures to exist as energy minima. In terms of its approach, the work can be divided into two relatively independent sections.

The first three chapters focus on geometric features of complex intermetallic structures, telling a continuous story in which our viewpoint gradually evolves. Chapter 1 uses $Mg_{44}Rh_7$ as a model system to demonstrate how one can systematically search for chemically meaningful features within a geometrically complex crystal. The importance of the features we highlight is supported by experimental site preferences and calculated Mulliken populations. Chapter 2 addresses a seemingly impossible feature of a family of cubic crystals—pairs of perpendicular pseudo-fivefold axes in their X-ray diffraction patterns. We account for this property and nearly all atomic sites by describing the crystals as collections of three-dimensional projections of a four-dimensional Platonic solid. Chapter 3 further develops this projection method, showing that the same family of distinct structures can be expressed as a single projection of an eight-dimensional lattice. The projection not only simplifies the crystals mathematically (from a unit cell with hundreds of atoms to a unit cell with just one), but unifies them as well.

The fourth chapter differs from the others in that it focuses on the electronic structure of intermetallic crystals, rather than their geometry. We consider the traditional explanation for Hume-Rothery's electron-counting rules, which is

based on the nearly free-electron model, and cast it into the language of linear combinations of atomic orbitals. Starting from a simple one-dimensional chain of atoms and progressing to complex γ-brass superstructures, we show that Hume-Rothery's observations can be rationalized in the same real-space way that chemists understand molecular electron-counting rules.

As both the higher-dimensional projections and electron-counting rules of complex intermetallics are linked to their X-ray diffraction patterns, we anticipate that the two sections of this thesis will become closely connected in future work.

BIOGRAPHICAL SKETCH

Rob Berger grew up in Longmeadow, Massachusetts, a fact he must generally follow with, "No, it's not near Boston." After graduating from Longmeadow High School in 2001, he began his undergraduate studies at Princeton. It was there that he first found solid-state chemistry, synthesizing geometrically frustrated magnetic materials in the lab of Prof. Robert Cava. Upon noticing that Ph.D. students get to wear poofy hats when they graduate, Rob came to Cornell in 2005. He has since worked with Profs. Stephen Lee and Roald Hoffmann, trying to make sense of some of nature's most amazing crystal structures. In the fall of 2009, Rob will finally try out a different part of the country, and begin a postdoc at Lawrence Berkeley National Lab in California.

To Mom and Dad.

ACKNOWLEDGMENTS

I am one of the few lucky Ph.D. students who can honestly say at the end of graduate school that I enjoyed just about every minute of it. For this, I owe a huge debt of gratitude to my co-advisors, Stephen Lee and Roald Hoffmann. Thank you for providing me with such interesting questions to explore, and with the freedom (and pizza) to explore them. I couldn't have possibly hoped for more knowledgeable, creative, and devoted teachers. Thank you, also, to Frank DiSalvo for your useful comments and feedback while serving on my committee.

My graduate work could not have been as productive or rewarding as it was had I not been surrounded by such talented people. Thank you to all members of the Lee and Hoffmann groups, past and present, from whom I've learned a great deal.

I chose to come to Cornell not only for its chemistry, but for a place I knew I would enjoy living. My friends in Ithaca have proven that decision right, and have managed to keep me sane. Thank you for ping pong, karaoke, the Big Red Barn, and more failed attempts than I can count at that elusive Intramural Champion t-shirt. Thank you, as well, to my friends away from Ithaca for some memorable trips to Boston and Princeton, and for making sure all my free time is filled up with fantasy sports.

I owe so much of what I am and what I've accomplished to the love and support of my family. Thank you, Mom and Dad, for all the time and effort (and money) you've put in over the years to make sure the math side of my brain is well-fed—from driving me to music lessons, to buying me puzzle books, to giving me baseball statistics to calculate to keep me quiet as a little kid. Thank you, Mike and Anna, for the example you've set and for all the advice you've

given me. And thank you, Grandma and Grandpa, for your unreasonably high opinion of me, regardless of whether it's deserved.

My choice of advisors resulted in one last bit of good fortune. As a teaching assistant in Stephen's undergraduate chemistry course, I met my wonderful girlfriend. Thank you, Spencer, for your endless supply of love, patience, understanding, and white chocolate-chip cookies.

TABLE OF CONTENTS

LIST OF TABLES

LIST OF FIGURES

CHAPTER 1

TACKLING COMPLEXITY: THE SEARCH FOR CHEMICAL ORDER IN LARGE INTERMETALLIC UNIT CELLS

Life is infinitely stranger than anything which the mind of man could invent.
—Sherlock Holmes, "A Case of Identity" by Sir Arthur Conan Doyle[1]

The first three chapters of this thesis present with permission our series of papers on complex ionic and intermetallic crystal structures, published in *Chemistry: A European Journal* in 2007 and 2008. In the titles of these chapters, one can see a clear progression in our thinking about these compounds, from three to four to eight dimensions. This was in no way our intent, or even something we could have foreseen, at the beginning of this project. Our goal was to find geometrical and electronic patterns in these complex crystal structures, in order to make them more memorable and more chemically meaningful to the viewer, and to provide some insight into why they exist as energy minima. It was in pursuit of this goal that we eventually added fictitious dimensions to our view, in order to account for observations that could not be explained simply or naturally in three dimensions.

The first paper in our series, "A Quantum Mechanically Guided View of $Mg_{44}Rh_7$" (Robert F. Berger, Stephen Lee, and Roald Hoffmann),[2] is presented with permission in this chapter. In this paper, which was featured on the cover of *Chemistry: A European Journal* (Figure 1.1), there are only the earliest signs of the higher-dimensional thinking that is to come. We present a new geometric description of $Mg_{44}Rh_7$, a compound with 408 atoms in its cubic unit cell. Using both experimental site preferences and LDA-DFT-calibrated extended Hückel

Figure 1.1: The cover of *Chemistry: A European Journal*, Volume 13, Issue 28 (September 28, 2007).

(eH) calculations as guides, we highlight the structural units within $Mg_{44}Rh_7$ that reflect the electron-richness or electron-poorness of each crystallographic site. The units that best account for these site preferences and electron populations are 34- and 25-atom fragments of the Ti_2Ni structure, rather than the variety of clusters often used to describe complicated intermetallic and ionic structures. These Ti_2Ni pieces, located using a systematic search algorithm, fit together in a beautifully intricate network. An examination of this network reveals some surprising geometric features of $Mg_{44}Rh_7$, including a fractal-like arrangement of similar atomic formations on different length scales, geometrically connected to an approximate fivefold symmetry.

1.1 Introduction

When chemists think of intermetallic crystal structures, we tend to focus on a few simple structures with just one or two atoms per unit cell. It is indeed

true that many intermetallic structures are variants of the body-centered cubic, face-centered cubic, and hexagonal close-packed structures. However, a survey of known crystal structures reveals that a significant fraction of intermetallics have much more complex structures, with anywhere from several hundred to over one thousand atoms per unit cell.[3–6] Given our abiding love affair with simplicity, these complicated structures, if not avoided, are often viewed as a curiosity. They do not generally form a starting point for our understanding of metals, metallic bonding, or metallic crystal structures. However, if nature has chosen them over all other possible arrangements of several hundred atoms, they must carry within them some basic information about which structural features drive an intermetallic compound to exist.

The atomic positions in these complex structures are so varied that in order to even start making sense of them, the curious scientist must search for some description which allows him or her to organize the atoms into simple, recognizable patterns. Pattern seekers often adopt one of several approaches. In a first such approach, complicated structures may be described in terms of constellations of atoms—"clusters" that make the structures easier to visualize and remember. In another approach, complex intermetallics are discussed in terms of their similarities to simpler, better understood structures. And in still a third approach, these structures are described in terms of their coordination polyhedra—the sets of nearest neighbors around each atom.

Each of these modes of pattern recognition can be immensely helpful, at the very least as a geometrical mnemonic device. Geometry is powerful, meaningful, and deep. But there is more to chemistry than geometry, and approaches to understanding a crystal structure must strive to identify the patterns that are

chemically meaningful. When dealing with complicated structures, this goal is difficult to accomplish. For example, in the "cluster" approach to intermetallics, the assemblages of atoms discussed are not actually clusters in a chemical sense, because they are not in any way isolated from the rest of the structure. They are simply arbitrary sets of atoms singled out to facilitate visualization of the structure.

In this paper, we use quantum mechanics of the simplest sort to guide our description of a complicated intermetallic structure. Using $Mg_{44}Rh_7$, which crystallizes in the cubic space group $F\bar{4}3m$ (No. 216), as our system of choice, we build up a structural description by drawing from each of the pattern recognition modes mentioned above. Starting with a conventional cluster description of $Mg_{44}Rh_7$, we locate familiar repeating motifs from a simpler structure type throughout the unit cell. From these we build up coordination polyhedra in a new way that suggests an almost fractal character to the structure. The difference from a conventional cluster approach is that by incorporating electronic structure calculations in our geometric description, we emphasize those geometric features that are implicated by quantum mechanics to be important to the stability and bonding of the compound. By constructing a description that is both chemically meaningful and geometrically palatable, one might say we try to have our quantum theory and eat it too. The ultimate goal in this approach is to determine which features allow such beautifully complicated intermetallic structures to exist.

1.2 Current Understanding of $Mg_{44}Rh_7$

When the crystal structure of $Mg_{44}Rh_7$ was solved by Westin in 1971,[7] it provided solid-state chemists with a puzzle. Since then, a series of well-crafted geometric descriptions have given us several coherent ways of looking at the structure, which has 408 atoms in its cubic unit cell. Samson and Hansen[8] built the $Mg_{44}Rh_7$ structure from icosahedra, pentagonal prisms, and Friauf polyhedra, noting in particular the prevalence of fivefold symmetry. Subsequently, Andersson[9] built the structure from tetrahedra and octahedra, packing them together to form pyrochlore and Keggin units.

Others have described $Mg_{44}Rh_7$ using the cluster concept, an approach first introduced by Bradley and Jones.[10] The cluster view of $Mg_{44}Rh_7$, shown in Figure 1.2, describes the structure in terms of a face-centered cubic Bravais lattice of four distinct clusters of atoms. These clusters are centered at the high-symmetry points of the unit cell—$(0, 0, 0)$, $(\frac{1}{4}, \frac{1}{4}, \frac{1}{4})$, $(\frac{1}{2}, \frac{1}{2}, \frac{1}{2})$, and $(\frac{3}{4}, \frac{3}{4}, \frac{3}{4})$. Several other structures with similarly-sized cubic unit cells[a] have also been described in terms of clusters.[27,28] Because the four clusters provide a convenient starting point for our analysis of the $Mg_{44}Rh_7$ structure, we now describe each of these clusters in greater detail.

[a]These structures include $Li_{22}Pb_5$,[11] Na_6Tl,[8] Mg_6Pd,[12] $Cu_{41}Sn_{11}$,[13,14] $Sm_{11}Cd_{45}$,[15] $Zn_{78}Fe_{22}$,[16] $Li_{21}Si_5$,[17,18] $Zn_{6.5}(Fe,Ni)$,[19] $Al_{69}Ta_{39}$,[20] $Mg_{29}Ir_4$,[21] $Zn_{20.44}Mo$,[22] $Zn_{21}Pt_5$,[23–25] and $Li_{13}Na_{29}Ba_{19}$.[26] Each of these compounds crystallizes in space group $F\bar{4}3m$ (No. 216), has between 396 and 488 atoms in its cubic unit cell, and can be described in terms of distinct clusters centered at the high-symmetry points of the crystal.

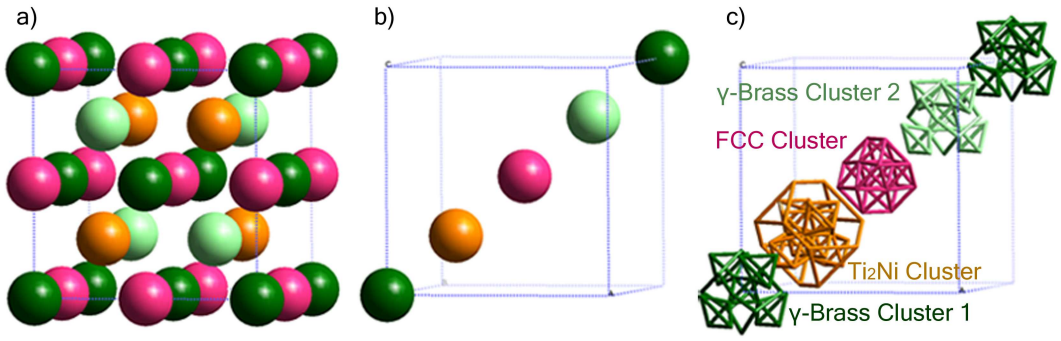

Figure 1.2: The arrangement of clusters in the $Mg_{44}Rh_7$ structure. a) The four unique clusters are represented by differently colored spheres. Clusters are centered at the high-symmetry points of the crystal, with four copies of each cluster in the cubic unit cell in a face-centered arrangement. b) Clusters are shown along the body diagonal, and c) their identities are revealed.

1.3 The Clusters in $Mg_{44}Rh_7$

Of the four crystallographically distinct clusters in the $Mg_{44}Rh_7$ structure, two are 26-atom units known as γ-brass clusters. The γ-brass cluster, so named for its presence in Cu_5Zn_8, is most commonly viewed as a set of four nested polyhedra.[10] The cluster has four distinct atomic sites, named for each of these polyhedra, as shown in Figure 1.3a-d. From the cluster center outward, the four sites are: inner tetrahedron (IT), outer tetrahedron (OT), octahedron (OH), and cubo-octahedron (CO). While these designations make the cluster easier to visualize, the connections shown between atoms are not always as chemically meaningful. For example, the cubo-octahedron connects atoms on the order of 5 Å apart—significantly longer than any reasonable bond distance.

An alternative view of the γ-brass cluster places together the IT and CO sites in a tetrahedron of tetrahedra, and the OT and OH sites in an adamantane-like

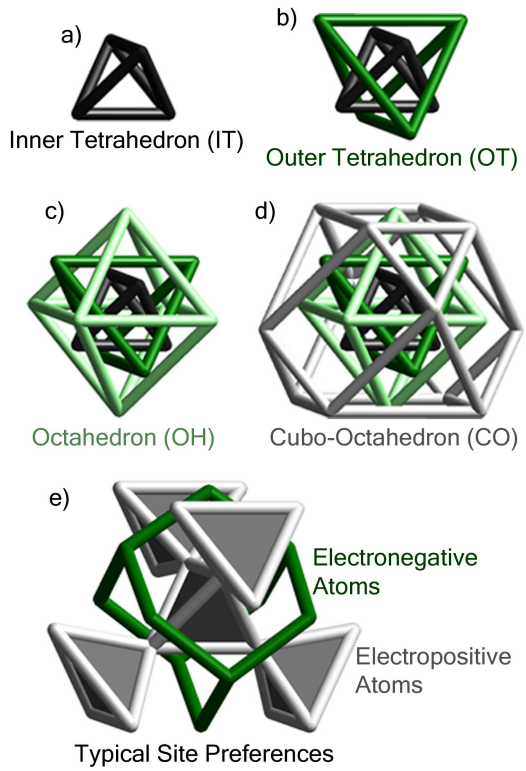

Figure 1.3: The γ-brass cluster, viewed as four nested polyhedra: a) an inner tetrahedron, b) an outer tetrahedron, c) an octahedron, and d) a cubo-octahedron. e) Alternatively, the cluster can be seen as a tetrahedron of tetrahedra and an adamantane cage.

cage. This construction, shown in Figure 1.3e, is more suggestive of the experimental site preferences in many γ-brass variants. In γ-brass itself (Cu_5Zn_8), for example, Zn atoms occupy the IT and CO sites shown in gray, while Cu atoms occupy OT and OH shown in green.[29] More generally, electronic structure calculations have shown that the less electronegative element in a γ-brass variant prefers the IT and CO sites, while the more electronegative element prefers OT and OH.[30]

In addition to the two 26-atom γ-brass clusters, the $Mg_{44}Rh_7$ structure also contains a 34-atom unit known as a Ti_2Ni cluster, so named for its similarity to

the Ti_2Ni structure. Once again, the four distinct sites in this cluster can conveniently be classified as nested polyhedra, as shown in Figure 1.4a-d. The sites are: octahedron (OH), cubo-octahedron[b] (CO), outer tetrahedron (OT), and truncated tetrahedron (TT). This cluster has previously been described as a smaller 22-atom cluster,[27] but for reasons that will become clear soon, we extend it farther. In compounds with the Ti_2Ni structure, experimental site preferences usually place the more electronegative element at the OT site shown in orange.[6] In Ti_2Ni itself, for example, Ni atoms occupy the OT site and Ti atoms occupy the remaining sites.[32] The Ti_2Ni structure, an interlocking network of these Ti_2Ni "clusters," is shown in Figure 1.4e. A single one of these 34-atom units is emphasized, and typical experimental site preferences are indicated.

The fourth and final cluster in $Mg_{44}Rh_7$ will here be described as a 16-atom face-centered cubic unit. This cluster, shown in Figure 1.5, can be viewed in two ways. First, it can be seen as an inner tetrahedron (IT) and a truncated tetrahedron (TT), as in Figure 1.5a-b. Alternatively, as in Figure 1.5c, the cluster can be viewed as parts of three layers of cubic closest packing. Because all atoms in a true face-centered cubic structure are crystallographically equivalent, the cluster concept does not allow us to predict the relative electronegativities of the two different sites, IT and TT.

These four distinct clusters, when placed at the high-symmetry points of the $Mg_{44}Rh_7$ unit cell, give a full atomistic description of the structure. Each of the fourteen crystallographically inequivalent sites in $Mg_{44}Rh_7$ lies at a distinct site in one of these clusters.

[b]This is a cubo-octahedron in name only. It is very distorted, and can be more accurately described as the outer layer of a pyrochlore unit.[31]

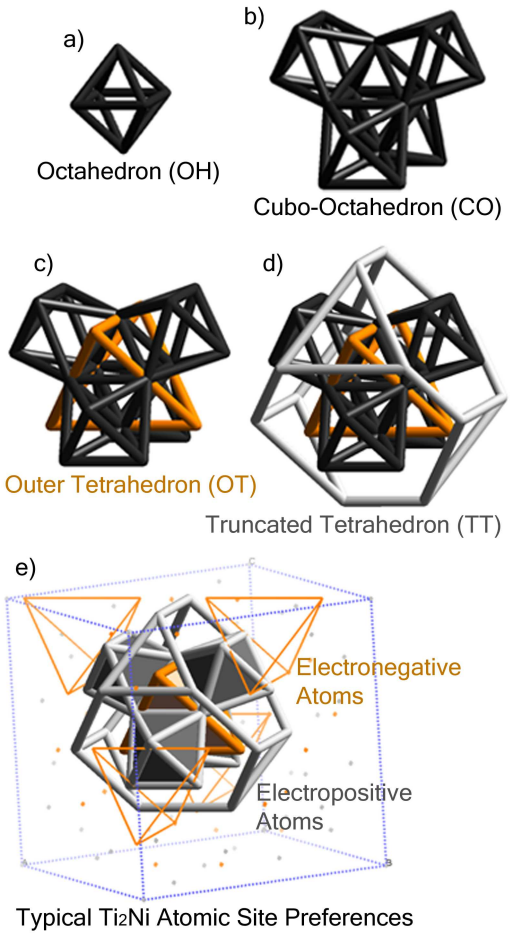

Figure 1.4: The Ti_2Ni cluster, viewed as four nested polyhedra: a) an octahedron, b) a cubo-octahedron that forms octahedra sharing faces with the central octahedron, c) an outer tetrahedron, and d) a truncated tetrahedron. e) The cluster is also shown in the Ti_2Ni structure itself.

1.4 Site Preferences in $Mg_{44}Rh_7$

Based on typical site preferences in the separate γ-brass, Ti_2Ni, and face-centered cubic structures, one can partially rationalize which sites in $Mg_{44}Rh_7$ are likely to be occupied by Mg and Rh. Because Rh (2.28 on the Pauling electronegativity scale) is significantly more electronegative than Mg (1.31), one ex-

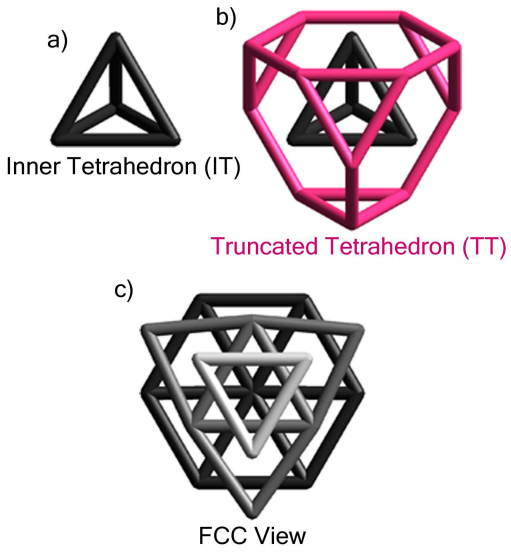

Figure 1.5: The face-centered cubic cluster, first viewed as nested polyhedra: a) an inner tetrahedron and b) a truncated tetrahedron. c) Alternatively, the atoms are shown in cubic close-packed layers.

pects Rh atoms to occupy some combination of the OT and OH sites of the γ-brass clusters (see Figure 1.3) and the OT site of the Ti_2Ni cluster (see Figure 1.4), the electronegative sites of these two structure archetypes. The left half of Figure 1.6 indicates that this prediction is fairly accurate. Of the fourteen crystallographically distinct sites in $Mg_{44}Rh_7$, eleven are occupied by Mg atoms (red vertices), and three by Rh (blue vertices). The three Rh sites are the OT site of γ-brass cluster 1 (γ1-OT[c]), the OH site of γ-brass cluster 2 (γ2-OH), and the OT site of the Ti_2Ni cluster (Ti_2Ni-OT).

Although these site preferences are not entirely surprising, they at the same time show the limitations of the cluster model. The cluster model makes no

[c]Here we begin to introduce our own nomenclature for the crystallographic sites in $Mg_{44}Rh_7$. In the Supporting Information (available online), we provide the names of the sites in past literature about the compound.

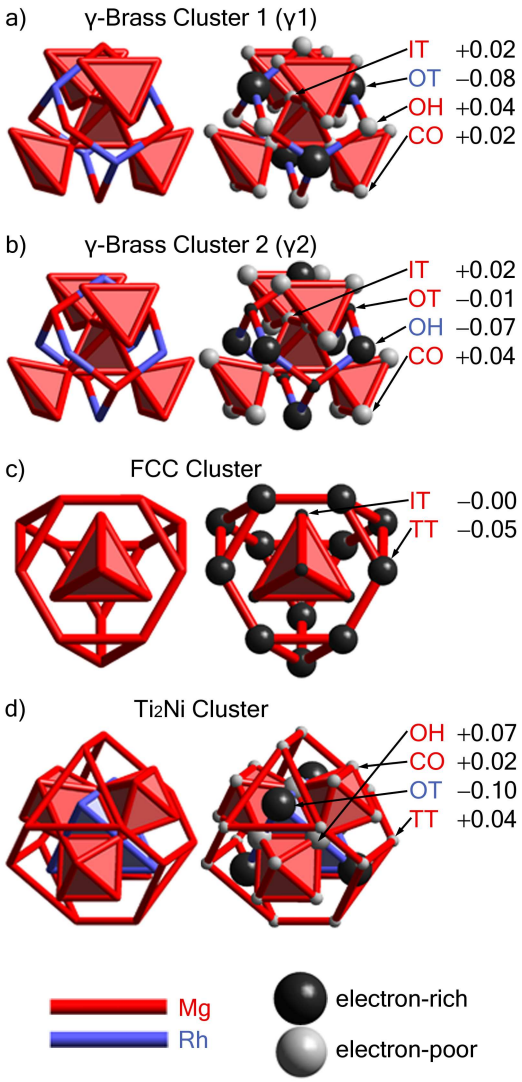

Figure 1.6: On the left, site placements in the four clusters of $Mg_{44}Rh_7$. The three Rh sites in the structure are γ1-OT, γ2-OH, and Ti_2Ni-OT. On the right, Mulliken populations for the homoatomic eH calculation of $Mg_{44}Rh_7$. Charges of greater magnitude are represented by larger spheres. The three most electron-rich sites are occupied by Rh, the more electronegative element.

distinction between the OT and OH sites of the two different γ-brass clusters. It therefore does not explain why the OT site of one γ-brass cluster and the OH site of the other are occupied by Rh.

A quantum mechanically guided description of $Mg_{44}Rh_7$, as we will see, need not have this limitation. To lead us toward understanding the site preferences and constructing such a quantum mechanical description, we use Mulliken populations based on simple electronic structure calculations.

The procedure used to calculate Mulliken populations of the fourteen sites in $Mg_{44}Rh_7$ is given in the Computational Methods section of this paper. The results of this calculation are shown in the right half of Figure 1.6. Black and white spheres, their radii scaling with the magnitudes of the charges, are used to represent electron-rich and electron-poor sites. We note two key results of this calculation. First, the three most electron-rich sites are the three sites occupied by Rh atoms. This is expected, as Rh is the more electronegative element. Therefore, extended Hückel Mulliken populations agree with the experimentally known site preferences. The second result is more surprising. The Mulliken populations tell us that after the three Rh sites, the next most electron-rich site is the TT site of the face-centered cubic cluster (FCC-TT), which is occupied by Mg. Based on the cluster concept described earlier, we might have expected the remaining OT and OH sites in the γ-brass clusters (γ2-OT and γ1-OH) to be more electron-rich. However, after the three Rh sites, the FCC-TT site is the next most electron-rich by a significant margin.

The Mulliken populations suggest that there are features of $Mg_{44}Rh_7$ which the cluster concept alone cannot explain. At the heart of our problem, we must devise a description that differentiates the γ1-OT and γ2-OH sites, which are

quite electron-rich and occupied by Rh, from the γ2-OT and γ1-OH sites, which are less electron-rich and occupied by Mg. Also, our description must explain why the FCC-TT site is as electron-rich as it is. From this point forward, we use these facts to help us build upon the cluster view, and guide us toward a more telling description of the $Mg_{44}Rh_7$ structure. In doing so, we will show how some interesting geometric features arise naturally from an elaborate twinning network of the clusters.

1.5 Searching for Less Obvious Clusters

The previous results are tantalizing. They suggest that a cluster description can be used to rationalize some but not all of the atomic site preferences and Mulliken populations in the $Mg_{44}Rh_7$ structure. We posit that the limitation of the current cluster method is not inherent in the use of clusters, but rather a result of the fact that the clusters considered so far are centered solely at points of high crystallographic symmetry. While visually appealing, there is no reason that high-symmetry clusters are more chemically meaningful than those at other locations in the unit cell. We proceed to examine critically and systematically the $Mg_{44}Rh_7$ structure for clusters similar to those previously described, but which are not located at high-symmetry points.

Which cluster types might we search for? In the case of $Mg_{44}Rh_7$, the natural cluster types are the three already found at high-symmetry points—the γ-brass, Ti_2Ni, and FCC cluster types. As we are to use this cluster analysis to explain site preferences and Mulliken populations, and as the FCC structure is an elemental structure in which all sites are equivalent, we limit our search to the γ-brass and

Ti_2Ni clusters.

We first search the unit cell for γ-brass clusters. As discussed earlier, the innermost layer of a γ-brass cluster (Figure 1.3a) is the inner tetrahedron. We therefore begin by looking for all distinct tetrahedra in the $Mg_{44}Rh_7$ structure. To ensure that these tetrahedra are nearly regular in geometry, we require that pairs of atoms within a tetrahedron are separated by no more than 3.52 Å—10% longer than the distance between nearest neighbors in elemental Mg. There are twenty-three distinct tetrahedra in $Mg_{44}Rh_7$ that obey this criterion. We next determine which of these twenty-three tetrahedra also possess the second layer of the γ-brass cluster, the outer tetrahedron (Figure 1.3b). The second layer consists of four atoms that cap each face of the inner tetrahedron, forming four more face-sharing tetrahedra. We therefore look for candidates with four face-sharing tetrahedra (again with contacts no longer than 3.52 Å) around the inner tetrahedron.

As shown in Table 1.1, only six of the twenty-three tetrahedra are the centers of the two innermost layers of the γ-brass cluster, the inner and outer tetrahedra. For these six remaining candidates, we continue this process, checking whether the third layer (Figure 1.3c, the octahedron) and fourth layer (Figure 1.3d, the cubo-octahedron) of the γ-brass cluster are present. The result is that the only two of these six candidates that contain all four γ-brass sites are the two previously described γ-brass clusters centered at high-symmetry points. The other four candidates, as it turns out, are contained entirely within the outer layers of one of these two high-symmetry γ-brass clusters. This means that, outside of the two conventional γ-brass clusters, the $Mg_{44}Rh_7$ structure does not have even so much as the two innermost shells of a γ-brass cluster elsewhere in the

structure.

Table 1.1: γ-Brass clusters in the $Mg_{44}Rh_7$ structure.

Atoms in tetrahedron (all contacts ≤ 3.52 Å)	# of face-sharing tetrahedra	Complete γ-brass cluster?	Identity
γ1-IT,IT,IT,IT	4	Yes	γ-brass cluster 1
γ2-IT,IT,IT,IT	4	Yes	γ-brass cluster 2
γ1-IT,IT,IT,OT	4	No	
γ1-IT,IT,OT,OH	4	No	
γ2-IT,IT,IT,OT	4	No	
γ2-IT,IT,OT,OH	4	No	

The search for copies of the Ti_2Ni cluster proves more interesting. Recall that the innermost layer of a Ti_2Ni cluster (Figure 1.4a) is the octahedron. We therefore begin by searching for all the octahedra in $Mg_{44}Rh_7$. Again, we require that all atoms within an acceptable octahedron are located no more than 3.52 Å from their four nearest neighbors in the octahedron. As indicated by the first column of Table 1.2, only six such octahedra exist in the $Mg_{44}Rh_7$ structure. We narrow this list further by determining which of these candidates possess the second layer of the Ti_2Ni cluster, the cubo-octahedron (Figure 1.4b). The second layer consists of twelve atoms that create four octahedra sharing faces of the central octahedron. We therefore look for candidates with four face-sharing octahedra (again with contacts no longer than 3.52 Å) around the central octahedron. This leaves three candidates, as the second column of Table 1.2 shows. Continuing the examination of these three remaining candidates, we find that all three also possess the third layer (Figure 1.4c, the outer tetrahedron) and fourth layer (Figure 1.4d, the truncated tetrahedron) of the Ti_2Ni cluster. One of them (the octahedron consisting of six Ti_2Ni-OH atoms) is simply the conventional Ti_2Ni

cluster centered at a high-symmetry point. The other two, which are not centered at high-symmetry points, are new to us and will be discussed further in the next section.

Table 1.2: Ti_2Ni clusters in the $Mg_{44}Rh_7$ structure.

Atoms in octahedron (all contacts ≤ 3.52 Å)	# of face-sharing octahedra	Complete Ti_2Ni cluster?	Identity
Ti_2Ni-OH, Ti_2Ni-OH Ti_2Ni-OH, Ti_2Ni-OH Ti_2Ni-OH, Ti_2Ni-OH	4	Yes	Ti_2Ni cluster
Ti_2Ni-OH, Ti_2Ni-OH Ti_2Ni-OH, Ti_2Ni-CO Ti_2Ni-CO, Ti_2Ni-CO	4	Yes	Ti_2Ni twin 1
γ1-CO, Ti_2Ni-OH Ti_2Ni-CO, Ti_2Ni-CO Ti_2Ni-TT, Ti_2Ni-TT	4	Yes	Ti_2Ni twin 2
FCC-IT, FCC-IT FCC-IT, FCC-TT FCC-TT, FCC-TT	3	No	Ti_2Ni partial twin 1
γ2-CO, γ2-CO Ti_2Ni-TT, FCC-IT FCC-TT, FCC-TT	3	No	Ti_2Ni partial twin 2
γ1-OH, γ1-CO γ2-CO, Ti_2Ni-CO Ti_2Ni-TT, FCC-TT	3	No	Ti_2Ni partial twin 3

1.6 Understanding Site Preferences: γ1-OT and γ2-OH vs. γ2-OT and γ1-OH

In the previous section, it was concluded that, while the $Mg_{44}Rh_7$ structure contains no copies of the γ-brass cluster aside from those centered at high-symmetry points, two additional copies of the Ti_2Ni cluster are present, and could be worth further analysis. Figure 1.7 shows where these two "twins" of the Ti_2Ni cluster are located as compared to the high-symmetry clusters. In Figure 1.7a, we begin with several conventional clusters (i.e., clusters centered at high-symmetry points)—one Ti_2Ni cluster, three FCC clusters, and one γ-brass 1 cluster. Figure 1.7b highlights thirty-four atoms at the interface of the conventional clusters which, as Figure 1.7c shows, constitute one of the twins of the Ti_2Ni cluster. Although this set of atoms, which we will refer to as Ti_2Ni twin 1, lacks the true tetrahedral symmetry of the conventional Ti_2Ni cluster, it has all thirty-four atoms with only minor distortion. Similarly, the bottom half of Figure 1.7 shows the second type of Ti_2Ni twin, which we will refer to as Ti_2Ni twin 2. At the interface of one conventional Ti_2Ni, two FCC, two γ-brass 1, and one γ-brass 2 cluster (Figure 1.7d), another group of thirty-four atoms (Figure 1.7e) is shown to be a twin of the Ti_2Ni cluster (Figure 1.7f).

Taken alone, the observation of twins of the Ti_2Ni cluster is nothing more than a geometric curiosity. However, when considered along with the experimental Mg vs. Rh site preferences, the twins take on a more fundamental role in describing the electronic structure of $Mg_{44}Rh_7$. As it turns out, we may use the original Ti_2Ni cluster and its twins to account for the Mg vs. Rh site preferences in $Mg_{44}Rh_7$—in particular, to sort out the mystery of why Rh atoms occupy dif-

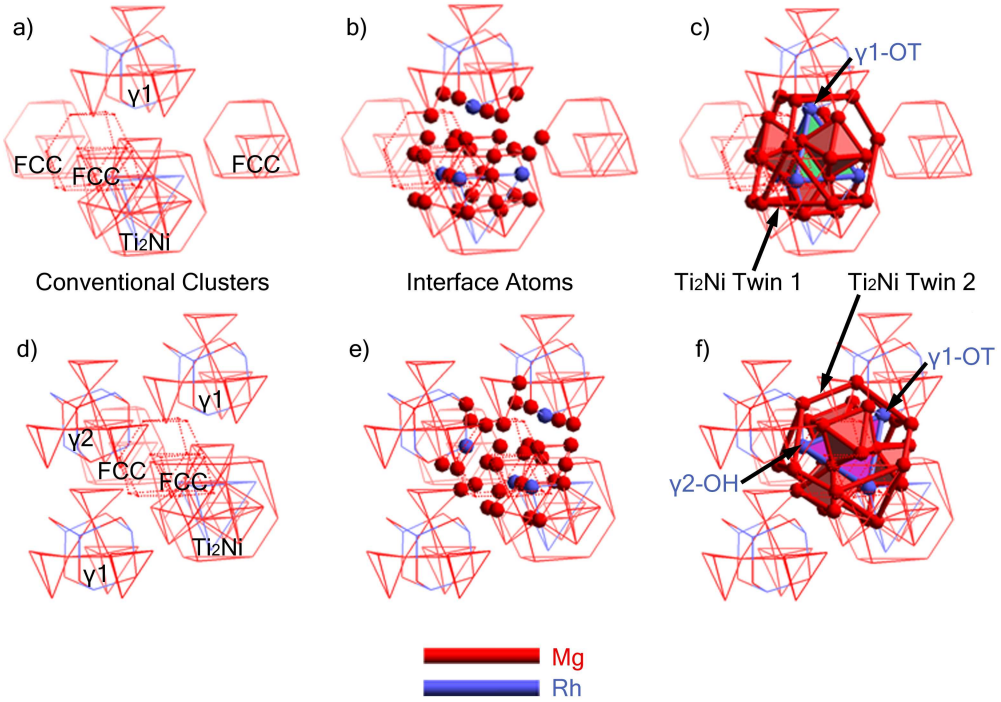

Figure 1.7: Two types of twins of the Ti_2Ni cluster, constructed at the interfaces of the conventional clusters. a,d) Conventional clusters are centered at high-symmetry points in the crystal. b,e) Thirty-four atoms at the conventional cluster interfaces c,f) are connected to form Ti_2Ni twins.

ferent sites in the two γ-brass clusters.

Without even considering the symmetry of $Mg_{44}Rh_7$ or the names of the various crystallographic sites, one can look at the Ti_2Ni cluster (Figure 1.6d) and twins (Figure 1.7c,f), and see that they have strong similarities. In all three 34-atom units, there are exactly four Rh atoms, and they occupy the four positions on the outer tetrahedron. These are exactly the positions at which we would expect electronegative atoms to be found, based on known compounds with the Ti_2Ni structure (see Figure 1.4). However, because the Ti_2Ni fragments are crystallographically inequivalent, the Rh atoms on their outer tetrahedra have

different crystallographic names. In the high-symmetry Ti_2Ni cluster, the four Rh atoms are all located at Ti_2Ni-OT positions. In Ti_2Ni twin 1 (Figure 1.7c), they occupy three Ti_2Ni-OT positions and one $\gamma 1$-OT position. And in Ti_2Ni twin 2 (Figure 1.7f), they occupy two Ti_2Ni-OT positions, one $\gamma 1$-OT position, and one $\gamma 2$-OH position.

Thus, the tendency of electronegative Rh atoms to occupy the positions on the outer tetrahedra of Ti_2Ni clusters and twins explains why they are present at the $\gamma 1$-OT and $\gamma 2$-OH sites, and not at the $\gamma 2$-OT and $\gamma 1$-OH sites. Rather than seeing the three Rh sites in $Mg_{44}Rh_7$ as a hodgepodge of positions on different clusters, it is therefore less mysterious to view them as the positions on the outer tetrahedron of each occurrence of a Ti_2Ni cluster or twin.

1.7 Rationalizing Mulliken Populations: The FCC-TT Site

That the Ti_2Ni cluster and twins successfully account for the Mg vs. Rh site preferences in $Mg_{44}Rh_7$ is most encouraging. But it still does not answer the question of why FCC-TT is the most electron-rich of the Mg sites. This question can be addressed by taking our twinning picture one step farther, and noting that the $Mg_{44}Rh_7$ structure contains yet more fragments of Ti_2Ni. Recall from Table 1.2 that, in addition to the octahedra at the centers of the high-symmetry Ti_2Ni cluster and its two twins, there are three more types of octahedra in the $Mg_{44}Rh_7$ structure. As it turns out, each of these three octahedra forms the center of a 25-atom partial twin of the Ti_2Ni cluster, illustrated in Figure 1.8. Each of these partial twins is missing nine atoms from the conventional cluster—three from the cubo-octahedron and six from the truncated tetrahedron—which are

highlighted in Figure 1.8b. Unlike the partial γ-brass clusters that were excluded from consideration earlier in this paper, these partial Ti_2Ni twins do not reside within the previously established Ti_2Ni cluster or twins.

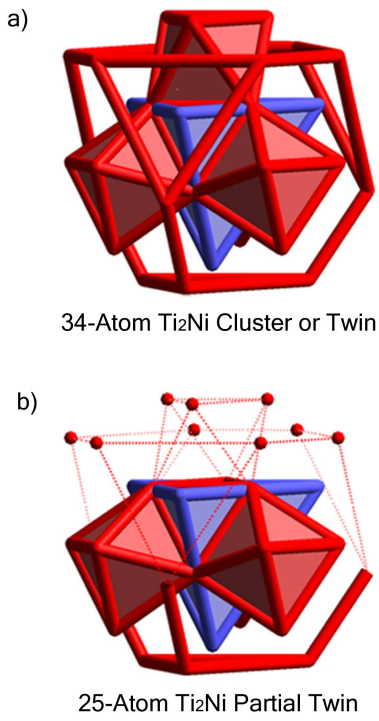

Figure 1.8: The atoms that comprise the Ti_2Ni partial twins in $Mg_{44}Rh_7$. As compared to a) the Ti_2Ni cluster and twins previously discussed, b) the Ti_2Ni partial twins lack nine atoms (three from the cubo-octahedron and six from the truncated tetrahedron) that are significantly displaced from their original positions.

The placements of these three types of Ti_2Ni partial twins within the $Mg_{44}Rh_7$ structure are shown in Figure 1.9. Once again, their importance becomes apparent when one notes which sites are on their outer tetrahedra. In Ti_2Ni partial twin 1 (Figure 1.9b), the outer tetrahedron consists of one Rh atom at a Ti_2Ni-OT position and three Mg atoms at FCC-TT positions (recall that the FCC-TT site is by Mulliken population the most electron-rich Mg site). In partial

twin 2 (Figure 1.9c), the outer tetrahedron consists of one Rh atom at a Ti_2Ni-OT position, a second Rh atom at a γ2-OH position, and two Mg atoms at FCC-TT positions. Finally, in partial twin 3 (Figure 1.9d), the outer tetrahedron consists of one Rh atom at a Ti_2Ni-OT position, a second Rh atom at a γ1-OT position, a third Rh atom at a γ2-OH position, and one Mg atom at a FCC-TT position.

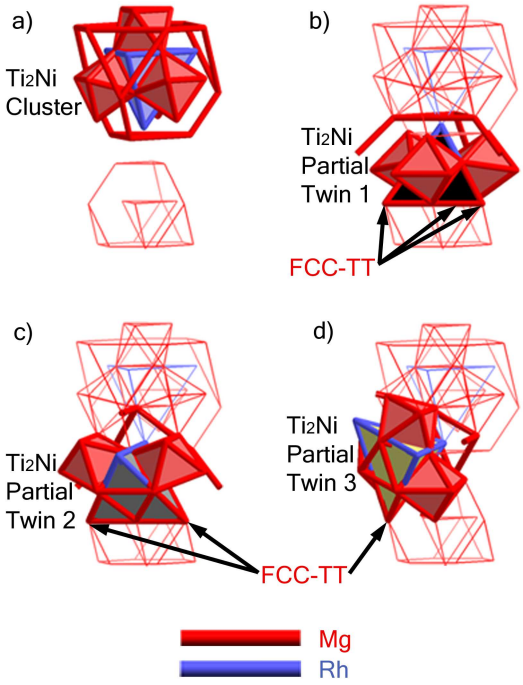

Figure 1.9: Three types of partial twins of the Ti_2Ni cluster, constructed at the interfaces of the conventional clusters. a) Conventional clusters are centered at high-symmetry points in the crystal. b-d) Twenty-five atoms at the conventional cluster interfaces are connected to form Ti_2Ni partial twins.

To sum up, each of the three types of Ti_2Ni partial twins have outer tetrahedra consisting of some combination of the three Rh sites and the single most electron-rich Mg site—the FCC-TT site. This suggests why in our eH electronic structure calculations, FCC-TT was the most electron-rich of the eleven Mg sites in $Mg_{44}Rh_7$. This result can now be explained by the observation that the FCC-

TT site lies on the outer tetrahedra of all three types of Ti_2Ni partial twins. To put it another way, because the FCC-TT site has an environment similar to that of the three Rh sites once we allow ourselves to see the partial twins, it is not surprising that the FCC-TT site is nearly as electron-rich as the Rh sites.

The twinning of Ti_2Ni clusters appears to correlate with the electron-richness of the various crystallographic sites in $Mg_{44}Rh_7$. In Table 1.3, we further demonstrate this correlation by showing how the Mulliken population of an atom varies with the number of Ti_2Ni fragments in which it appears on the outer tetrahedron. We see that the larger the number of ways an atom can be shown on the outer tetrahedron of a Ti_2Ni unit, the more electron-rich that atom is in our electronic structure calculations.

Table 1.3: Ranking the Mulliken populations.

Site	Atom Type	Mulliken Population	# of appearances on outer tetrahedron of Ti_2Ni fragment
Ti_2Ni-OT	Rh	–0.10	20
γ1-OT	Rh	–0.08	10
γ2-OH	Rh	–0.07	8
FCC-TT	Mg	–0.05	5
γ2-OT	Mg	–0.01	0
FCC-IT	Mg	–0.00	0
γ1-IT	Mg	+0.02	0
γ1-CO	Mg	+0.02	0
γ2-IT	Mg	+0.02	0
Ti_2Ni-CO	Mg	+0.02	0
γ1-OH	Mg	+0.04	0
γ2-CO	Mg	+0.04	0
Ti_2Ni-TT	Mg	+0.04	0
Ti_2Ni-OH	Mg	+0.07	0

1.8 Fivefold Symmetry and the Edge-Capped Stella Quadrangula

In the previous section, we found that the four most electron-rich sites in the $Mg_{44}Rh_7$ structure all lie on electron-rich positions of the Ti_2Ni fragments. This modified cluster view successfully accounts for the site preferences and the ordering of Mulliken populations in $Mg_{44}Rh_7$. Nonetheless, there are some potentially troubling aspects of this cluster picture. Perhaps the most troubling aspect of our current description is its complete focus on individual Ti_2Ni fragments, rather than the interplay among them. We have yet to describe how the Ti_2Ni pieces fit together within the larger crystal structure. And yet, the interplay among the various Ti_2Ni fragments must have important consequences to the structure. For example, as we have already seen, each atom at the most electron-rich site in the $Mg_{44}Rh_7$ structure (Ti_2Ni-OT) sits simultaneously on twenty Ti_2Ni pieces. Not only do Ti_2Ni fragments lie near each other, they in fact overlap with one another in what seems at first a structurally complex manner.

In this section, we begin to explore the structural interplay among the Ti_2Ni fragments in $Mg_{44}Rh_7$. We will focus our attention on just the core region of each Ti_2Ni piece. In this manner, we will find components that do not overlap spatially, but instead share faces, edges, and vertices with one another. As such sharings are familiar to solid-state chemists, the juxtaposition of the Ti_2Ni fragments becomes much easier to visualize.

We begin our simplified description in Figure 1.10, directing much of our focus to the electron-rich outer tetrahedron of each Ti_2Ni piece. Each panel of this figure covers the same region in the $Mg_{44}Rh_7$ structure, but emphasizes a

particular feature of the structure. Panels 1.10a-e emphasize different individual 34-atom Ti_2Ni clusters or twins in the region. As these pictures show, and as we discussed above, the various Ti_2Ni fragments lie in an overlapping arrangement. Our understanding of the relative placement of these fragments sharpens if we focus just on the outer tetrahedron of each Ti_2Ni piece. Each of these outer tetrahedra consists of four Rh atoms. In Figure 1.10f, we examine five of these outer tetrahedra, represented as opaque blue, green, and purple units. (Each color of tetrahedron represents a crystallographically distinct Ti_2Ni cluster or twin, consistent with the first five panels of the figure.) These five outer tetrahedra share faces, edges, and vertices with one another, but unlike the full Ti_2Ni pieces, do not overlap in space. As Figure 1.10f shows, the outer tetrahedra take on the appearance of a fivefold wheel. For the sake of clarity, only one fivefold wheel is shown. But there are actually five more crystallographically equivalent interpenetrating wheels sharing the same conventional (blue) Ti_2Ni cluster.

In Figure 1.11, we extend beyond the fivefold wheels to build an even larger unit consisting of the outer tetrahedra of Ti_2Ni fragments. The previously described fivefold wheel (Figure 1.11a) is actually part of an icosahedron (Figure 1.11b). The twenty tetrahedra that comprise this icosahedron[d] (nineteen of which are slightly distorted) are all outer tetrahedra of the various types of Ti_2Ni clusters, twins, and partial twins (Figure 1.11c). This is consistent with the fact that each Rh atom at a Ti_2Ni-OT site is part of twenty different Ti_2Ni units (see Table 1.3). We extend this picture farther in Figure 1.11d by showing that the icosahedron of Ti_2Ni outer tetrahedra is part of an even larger unit—a formation consisting of four interlocking icosahedra, in which each tetrahedron is the outer tetrahedron of a Ti_2Ni cluster, twin, or partial twin.

[d] An icosahedron with an atom in its center can also be viewed as twenty face-sharing tetrahedra.

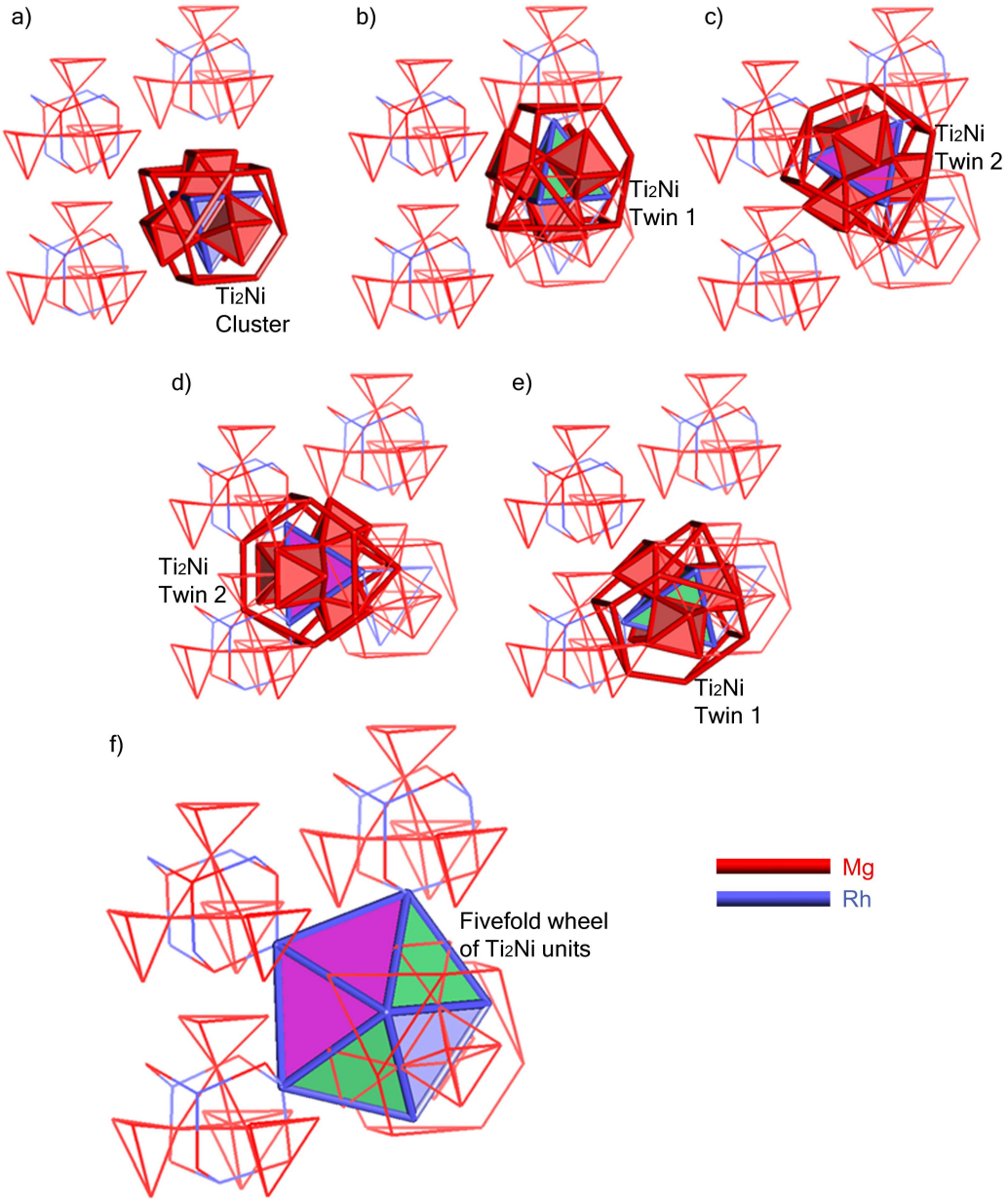

Figure 1.10: Six views of the same region of the $Mg_{44}Rh_7$ structure: a) the conventional cluster view, b-e) four views showing twins of the Ti_2Ni cluster at the interfaces of the conventional clusters, and f) a view emphasizing the fivefold symmetry that accompanies this twinning of the Ti_2Ni cluster.

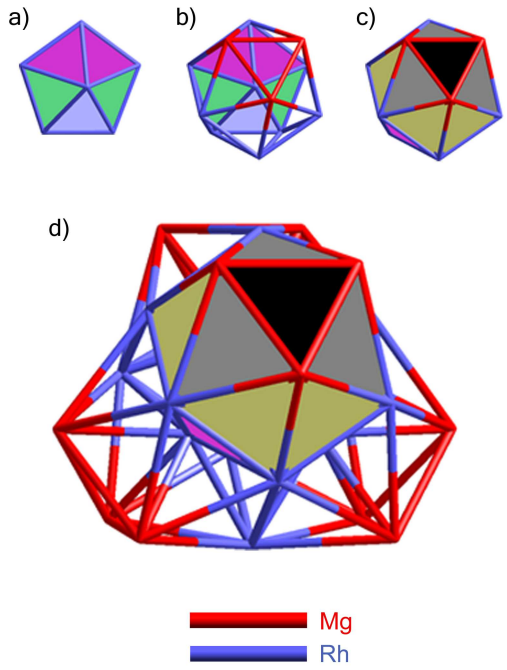

Figure 1.11: Larger features of fivefold symmetry in the $Mg_{44}Rh_7$ structure. a) The fivefold wheel of outer tetrahedra of Ti_2Ni fragments is part of b,c) an icosahedron of such outer tetrahedra. This icosahedron is in turn part of d) a formation of four interlocking icosahedra.

Although Figure 1.11 illustrates how the various outer tetrahedra fit together, it does not yet give us a sense of where the distinct crystallographic sites lie in the $Mg_{44}Rh_7$ structure. In Figure 1.12, we build this same construction from the center outward, one crystallographic site at a time. We start with the outer tetrahedron of the conventional high-symmetry Ti_2Ni cluster, consisting of four Ti_2Ni-OT atoms (Figure 1.12a). We cap the four faces of this tetrahedron with Rh atoms at the γ1-OT positions, forming the outer tetrahedra of Ti_2Ni twin 1 (Figure 1.12b). Next, we cap the edges of the resulting polyhedron with six Rh atoms at the γ2-OH positions, forming the outer tetrahedra of Ti_2Ni twin 2 (Figure 1.12c). Finally, we cap the edges again with twelve Mg atoms at the

FCC-TT positions, forming the outer tetrahedra of all three types of Ti_2Ni partial twins (Figure 1.12d).

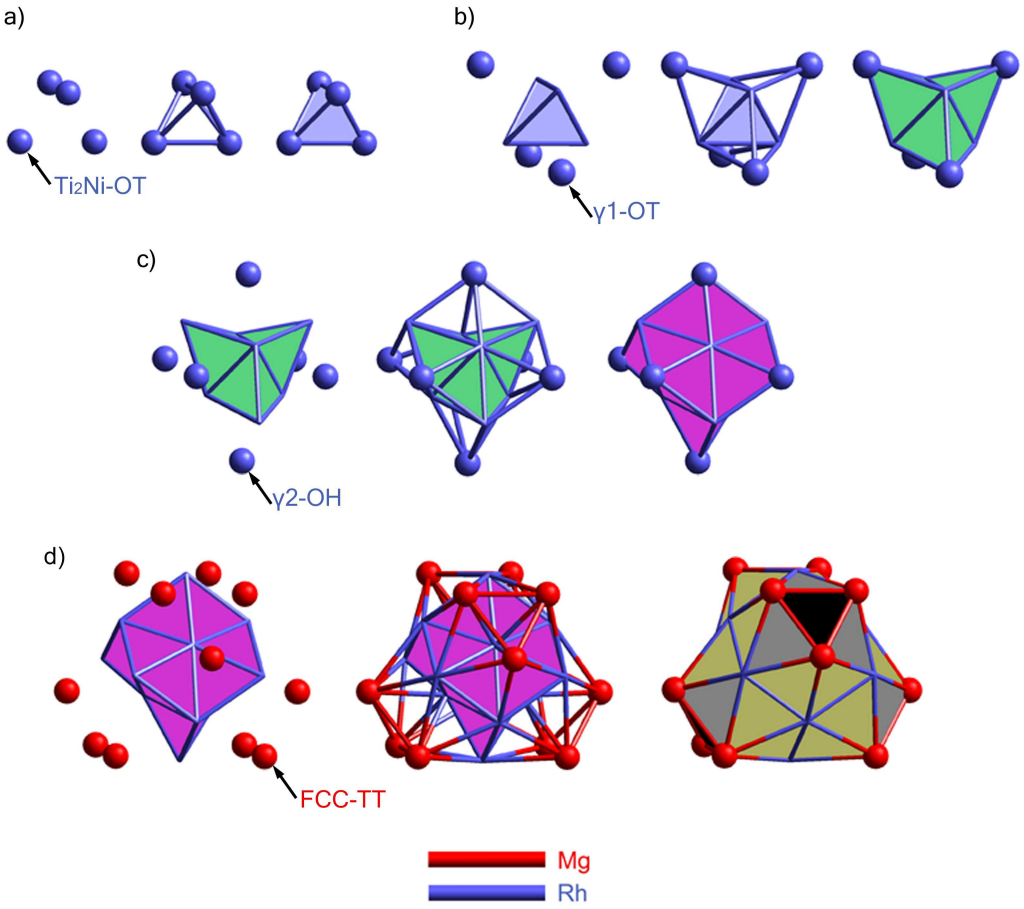

Figure 1.12: An alternate way to build up the interlocking icosahedra, this time from center outward. a-d) The outer tetrahedra of the various Ti_2Ni fragments are placed face-to-face to form the same 26-atom arrangement as shown earlier.

This set of twenty-six atoms in Figure 1.11d and 1.12d is known as an edge-capped stella quadrangula, and has been previously noted for its prevalence in intermetallic and ionic structures.[e] We see here that the outer tetrahedra of the

[e]When Nyman and Andersson introduced the edge-capped stella quadrangula, they suggested that it is the furthest extent to which tetrahedra can be packed in space without severe distortion. They also asserted that the stella quadrangula and its edge-capped variants are important building units in many intermetallic and ionic structures.[33,34]

various Ti_2Ni units in $Mg_{44}Rh_7$ form an edge-capped stella quadrangula. As demonstrated in Figure 1.13 via Mulliken populations, this edge-capped stella quadrangula proves to be the essential unit not just in locating the electron-rich atoms on the outer tetrahedra of Ti_2Ni pieces, but in understanding all the crystallographic sites in the $Mg_{44}Rh_7$ structure.

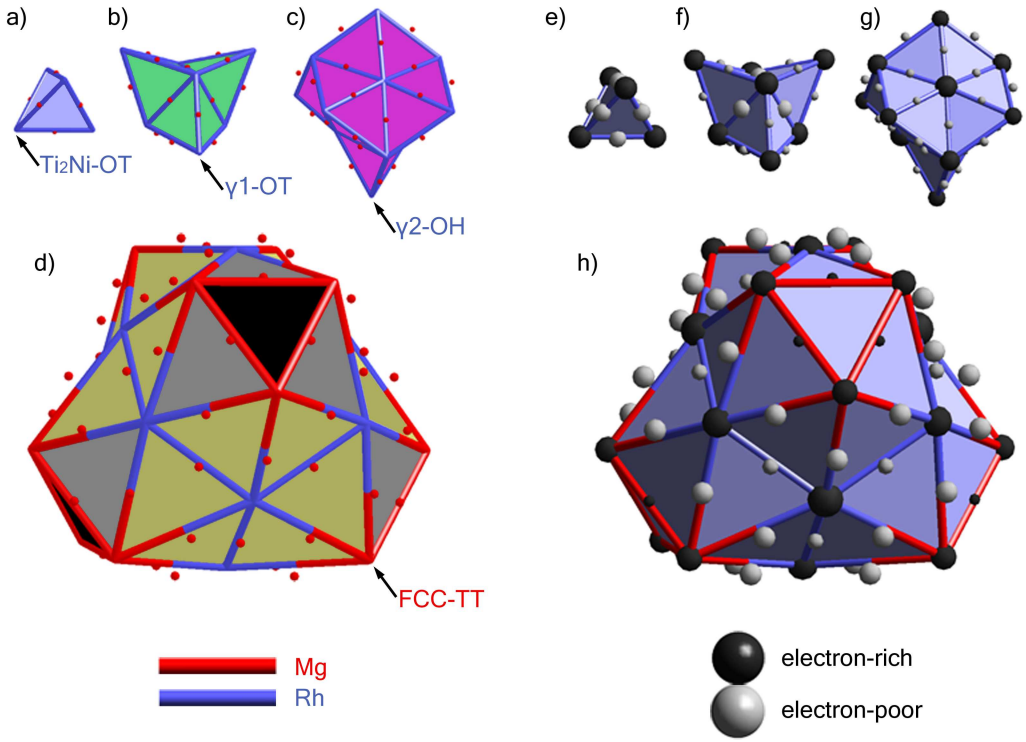

Figure 1.13: Site preferences and Mulliken populations within the edge-capped stella quadrangula. a-d) The edge-capped stella quadrangula is again built in layers, this time with Mg atoms at the center of each edge. e-h) Mulliken populations show that electron-rich atoms occupy the vertices, while electron-poor or neutral atoms occupy the edge-centers.

1.9 The Electronic Basis of the Stella Quadrangula Model

In the left half of Figure 1.13, we again build the edge-capped stella quadrangula from center outward, this time showing all the atoms in the vicinity, rather than just those on the outer tetrahedra of Ti_2Ni fragments. The newly introduced atoms, all of which are Mg and are represented by red balls, are located at roughly the center of each edge of this construction.

We now come to an important point. As shown in the right half of Figure 1.13, the atoms on the vertices and those on the edges differ *electronically*. The atoms on the vertices of the edge-capped stella quadrangula (i.e., those on the outer tetrahedra of Ti_2Ni fragments) are electron-rich, while the atoms on the edges are electron-poor or neutral.

This construction therefore illustrates a potentially chemically significant order in the $Mg_{44}Rh_7$ structure. Rather than describing the structure as a hodgepodge of clusters in which site preferences and Mulliken populations are somewhat mysterious, we now describe it in terms of a single building block from which the site preferences and relative Mulliken populations follow naturally. We now see an edge-capped stella quadrangula in which electron-rich atoms occupy the vertices, and electron-poor or neutral atoms lie at the center of each edge.

1.10 Surprising Features of $Mg_{44}Rh_7$

Our description of $Mg_{44}Rh_7$ highlights some remarkable features of the structure. One such feature is the presence of the same repeating motif—the edge-

capped stella quadrangula—on different length scales within $Mg_{44}Rh_7$. The edge-capped stella quadrangula is identical to a grouping we introduced early in this paper, but referred to by a different name. As shown in Figure 1.14, the 26-atom edge-capped stella quadrangula is fully equivalent to the 26-atom γ-brass cluster. But there is an important difference between the γ-brass clusters we described in Figure 1.3 and the edge-capped stella quadrangula we introduced in Figure 1.11. The γ-brass clusters occur on roughly the length scale of the chemical bond (nearest neighbors lie between 2.69 and 3.88 Å apart), and include all atoms within a given region of the $Mg_{44}Rh_7$ structure. The edge-capped stella quadrangula we introduced in Figure 1.11, however, is on a longer length scale (nearest neighbors lie between 5.56 and 6.43 Å apart), and does not include all atoms in the region. It includes only the most electron-rich atoms in the $Mg_{44}Rh_7$ structure—the three Rh sites, and the most electron-rich Mg site.

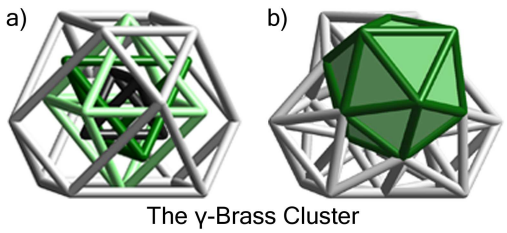

Figure 1.14: Two views of the 26-atom γ-brass cluster. The cluster can be described a) as nested polyhedra or b) as an edge-capped stella quadrangula, consisting of four interlocking icosahedra.

This suggests a fractal-like hierarchy in the $Mg_{44}Rh_7$ structure. At the length scale of chemical bonds, atoms arrange themselves in 26-atom γ-brass clusters, which are equivalent to edge-capped stellae quadrangulae. Meanwhile, the most electron-rich atoms in the structure fix their positions at the vertices of larger 26-atom edge-capped stellae quadrangulae. All of these polyhedra

on different length scales interpenetrate to form the intricate $Mg_{44}Rh_7$ structure that nature so cleverly devised.

The second remarkable feature of $Mg_{44}Rh_7$ is the prevalence of fivefold symmetry in its diffraction pattern. As illustrated throughout this paper, and previously by Samson and Hansen,[8] the $Mg_{44}Rh_7$ structure is filled with features of approximate fivefold symmetry, in the form of fivefold wheels, icosahedra, and edge-capped stellae quadrangulae. The structure as a whole also exhibits a push toward fivefold symmetry, which manifests itself not only in the crystallographic geometry, but also in a striking way in reciprocal space. Note the approximate fivefold symmetry in the simulated single crystal diffraction pattern of $Mg_{44}Rh_7$ in the [110] direction,[35] shown in Figure 1.15.

Interestingly, the fivefold symmetry in $Mg_{44}Rh_7$ is along the $\langle 110 \rangle$ directions, rather than the $\langle 1\tau 0 \rangle$ directions more commonly associated with quasicrystal approximants.[36] Although the apparent fivefold symmetry in $Mg_{44}Rh_7$ cannot be true crystallographic symmetry, the diffraction pattern can apparently approach fivefold symmetry as a limit as fivefold formations within the structure become increasingly decorated. This approximate fivefold symmetry could well be an essential part of the stability of the compound.

1.11 Conclusion

We have presented a new description of the $Mg_{44}Rh_7$ structure. There are several features of our lengthy description that we believe are worth noting. First, the computational methods used in this paper are simple enough to allow for calculations of even the largest known intermetallic and ionic crystal structures,

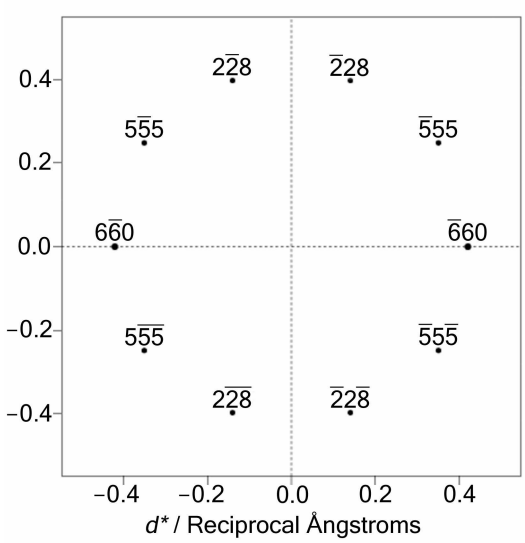

Figure 1.15: Simulated single crystal X-ray diffraction pattern of $Mg_{44}Rh_7$, viewed in the [110] direction. Only the ten brightest peaks are shown. We provide a more complete list of peaks in the Supporting Information (available online).

which have upwards of one thousand atoms per unit cell. But perhaps more importantly, our approach suggests a general way in which large intermetallic structures can be understood. As long as one chooses an appropriate cluster to search for, our approach can be generalized to a wide variety of structures. The search algorithm we employed, which checks the entire unit cell for copies of a given atomic arrangement, is an unbiased way to locate a given geometric feature.

The concept of identifying important building units and searching for them in a structure is already deeply ingrained in the minds of chemists. When organic chemists view molecules, their eyes are drawn to familiar motifs such as aromatic rings and cyclohexane rings, from which they have come to expect certain chemical behaviors. The approach in this paper is predicated on this same

idea of systematically searching for familiar (and in our case, fundamentally intermetallic) chemical units, such as the 26-atom γ-brass cluster or the 34-atom Ti_2Ni cluster, to explore an unfamiliar crystal structure.

The concept of viewing a solid-state structure as a combination of overlapping atomic clusters (as in Figures 1.7, 1.9, and 1.10) is also one with a parallel in organic chemistry—namely, resonance. When organic chemists invoke resonance, they draw multiple configurations of two-electron bonds because just one configuration cannot satisfactorily describe the electronic structure. Likewise, we highlight multiple copies of overlapping clusters[f] because just one cluster cannot account for all site preferences and Mulliken populations in $Mg_{44}Rh_7$. Our observation that the most electron-rich sites in $Mg_{44}Rh_7$ are those that appear on the outer tetrahedra of the most Ti_2Ni fragments, is equivalent to saying the most electron-rich atoms are those that lie at electron-rich positions in the greatest number of resonance structures.

Because we use electronic structure calculations as a guide, the goal of our approach is to uncover geometric features that are more likely to be of chemical importance to the compound. These features—notably the fractal-like structure with edge-capped stellae quadrangulae on different length scales, and the approximate fivefold symmetry of the $\langle 110 \rangle$ single crystal diffraction patterns—are present in many other complicated intermetallic and ionic structures. Only by cataloguing these and similar features in a variety of structures can we hope to explore the open question of what drives such complex crystal structures to exist.

[f] When dealing with solid-state structures, one who applies this technique is often said to wear "Schnering's spectacles".[37]

1.12 Computational Methods

We used LDA-DFT-calibrated extended Hückel (eH) calculations to derive the experimentally known Mg vs. Rh site preferences in $Mg_{44}Rh_7$. Using the same "generic" atomic parameters at all atomic sites in $Mg_{44}Rh_7$, Mulliken populations were calculated, and the more electronegative Rh atoms were assumed to prefer sites with larger Mulliken populations. This assumption has been successfully employed to derive intermetallic site preferences many times in the past.[30,38–42] But before Mulliken populations could be calculated, atomic parameters for the eH calculation of $Mg_{44}Rh_7$ were calibrated against LDA-DFT calculations to ensure that they were physically reasonable.

As a first step in the parameter calibration process, a "parent compound" was selected—one with a somewhat similar stoichiometry and structure to the compound of interest, but with a unit cell small enough to allow LDA-DFT calculations. In this case, a reasonable choice was Mg_5Rh_2, which crystallizes in hexagonal space group $P6_3/mmc$ (No. 194).

Next, the LDA-DFT band structure of the parent compound Mg_5Rh_2 was calculated using the VASP package[43–46] with ultra-soft Vanderbilt pseudopotentials.[47] Starting with the experimentally determined crystal structure of Mg_5Rh_2,[48] unit cell dimensions and atomic positions were optimized using a $3 \times 3 \times 3$ Monkhorst-Pack *k*-point mesh.[49] Charge density was then calculated using a $5 \times 5 \times 5$ Monkhorst-Pack *k*-point mesh. Finally, the LDA-DFT band structure of Mg_5Rh_2 shown in Figure 1.16a was calculated *k*-point by *k*-point, using the previously determined charge density.

After this LDA-DFT band structure was calculated, eH atomic parameters of

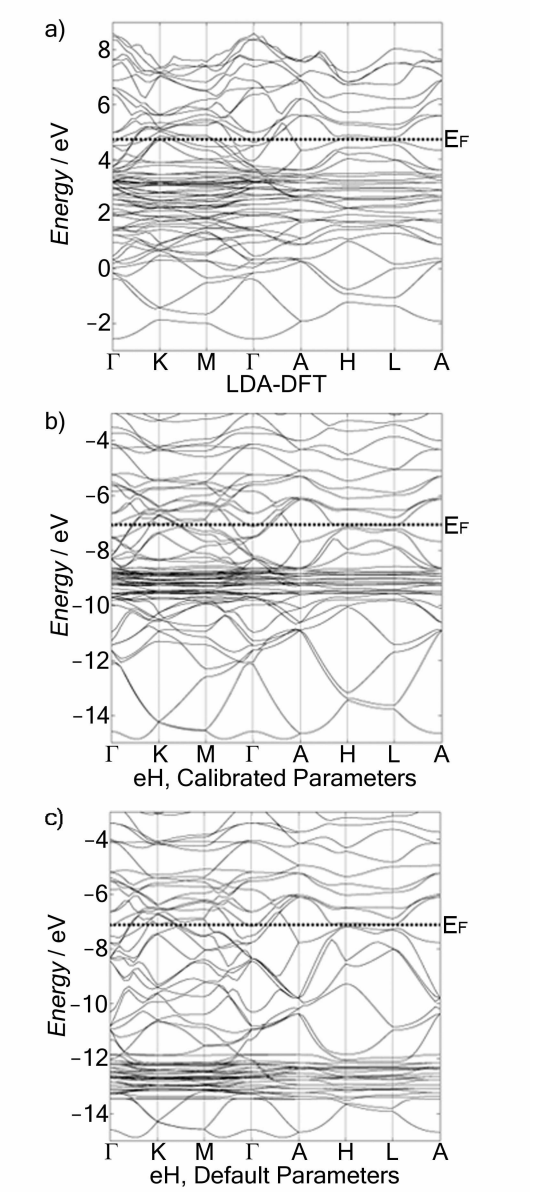

Figure 1.16: Band structures of Mg_5Rh_2 near the Fermi energy, calculated using a) LDA-DFT methods, b) extended Hückel methods with atomic parameters calibrated to mimic the LDA-DFT band structure, and c) extended Hückel methods with default Mg and Rh parameters. $\Gamma = (0, 0, 0)$, K = $(-\frac{1}{3}, \frac{2}{3}, 0)$, M = $(0, \frac{1}{2}, 0)$, A = $(0, 0, \frac{1}{2})$, H = $(-\frac{1}{3}, \frac{2}{3}, \frac{1}{2})$, and L = $(0, \frac{1}{2}, \frac{1}{2})$.

Mg and Rh were adjusted until they generated an eH band structure of Mg_5Rh_2 with features similar to the LDA-DFT band structure. All eH calculations were carried out with the YAeHMOP package,[50] using experimentally determined crystal structures rather than theoretically optimized geometries. The eH atomic parameters that provided the closest match to the LDA-DFT band structure were: H_{ii}(Mg 3*s*) = −9.0 eV, ζ_s = 1.1; H_{ii}(Mg 3*p*) = −4.5 eV, ζ_p = 1.1; H_{ii}(Rh 5*s*) = −8.09 eV, ζ_s = 2.135; H_{ii}(Rh 5*p*) = −4.57 eV, ζ_p = 2.1; H_{ii}(Rh 4*d*) = −9.0 eV, $\zeta 1_d$ = 4.29, $\zeta 2_d$ = 1.70, $c1_d$ = 0.5807, $c2_d$ = 0.5685. Figure 1.16b shows the eH band structure generated using these calibrated parameters, while Figure 1.16c shows the eH band structure generated using default parameters.[51]

As the pictures suggest, raising the Rh 4*d* orbital energies from H_{ii}(Rh 4*d*) = −12.5 eV to H_{ii}(Rh 4*d*) = −9.0 eV substantially improves the fit between eH and LDA-DFT calculations. Aside from this adjustment of the Rh 4*d* orbital energies, all other eH default atomic parameters seemed reasonable. While not identical to the LDA-DFT band structure, the calibrated eH band structure mimics many of the LDA-DFT features, especially near the Fermi energy. Such calibration methods have proven reliable in the past.[30,42,52–54]

Using our newly calibrated eH atomic parameters, Mulliken populations were calculated for the structure of interest, $Mg_{44}Rh_7$. All atomic sites were given Mg parameters (the majority element), so as not to bias the calculation toward the experimentally known site preferences. Mulliken populations were averaged over sixty uniformly distributed *k*-points in the ($k_x > 0$, $k_y > 0$, $k_z > 0$, $k_x \geq k_y \geq k_z$) portion of the first Brillouin zone.

1.13 Acknowledgment

This research was supported by the National Science Foundation (through grant DMR-0504703). We thank Daniel C. Fredrickson for pointing out to us the similarity of the cluster view in intermetallic systems to resonance structures in organic chemistry.

CHAPTER 2

EXPLAINING THE IMPOSSIBLE: THE NEED FOR A FICTITIOUS FOURTH DIMENSION

Why, sometimes I've believed as many as six impossible things before breakfast.
—The White Queen, *Through the Looking-Glass* by Lewis Carroll[55]

While our first paper[2] provides some insight into the origin of structural fivefold symmetry in complex intermetallic compounds, it also highlights some new mysteries that demand our attention. Perhaps most notably, the tenfold X-ray diffraction pattern of $Mg_{44}Rh_7$ (Figure 1.15) flies in the face of what chemists know about three-dimensional (3-D) point groups and space groups, in two ways. For one, fivefold rotational symmetry is incompatible with crystalline translational symmetry. But even ignoring the fact that we are concerned with crystals, no 3-D point group had fivefold symmetries along the ⟨110⟩ directions where they lie in $Mg_{44}Rh_7$. Yet, $Mg_{44}Rh_7$ is not an isolated case. We know of seven other intermetallic structure types that exhibit the same diffraction paradox: $Li_{21}Si_5$, $Zn_{13}(Fe,Ni)_2$, Mg_6Pd, Na_6Tl, $Zn_{91}Ir_{11}$, $Li_{13}Na_{29}Ba_{19}$, and $Al_{69}Ta_{39}$. All belong to the $F\bar{4}3m$ space group, have roughly 400 atoms in their cubic unit cells, and are built up at least partially from the γ-brass structure.

Our second paper, "The Mystery of Perpendicular Fivefold Axes and the Fourth Dimension in Intermetallic Structures" (Robert F. Berger, Stephen Lee, Jeffreys Johnson, Ben Nebgen, Fernando Sha, and Jiaqi Xu),[56] seeks to resolve this diffraction paradox. The paper, presented with permission in this chapter, marks our first venture into higher-dimensional space. Our resolution to the paradox is based on the largest of all 4-D Platonic solids, the 600-cell. We first

review 4-D polyhedroids and the 600-cell, aiming to build the reader's higher-dimensional intuition. We then show that the positions of common atoms in the $F\bar{4}3m$ structures lie close to the vertex positions in a 3-D projection of the 600-cell. Next, we explain how the introduction of the 600-cell resolves the tenfold diffraction paradox. Finally, we show that for certain ideal projected cluster sizes, which match those of the clusters found in the actual $F\bar{4}3m$ structures, constructive interference leading to tenfold diffraction symmetry is optimized. These ideal cluster sizes relate to each other by factors of the golden mean ($\tau = \frac{1+\sqrt{5}}{2}$).

2.1 Introduction

Consider the enigma of complex intermetallic crystal structures, thermodynamically stable atomic arrangements with hundreds or even thousands of atoms within the unit cell. Characteristic examples are $Li_{21}Si_5$, $Mg_{44}Rh_7$, and $Al_{69}Ta_{39}$, compounds which crystallize in the $F\bar{4}3m$ space group, with large numbers in their stoichiometric ratios and correspondingly large unit cells. Is there some pattern to these complex crystal structures which eludes the casual observer but which can explain essential features of their structures?

In this paper we will uncover one such pattern. The starting point will be diffraction. We shall find that the diffraction patterns of the above structures contain a pseudo-tenfold symmetry with an attached paradox. The mystery will not be that tenfold diffraction symmetry is incompatible with crystalline symmetry. That peculiarity has already been explored in the context of quasicrystal approximants.[36] The paradox we refer to is a simpler one.

The compounds $Li_{21}Si_5$, $Mg_{44}Rh_7$, and $Al_{69}Ta_{39}$ all adopt cubic crystal structures with pseudo-fivefold symmetry along the [110] direction. In cubic symmetry, the [110] direction has five other symmetry-equivalent directions. These compounds therefore have pseudo-fivefold symmetry axes along [110], $[1\bar{1}0]$, [011], $[01\bar{1}]$, [101], and $[10\bar{1}]$: three pairs of perpendicular pseudo-fivefold axes. The paradox is that no 3-D point group contains a single pair of perpendicular fivefold symmetry axes, let alone three such pairs.

The solution to this paradox is simple yet unexpected. While there are no 3-D point groups with perpendicular fivefold symmetries, there are 4-D point groups with orthogonal fivefold symmetries. The common atomic sites of these $F\bar{4}3m$ structures prove to be connected to one such 4-D point group. We will show that the common atomic sites of $Li_{21}Si_5$, $Mg_{44}Rh_7$, and $Al_{69}Ta_{39}$ lie at the 3-D projected points of a very symmetrical 4-D object. It is this 4-D object which has exact orthogonal fivefold symmetries. Of course, these fivefold symmetry operations are no longer exact once projected into 3-D space. But after projection, enough of their fivefold symmetry is retained that a pseudo-tenfold symmetric diffraction pattern (tenfold due to the pseudo-fivefold symmetry coupled with Friedel's Law[57]) is observed even in three dimensions.

This paper therefore begins with the observation of pseudo-tenfold diffraction symmetry in the aforementioned crystal structures. It then examines those atoms in these crystal structures principally responsible for the observed pseudo-tenfold diffraction symmetry.

At this point we begin our analysis of 4-D objects. We will show that 4-D objects can be understood through 3-D images of them, in much the same way that ordinary 2-D images are used to understand 3-D solids. We will therefore

consider 3-D images of a particular 4-D object—an object with perpendicular fivefold symmetries. We show that this object, once projected into 3-D space, retains a pseudo-tenfold diffraction symmetry.

We find that at certain ideal configurations and sizes, these diffraction images are optimal. Connecting these mathematical ideas to the actual reality of the true $Li_{21}Si_5$, $Mg_{44}Rh_7$, and $Al_{69}Ta_{39}$ crystal structures, we will find that the atoms of these crystal structures lie near sites of the projected 4-D object, and therefore exhibit pseudo-tenfold diffraction symmetry. At the same time, they have interatomic distances which optimize constructive interference in their diffraction patterns.

The story we create builds upon the observations of others. While the types of structures we describe—intermetallic crystal structures with regions consisting entirely of close-packed, slightly distorted tetrahedra—have a rich history of efforts to catalog and systematize their geometries,[58–64] we will mention only the observations most directly relevant to this paper. First among these was the realization by Samson and co-workers[3,5,8,12] that large cubic intermetallic structures such as $NaCd_2$ and Cd_3Cu_4 contain a pseudo-fivefold symmetry perpendicular to their crystallographic $\langle 110 \rangle$ directions. This same pseudo-fivefold symmetry was later observed by Khare and co-workers[65] for the γ-brass structure, and it was pointed out that the axes were inconsistent with those in known quasicrystals and quasicrystal approximants.[a] Later came the observation by Nyman, Andersson, Hyde, and others[33,34,68] that the γ-brass structure, among other tetrahedrally close-packed structures, is one in which the edge-capped stella quadrangula plays a central role. (We review the edge-capped stella quad-

[a] Although there are differences between the $\langle 110 \rangle$ and $\langle 1\tau 0 \rangle$ directions, Dong and others[66,67] have analyzed the relationships between γ-brasses and approximants of icosahedral and decagonal quasicrystals.

rangula later in this paper for readers unfamiliar with it.) And finally, there is the more recent work of Sadoc and Mosseri,[69,70] who recognized that the fundamental clusters of structures such as Cr_3Si, α-Mn, and γ-brass bear a clear relationship with the 4-D Platonic solid, the 600-cell. All of these observations are fundamentally connected and, as we hope to show for the $Li_{21}Si_5$, $Mg_{44}Rh_7$, and $Al_{69}Ta_{39}$ structures, tell different aspects of a single unified story.

2.2 Large $F\bar{4}3m$ Intermetallic Structures

2.2.1 Description of Their Structures

Seven structure types listed in *Pearson's Handbook of Crystallographic Data for Intermetallic Compounds*[6] in the space group $F\bar{4}3m$ contain approximately 400 atoms in their unit cells. Compounds for which X-ray single crystal data sets have been recorded and solved include $Li_{21}Si_5$,[17,18] $Zn_{21}Pt_5$,[23–25] $Cu_{41}Sn_{11}$,[13,14] $Mg_{44}Rh_7$,[7] $Zn_{39}Fe_{11}$,[16] $Mg_{44}Ir_7$,[71] $Zn_{13}(Fe,Ni)_2$,[19] Mg_6Pd,[12] $Mg_{29}Ir_4$,[21] Na_6Tl,[8] $Zn_{91}Ir_{11}$,[28] $Li_{13}Na_{29}Ba_{19}$,[26] and $Al_{69}Ta_{39}$.[20] To varying degrees, these structure types are all based on a simpler parent structure, γ-brass.[10] In this paper we will restrict our attention to the above thirteen solved crystal structures. (Of a total of fifteen known to us, these thirteen bear the simplest connection to the γ-brass structure.) We review the essential features of this simpler structure first.

The γ-brass structure is illustrated in Figure 2.1a. The structure is a cubic *I*-centered arrangement of the 26-atom cluster shown in this figure, a cluster composed of four distinct sites: IT (inner tetrahedron), OT (outer tetrahedron), OH (octahedron), and CO (cubo-octahedron). In accord with the *I*-centering

condition, there are two of these 26-atom clusters per cubic unit cell.

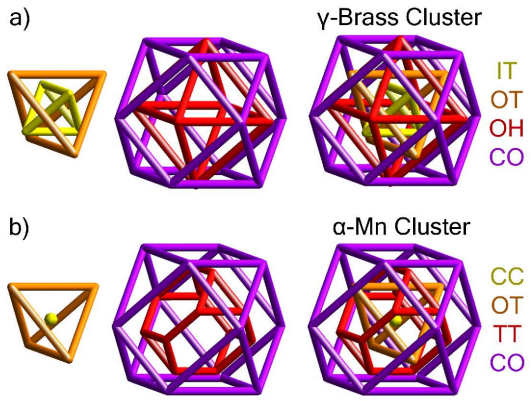

Figure 2.1: Two atomic clusters common to the $F\bar{4}3m$ intermetallic structures: a) the 26-atom γ-brass cluster and b) the 29-atom α-Mn cluster. Clusters are shown as nested polyhedra, with each crystallographic site represented by a color (inner tetrahedron or cluster center: yellow; outer tetrahedron: orange; octahedron or truncated tetrahedron: red; and cubo-octahedron: purple).

The simplest of the large unit-celled $F\bar{4}3m$ structures, $Li_{21}Si_5$, $Zn_{21}Pt_5$, and $Cu_{41}Sn_{11}$, are $2 \times 2 \times 2$ ordered superstructures of γ-brass. The *a*-, *b*-, and *c*-axes of these crystals are each twice as long as the corresponding axis length in γ-brass; these crystals' unit cells therefore have eight times the volume of γ-brass. Instead of two 26-atom clusters per unit cell, there are sixteen.

All of these structures are *F*-centered. *F*-centering requires each cluster to have three translationally equivalent clusters, and hence these sixteen clusters can be reduced to four translationally inequivalent ones. In the space group $F\bar{4}3m$, these four clusters are also not related by any point group operation. They are all crystallographically unique.

Specifying the atomic site positions (and the atom types) of these four clusters identifies these structures. In Figure 2.2, we show the four crystallographi-

cally inequivalent clusters of $Li_{21}Si_5$. The four clusters lie inside a single primitive unit cell. As this picture further shows, the four inequivalent clusters lie in a cubic cell at $(0,0,0)$, $(\frac{1}{4},\frac{1}{4},\frac{1}{4})$, $(\frac{1}{2},\frac{1}{2},\frac{1}{2})$, and $(\frac{3}{4},\frac{3}{4},\frac{3}{4})$. We will refer to these four clusters as the Z, Q, H and T clusters (the clusters being respectively at *z*ero, a *q*uarter, a *h*alf, and *t*hree-quarters of the cell dimension).

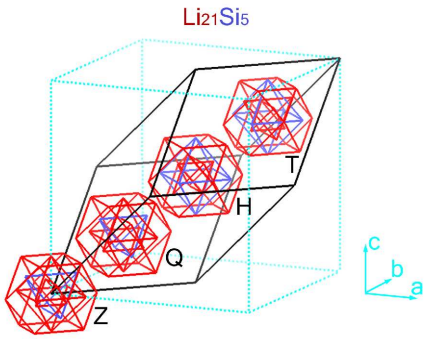

Figure 2.2: The four crystallographically inequivalent γ-brass clusters in $Li_{21}Si_5$ (Li: red; Si: blue), shown in both the primitive unit cell (black) and the cubic unit cell (cyan). The clusters are centered in the cubic cell at Z = $(0,0,0)$, Q = $(\frac{1}{4},\frac{1}{4},\frac{1}{4})$, H = $(\frac{1}{2},\frac{1}{2},\frac{1}{2})$, and T = $(\frac{3}{4},\frac{3}{4},\frac{3}{4})$.

As Figure 2.2 shows, differences exist between the four clusters: in $Li_{21}Si_5$, the Si atoms occupy different positions in the different clusters (for the Z and Q clusters the Si atoms lie on the OT sites, while for the H and T clusters they lie on the OH sites).[b] But in the $F\bar{4}3m$ family of structures, clusters can differ to an even greater extent. Clusters can have radically different atomic sites. One such different cluster is illustrated in Figure 2.1b. This cluster, found in $Zn_{91}Ir_{11}$, does not have any atoms at either the IT or OH sites, but instead has atoms at the center of the cluster (CC) and in a truncated tetrahedron (TT). This new cluster type is generally referred to as an α-Mn cluster, due to its similarity to

[b] In addition, there is an interesting variation among the orientations of the various clusters in $Li_{21}Si_5$. As careful examination of Figure 2.2 shows, the orientation of the inner tetrahedron of the H cluster is inverted with respect to the orientations of the Z, Q, and T clusters.

the principal constituent cluster of that structure type.[72]

Other cluster types with descriptive names such as Ti_2Ni, bcc, and fcc (so named because of clear connections to these parent structures) also exist.[c] But all cluster types are composed of just the six aforementioned types of atomic sites (CC, IT, OT, OH, TT, and CO). There are always four crystallographically inequivalent clusters located at Z, Q, H, and T. All sites can therefore comfortably be labeled with a three-letter designation (e.g., HTT would refer to a truncated tetrahedral site centered at $(\frac{1}{2}, \frac{1}{2}, \frac{1}{2})$). In this article, these three-letter designations will prove more useful than the traditional names based on descriptive names such as α-Mn or Ti_2Ni.

In this paper, we will consider eight structure types (as we shall see, our definition of structure type will be slightly different from the standard definition). We will consider only those structures which are traditionally considered to contain a γ-brass cluster. This includes thirteen of the fifteen $F\bar{4}3m$ $2 \times 2 \times 2$ compounds known to us for which a single crystal structure has been solved.[d]

2.2.2 Pseudo-Tenfold Diffraction Along the $[1\bar{1}0]$ Direction

In Figure 2.3, we show single crystal X-ray diffraction images[35] for two of the $F\bar{4}3m$ family of structures, $Zn_{39}Fe_{11}$ and $Na_{29}Li_{13}Ba_{19}$. We have chosen these two structures as they are the two structures where pseudo-tenfold symme-

[c] These alternate names are important in their own right. We have recently shown, for example, that the Ti_2Ni cluster plays a fundamental role in understanding quantum calculations on the $Mg_{44}Rh_7$ structure.[2]

[d] The remaining two structures, $Zn_{20.44}Mo$[22] and $Cd_{45}Sm_{11}$,[15] contain clusters based on the body-centered cubic (bcc) structure. While the ideas of this paper can be applied to the remaining two structures (recall that γ-brass is itself a defect bcc structure), the inclusion of these structures would require several multi-page excursions, of a length suited perhaps for another full article.

try is strongest, but as the Supporting Information (available online) illustrates, pseudo-tenfold diffraction is present in the remaining members of the family as well. In Figure 2.3, we show reflections orthogonal to the $[1\bar{1}0]$ direction. We show only the most intense peaks.

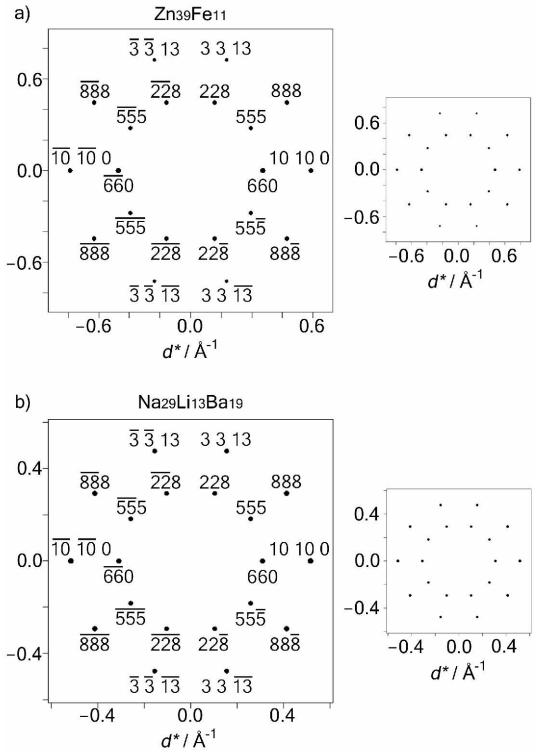

Figure 2.3: Simulated single crystal X-ray diffraction patterns of a) $Zn_{39}Fe_{11}$ and b) $Na_{29}Li_{13}Ba_{19}$, viewed in the $[1\bar{1}0]$ direction. Only the brightest peaks are shown. They exhibit a striking pseudo-tenfold symmetry. As all the strongest reflections are normal to the $\langle 110 \rangle$ directions, this figure reveals all the most intense peaks of these structures. See Table 2.1.

The diffraction images of Figure 2.3 exhibit a pseudo-tenfold symmetry. Diffraction spots appear in two distinct rings. For the inner ring, strong reflections include 660, 555, and 228; for the outer ring, they include 10100, 888, and 3313. These *hkl* indices belong to an understandable general pattern related to the Fibonacci sequence.

Recall in the Fibonacci sequence $(1, 1, 2, 3, 5, 8, 13, \ldots)$, each number is the sum of the two previous numbers of the sequence. Let us call a given Fibonacci sequence number h_i, the numbers preceding and following this number then being $h_{i\pm1}$. Consider now the set of *hkl* reflections, $(2h_i, 2h_i, 0)$, $(h_{i+1}, h_{i+1}, h_{i+1})$, and $(h_{i-1}, h_{i-1}, h_{i+2})$ (we use commas and parentheses here for the sake of clarity). The rings of peaks previously mentioned then correspond to the sets where h_i are respectively 3 and 5. For example for $h_i = 3$, these peaks correspond to $(2h_i, 2h_i, 0) = 660$, $(h_{i+1}, h_{i+1}, h_{i+1}) = 555$, and $(h_{i-1}, h_{i-1}, h_{i+2}) = 228$. The connection to the Fibonacci sequence will prove to run deeper than the above observations. But in order to appreciate these connections, we will need a number of additional concepts.

How is it that different structure types with differing atomic positions can all exhibit pseudo-fivefold symmetry? A suggestive clue to the answer to this question is given in Table 2.1, which lists relative intensities[35] of the six most intense symmetry-inequivalent diffraction peaks of $Zn_{39}Fe_{11}$ and $Na_{29}Li_{13}Ba_{19}$. These peaks belong to the two previously discussed rings of pseudo-tenfold diffraction. As this table shows, peaks within a given ring are not uniform in intensity. This lack of uniformity provides a measure of the incompleteness of the tenfold symmetry.

In this same table, we also give the calculated intensities using only those atomic positions shared across the full family of $F\bar{4}3m$ structures (there are twelve such positions). Restricting the diffraction pattern to these common atoms improves the uniformity in diffraction intensities (i.e., the overall pseudo-tenfold symmetry). Not shown, but equally true, is that this restriction improves the diffraction symmetry of the full family of $F\bar{4}3m$ structures. We therefore con-

Table 2.1: Strongest X-Ray reflection intensities for $Zn_{39}Fe_{11}$ (left) and $Li_{13}Na_{29}Ba_{13}$ (right).

$Zn_{39}Fe_{11}$ reflection	All atoms	Common sites	$Li_{13}Na_{29}Ba_{19}$ reflection	All atoms	Common sites
660	100%	100%	660	79%	94%
555	40%	50%	555	52%	58%
228	54%	65%	228	55%	61%
10 10 0	67%	84%	10 10 0	100%	100%
888	58%	72%	888	78%	88%
3 3 13	22%	33%	3 3 13	59%	71%

clude that the origin of the pseudo-tenfold symmetry lies in the common atoms.

Trying to understand the common atoms brings us to the heart of this paper. It is a heart which involves geometrical concepts of a sort not familiar to most of us. The very perpendicularity of the pseudo-fivefold axes, coupled with the absence of any 3-D point group with perpendicular fivefold axes, forces unusual geometrical concepts upon us.

We shall see that the key idea will be the introduction of a fictitious fourth dimension. This fourth dimension will have a number of concrete uses. It will allow us to create perpendicular fivefold axes which perfectly align with the $\langle 110 \rangle$ directions of these crystals. It will also allow us to create a continuous array of perfectly regular face-sharing tetrahedra, a geometrical array which many of us know cannot be achieved in three dimensions.

2.3 Four-Dimensional Platonic Solids

2.3.1 Projected Views of Three-Dimensional Platonic Solids

The 4-D geometry we will use is connected to 4-D Platonic solids. 4-D Platonic solids may seem at first a forbidding topic. But as we hope to show, many of the same tricks used to understand 3-D Platonic solids can be applied to 4-D Platonic solids. In particular, we note that much of our understanding of 3-D objects is based on 2-D pictures of them. We have trained ourselves to look at these 2-D pictures and convert them in our minds into 3-D solids. In exactly the same way, in this article we will consider 3-D images of 4-D solids and use our minds to turn these 3-D images into representations of a true 4-D object.

We begin by considering ordinary 3-D Platonic solids, 3-D polyhedra where all vertices, edges, and faces are identical. In this article, we consider four of the five 3-D Platonic solids: the tetrahedron, the octahedron, the dodecahedron, and the icosahedron. These Platonic solids are illustrated in Figure 2.4. The tetrahedron is of T_d point group symmetry, the octahedron of O_h symmetry, and the dodecahedron and icosahedron of I_h symmetry. Furthermore, the dodecahedron and icosahedron are duals of each other: atoms placed at the center of the faces of one polyhedron lie at the vertices of the other polyhedron.

We begin our account by carefully considering the views of these Platonic solids along their symmetry axes. (As we shall see, 4-D Platonic solids are also most clearly viewed down their symmetry axes.) In Figure 2.5, we show the octahedron down its fourfold axis and the dodecahedron down its five-, three-, and twofold axes. Each of these views will teach us general principles useful in

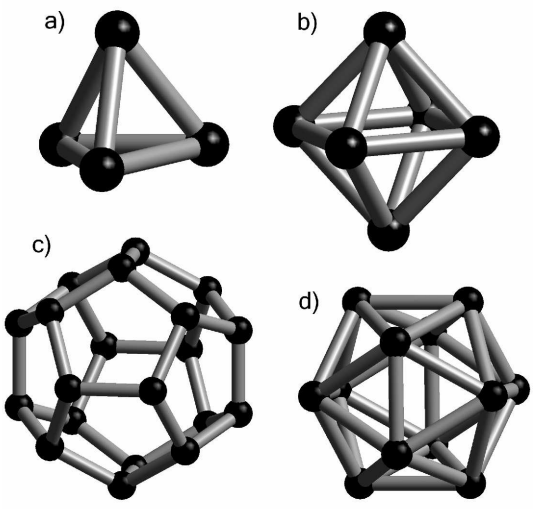

Figure 2.4: Four of the five 3-D Platonic solids: the a) tetrahedron, b) octahedron, c) dodecahedron, and d) icosahedron.

understanding 4-D solids.

We begin with the octahedron. The octahedron is composed of six vertices and eight faces. But only five of its vertices and four of its faces are visible in Figure 2.5. The reason is obvious. Upon projection into the plane of the picture, half of the polyhedron is obscured by the other half.

We may view this missing half from two very different viewpoints. If we are to view Figure 2.5a as a picture of a real 3-D octahedron, we then assume that the other half of the octahedron is hidden from view, but actually exists as the underside of the polyhedron. Equally relevant, however, is another more 2-D perspective. Imagine that Figure 2.5a actually represents a true 2-D object (a 2-D object created by projecting the 3-D octahedron into the 2-D space). From this viewpoint, only half of the 3-D octahedron has been successfully projected into 2-D space. The other half cannot be successfully projected as this would force vertices to be projected into the interior of the first half. If vertices are to

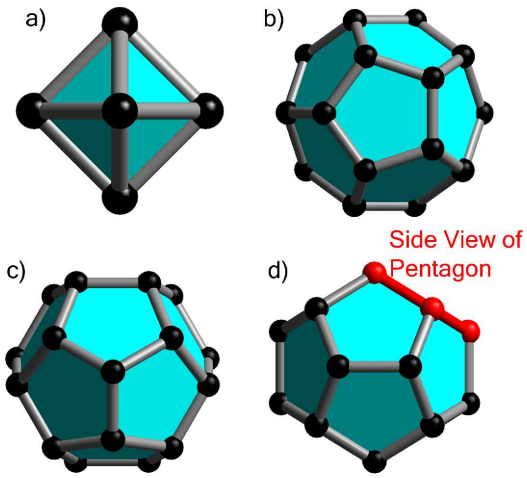

Figure 2.5: Various 3-D polyhedra viewed down their symmetry axes. a) An octahedron viewed down its fourfold axis, and a dodecahedron viewed down its b) fivefold, c) threefold, and d) twofold axes (with a pentagonal face that appears as a line segment shown in red).

become atoms, such a mapping would place atoms at chemically unreasonable distances with respect to other atoms.

A similar distinction will take place with 3-D projections of a 4-D Platonic solid. In some cases, vertices will be present, but hidden by the upper side of the 3-D polyhedron. In other cases, some atoms will not be projected, as such projection would place the new atoms into the interior volume already occupied by other projected atoms. In this paper, we will refer to the former as vertices (or atoms) hidden from view, and the latter as atoms in the shadow of other atoms.

Further important features can be extracted from the three views of the dodecahedron. We begin with the fivefold view (Figure 2.5b). Just fifteen of the vertices and six of the faces of the dodecahedron can be seen in this view. Of the six visible pentagons, only the central pentagon appears perfectly regular, while the remaining five take on a somewhat compressed shape (although in the 3-D

polyhedron, they are just as regular as the central pentagon).

The compressed aspect of the outer pentagons has two components to it. First, the projected area of the compressed pentagons is smaller than that of the central pentagon. Second, the edges of the polyhedron which lie at the sharpest angle with respect to the plane of the picture are somewhat shorter in appearance. Both components will later prove important in understanding 4-D Platonic solids.

The threefold view of the dodecahedron (Figure 2.5c) tells a similar story. Only six of the pentagonal faces are visible, the central three of which take on a distinctly more regular appearance than the outer three, the outer three pentagons having both significantly less area and (as some of the outer pentagons' edges are fairly perpendicular to the plane of the picture) significantly shortened edge lengths.

Of special interest is the dodecahedron viewed down the twofold axis (Figure 2.5d). At first glance only four of the pentagonal faces can be seen, the central two of which take on the most regular appearance. In this view, however, there are four additional pentagonal faces which lie at the periphery of the projected view. These additional four pentagons are exactly orthogonal to the plane of the paper. The projected area of these pentagons is exactly zero; these four perpendicular polygons take on the appearance of line segments. (For the sake of clarity, one of these orthogonal pentagons is shown in red in Figure 2.5d.)

In this view, there are four additional faces which lie completely hidden by the visible faces. The number of hidden faces exactly equals the number of visible faces. This equality is not an accident. A dodecahedron has inver-

sion symmetry. Upon inversion, the visible faces switch places with the hidden faces. The four peripheral faces which appeared as simple line segments in Figure 2.5d are equally pertinent here. The centers of the four peripheral faces lie exactly halfway between the visible and the hidden faces. If we were to use the terminology of a sphere, the four visible faces lie in one hemisphere, the four hidden faces lie in the other hemisphere, and the centers of the four peripheral faces lie exactly on the equator.

We see finally one additional point which will later prove useful in understanding 4-D solids. Whenever the direction of the projection is perpendicular (i.e., normal) to a given face, the given face preserves its symmetry upon projection. Thus, the fivefold view of the dodecahedron in Figure 2.5 is exactly normal to the central pentagonal face of the projection. It is therefore only in this fivefold view that the pentagonal symmetry of the original dodecahedron is perfectly preserved.

2.3.2 Identical Vertices, Edges, Faces, and Polyhedra

Before giving actual 3-D images of 4-D solids, we need to make some general observations about 4-D Platonic solids. Our observations begin with lower-dimensional Platonic solids: regular polygons and regular polyhedra. Regular polygons are 2-D objects with identical vertices (which are 0-D) and identical edges (which are 1-D). For 3-D regular polyhedra, there is the additional requirement of identical faces (which are 2-D). The salient point here is that in moving from 2-D polygons to 3-D polyhedra, we have added just one new component to our geometric description, the face, and that this new component is of

one higher dimension than the highest dimension of the remaining components (the vertices and the edges).

It should therefore not be surprising that 4-D Platonic solids will consist of identical vertices (0-D), edges (1-D), faces (2-D), *and* polyhedra (3-D). The polyhedra which are the constituent parts of a 4-D solid are traditionally referred to as cells. The 4-D solids themselves are called 4-D polytopes or polyhedroids.[73,74] There are just six 4-D Platonic solids,[75,76] of which three will be discussed in this article.

We may approach our understanding of 4-D Platonic solids in a second, we hope, intuitive manner. Again, intuition needs to be based on our understanding of lower-dimensional Platonic solids. A 2-D Platonic solid, a regular polygon, is composed of vertex-sharing (vertices are 0-D) line segments (lines are 1-D) which are each canted with respect to each other and which wrap around an area (an area is 2-D). A 3-D Platonic solid is composed of edge-sharing (edges are 1-D) polygons (polygons are 2-D) which are canted with respect to each other and which wrap around a volume (a volume is 3-D). By analogy, we infer a 4-D Platonic solid is composed of face-sharing (faces are 2-D) polyhedra (polyhedra are 3-D) which are canted with respect to each other and which wrap around a (fictitious) hypervolume (the hypervolume is 4-D).

2.3.3 The 16-Cell

The eight points $(\pm 1, 0, 0, 0)$, $(0, \pm 1, 0, 0)$, $(0, 0, \pm 1, 0)$, and $(0, 0, 0, \pm 1)$ prove to be the vertices of one of the six 4-D Platonic solids. Each of these points can be thought of as a 4-D vector. Distances between pairs of vertices are therefore

readily calculable. Each vertex has six nearest neighbors (for simplicity we shall say nearest-neighboring vertices are bonded to one another): for example, the point $(1, 0, 0, 0)$ has the six points $(0, \pm 1, 0, 0)$, $(0, 0, \pm 1, 0)$, and $(0, 0, 0, \pm 1)$ at a distance of $\sqrt{2}$ away from it. As there are eight vertices, six bonds per vertex, and each bond is shared by two vertices, there are twenty-four bonds ($24 = 8 \times 6 \div 2$) in this polyhedroid.

Both vertices of a pair of nearest neighbors (e.g., $(1, 0, 0, 0)$ and $(0, 1, 0, 0)$) are mutually bonded to exactly four other vertices (in this case, $(0, 0, \pm 1, 0)$ and $(0, 0, 0, \pm 1)$). As each of these latter four vertices is bonded to both of the originally bonded atoms, there are therefore four triangles of bonded atoms. The original bond lies simultaneously on four triangular faces. As there are twenty-four bonds, four triangles which share a common bond, and as a triangle is always composed of three bonds, there are thirty-two triangular faces ($32 = 24 \times 4 \div 3$) in this polyhedroid.

Consider one triangle of bonded atoms (e.g., $(1, 0, 0, 0)$, $(0, 1, 0, 0)$, and $(0, 0, 1, 0)$). There prove to be exactly two vertices which are bonded to all three vertices of a bonded triangle. In the current example, the pair of vertices at $(0, 0, 0, \pm 1)$ are both bonded to all three vertices of the triangle. Either of these latter vertices, together with the initial triangle of bonded vertices, forms a tetrahedron. There are therefore exactly two tetrahedra which share a common triangular face. As there are thirty-two triangular faces, two tetrahedra which share a common face, and as a tetrahedron always has four faces, there are sixteen tetrahedra ($16 = 32 \times 2 \div 4$) in this polyhedroid.

It will also prove useful to know the number of tetrahedra which share a common vertex. To calculate this number, we note that the number of vertices

$\times$ the number of tetrahedra which share a given vertex $\div$ the number of vertices per tetrahedron = the number of tetrahedra in the polyhedroid. There are eight vertices in the polyhedroid, four vertices per tetrahedron, and sixteen tetrahedra in the 4-D solid. Applying the above formula we find $8 \times n \div 4 = 16$, where n equals the number of tetrahedra which share a common vertex. We therefore find that the number of tetrahedra which share a common vertex is eight.

In summary, every vertex is shared by eight tetrahedra, every bond is shared by four triangles, and every face is shared by two tetrahedra. In addition, the number of vertices is eight, edges (or bonds) twenty-four, faces (or triangles) thirty-two, and cells (or tetrahedra) sixteen. These latter numbers obey the 4-D Euler relation:[76] the number of vertices − the number of edges + the number of faces − the number of polyhedra = zero, as $8 - 24 + 32 - 16 = 0$. All vertices, edges, faces, and polyhedra (cells) are identical. The object described above is therefore a 4-D Platonic solid. It is commonly referred to as the 16-cell, as it is composed of sixteen tetrahedral cells.

2.3.4 Three-Dimensional Projections of the 16-Cell

We now show our first picture of the 16-cell. Our picture will be a 3-D projection of this 4-D polyhedroid. Our picture perforce will be 2-D in nature, but unlike many literature pictures, will be based on standard 3-D crystal graphics packages. Because chemists are so experienced at viewing the output of 3-D crystal graphics packages, we will be able to consider these pictures as being 3-D in nature. (As a further aid, we include stereograms of some of these same pictures in the Supporting Information, available online.) It will therefore be easy

to envision these pictures as representing 3-D projected solids, and furthermore to recognize that the projected vertices and edges could be seen as actual atomic site positions and bonds.

To create a 3-D projected image of the 4-D 16-cell, we need to decide upon the direction (or view) of the projection. We will use the symmetry of the 16-cell coupled with insights based on 2-D projections of 3-D solids to guide our choice. Consider again the fivefold view of the dodecahedron (Figure 2.5b). We can think of this view as emanating from the choice of the central pentagonal face of this figure. As this pentagon is 2-D, exactly one dimension less than the complete dodecahedron, this face is normal to a unique perpendicular axis. As Figure 2.5 shows, if we choose a projected view which is along this perpendicular axis, the fivefold symmetry remains perfectly preserved even after projection.

We use this same technique for the 16-cell. In this case, we need to consider not just a central 2-D face, but a central 3-D cell (polyhedron). In 4-D space, there will be a unique direction perpendicular to the 3-D space defined by this cell. We can choose this direction as the direction of projection. We will therefore choose one of sixteen tetrahedra in the 16-cell to be the central cell, and choose the direction of projection to be perpendicular to this tetrahedron. By analogy to the preserved fivefold symmetry of the dodecahedron in Figure 2.5b, this projected 3-D image of the 4-D 16-cell will preserve the symmetry of the central tetrahedron.

In Figure 2.6, we show this projected view. We choose for this illustration a view which places the central tetrahedron along its threefold axis, Figure 2.6a. Recall that each triangular face of the 16-cell is shared by two tetrahedra. Thus

each of the triangular faces must belong to a second tetrahedron besides the central tetrahedron. These second tetrahedra can be seen by placing an additional capping atom on each of the triangular faces of the initial tetrahedron.

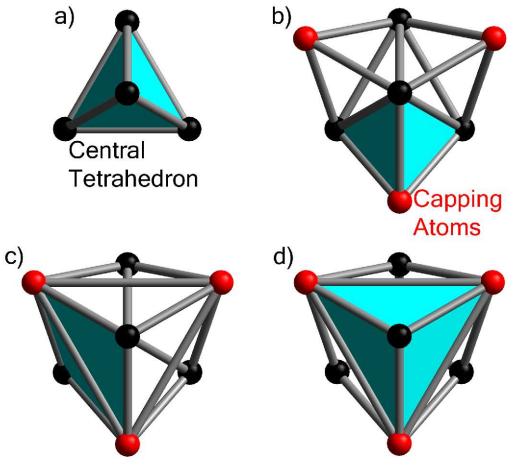

Figure 2.6: A T_d 3-D projection of the 16-cell. a) The central tetrahedral cell. Central tetrahedron with b) face-sharing, c) edge-sharing, and d) vertex-sharing tetrahedra highlighted in cyan (central tetrahedral vertices: black; capping tetrahedral vertices: red). Capping vertices are slightly displaced for the sake of clarity (see Appendix).

One of the triangular faces of the central tetrahedron is hidden from view by the other triangles. Down the threefold view, its capping atom will not be visible. But, the three remaining capping atoms will be visible and are shown in Figure 2.6b. Each of these capping atoms taken together with its neighboring triangle of bonded vertices forms an additional requisite tetrahedron. These tetrahedra are somewhat compressed (this is especially clear in the stereograms in the Supporting Information, available online). We can understand this compression in light of our earlier observation, that as one proceeds away from the center of the projection, faces and cells often become more and more compressed.

The four central tetrahedral atoms together with the four capping atoms make a total of eight atoms. As described in the last section, there are exactly eight atoms in the 16-cell. We have therefore considered all the vertices of this polyhedroid. But we have not as yet considered all the tetrahedral cells.

Additional tetrahedra can be found among the seven visible vertices of Figure 2.6b. There are four such tetrahedra. Three of these new tetrahedra emanate from a pair of atoms of the central tetrahedron coupled with a pair of the capping atoms. These new tetrahedra are edge-sharing with respect to the central tetrahedron (Figure 2.6c). A final tetrahedron is formed by a central tetrahedral atom (the one at the center of the picture) together with all three of the visible capping atoms (Figure 2.6d). All of these additional tetrahedra are compressed after 3-D projection.

There are therefore eight tetrahedra to be found in Figure 2.6 (8 = 1+3+3+1). All eight of these tetrahedra have the central atom of the threefold projection as one of their constituent atoms. We recall from the last section that every vertex is shared by exactly eight tetrahedra. Figure 2.6 therefore illustrates all the tetrahedra which share the central atom of the threefold projection.

There are of course sixteen tetrahedra in the 16-cell. Only eight of its tetrahedra are seen in Figure 2.6. The reason for this can be traced to the lone capping atom which lies hidden from view by the other atoms. As this lone atom is also shared by eight tetrahedra, there must be eight tetrahedra not visible in Figure 2.6. These eight missing tetrahedra, together with the eight tetrahedra which we have previously described, account for all sixteen tetrahedra of this polyhedroid.

2.3.5 The Projected 120-Cell

We now consider 4-D Platonic solids which contain fivefold symmetries. It may come as no surprise that such polyhedroids are 4-D analogs of the dodecahedron and the icosahedron. We begin with a 4-D Platonic solid which contains dodecahedral cells. The actual coordinates of this solid are given in the Supporting Information (available online). Here we will simply describe a 3-D projection of this polyhedroid. As the polyhedroid we are about to describe is composed of 120 identical dodecahedra, it is traditionally referred to as the 120-cell.

Recall that in making a projection, we need to choose a direction of projection. We choose this direction in the canonical way, by designating one of the dodecahedra of the 120-cell the central one, and finding the direction perpendicular to this dodecahedron. This projection as well as the 3-D coordinates it generates are given in the Supporting Information (available online). In this section, we will just give a descriptive view of the projected solid.

In Figure 2.7a, we illustrate (in green) the centrally projected dodecahedron viewed down a fivefold axis. In the 120-cell, each of the pentagonal faces of this dodecahedron is capped by another dodecahedron.[e] As there are twelve pentagons in a given dodecahedron, the central dodecahedron is capped by twelve additional dodecahedra. These twelve additional dodecahedra are partially illustrated in Figure 2.7b (eleven of the twelve dodecahedra are visible, and are illustrated in gray, cyan, and blue).

There are numerous exposed pentagonal faces among the eleven visible do-

[e] As mentioned previously, each face in a polyhedroid is always shared by two and only two polyhedra. This is analogous to the 3-D case, where each edge of a polyhedron is always shared by two and only two faces.

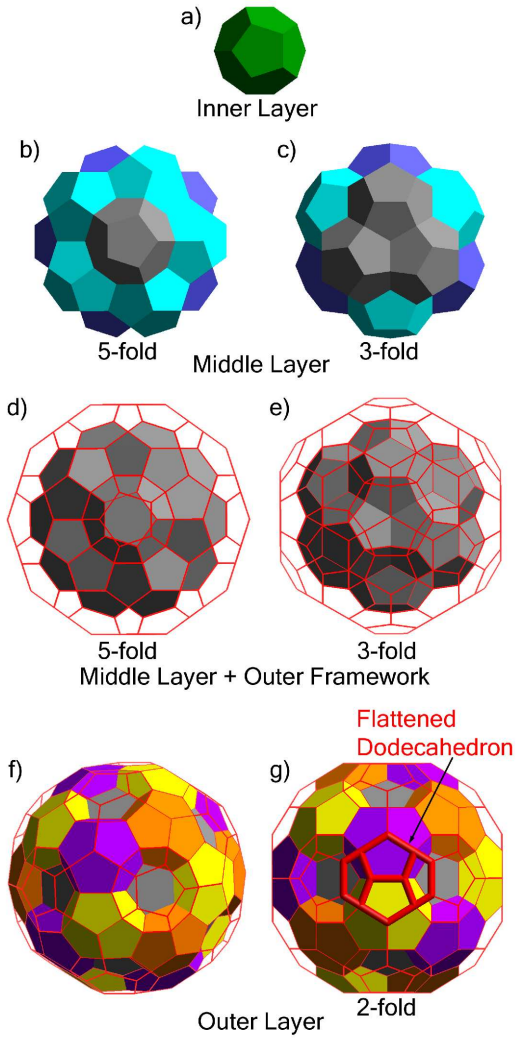

Figure 2.7: An I_h 3-D projection of half of the 120-cell, a 4-D polyhedroid. From center outward, a) a central dodecahedral cell (green), b) fivefold and c) threefold views of the twelve dodecahedral cells which are face-sharing to the central cell (gray, cyan, and blue), d) fivefold and e) threefold views outlining a layer of thirty-two dodecahedral cells which are face-sharing to the central thirteen cells (red mesh), f) a view of the thirty-two cells with one cell type opaque (orange, yellow, and purple), and g) a twofold view of (f) with one of the equatorial layer of thirty completely flattened dodecahedral cells highlighted in thick red cylinders.

decahedra of Figure 2.7b. In the 120-cell, there are capping dodecahedra on each of these pentagonal faces. To create this next shell of dodecahedra, we observe that there are two types of symmetry-inequivalent exposed pentagons in Figure 2.7b. Most exposed, and sitting directly above one of the pentagonal faces of the central dodecahedron, are twelve pentagons, all perfectly regular in appearance. One of these pentagons lies at the center of Figure 2.7b. We will place new exposed dodecahedra so that they perfectly cap these twelve regular pentagons.

There is, however, a second type of less exposed pentagonal face, which sits in the indentations of the illustrated cluster. These indented pentagonal faces appear in groups of three. One such grouping has been placed in the center of the view in Figure 2.7c. These threefold groupings of pentagonal faces will provide the underside of a new set of dodecahedra. As there are twenty such indentations, there will be twenty new indented dodecahedra.

The vertices belonging to these two additional types of dodecahedra are shown in Figures 2.7d,e. For the sake of clarity, we have grouped these vertices as a spherical framework, while retaining the form of the thirteen central dodecahedra as opaque polyhedra. In Figure 2.7d, we orient the figure along the fivefold axis. In the center of this figure, one of the new exposed dodecahedra can be seen. In Figure 2.7e, we rotate the perspective so that one of the indented dodecahedra lies at the center.

In Figure 2.7f, we illustrate these new dodecahedra by turning the indented dodecahedra into opaque objects (in yellow, orange, and purple, with no two adjacent indented dodecahedra being the same color). This figure illustrates not just the so-called indented dodecahedra, but, as indented dodecahedra share

faces with the so-called exposed dodecahedra, the exposed dodecahedra as well. As this figure shows, both exposed and indented dodecahedra are significantly compressed after 3-D projection (stereograms are given in the Supporting Information, available online).

Even more interesting is yet a fourth view of the projected solid (Figure 2.7g). In this perspective, we rotate the polyhedron of Figure 2.7f so that four coplanar pentagons lie at the center of the picture. The appearance of these four pentagons should be directly compared with the four pentagons visible in the twofold view of an ordinary 3-D dodecahedron (Figure 2.5d). Comparison shows that these four pentagons are identical in appearance. As we shall see, this identical appearance is not accidental. Rather, dodecahedra from the 4-D 120-cell polyhedroid have become so compressed under projection into the 3-D world that they have become absolutely flat, and have been reduced to being just four coplanar pentagons in appearance.

It turns out there are thirty of these absolutely flat dodecahedra, each lying directly above one of the bonds of the central dodecahedron. At this point we have described seventy-five dodecahedra: the one central one, its twelve nearest neighbors, the twelve exposed dodecahedra, the twenty indented ones, and the thirty completely flat dodecahedra ($75 = 1 + 12 + 12 + 20 + 30$). As the name of the 120-cell implies, there are forty-five remaining dodecahedra ($45 = 120 - 75$).

These remaining dodecahedra turn out to all lie in the shadow of the seventy-five other dodecahedra. Recall that cells in the shadow of other cells are polyhedra which, were they to be projected, would lie in the volumes already occupied by other polyhedra. The twofold 2-D projection of the 3-D dodecahedron is relevant here. In this earlier case, four of the twelve 2-D pentagonal

faces are visible, four of the 2-D faces have been reduced to 1-D line segments, and four of the 2-D faces lie in the shadow of the other faces.

Something very similar occurs in the projected 120-cell. Of the 120 3-D dodecahedra, forty-five of the dodecahedra project nicely (though are at times somewhat compressed) into 3-D space, thirty of the dodecahedra project into 2-D coplanar pentagons, and forty-five of the dodecahedra lie in the shadow of the other dodecahedra.

Let us call a 4-D sphere a spheroid. This spheroid can be divided into two equally-sized hemispheroids. The hemispheroids, like the initial spheroid, are 4-D in nature in just the same way that hemispheres, like spheres, are 3-D. Forty-five dodecahedra lie in one hemispheroid and are projected into 3-D space, forty-five dodecahedra lie in the other hemispheroid (in the shadow of the first) and are not projected, and thirty dodecahedra lie between the two hemispheroids.

Recalling that the abutting points between the two 3-D hemispheres of a sphere form a 2-D circle, the equator, the points abutting these two 4-D hemispheroids will also have a well-defined shape. Instead of an equatorial circle, this shape is an equatorial sphere. The centers of the thirty flat dodecahedra lie on this equatorial sphere.

This terminology helps us further understand the pictures in Figure 2.7d-g. In these pictures, the outermost vertices appear to lie on a sphere. This sphere is near the equatorial sphere to which the previous paragraph refers. This is important. In any 3-D projection of a 4-D polyhedroid, we need not consider any further cells once we reach the equatorial sphere; all further cells will lie in

the shadow of the other cells. And cells which lie on the equatorial sphere are readily identified because they are always flat.

2.3.6 The 600-Cell

We now turn to the 600-cell, the 4-D Platonic solid with the greatest number of cells, and the polyhedroid which is most relevant to the current paper. Six-hundred is a daunting number. Fortunately, there is a simple relation between the 600-cell and the 120-cell: the two are duals of each other. The 600-cell and the 120-cell therefore have the same relation to one another as do the icosahedron and dodecahedron. In 3-D, two polyhedra are duals of each other if the points at the centers of the faces of one polyhedron lie at the vertices of the other polyhedron.

Something analogous will happen for dual polyhedroids: the points at the centers of the cells of one polyhedroid lie at the vertices of the other polyhedroid. Thus, the dual of the 120-cell has a vertex at the center of each of the 120 cells of the 120-cell. The dual of the 120-cell has exactly 120 vertices.

As each cell of the 120-cell has twelve neighboring cells (see previous section), each vertex in the dual of the 120-cell will have twelve neighboring vertices. These vertices respect the original I_h symmetry of the dodecahedron, and form a perfect icosahedron around the central vertex. Consider any one of the twenty triangular faces of this icosahedron. Each of these faces, together with the center of the icosahedron, forms a tetrahedron (in 3-D this tetrahedron is not perfectly regular, but in 4-D it can be perfectly regular). Thus, if each vertex of the dual of the 120-cell has an icosahedron of vertices around it, each vertex is

shared by twenty tetrahedra.

The number of vertices × the number of tetrahedra which share a common vertex ÷ the number of vertices per tetrahedron = the number of cells. For the dual of the 120-cell, there are 120 vertices, twenty tetrahedra which share a common vertex, and four vertices per tetrahedron. Therefore, the dual of the 120-cell has exactly 600 cells (600 = 120 × 20 ÷ 4). These cells are all tetrahedra.

2.3.7 The Projected 600-Cell

We now construct a 3-D projection of the 600-cell. We choose the canonical direction for projection (i.e., the one orthogonal to the 3-D space defined by one of the cells of the 600-cell).[f] As projected images preserve the symmetry of the projected cell and as the cells of the 600-cell are tetrahedra, this 3-D projection will be of T_d symmetry. Its central tetrahedron is shown in Figure 2.8a. Following standard intermetallic nomenclature, this central tetrahedron is called the inner tetrahedron (IT).

In all polyhedroids, every face is shared by exactly two polyhedra. In the 600-cell, every triangular face is therefore shared by two tetrahedra. Each face of the central tetrahedron in Figure 2.8a is therefore the face of a second tetrahedron. By placing capping vertices on each face, we generate the four required

[f]There is another relevant direction for projecting the 600-cell. In this alternate projection, the center of projection is the volume directly surrounding one of the 120 vertices of the 600-cell. Under such a projection, the 600-cell projects into an I_h 3-D object. This 3-D object consists of a central vertex surrounded by the twelve vertices of an icosahedron, followed by the twenty vertices of a dodecahedron, followed by twelve vertices of a larger icosahedron. Finally come the thirty vertices of an icosidodecahedron. This icosidodecahedron lies on the equatorial sphere. This collection of polyhedra is related to the Bergman cluster of quasicrystalline fame.[36] This alternate projection is deeply relevant to intermetallic crystal structures, but structures of a type different from the ones discussed in the current article. See the Supporting Information (available online).

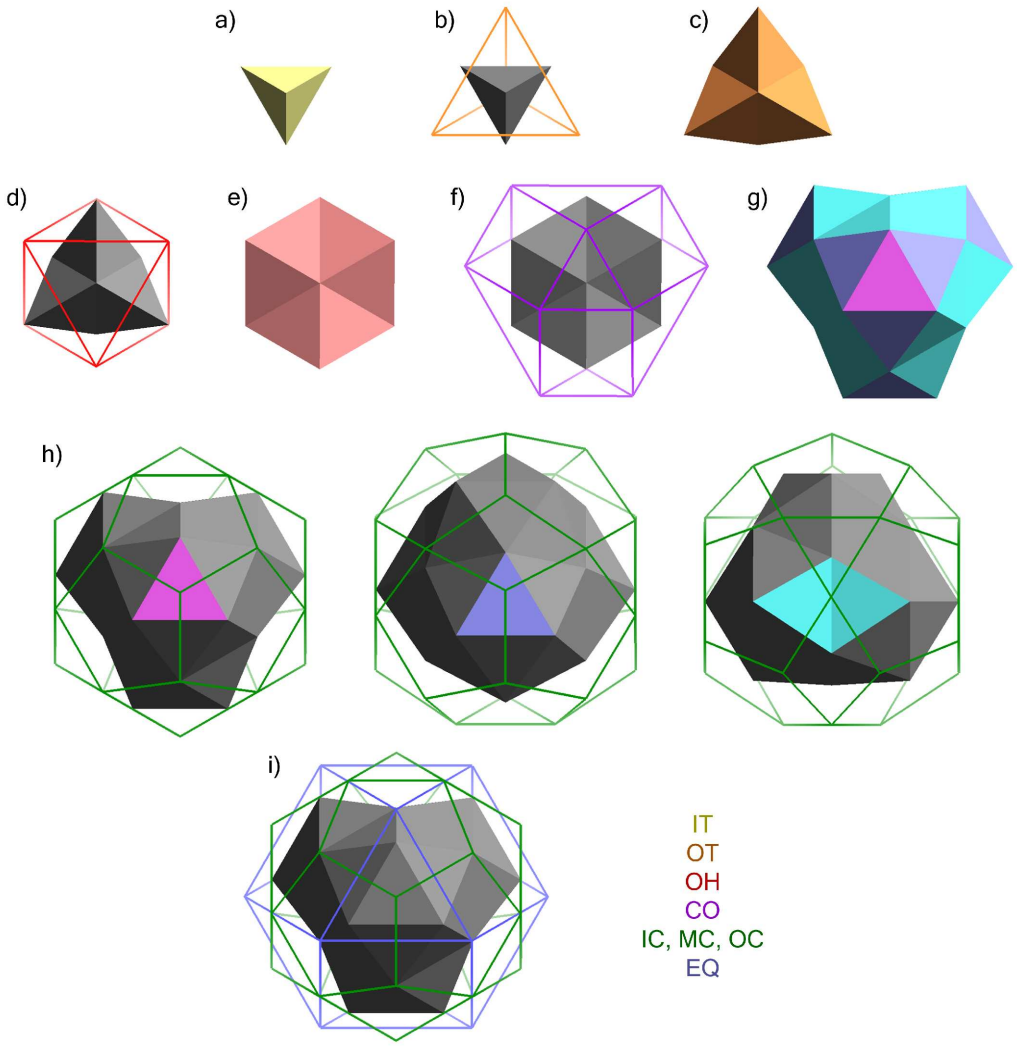

Figure 2.8: A T_d 3-D projection of half of the 600-cell, a 4-D polyhedroid. a) A central tetrahedral cell consisting of four IT vertices (yellow), b) four OT vertices capping its faces and c) the new triangular faces formed by the capping with OT (orange), d) six OH vertices capping these faces and e) the new triangular faces formed by the capping with OH (red), f) twelve CO vertices capping these faces (purple) and g) the three distinct triangular faces formed by the capping with CO (magenta, blue, and cyan), h) twenty-eight OC, MC, and IC vertices capping these faces (green framework), and i) twelve EQ vertices on the equator of the 600-cell (blue framework).

additional tetrahedra. As Figure 2.8b shows, these four capping vertices themselves lie at the corners of a larger outer tetrahedron (OT). The polyhedron formed by both the IT and OT sites is referred to as a stella quadrangula, and is shown in Figure 2.8c.

The exposed triangular faces of the stella quadrangula are all symmetry-equivalent, and form pairs of edge-sharing faces. These faces lie in an indented orientation with respect to each other. Three such pairs of indented faces are shown in Figure 2.8c. By $\overline{4}$ symmetry, there are three further pairs of indented faces which lie on the underside of the figure. We place six capping vertices, one above each pair of indented faces. The six new vertices are shown in Figure 2.8d. As this figure shows, the new vertices lie in an octahedron and are therefore called the octahedral sites (OH).

The exposed triangular faces of the IT-OT-OH cluster (Figure 2.8e) are all symmetry-equivalent, and again can be viewed as being composed of indented edge-sharing faces. Trios of these edge-sharing faces come together in the form of corrugated rosettes; one such rosette is at the center of Figure 2.8e. Above each pair of indented edge-sharing faces, we place a new capping vertex. As there are three such indented edge-sharing faces per rosette, and four rosettes in total, there are twelve new capping vertices. These capping vertices form a distorted cubo-octahedron (Figure 2.8f), the CO sites. The capped cluster composed of the IT-OT-OH-CO sites is an edge-capped stella quadrangula. A view of the edge-capped stella quadrangula is given in Figure 2.8g.

But the construction is not yet finished. There are three different kinds of exposed triangular faces in the edge-capped stella quadrangula. These faces are illustrated in Figure 2.8g. The most exposed of the three types of faces is shown

in magenta. Slightly less exposed are faces, edge-sharing to the most exposed faces, shown in blue. Finally, there are pairs of indented edge-sharing faces, shown in cyan.

We cap the most exposed faces, the less exposed faces, and the pairs of indented faces with new vertices. As there are four most exposed faces, twelve less exposed faces, and twelve pairs of indented faces, we place twenty-eight (28 = 4 + 12 + 12) new vertices onto our cluster. These twenty-eight vertices are drawn as a shell in Figure 2.8h. In this figure, we show the 28-vertex shell and the edge-capped stella quadrangula from three different perspectives: down the most exposed face (left), less exposed face (middle), and indented faces (right). Atoms capping respectively the most exposed, less exposed, and indented faces are termed OC (for outer capping), MC (for middle capping), and IC (for inner or indented capping). The capping atoms together with the faces beneath the capping vertices form new tetrahedra. These new tetrahedra are quite compressed. This compression is particularly clear in the stereogram given in the Supporting Information (available online).

We now come to the last site of the projected 600-cell. This site proves to lie exactly on the equatorial sphere of the 600-cell (for this reason, this site will be called EQ). The EQ site is most easily seen by recalling that every vertex in the 600-cell lies in the center of an icosahedron, and that every vertex of an icosahedron has five neighboring vertices which lie in a pentagon around it.

Examination of Figure 2.8h shows that the outer shell of twenty-eight atoms has twelve pentagonal faces. Near the center of these faces, but just below the plane of these faces, lies a CO atom. We can now envision that this CO atom, together with the pentagon of atoms above it, forms the underside of an extraor-

dinarily compressed icosahedron. We place the EQ atoms at the center of this compressed icosahedron. These EQ positions are shown in Figure 2.8i.

Beyond this point, projected vertices lie in the shadow of the other points and need not be further considered. In summary, the interior of the projected 600-cell consists of fifty-four vertices (4 IT +4 OT +6 OH +12 CO +12 IC +12 MC +4 OC = 54). On the equatorial sphere lie an additional twelve vertices (EQ). Fifty-four further sites lie in the shadow of the above sites, and are not included in the 3-D projection (by symmetry, the number of shadowed sites exactly equals the number of sites in the interior of the 3-D projection). As 120 = 54 + 12 + 54, we have accounted for all 120 vertices of the 600-cell.

Of the sites discussed, the first fifty-four of these 120 vertices will prove most important for the remainder of this paper. For the sake of convenience, we term the cluster formed by these fifty-four vertices the 54-cluster.

2.4 The $F\bar{4}3m$ Structures

In the previous section of this paper, we have seen that the 4-D Platonic solid composed of stuffed icosahedra, the 600-cell, can be projected into a 3-D space as a cluster with fifty-four interior and twelve equatorial vertices. These interior sites bear the names IT, OT, OH, CO, IC, MC, and OC. Earlier in the paper, we saw that the atoms of $F\bar{4}3m$ structures can be specified by three-letter designations, the first letter specifying the cluster origin and the final two letters the cluster site (CC, IT, OT, OH, TT, or CO). Most importantly, we see that four of the letter designations of the projected 600-cell are the same as those for $F\bar{4}3m$ cluster types: IT, OT, OH, and CO. This is not a duplication of symbols: there is

a real connection.

2.4.1 Linear, Stereographic, and Intermediate Projection

To explore the tie between the 4-D 600-cell polyhedroid and our cubic structures, we need a way to exactly specify the 3-D location of a given vertex of the projected 600-cell. To do so, we need to carefully examine what we mean by projection. The projections we are interested in will always be projections from 4-D space to 3-D space. But, as we know from cartography, there are numerous ways of projecting a sphere onto a plane: no one of these projections is inherently better than all others. The same will prove true in projecting the 4-D spheroids into 3-D space.

Scientists are most familiar with two different types of projection.[g] First, they are familiar with linear projection (see Appendix). But many of us are also familiar with a second type of projection, stereographic projection.[79] In Figure 2.9a,b, we give schematic views of both linear and stereographic projection. As we are most familiar with 2-D maps based on the 3-D globe, these schematics illustrate projection of 3-D space to 2-D space. As we shall see, these same ideas can be applied to projecting 4-D space to 3-D space.

As Figure 2.9a shows, we can imagine the hemisphere of a Platonic solid (in this figure, a dodecahedron) to lie on the surface of a transparent sphere. We place a light source sufficiently far away from this sphere that rays emanating from this light source are essentially parallel to one another. In linear projection, we place a plane normal to these rays of light on the opposite side of the sphere

[g]Other types of projection, of course, exist. In the problem of mapping the 600-cell from 4-D to 3-D, various techniques have been used, often requiring the introduction of disclinations.[77,78]

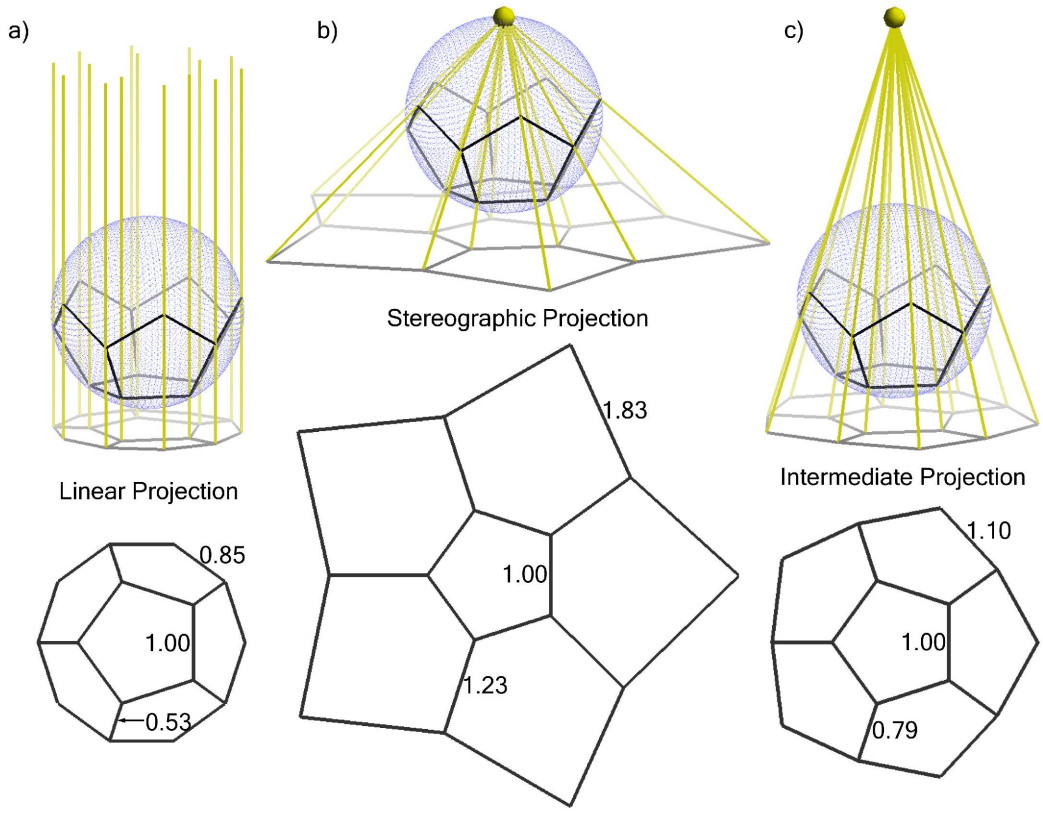

Figure 2.9: Schematic views of the three types of projection relevant to this paper: a) linear projection, b) stereographic projection, and c) intermediate projection. While bonds become unphysically short toward the outside of a linear projection and unphysically long toward the outside of a stereographic projection, bonds can retain reasonably constant lengths for a hemisphere with intermediate projection.

and locate the shadow of the Platonic solid.

In stereographic projection, we again consider a single light source, but this time place it directly on the surface of the sphere (at the point opposite the projected plane), as in Figure 2.9b. In stereographic projection, unlike linear projection, no vertices, bonds, or faces lie in the shadow of other vertices, bonds, or faces. But on a simple level, we tend to view stereographic projection as more distorted than linear projection.

On the plus side, both linear and stereographic projection preserve the fivefold axis directly opposite the light source. In the examples of Figure 2.9a,b, the point directly opposite the light source has fivefold symmetry and both the linear and stereographic projected images retain fivefold symmetry.

Bond lengths, however, prove an issue. These problems can be understood with just one look at Figure 2.9a,b. In stereographic projection, bond lengths can become unreasonably large toward the outside of the projected image. But linear projection also has issues, as bonds can become unreasonably short toward the outside of the projection. Bonds exactly parallel to the direction of projection have their lengths collapse to zero.

As neither stereographic nor linear projection is suitable for preserving bond lengths, and as uniform bond lengths are something chemists would like to see in any representation, we will need to consider new forms of projection. We wish to choose a method of projection which retains the ability to preserve the symmetry of the central point of the projection, and which does a superior job in preserving bond distances.

This new method of projection must be equally suited to 3-D projection onto a 2-D plane, as well as 4-D projection into 3-D space. In both cases, we wish to preserve the symmetry at the center of the projection (for the former at the center of a 2-D polygon, and for the latter at the center of a 3-D polyhedron) while at the same time keeping variation in bond distances (for the former for bonds in the 2-D plane, and for the latter for bonds in 3-D space) to a minimum.

The chemical entities studied in this paper are based on the 54-cluster of the projected 600-cell. We will therefore choose a projection which preserves the T_d

symmetry of the 54-cluster, and which does a reasonable job in keeping bond distances constant.

Our proposed projection is a simple one. We place the light source at a point intermediate between the location for stereographic projection (where it lies on the sphere or spheroid) and linear projection (where it lies infinitely far away), as in Figure 2.9c. As bond distances become too long in stereographic projection and too short in linear projection, we thus achieve a happy medium. (The distances can never all be equal, but one can aim for maximum similarity.)

Least squares optimization of bond distances shows that for the 54-cluster (a 4-D to 3-D projection), a light source 1.9 spheroid diameters away from the center of the projection preserves distances best (see Appendix). In Table 2.2, we compare a variety of bond lengths for linear, stereographic, and this alternate projection. (The choice of the ten distances given in Table 2.2 is not a random one: as we shall later discuss, these ten bond lengths may be used to derive the ten site parameters on which the 54-cluster is based.) As this table shows, bond lengths are much more constant with the new method. We call this projection method intermediate projection. The formulas and sites corresponding to the 54-cluster are given in the Appendix.

2.4.2 The $F\bar{4}3m$ Structures and 54-Clusters

With this choice of projection in hand, we are ready to establish the connection between the common atoms of the $F\bar{4}3m$ crystal structures and the 54-cluster derived from the 600-cell. First, let us get our bearings in the $F\bar{4}3m$ structures. As we have mentioned previously, this paper considers only those $F\bar{4}3m$ struc-

Table 2.2: Comparison of bond lengths in projected 54-clusters.

Bond	Linear (Å)	Stereographic (Å)	Intermediate (Å)
IT-IT	2.828	2.828	2.828
OT-IT	2.763	2.933	2.847
OH-IT	2.649	3.004	2.820
CO-IT	2.322	3.135	2.692
CO-OT	2.649	3.251	2.915
IC-OT	2.000	3.501	2.610
IC-CO	2.649	3.736	3.094
MC-OH	1.732	3.773	2.496
MC-CO	2.322	3.929	2.921
OC-CO	2.000	4.070	2.709
Mean	2.391	3.416	2.793
Std. dev.	0.377	0.445	0.172

tures which contain a γ-brass cluster. For ease of comparison, we convert the coordinates of the reported crystal structures so that these γ-brass clusters are centered at the origin.[h] These converted coordinates are given in the Supporting Information (available online).

The γ-brass cluster consists of IT, OT, OH, and CO atoms, and by placing this cluster at the origin, these sites are labeled ZIT, ZOT, ZOH, and ZCO. (Recall that Z, Q, H, and T refer to clusters centered at zero, a quarter, a half, and three-quarters along the cell body diagonal: the Z in these labels therefore specifies a cluster centered at the origin.) We now examine the atoms which lie just outside this cluster. We turn first to the $Li_{21}Si_5$ structure. As Figure 2.10 shows,

[h] In the $F\bar{4}3m$ space group, the Z, Q, H, and T sites are the 4a, 4b, 4c, and 4d special sites, all with equal T_d symmetry. It is therefore possible to translate the unit cell so that a γ-brass cluster centered at any of these positions is shifted to lie at the origin. In making such a translation, we must also pay attention to the orientation of the γ-brass cluster. As the γ-brass cluster is non-centrosymmetric, there are two possible orientations. The IT atom is located at (x, x, x); we have chosen this atom to always lie near $(0.95, 0.95, 0.95)$, rather than $(0.05, 0.05, 0.05)$.

surrounding the γ-brass core are three additional Li sites: QCO, TCO, and TOT sites.

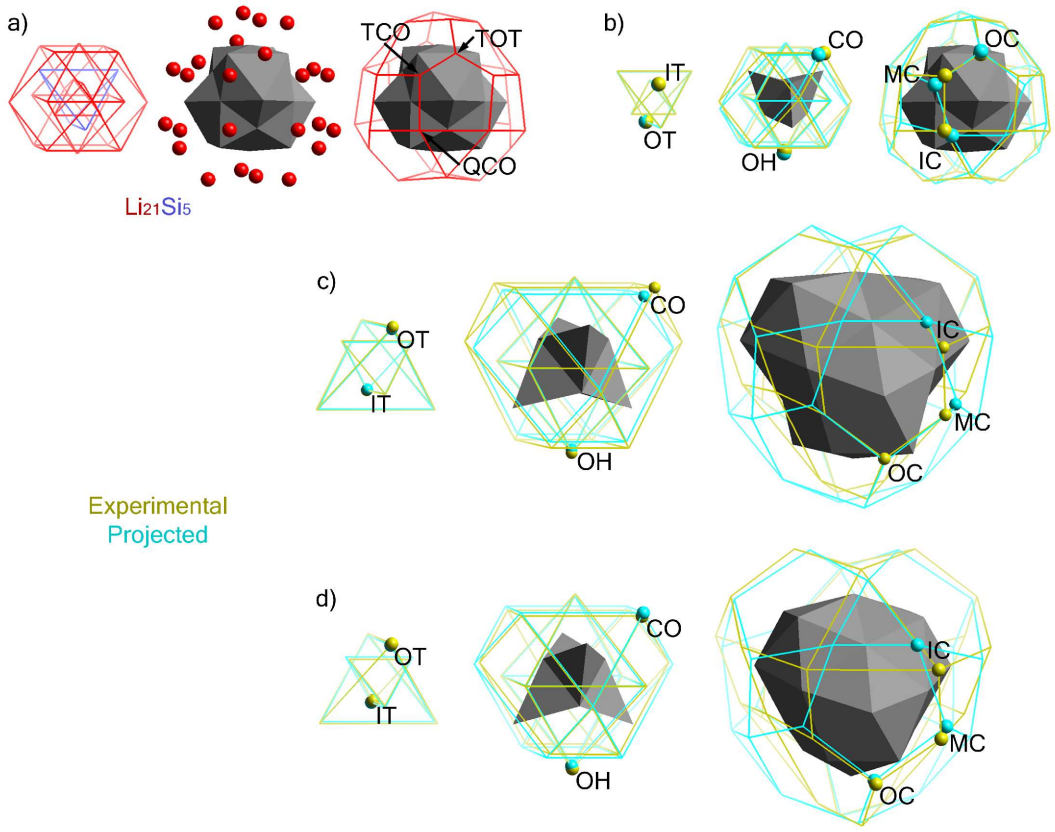

Figure 2.10: A 54-cluster in $Li_{21}Si_5$ where nearest neighbors are bonded to one another, shown a) by atom type (Li: red; Si: blue), and b) comparison of (a) with an intermediate projection of the 54-cluster (experimental sites: yellow; projected sites: cyan). Larger 54-clusters in c) $Mg_{44}Rh_7$ and d) $Li_{21}Si_5$, also compared to intermediate projections.

In Figure 2.10a (right), we draw the shell formed by the three additional sites. This shell has twenty-eight atoms in it. We recall that the 54-cluster also contains twenty-eight atoms placed in a shell around a 26-atom core. In Figure 2.10b, we directly compare the fifty-four atoms based on atoms at ZIT, ZOT, ZOH, ZCO, QCO, TCO, and TOT (shown in yellow) with the intermediate projected

54-cluster (shown in cyan). As this figure shows, the projected 54-cluster has vertices near the actual atomic sites of $Li_{21}Si_5$. The seven aforementioned sites therefore correspond to respectively the seven sites of the 54-cluster: IT, OT, OH, CO, IC, MC, and OC.

In Table 2.3, we list the atomic positions for the eight $F\bar{4}3m$ structure types.[i] Sites common to all structure types are given in italics. As the table shows, the eight structure types contain common sites at the seven aforementioned positions. All $F\bar{4}3m$ structures therefore contain a 54-cluster centered at the origin. But Table 2.3 also reveals additional sites common to all members of the $F\bar{4}3m$ family of structures. Can these additional common sites also be traced to 54-clusters?

Let us turn to clusters which might be centered at Q. An examination of Table 2.3 shows that only one of the eight structure types has a QIT atom. As an IT atom is an essential ingredient of any 54-cluster, at first glance we might conclude that there could be no common 54-cluster centered at Q. But we would be wrong.

The absence of QIT atoms does not imply the absence of a 54-cluster; rather it means that if there is a 54-cluster centered at Q, its length scale must be different from the length scale of the common 54-cluster centered at Z. If we are to examine Q-centered clusters, we must consider longer distances. We have not far to look. All eight structure types contain a QOT site. These QOT atoms also lie in a tetrahedron. The QOT atoms are separated from each other by distances

[i]For this article, we use Table 2.3 to define structure types. We assume two compounds which have the same atomic sites in Table 2.3 belong to the same structure type. Therefore, the $Li_{21}Si_5$ structure type includes $Zn_{21}Pt_5$ and $Cu_{41}Sn_{11}$, the $Mg_{44}Rh_7$ structure type includes $Zn_{39}Fe_{11}$ and $Mg_{44}Ir_7$, and the Mg_6Pd structure type includes $Mg_{29}Ir_4$. Elemental ordering over the sites is not taken into account in determining structure type. Actual elemental ordering is given, however, in the tables in the Supporting Information (available online).

Table 2.3: Atomic sites in the $F\bar{4}3m$ structures.

$Li_{21}Si_5$	$Mg_{44}Rh_7$	Zn_{13} $(Fe,Ni)_2$	Mg_6Pd	Na_6Tl	$Zn_{91}Ir_{11}$	$Li_{13}Na_{29}$ Ba_{19}	$Al_{69}Ta_{39}$
ZIT	*ZIT*	*ZIT*	*ZIT*	*ZIT*	*ZIT*	*ZIT*	*ZIT*
ZOT	*ZOT*	*ZOT*	*ZOT*	*ZOT*	*ZOT*	*ZOT*	*ZOT*
ZOH	*ZOH*	*ZOH*	*ZOH*	*ZOH*	*ZOH*	*ZOH*	*ZOH*
ZCO	*ZCO*	*ZCO*	*ZCO*	*ZCO*	*ZCO*	*ZCO*	*ZCO*
–	–	–	–	–	–	QCC	QCC
QIT	–	–	–	–	–	–	–
QOT	*QOT*	*QOT*	*QOT*	*QOT*	*QOT*	*QOT*	*QOT*
QOH	QOH	QOH	QOH	QOH	QOH	–	–
QCO	*QCO*	*QCO*	*QCO*	*QCO*	*QCO*	*QCO*	*QCO*
–	–	–	–	–	–	QTT	QTT
–	–	HCC	HCC	HCC	HCC	HCC	HCC
HIT	–	–	–	–	HIT	–	–
HOT	*HOT*	*HOT*	*HOT*	*HOT*	*HOT*	*HOT*	*HOT*
HOH	*HTT*	*HTT*	*HTT*	*HTT*	*HTT*	*HTT*	*HTT*
HCO	*HCO*	*HCO*	*HCO*	*HCO*	*HCO*	*HCO*	*HCO*
–	–	–	–	–	HOH	HTT	–
–	–	TCC	–	–	–	–	TCC
TIT	TIT	TIT	–	TIT	TIT	TIT	TIT
TOT	*TOT*	*TOT*	*TOT*	*TOT*	*TOT*	*TOT*	*TOT*
TOH	*TOH*	*TOH*	*TOH*	*TOH*	*TOH*	*TOH*	*TOH*
TCO	*TCO*	*TCO*	*TCO*	*TCO*	*TCO*	*TCO*	*TCO*

of approximately the golden mean ($\tau = \frac{1+\sqrt{5}}{2}$) times a typical metal bond length.

We now proceed to search for the remaining six sites of a 54-cluster. We recall that each of these six sites successively caps triangular faces formed by more central atoms. In Figure 2.10c, we show the cluster formed from the QOT, TOT, TOH, HTT, TOT, TCO, and HOT sites of the $Mg_{44}Rh_7$ system. We compare the cluster formed from these sites with the sites of the intermediate projected

54-cluster. As this figure shows, there is fair agreement between the crystal coordinates and the mathematically constructed 54-cluster.[j] The aforementioned sites therefore can be thought to correspond to the IT, OT, OH, CO, IC, MC, and OC sites of a 54-cluster whose nearest-neighboring distances are approximately τ times a standard metal bond length.

Table 2.3 shows that seven of the eight structure types have the above mentioned suite of atoms. However, the $Li_{21}Si_5$ structure, instead of containing the HTT site, has an HOH site. In Figure 2.10d, we show the cluster generated from the same set of atoms, but where the HTT site has been replaced by the HOH site. As this figure shows, this replacement in no way alters the presence of a 54-cluster.

The 54-clusters centered at Q are quite large with respect to the primitive unit cell. They are sufficiently large that the HOH atom in the $Li_{21}Si_5$ structure can provide the IC site for two neighboring 54-clusters. By contrast, in the $Zn_{91}Ir_{11}$ system, the HTT atoms are not shared by neighboring clusters. The former systems therefore require half the number of IC atoms that the latter systems require. There are six HOH atoms in an octahedron vs. twelve HTT atoms in a truncated tetrahedron. This change from an HTT site to an HOH site is therefore exactly what is required if two clusters are to share the same IC site.

As the HOH and HTT sites serve the same function, we consider for the sake of this paper that they are a common atomic site. We have used this view-

[j] Agreement is fair with the exception of the IC site. This is a general trend. The IC site is typically the site with the greatest disparity between mathematically constructed and experimentally observed positions. Recall that the IC site has highly compressed tetrahedra around it, and that as it caps two different triangular faces of the edge-capped stella quadrangula beneath it, the atomic site cannot readily move to decompress these tetrahedra. For these reasons, the tetrahedra around the IC atoms are the least regular in appearance and therefore, we suspect, the least ideal.

point in both Tables 2.3 and 2.4. We see that there is a common Q-centered 54-cluster throughout the $F\bar{4}3m$ family. In exactly the same manner, we can search for other 54-clusters. There are many to be found, an average of 4.5 clusters per structure type, the full list of which are given in Table 2.4. (In Table 2.4, we present the eight structure types in just six groupings, because two pairs of structure types, Mg_6Pd and $Zn_{13}(Fe,Ni)_2$, as well as Na_6Tl and $Zn_{91}Ir_{11}$, have the exact same list of 54-clusters.)

Table 2.4, in addition to showing the atomic sites of a given 54-cluster, also attempts to give some measure of the average distances found in each cluster. As each cluster has many nearest-neighbor distances, and as the atomic sites at which the atoms lie are high-symmetry points, some thought is called for in the calculation of average distances.

In this paper, we consider the following: IT, OT, and OC atoms lie at (x, x, x) special positions; OH atoms lie at $(x, 0, 0)$; and finally, CO, IC, and MC atoms lie (with the above-mentioned exception of the HOH site) at (x, x, z) positions. Therefore, one geometric parameter defines the IT, OT, OH, and OC positions, while two parameters define the CO, IC, and MC positions. There are a total of ten parameters needed to define the size and shape of a 54-cluster.

We can therefore define any 54-cluster with the appropriate choice of ten nearest-neighbor distances. We choose these canonical distances by considering links between a given atom and atoms more centrally located in the cluster. The ten distances chosen are IT-IT, OT-IT, OH-IT, CO-IT, CO-OT, IC-OT, IC-CO, MC-OH, MC-CO and OC-CO. In this list, the IT-IT distance defines the single parameter of the IT position, the OT-IT bond defines the single parameter of the OT position, and so forth.

Table 2.4: All 54-clusters in the $F\bar{4}3m$ structures.

Center	$a\div$ avg. dist.	Std. dev. (Å)	IT	OT	OH	CO	IC	MC	OC
				$Li_{21}Si_5$, $Zn_{21}Pt_5$, and $Cu_{41}Sn_{11}$					
Z	6.62	0.12	*ZIT*	*ZOT*	*ZOH*	*ZCO*	*QCO*	*TCO*	*TOT*
Q	6.62	0.20	QIT	*QOT*	QOH	*QCO*	*HCO*	*ZCO*	*ZOT*
H	6.42	0.37	*HOT*	HIT	*HOH*	*HCO*	*QCO*	*TCO*	TIT
T	6.64	0.15	TIT	*TOT*	*TOH*	*TCO*	*ZCO*	*HCO*	*HOT*
Z	3.70	0.38	*ZOT*	*TOT*	*HOH*	QOH	*HOT*	*HCO*	*QOT*
Q	3.81	0.29	*QOT*	*ZOT*	*TOH*	*HOH*	*TOT*	*TCO*	*HOT*
H	3.62	0.55	HIT	TIT	*ZOH*	QOH	*ZCO*	*ZCO*	QIT
T	3.70	0.38	*TOT*	*HOT*	QOH	*ZOH*	*QOT*	*QCO*	*ZOT*
				$Mg_{44}Rh_7$, $Zn_{39}Fe_{11}$, and $Mg_{44}Ir_7$					
Z	6.68	0.18	*ZIT*	*ZOT*	*ZOH*	*ZCO*	*QCO*	*TCO*	*TOT*
T	6.78	0.20	TIT	*TOT*	*TOH*	*TCO*	*ZCO*	*HCO*	*HOT*
Q	3.78	0.57	*QOT*	*ZOT*	*TOH*	*HTT*	*TOT*	*TCO*	*HOT*
T	3.77	0.65	*TOT*	*HOT*	QOH	*ZOH*	*QOT*	*QCO*	*ZOT*
				$Zn_{13}(Fe,Ni)_2$, Mg_6Pd, and $Mg_{29}Ir_4$					
Z	6.75	0.15	*ZIT*	*ZOT*	*ZOH*	*ZCO*	*QCO*	*TCO*	*TOT*
Q	3.49	0.96	*QOT*	*ZOT*	*TOH*	*HTT*	*TOT*	*TCO*	*HOT*
T	3.67	0.69	*TOT*	*HOT*	QOH	*ZOH*	*QOT*	*QCO*	*ZOT*
				Na_6Tl and $Zn_{91}Ir_{11}$					
Z	6.71	0.16	*ZIT*	*ZOT*	*ZOH*	*ZCO*	*QCO*	*TCO*	*TOT*
T	6.82	0.14	TIT	*TOT*	*TOH*	*TCO*	*ZCO*	*HCO*	*HOT*
Q	3.63	0.65	*QOT*	*ZOT*	*TOH*	*HTT*	*TOT*	*TCO*	*HOT*
H	3.79	0.42	*HOT*	*QOT*	*ZOH*	*TOH*	*ZOT*	*ZCO*	*TOT*
T	3.77	0.72	*TOT*	*HOT*	QOH	*ZOH*	*HTT*	*QCO*	*ZOT*
				$Li_{13}Na_{29}Ba_{19}$					
Z	6.77	0.34	*ZIT*	*ZOT*	*ZOH*	*ZCO*	*QCO*	*TCO*	*TOT*
T	7.77	0.45	TIT	*TOT*	*TOH*	*TCO*	*ZCO*	*HCO*	*HOT*
Q	3.51	0.92	*QOT*	*ZOT*	*TOH*	*HTT*	*TOT*	*TCO*	*HOT*
H	3.83	0.76	*HOT*	*QOT*	*ZOH*	*TOH*	*ZOT*	*ZCO*	*TOT*
				$Al_{69}Ta_{39}$					
Z	6.75	0.14	*ZIT*	*ZOT*	*ZOH*	*ZCO*	*QCO*	*TCO*	*TOT*
Q	3.42	0.95	*QOT*	*ZOT*	*TOH*	*HTT*	*TOT*	*TCO*	*HOT*
H	3.62	0.66	*HOT*	*QOT*	*ZOH*	*HCO*	QTT	*ZCO*	*TOT*

We may directly calculate these ten canonical distances from knowledge of the ten atomic site parameters. And conversely, the ten atomic site parameters can be specified from the ten canonical distances. While atomic site parameters are the most typical way to represent atomic positions, the canonical distances are nonetheless of interest. In intermediate projection, bond distances are fairly constant across all bonds in the 54-cluster. When the canonical bond distances are close to each other in value, the atoms will therefore prove to lie particularly near the positions of an intermediate projected 54-cluster.

In the Supporting Information (available online), we present canonical nearest-neighbor distances for all 54-clusters found in the $F\bar{4}3m$ structures. In Table 2.4, we present a summary of this data. In particular, we show the ratio of the *a*-axis cell length divided by the average of the ten canonical distances. With this value, we also show the standard deviation among the ten canonical bond distances. As Table 2.4 shows, for all but one of the myriad 54-clusters, calculated ratios are in the range of either 6.4-6.8 or 3.4-3.9. The former range corresponds to nearest-neighbor distances at ordinary bond lengths, the latter to the golden mean times that number.

Table 2.4 also shows that for the former range, the standard deviation of bond lengths centers around the value of 0.2 Å. This value can be directly compared to the ideal mathematical variation of 0.17 Å (associated with the intermediate projection method) shown in Table 2.2. The actual variation in bond lengths is not much greater than that which is mathematically obtainable. For 54-clusters in the 3.4-3.9 range, the variation in cluster distances is greater, with the smallest standard deviations near 0.6 Å in value. This more than doubling in standard deviations is partially accounted for by the increase of the actual

cluster distances. But note that as there are an average of 4.5 54-clusters per structure type, but only twenty or so atomic parameters per structure type, uniformly small standard deviations across all cluster sizes are difficult to achieve.

We present this same data graphically in Figure 2.11. In this figure, we plot the ratio of cell axis length ÷ average nearest-neighbor distance, together with its corresponding standard deviation for all clusters of all thirteen structures belonging to the eight structure types. This figure shows clearly the two apparent size ratios: a ÷ average distance values of either approximately 4 or 6. One of the primary goals for the remainder of this paper will be to account for these most common size ratios.

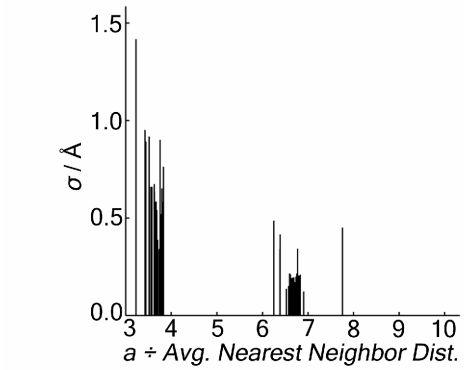

Figure 2.11: The standard deviation vs. mean nearest-neighbor distance in each experimental occurrence of the 54-cluster in the $F\bar{4}3m$ structures. The same data is given in tabular form in the Supporting Information (available online).

2.5 Diffraction of a Single 54-Cluster

We have seen there is a relation between the atomic sites in the $F\bar{4}3m$ structures and the 3-D projected image of the 4-D 600-cell. We now examine how the five-

fold symmetry operations of the 4-D 600-cell are retained as pseudosymmetries in its 3-D projection.

There are an enormous number of fivefold symmetries in the full 4-D 600-cell. If we recall that every pair of adjacent vertices (i.e., every bond) of the 600-cell is bisected by a pentagonal face of the dual 120-cell, and that each of these pentagonal faces has fivefold symmetry, we recognize that every bond in the 600-cell defines a set of fivefold symmetry operations. Before projection, all bonds have exact fivefold symmetry.

After 3-D projection, different bonds differ in the extent to which they retain their fivefold symmetry. The bonds nearest the center of projection retain the most of the original fivefold symmetry. (Recall that the symmetry of the exact center of the projection is perfectly preserved, and that the further one travels from this center, the more imperfect the resultant images usually become.) In the 3-D projection discussed in this paper, we have chosen the center of the projection to be the center of one of the tetrahedral cells of the 600-cell. There are six fivefold axes which lie nearest this center: the six edges of the central tetrahedron. The fivefold symmetry is best preserved for these six axes.

In Figure 2.12a, we redraw the 54-cluster so that one of the six edges of its central tetrahedron is placed at the center of the image. In Figure 2.12b, we consider this exact same orientation, but keep only the bonds which appear as pentagons or decagons in the projected image. It may be seen that fifty of the fifty-four atoms lie either at the center of this view or on a pentagon or decagon.

In Figure 2.12c,d, we show the perpendicular view of the core atoms, and the individual pentagons. It may be seen that there are four core atoms (Fig-

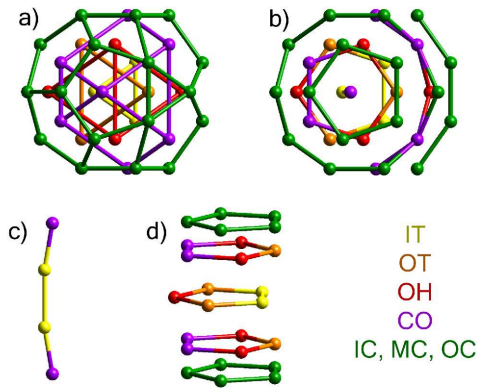

Figure 2.12: Features of pseudo-fivefold symmetry in the linear projection of a 54-cluster. a) A view of the 54-cluster along one of the bonds of its central tetrahedron, b) the pentagons and the decagon within this unit, and a perpendicular view of c) the four core atoms and d) five pentagons. From the center outward, sites are shown in yellow, orange, red, purple, and green. See Figure 2.8 for site names.

ure 2.12c) and five different pentagons (Figure 2.12d). The structure of the so-called decagon is more complex and is not shown in this figure. It consists of twenty-one atoms with an approximate fivefold symmetry to them.[k]

2.5.1 Plane Waves and the 54-Cluster

We now turn to the diffraction image of the 54-cluster. As yet, we have not placed the cluster into a crystalline unit cell. Even so, we can generate relevant images. Consider the Fourier transform[l] of the 54-cluster,

[k]The so-called decagon could be viewed as five pentagons with four defect sites. But we need not enter the full complexity of the decagon, as our primary interest is the pseudo-tenfold diffraction symmetry normal to the [110] direction. As readers familiar with diffraction theory know, in such cases we need only consider the 2-D projection of atoms normal to the desired direction to calculate exact structure factors.[80] Figure 2.12b gives an adequate view of this 2-D projected structure.

[l]For those accustomed to seeing X-ray diffraction patterns, the use of Fourier transforms here may seem unorthodox. The Fourier transforms used in this paper resemble more closely

$$F_{\vec{k}} = \sum_{j=1}^{54} e^{2\pi i \vec{k}\cdot\vec{r}_j}.$$

Note that the constant scattering factor for each atom is taken to be unity.[m] To apply this Fourier transform, we need to explicitly determine the fifty-four $\vec{r}_j$ coordinates. We consider both a linear and an intermediate projected 54-cluster. Looking ahead to the actual crystal structure, we define an IT-IT bond to run in the $[1\bar{1}0]$ direction. We further consider only those $\vec{k}$ which are orthogonal to this direction. With these givens, we can calculate the magnitude of $F_{\vec{k}}$ as a function of $\vec{k}$. This is plotted in Figure 2.13. (Figure 2.13a,b are respectively the diffraction images of the linear and intermediate projected 54-clusters.)

As this figure shows, there are a few particularly large peaks in the Fourier transform. Especially towards the center of this diffraction image, these peaks appear in rings of ten. Three such possible rings are shown in Figure 2.13. In the innermost ring, labeled 4, all ten reflections are clearly visible. For the ring labeled 6, six of the ten peaks are clear for both the linear and the intermediate projected 54-clusters. The remains of four additional peaks can also be discerned in the intermediate projected 54-cluster diffraction pattern. For the ring labeled 10 of the linear projected 54-cluster, only the reflections along the horizontal axis (the $[k_1 k_1 0]$ direction) are present. By contrast, for the interme-

the Fourier transforms used to study clusters in the gas phase, and can be seen as the analog of diffraction patterns without the constraints of a unit cell. As in a diffraction pattern, the $\vec{k}$–vector corresponds to the direction and frequency of plane waves running through the cluster, and the contours to the degree to which atoms constructively interfere with the waves.

[m] By taking the scattering factor of each atom to be unity, we do not treat the coloring problem in this paper. We cannot expect the type of 4-D to 3-D projection in this paper to hold the key to the coloring problem, as evidenced by the different atomic site preferences in the small and large 54-clusters throughout this family of structure types. While the large clusters tend to consist mainly of larger and/or more electronegative atoms, the small clusters have no obvious occupancy pattern. Still, we expect that the answer to the coloring problem is closely related to this projection method, and we plan to explore this point in our subsequent work.

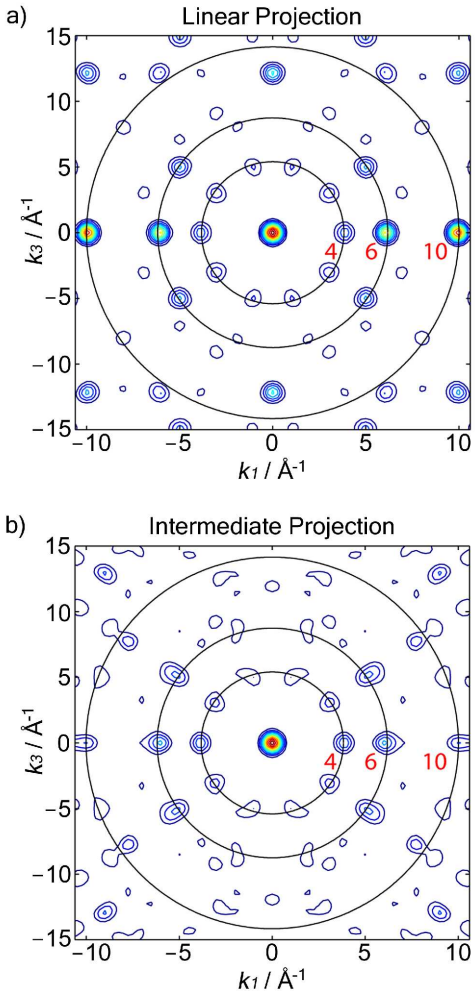

Figure 2.13: Two-dimensional cross-section of the Fourier transforms of a) a linear projection and b) an intermediate projection of the 54-cluster, viewed along the $[1\bar{1}0]$ direction. These cross-sections contain points of the form $k_1k_1k_3$. IT-IT distances of 2.40 and 2.03 Å were assumed in order that the $(k_1\overline{k_1}0)$ planes divide the 54-cluster into k_1 segments, as in Figure 2.14. Both plots are divided into twelve equally spaced contours, where redder lines represent greater constructive interference, and bluer lines less.

diate projected 54-cluster, the ring labeled 10 reveals an additional set of four peaks. All of the above peaks lie at similar orientations along the concentric rings, orientations which correspond to a pseudo-tenfold diffraction symmetry.

Let us consider real-space pictures, based at first just on a linear projected 54-cluster, which correspond to these major peaks. In Figure 2.14a, we show a picture of the 54-cluster with bonds represented as line segments. In Figure 2.14b-d, we show this same cluster, but with all the bonds removed for visual clarity. In addition, we show plane waves whose reciprocal lattice vectors are $(k_1\overline{k_1}0)$ partitioning the 54-cluster into respectively 4, 6, and 10 segments. (More exactly, the projected 54-cluster OC-OC distance is chosen to be respectively 4, 6, or 10 times the plane wave wavelength.)

It can be seen that there is a correspondence between these three $(k_1\overline{k_1}0)$ plane waves and the projected 54-cluster. In all three cases, the vertices of the 54-cluster lie near the crests of the plane waves. These three wavelengths lead to excellent intracluster constructive interference, and hence strong diffraction peaks. In the case where the projected 54-cluster OC-OC distance is 10 times the wavelength (Figure 2.14d), constructive interference is nearly ideal.

Numbers such as 4, 6, and 10 are of interest. In particular, if we divide these numbers by two, they correspond to integers in the Fibonacci sequence $(1, 1, 2, 3, 5, 8, 13, \ldots)$. The 54-cluster has the remarkable property that interatomic spacings are related to the Fibonacci sequence. This remarkable property can be directly traced to the 600-cell itself.

The Fibonacci sequence is furthermore naturally connected to the golden mean ($\tau = \frac{1+\sqrt{5}}{2}$): ratios of adjacent members of the Fibonacci sequence quickly

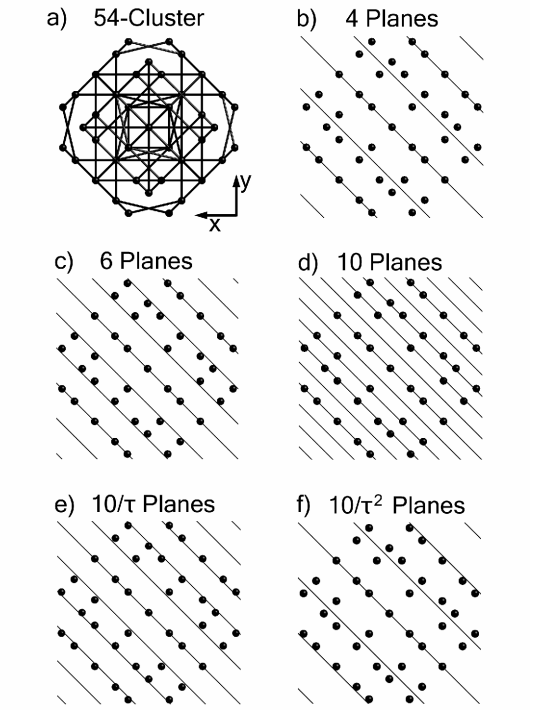

Figure 2.14: a) A linear projection of the 54-cluster, shown with an OC-OC distance equal to b) 4, c) 6, d) 10, e) $10/\tau$, and f) $10/\tau^2$ (where τ is the golden mean) spacings of plane waves whose reciprocal lattice vectors are $(k_1\overline{k_1}0)$. Diagonal lines represent the crests of the respective plane waves. The cluster achieves significant constructive interference with the waves at each of the illustrated sizes.

converge to the golden mean. In Figure 2.14b,c,e,f, we compare plane waves that partition the cluster into 6 and 4 segments to plane waves that partition the cluster into $10/\tau$ (6.18) and $10/\tau^2$ (3.82) segments. (We choose ratios related to 10 because for this integer value, constructive interference is already nearly ideal.) As shown in Figure 2.14e,f, these two non-integer values have excellent constructive interference.

We quantitatively evaluate the relation of the $10/\tau$ and $10/\tau^2$ waves in the original Figure 2.13. Recalling that for plane waves, the wavelength λ deter-

mines the length of $\vec{k}$ ($\lambda|\vec{k}| = 1$), we directly place onto Figure 2.13 circles whose radii correspond to the plane waves labeled 10, $10/\tau$, and $10/\tau^2$ in Figure 2.14. The three rings labeled 10, 6, and 4 in Figure 2.13 actually correspond to the 10, $10/\tau$ (6.18), and $10/\tau^2$ (3.82) plane waves of Figure 2.14. Re-examination of Figure 2.13a shows that the calculated peak maxima lie almost exactly on the calculated ring positions. (By contrast, had we placed plane waves corresponding to wavelengths of either 4.00 or 6.00 cluster spacings, we would have seen a significant misalignment between ring sizes and diffraction peak maxima.)

In Figure 2.13b, the illustrated rings were created in an identical manner, but for an intermediate projected 54-cluster.[n] Comparison of Figures 2.13a,b shows that ideal constructive interference depends much more on the values 10, $10/\tau$, and $10/\tau^2$ than on the projection method used. It is these wavelengths and the subtle regularities of the 600-cell, rather than the projection method, which are responsible for optimal intracluster constructive interference.

These facts are of central relevance to the paper. In particular, these results suggest that if one were to have a pair of 54-clusters of different sizes, but with a size ratio between clusters of either τ or τ^2, one might have not just optimal intracluster interference, but intercluster interference as well. In Figure 2.15, we show two 54-clusters with an intercluster size ratio of τ.

As this figure shows, plane waves can constructively interfere equally well for two differently-sized 54-clusters whose size ratio is near the golden mean. Such pairs of differently-sized clusters are more fully considered in the next section of this paper. For now, note that differently-sized clusters are not just a hypothetical musing. Rather as we have previously discussed, differently-sized

[n] In the intermediate projected 54-cluster, two IC atoms which lie along the $[1\bar{1}0]$ direction with respect to each other were used to define the 10, $10/\tau$, and $10/\tau^2$ plane wave wavelengths.

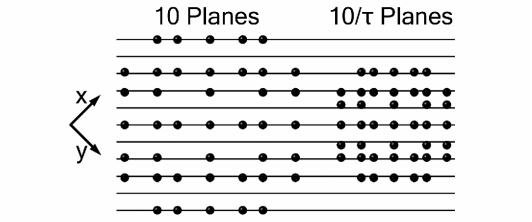

Figure 2.15: Linear projections of two 54-clusters differing in size by a factor of τ, the golden mean, shown with plane waves whose reciprocal lattice vectors are $(k_1\overline{k_1}0)$. Horizontal lines indicate the crests of the plane waves. At these particular sizes, the two clusters can simultaneously achieve significant constructive interference.

54-clusters whose size ratios are near the golden mean are extremely common in the $F\overline{4}3m$ family of structures.

2.5.2 Three-Dimensional Bravais Space Groups Compatible with the 54-Cluster

In the previous sections of this paper, we found that a single 54-cluster has both T_d and pseudo-fivefold symmetry. There are six pseudo-fivefold axes, each running along one of the edges of the inner tetrahedron (IT) of the 54-cluster. We now determine the crystalline symmetry consequences of the above statements.

First, we assume the symmetry of the actual crystal emanates from the 54-cluster itself: it should be of no higher or no lower symmetry than the 54-cluster's T_d symmetry. We therefore require that the highest symmetry site of the crystal is of T_d symmetry. There are five space groups which meet this requirement: $P\overline{4}3m$, $F\overline{4}3m$, $I\overline{4}3m$, $Pn\overline{3}m$, and $Fd\overline{3}m$. Happily, all the cubic struc-

tures which we know to exhibit pseudo-fivefold symmetry along their ⟨110⟩ directions belong to one of these five space groups. These include not just the structures which are the primary concern of this paper, but also the three most complex of all cubic structures: Cd_3Cu_4 ($F\bar{4}3m$),[5] $NaCd_2$ ($Fd\bar{3}m$),[3] and Mg_2Al_3 ($Fd\bar{3}m$).[4,81]

The requirement that the highest site symmetry be T_d not only specifies the possible space groups, but also determines the orientation of the 54-cluster within the cubic unit cell. For a T_d cubic unit cell, the $\bar{4}$ axes always run along the ⟨100⟩ directions, while the threefold axes run in the ⟨111⟩ directions. The edges of the inner tetrahedron define the *m* setting (the third setting, the ⟨110⟩ directions). The edges of the inner tetrahedron therefore must lie in the ⟨110⟩ directions.

As the edges of the inner tetrahedron are the best preserved pseudo-fivefold symmetry axes of the 54-cluster, the most clear pseudo-fivefold symmetry axes lie along the six ⟨110⟩ directions. This is the exact result which we set out to rationalize at the beginning of this paper. Every indication is therefore that the construction of the 4-D 600-cell and its projection, the 54-cluster, plays a critical role in the observed pseudo-tenfold diffraction patterns.

2.5.3 Crystalline 54-Cluster Interference

But we can go further. Let us consider a single crystallographically inequivalent 54-cluster, and let us place it into a cubic unit cell. As the crystal structures which interest us are all *F*-centered, we make the unit cell *F*-centered. We now specify the size of the cluster relative to the size of the unit cell. As a measure

of the former, we consider the IT-IT distance. (As the 600-cell is a Platonic solid, all nearest-neighbor distances are originally the same, and therefore all nearest-neighbor distances initially equal the IT-IT distance.) For the latter, we use the *a*-axis length.

We consider a ratio of *a*-axis ÷ IT-IT distance ranging in value from 3 to 35, and calculate across this range the diffraction pattern. A few of these results are illustrated in Figure 2.16. (Figure 2.16 top and bottom are respectively the calculated diffraction patterns for a linear and an intermediate projected 54-cluster. The results presented in this figure use the same delta-function-like atomic form factors as were used for the isolated 54-clusters.) All ratios calculated exhibit a pseudo-tenfold diffraction. Thus, the size ratio is not a factor in the overall pseudo-fivefold symmetry. (This is as we would expect: the pseudo-fivefold symmetry is a consequence of the finite 4-D cluster, and is therefore independent of 3-D cell axis length.)

But even within the constraint of pseudo-fivefold symmetry, there is an enormous variation in diffraction patterns. We observe two trends. First, at the largest ratios, the pseudo-tenfold diffraction peaks are distributed over a number of neighboring *hkl* reflections, but at smaller ratios, the pseudo-tenfold diffraction coalesces into single peaks. A second distinction is also present. As Figure 2.16 shows, the most intense peaks shift in their positions.

To aid our understanding of these shifts, we place directly onto the diffraction images in Figure 2.16 a constant ring which corresponds to the ring labeled 4 in Figure 2.13, previously calculated for the isolated 54-cluster. As Figure 2.16 shows, the actual diffraction pattern fluctuates with respect to the isolated cluster ring.

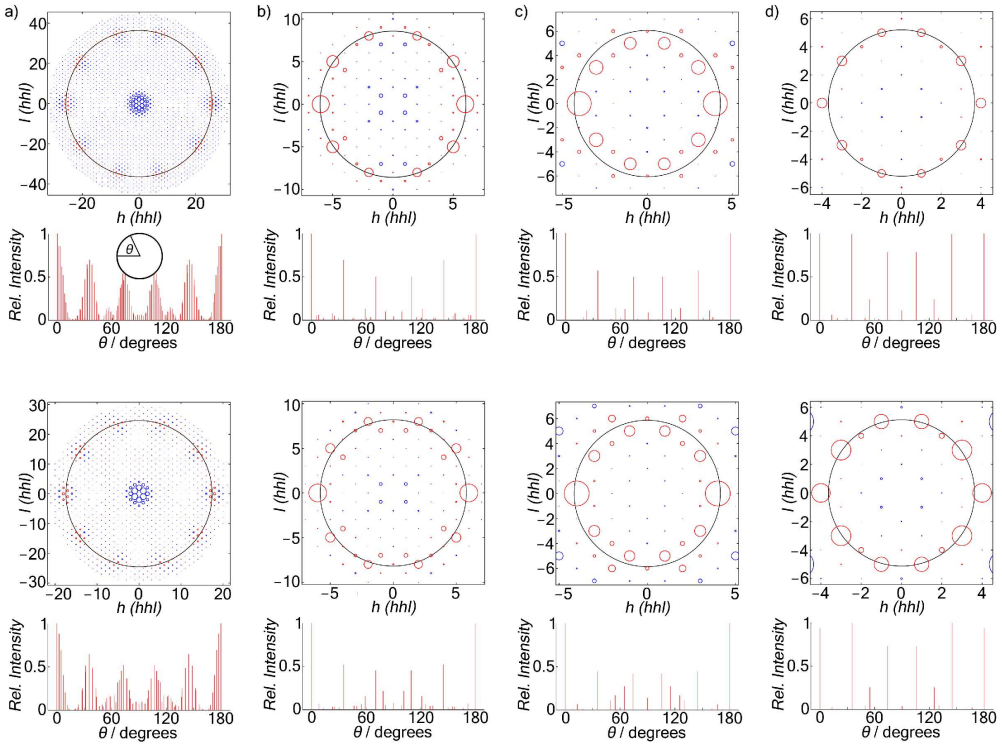

Figure 2.16: The 2-D (blue and red) and circular 1-D (red) diffraction patterns for linear (top row) and intermediate (bottom row) projections of the 54-cluster placed in an F-centered cubic cell, illustrating the dependence of peak sharpness on the relative sizes of the unit cell and the cluster. Unit cell axes are a) 25 (linear) and 20 (intermediate), b) 5.9 (linear) and 6.7 (intermediate), c) 4.2 (linear) and 4.8 (intermediate), d) 3.6 (linear) and 4.2 (intermediate) times the IT-IT distance. A ring corresponding to peak maxima of an isolated 54-cluster (the ring labeled 4 in Figure 2.13) is shown as a black circle. For both types of projection, optimal peak sharpness and location (vis-à-vis the black circle) occur where the cell axis is approximately 6 (panel b) or 4 (panel d) times the IT-IT distance.

If the diffraction peaks of Figure 2.16 are not fully in accord with the Fourier transform of the isolated cluster, then there must be a less-than-ideal constructive interference present in the diffraction pattern. Intracluster and intercluster planes must not be fully aligned. Constructive interference can only be optimal when the diffraction peaks of Figure 2.16 lie on the isolated 54-cluster ring positions.

An examination of data across the full range of calculated sizes suggests that for some specific size ratios, there is optimal agreement between isolated and crystalline 54-cluster diffraction patterns. The two best ones are illustrated in Figure 2.16b,d. The first is found near a size ratio of 6, the second near a size ratio of 4 (the specific optimal value itself shifts somewhat depending on the method of projection). In both of these cases, intense reflections lie directly on the illustrated ring.

A simple metric which could quantitatively evaluate what the naked eye sees would be useful. Such a metric would need two components. On the one hand, it would measure the degree to which peaks coalesce. On the other hand, it would measure the proximity of the coalesced peak to those which were calculated for the isolated 54-cluster. Interestingly, as pseudo-tenfold symmetry appears to play an equal role in all the diffraction images, the desired metric need not measure tenfold symmetry.

A pithy metric proves cumbersome to find. We develop it in two steps. First, we consider the ring of the isolated 54-cluster corresponding to a size ratio of 4. Intracluster diffraction is optimal for points along this ring. We now determine which *hkl* peaks lie nearest these optimal values. To do so, we consider the reciprocal lattice itself. The reciprocal lattice has vertices which correspond to

specific *hkl*, and edges (connections between neighboring vertices) which might intersect the ring. We consider only those *hkl* whose attached edges intersect the ring. The selected *hkl* are shown in red in Figure 2.16.

At the base of each panel of Figure 2.16, we show the selected diffraction peaks in a separate graph. These graphs plot the intensities of the selected diffraction peaks as a function of the angles to which they correspond along the ring. As these figures show, for all size ratios, the diffraction patterns take on a pseudo-tenfold symmetry. There are ten major peaks distributed symmetrically around the ring (six of which are given in the basal pictures); each peak has a number of satellite peaks.

We now establish the first half of the desired metric. We divide the 180° graphs into five cohorts of peaks, each corresponding to a 36° range of peaks. We then select the strongest peak in each cohort (its intensity is called I_1), and take its ratio with respect to the second strongest peak (whose intensity is I_2). We calculate the geometric mean of these ratios. As by symmetry, these five cohorts always consist of just three sorts, we take the geometric mean of just the three symmetry-inequivalent cohorts. This geometric mean provides a measure of how peaked any given diffraction pattern is.

We now consider the actual position of these strongest five peaks relative to the ring itself. We calculate the distance between the three distinct most intense peaks and a set of three points lying on the illustrated ring with ideal tenfold symmetry, and take the geometric mean of these distances. We now multiply these two geometric means together. This product can be thought of as a measure of the accord between intracluster and intercluster constructive interference.

In Figure 2.17a,b, we plot this product for both a linear and an intermediate projected 54-cluster. In the case of linear projection, there are two strong and sharp peaks at size ratios of 3.9 and 5.8. For intermediate projection, the corresponding values are 4.0 and 6.9. For ease of comparison, we also replot, in Figure 2.17c, the data based on the actual crystal structures. As we have previously shown, experimentally there are two observed size ratios, the first mainly ranging from 3.5 to 3.8, the second more sharply peaked at values around 6.6 to 6.8.

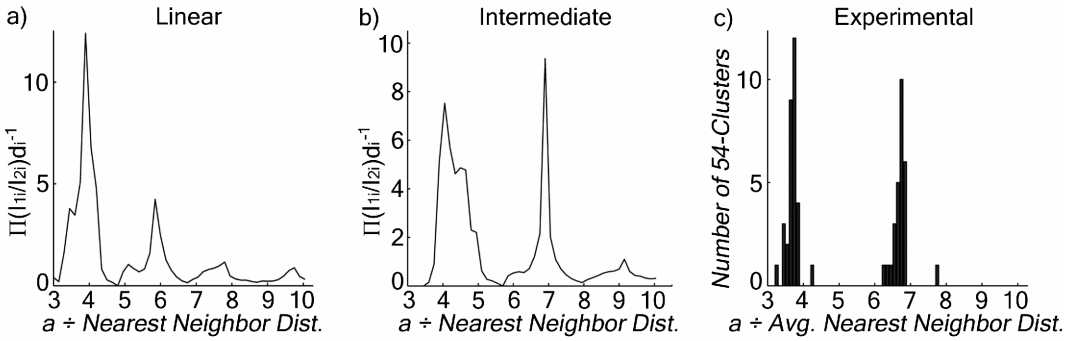

Figure 2.17: The combined metric (see text) which assesses both the diffraction peak sharpness and peak positions for the a) linear and b) intermediate projections of the 54-cluster in an *F*-centered cubic cell, plotted vs. the cell-to-cluster size ratio. c) The frequency of each size of 54-cluster in experimental crystal structures. The two distinct ranges of theoretically optimal cluster sizes are matched by experiment.

Both projected clusters and the experimental data agree that there are two optimal size ratios, one near 4 and the other near 6. The observed experimental range lies somewhere between the values obtained from the linear and the intermediate projection methods. Perhaps not too surprising, in the case of the smaller cluster (the clusters with size ratios of 6), the intermediate projection fares better at quantitative rationalization. For the smaller cluster, the inter-

atomic distances are metal bonds themselves. Intermediate projection, with its more constant bond distances, is therefore more reasonable than linear projection (see Table 2.2).

In some ways, however, the results of Figure 2.17 appear surreal. The calculated results are derived solely from geometrical considerations, the mathematical construction of clusters with optimal constructive fivefold diffraction, while the experimental results are presumably due to the optimization of the Schrödinger equation. The agreement between theory and experiment is therefore curious.

2.6 Fivefold Symmetry of Multiple 54-Clusters

In previous sections of this paper, we found that only at specific length scales does the 54-cluster have its most constructive intracluster interference (Figure 2.14). We have further suggested that two clusters with different length scales can constructively interfere with one another if their length scales are related by the golden mean (Figure 2.15).

Crystallographic data for the $F\bar{4}3m$ family of structures (Figure 2.17c) bears out these theoretical constructions with numerous 54-clusters at two predominant length scales. The length scale of the smaller 54-clusters are dictated by metal bond distances; the length scale of the larger clusters are larger by a factor of roughly the golden mean. Experimental results are therefore in good agreement with theoretical conjecture.

But this agreement by itself does not rigorously prove the conjecture. In

this section of the paper, we explicitly calculate the diffraction pattern of two distinct clusters within one unit cell. We consider especially the case where the two different clusters are centered at different points, as this seemingly could most easily violate real space pseudo-fivefold symmetry.

As we consider here for the first time the diffraction of two 54-clusters, we must for the first time consider interference effects between two clusters not related by translational symmetry. We need to take into account the orientation of 54-clusters with respect to each other. The 54-cluster orientation is an issue because this cluster has T_d symmetry. There are two ways to align a tetrahedron with respect to the symmetry of a cubic unit cell, and therefore two ways to orient the 54-cluster. Considering the central IT tetrahedron of the 54-cluster, we can have one of its triangular faces pointing along either the [111] or $[\overline{111}]$ direction. We shall call the former orientation regular (r or R), and the latter orientation inverted (i or I).

We may then develop the following nomenclature: small and large Roman letters will signify respectively small- and large-scaled 54-clusters. R would refer to a large-scaled 54-cluster with the regular orientation. Combining these names with the Z, Q, H, and T notation, we can generate an efficient naming scheme. Qi for example will specify a small-scaled 54-cluster with the inverted orientation, centered at $(\frac{1}{4}, \frac{1}{4}, \frac{1}{4})$.

In Figure 2.18a, we consider one regular and one inverted cluster located at respectively Z and Q. (We choose Z and Q because, as Table 2.4 shows, these are the most common cluster centers.) We calculate the diffraction pattern for cell-to-cluster size ratios ranging from 3 to 35, using the product established in the preceding section to assess the diffraction pattern. As Figure 2.18a shows, there

are a number of optimal size ratios of the two clusters. The globally optimal ratio is for one cluster to have a size ratio of 6 (i.e., r or i) while the other has a size ratio of 4 (i.e., R or I). The second most optimal ratio is for both clusters to have size ratios of 4.

The figure shows two identical globally optimal peaks. We can apply our nomenclature to verify that they should be identical. The first of the two optimal peaks corresponds to the pair of 54-clusters Zr·QI, while the second is for two clusters ZR·Qi. Now consider the effect on the first two clusters if they are inverted about the point $(\frac{1}{8}, \frac{1}{8}, \frac{1}{8})$. In this operation, the Z and Q sites switch labels. Furthermore, r and I convert to respectively i and R. Thus, Zr·QI becomes Qi·ZR, and the aforementioned peaks are symmetry-equivalent. (Note Qi·ZR = ZR·Qi.)

We place, directly on the figure, crosses which correspond to the experimentally determined pairs of clusters. (In addition to pairs of clusters centered at Z and Q, we also include pairs of clusters located at Q and H, H and T, or T and Z sites. We do so because the calculated contour maps are equally valid for all pairs of neighboring centers.) Agreement between theory and experiment is good. The largest number of peaks are found at Zr·QI and ZR·Qi. In addition, there are a few experimentally observed points which lie near the second most optimal geometry, ZR·QI, and three points at Zr·Qi. (The presence of these last points is the subject of the last paragraph in this section.)

We now turn to the cases of Zr·Qr, Zr·QR, ZR·Qr, and ZR·QR. We examine these cases in light of our earlier observations for the Zr·QI peaks. We first note two geometrical issues. First, we observe that one cannot have Zr and ZR clusters simultaneously in the same crystal structure. This is so because the

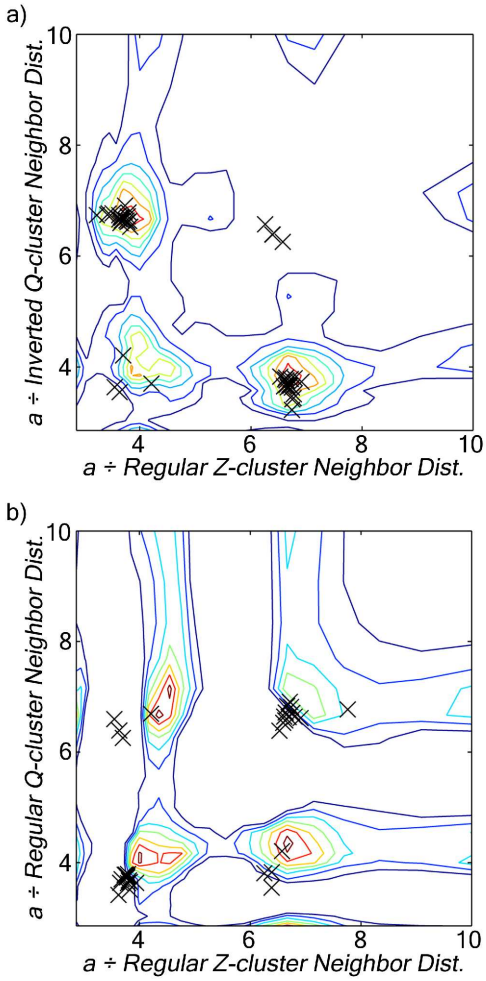

Figure 2.18: Contour plots of the combined metric (see text) which assesses both diffraction peak sharpness and peak positions for F-centered cubic unit cells containing the intermediate projections of two 54-clusters centered respectively at Z and Q, a) with clusters with inverted orientation with respect to each other and b) with the same orientation. Both plots are divided into seven equally spaced contours, where redder lines represent larger values, and bluer lines smaller values. Crosses indicate experimentally observed arrangements of pairs of clusters. See text for discussion.

ZIT atom provides the IT site of the Zr cluster, but ZOT provides not just the OT site of the Zr cluster but the IT site of the ZR cluster. In a 54-cluster, the IT tetrahedron has one orientation while the OT tetrahedron has the opposite orientation. Thus, the ZOT site cannot simultaneously be the OT site of a Zr cluster and the IT site of a ZR cluster.

Second, we note Zr and Zi are not compatible. In Zr, we would have a regularly oriented IT and therefore an inverted OT, while in Zi we would have an inverted IT and regularly oriented OT. Zr and Zi are not compatible, as an inverted (or regular) OT and an inverted (or regular) IT would lie too close to one another to be simultaneously present. (For a similar reason, QI and QR are not found together.)

These two geometrical observations place considerable constraints on the Zr·Zr, Zr·ZR, ZR·Zr, and ZR·ZR peaks. As we have seen in Figure 2.18a, the Zr·QI configuration is quite common. If the crystal in question has the Zr·QI configuration, then the presence of Zr and QI rules out the presences of respectively Zi or ZR and Qi or QR. (Qi and QI can not be simultaneously present for the same reason Zr and ZR can not be simultaneously present.) However, ZI and Qr are compatible with Zr and QI. Since we are at this point interested in a pair of clusters with the same orientation, the only admissible possibilities would be Zr·Qr and ZI·QI. We further note that following inversion, ZI·QI becomes ZR·QR.

We therefore expect that as Zr·QI is quite common, the two most common orientations among Zr·Qr, Zr·QR, ZR·Qr, and ZR·QR would be Zr·Qr and ZR·QR. The experimental data of Figure 2.18b confirm this hypothesis. The majority of experimental data is for these two cluster pairs, with a few Zr·QR

cluster pairs also present.

The experimental data is therefore compatible with the theoretical calculations. We end this section, however, with one caveat. The theoretical calculations do not unambiguously anticipate the experimental results. There is one additional possibility compatible with theory which is not most commonly observed. It could have been that Zr·QR (rather than Zr·QI) was most commonly observed. ZI and Qi are compatible with Zr·QR. As a consequence, ZI·QR and Zr·Qi would also have been seen. This second possibility is what allows for the experimental pairs which lie off the global maxima of Figures 2.18a,b.

2.7 Conclusion

In this paper, we have shown that the pseudo-fivefold symmetries of a number of complex solid-state compounds can be understood by considering the higher-dimensional Platonic solid, the 600-cell. In the preface to his classic work on higher-dimensional Platonic solids, *Regular Polytopes*, H.S.M. Coxeter talks of the dazzling beauty of 4-D solids. He quotes Lobatschewsky, who wrote, "there is no branch of mathematics, however abstract, which may not some day be applied to phenomena of the real world".[76] Solid-state chemists are blessed that it is in our field where such dazzling and beautiful mathematical constructs as the 600-cell can take hold.

In some ways it is not an accident. One of the central concerns of solid-state chemists is the filling of space with polyhedra. Furthermore, most binary compounds are metals, and their structures are often built up of tetrahedra. The complexity of many crystal structures is a consequence of these statements. For,

as we know, it is not possible to fill space solely with regular tetrahedra.

We may think of the intrusion of the 4-D 600-cell into solid-state chemistry as a consequence of the above. Just as the exterior of a 3-D polyhedron is a curved 2-D surface, the exterior of a 4-D polyhedroid is a curved 3-D volume.[o] But what a volume! Every vertex is in the center of an icosahedron, every icosahedron is composed of twenty perfectly regular tetrahedra, and all faces of all tetrahedra lie on the face of an adjacent tetrahedron. Were such an object to exist in ordinary 3-D space, we would reasonably expect that there would be numerous phases which would adopt its structure. Even in curved space, we can imagine (and we hope in this paper have shown) such a geometrical object is of use.

But at the same time, we view the 600-cell as just a point of departure. We suspect its point group and representations of its point group will also play a significant role in the understanding of complex intermetallic structures. The point group of the 600-cell has 14,400 elements;[76] its irreducible representations are of a complexity far beyond those encountered in 3-D point groups. The utility of the point group and its representations in simplifying and classifying solutions to the Schrödinger equation is well known.

The 600-cell is just one of many geometrical objects which belongs to this point group. In a previous paper, we have spoken of an edge-capped stella quadrangula whose edges are decorated with new atoms.[2] In an analogous manner, we can envision decorated 600-cells. But the 600-cell point group may have more far-reaching consequences. Just as regular quasicrystals have I_h point group symmetry,[36] we may envision new quasicrystals which belong to the 600-

[o]Both the 2-D exterior surface of the 3-D polyhedra and the 3-D exterior volume of a 4-D polyhedroid are curved, as the individual exterior elements (respectively 2-D polygons and 3-D polyhedra) are canted with respect to each other so that they can wrap around the respectively 3-D and 4-D spaces.

cell point group.[82] Such further constructs seem worthy of investigation.

2.8 Appendix

2.8.1 Linear Projection of the 16-Cell

The eight vertices of the 16-cell can be described in Cartesian coordinates by $(\pm 1, 0, 0, 0)$, $(0, \pm 1, 0, 0)$, $(0, 0, \pm 1, 0)$, and $(0, 0, 0, \pm 1)$. In 4-D, each vertex is distance 1 from the origin, and has six nearest neighbors at a distance of $\sqrt{2}$. In order to find the matrix that creates a linear 3-D projection of the 16-cell, we must define the direction of projection. As discussed earlier in this article, we choose the direction of projection to be orthogonal to the central tetrahedron (thus preserving the symmetry of this tetrahedron). We arbitrarily choose the central tetrahedron to have vertices at $(1, 0, 0, 0)$, $(0, 1, 0, 0)$, $(0, 0, 1, 0)$, and $(0, 0, 0, 1)$. We would like these four points to be projected onto the vertices of a 3-D tetrahedron, whose vertices we (again somewhat arbitrarily) place at $(-1, -1, -1)$, $(-1, 1, 1)$, $(1, -1, 1)$, and $(1, 1, -1)$. The desired projection matrix M_{16} can now be found by solving the system of linear equations represented by,

$$M_{16} \begin{pmatrix} 1 & 0 & 0 & 0 \\ 0 & 1 & 0 & 0 \\ 0 & 0 & 1 & 0 \\ 0 & 0 & 0 & 1 \end{pmatrix} = \begin{pmatrix} -1 & -1 & 1 & 1 \\ -1 & 1 & -1 & 1 \\ -1 & 1 & 1 & -1 \end{pmatrix}.$$

The solution to this system of equations is,

$$M_{16} = \begin{pmatrix} -1 & -1 & 1 & 1 \\ -1 & 1 & -1 & 1 \\ -1 & 1 & 1 & -1 \end{pmatrix} \begin{pmatrix} 1 & 0 & 0 & 0 \\ 0 & 1 & 0 & 0 \\ 0 & 0 & 1 & 0 \\ 0 & 0 & 0 & 1 \end{pmatrix}^{-1} = \begin{pmatrix} -1 & -1 & 1 & 1 \\ -1 & 1 & -1 & 1 \\ -1 & 1 & 1 & -1 \end{pmatrix}.$$

When the matrix M_{16} is applied to the 4-D coordinates of the eight vertices of the 16-cell, the result is a 3-D projection with T_d symmetry,

$$M_{16} \begin{pmatrix} 1 & 0 & 0 & 0 & -1 & 0 & 0 & 0 \\ 0 & 1 & 0 & 0 & 0 & -1 & 0 & 0 \\ 0 & 0 & 1 & 0 & 0 & 0 & -1 & 0 \\ 0 & 0 & 0 & 1 & 0 & 0 & 0 & -1 \end{pmatrix} = \begin{pmatrix} -1 & -1 & 1 & 1 & 1 & 1 & -1 & -1 \\ -1 & 1 & -1 & 1 & 1 & -1 & 1 & -1 \\ -1 & 1 & 1 & -1 & 1 & -1 & -1 & 1 \end{pmatrix}.$$

The attentive reader may notice that this 3-D projection of the 16-cell is actually a cube. Therefore, while our method did not require it, this projection has O_h symmetry, of which T_d is a subgroup. While one of course does not need four dimensions to generate a cube, this method can be applied to more complicated 4-D polyhedroids for which projection proves more useful.

2.8.2 Linear Projection of the 600-Cell

We now use this same method to generate a 3-D projection of the 600-cell with T_d symmetry. The 120 vertices of the 600-cell can be described in Cartesian coordinates by $(\pm\frac{1}{2}, \pm\frac{1}{2}, \pm\frac{1}{2}, \pm\frac{1}{2})$ (16 vertices), $(0, 0, 0, \pm 1)$ (8 vertices), and all even permutations of $\frac{1}{2}(\pm 1, \pm\tau, \pm\frac{1}{\tau}, 0)$ (96 vertices, τ is the golden mean). In 4-D, each vertex is distance 1 from the origin, and has twelve nearest neighbors at a distance

of $\frac{1}{\tau}$. We arbitrarily choose the central tetrahedron to consist of the four mutually nearest-neighboring vertices at $(1,0,0,0)$, $\frac{1}{2}(\tau,0,\frac{1}{\tau},1)$, $\frac{1}{2}(\tau,1,0,\frac{1}{\tau})$, and $\frac{1}{2}(\tau,\frac{1}{\tau},1,0)$. We would again like these four points to be projected onto $(-1,-1,-1)$, $(-1,1,1)$, $(1,-1,1)$, and $(1,1,-1)$ in 3-D space. The desired projection matrix M_{600} can now be found by solving the system of linear equations represented by,

$$M_{600}\begin{pmatrix} 1 & \frac{\tau}{2} & \frac{\tau}{2} & \frac{\tau}{2} \\ 0 & 0 & \frac{1}{2} & \frac{1}{2\tau} \\ 0 & \frac{1}{2\tau} & 0 & \frac{1}{2} \\ 0 & \frac{1}{2} & \frac{1}{2\tau} & 0 \end{pmatrix} = \begin{pmatrix} -1 & -1 & 1 & 1 \\ -1 & 1 & -1 & 1 \\ -1 & 1 & 1 & -1 \end{pmatrix}.$$

The solution to this system of equations is,

$$M_{600} = \begin{pmatrix} -1 & -1 & 1 & 1 \\ -1 & 1 & -1 & 1 \\ -1 & 1 & 1 & -1 \end{pmatrix}\begin{pmatrix} 1 & \frac{\tau}{2} & \frac{\tau}{2} & \frac{\tau}{2} \\ 0 & 0 & \frac{1}{2} & \frac{1}{2\tau} \\ 0 & \frac{1}{2\tau} & 0 & \frac{1}{2} \\ 0 & \frac{1}{2} & \frac{1}{2\tau} & 0 \end{pmatrix}^{-1} = \begin{pmatrix} -1 & 1+2\tau & 1 & -1 \\ -1 & -1 & 1+2\tau & 1 \\ -1 & 1 & -1 & 1+2\tau \end{pmatrix}.$$

Applying this matrix M_{600} to the 4-D coordinates of the 600-cell produces a 3-D projection of the polyhedroid with T_d symmetry. The full list of 4-D and 3-D coordinates of the 600-cell under this linear projection are given in the Supporting Information (available online). In the second column of Table 2.5 are the 3-D coordinates of the seven distinct sites in the 54-cluster discussed in this paper, as projected linearly from the 600-cell.

Table 2.5: The 3-D coordinates of various projections of the 600-cell.

Site	Linear (γ=∞)	Stereographic (γ=1)	Intermediate (γ=1.9)
IT	(–1.000, –1.000, –1.000)	(–1.000, –1.000, –1.000)	(–1.000, –1.000, –1.000)
OT	(1.618, 1.618, 1.618)	(1.740, 1.740, 1.740)	(1.679, 1.679, 1.679)
OH	(0.00, 0.00, 3.236)	(0.00, 0.00, 3.650)	(0.00, 0.00, 3.439)
CO	(–0.618, –2.618, –2.618)	(–0.757, –3.207, –3.207)	(–0.683, –2.894, –2.894)
IC	(1.618, 1.618, 3.618)	(2.302, 2.302, 5.147)	(1.914, 1.914, 4.279)
MC	(–4.236, –1.000, –1.000)	(–6.694, –1.580, –1.580)	(–5.236, –1.236, –1.236)
OC	(–2.618, –2.618, –2.618)	(–4.442, –4.442, –4.442)	(–3.329, –3.329, –3.329)

2.8.3 Stereographic and Intermediate Projections of the 600-Cell

Having already found the T_d linear projection of the 600-cell, we must stretch or shrink regions of that projection in order to generate the stereographic and intermediate projections. As with the linear projection, we would like the vertices $(1,0,0,0)$, $\frac{1}{2}(\tau,0,\frac{1}{\tau},1)$, $\frac{1}{2}(\tau,1,0,\frac{1}{\tau})$, and $\frac{1}{2}(\tau,\frac{1}{\tau},1,0)$ to form a tetrahedron at the center of these projections. This means positioning the "light" opposite the center of this tetrahedron, in the direction $\frac{-(\tau+1,\tau-1,\tau-1,\tau-1)}{2\sqrt{2}}$. We define γ as the distance from the point on the 600-cell at the center of the projection to the "light", in 600-cell diameters. Thus, a stereographic projection corresponds to γ=1, the intermediate projection we use in this paper corresponds to γ=1.9, and a linear projection corresponds to γ=∞. We can now calculate the projected 3-D coordinates (b_1,b_2,b_3) of any 4-D vertex (a_1,a_2,a_3,a_4) for any value of γ,

$$\begin{pmatrix} b_1 \\ b_2 \\ b_3 \end{pmatrix} = \frac{M_{600} \begin{pmatrix} a_1 \\ a_2 \\ a_3 \\ a_4 \end{pmatrix}}{2\gamma - 1 + \frac{\begin{pmatrix} \tau+1 & \tau-1 & \tau-1 & \tau-1 \end{pmatrix}}{2\sqrt{2}} \begin{pmatrix} a_1 \\ a_2 \\ a_3 \\ a_4 \end{pmatrix}}.$$

As a final step, not shown in the above expression, we multiply all the 3-D coordinates by a constant such that the IT coordinates are $(-1,-1,-1)$, $(-1,1,1)$, $(1,-1,1)$, and $(1,1,-1)$, so they can be more easily compared. In the third and fourth columns of Table 2.5 are the seven distinct sites in the 54-cluster, as projected from the 600-cell with $\gamma = 1$ (stereographic) and $\gamma = 1.9$ (intermediate). As expected, the outer layers of the cluster are more stretched out as the projection moves closer to stereographic.

2.9 Acknowledgment

This research was supported by the National Science Foundation through grant DMR-0504703. We thank Dr. Ji Feng for suggesting stereographic projection. We thank Aaron Bloomfield, Julie Fichot, and Adrian So for their separate work in our laboratory on the $Li_{21}Si_5$ structure. We thank Roald Hoffmann for his support through every stage of this work, from discussions over the ideas behind this paper to the final preparation of the manuscript.

CHAPTER 3

SLICING UP HYPERSPACE: WHY SOME CRYSTALS ARE SIMPLER IN EIGHT DIMENSIONS (REALLY)

Take *that*, you lousy dimension!

—Chief Wiggum, *The Simpsons*[83]

Like the first one,[2] our second paper[56] provokes new questions as it resolves the old ones. While it explains the origins of tetrahedral packing and pseudo-tenfold diffraction symmetry in complex intermetallic structures, the paper does not truly define a method for generating projected crystal structures. There is a reason for this. The starting point for the projection method we desire—a crystal lattice (as opposed to a finite object) that has 600-cell point group symmetry—does not exist in 4-D space. Thus, the process described in the second paper, which generates crystal structures by placing finite objects on different length scales throughout the unit cell, is akin to the process of cutting and pasting. For this reason, we move into 8-D space in our third paper, "Laves Phases, γ-Brass, and $2 \times 2 \times 2$ Superstructures: A New Class of Quasicrystal Approximants and the Suggestion of a New Quasicrystal" (Robert F. Berger, Stephen Lee, Jeffreys Johnson, Ben Nebgen, and Adrian Chi-Yau So).[84] The paper, presented with permission in this chapter, was featured on the cover of *Chemistry: A European Journal* (Figure 3.1).

This work once again focuses on a variety of cubic intermetallic structure types. These include some of the most common such structure types ($MgCu_2$, Cu_5Zn_8, Ti_2Ni, and α-Mn), as well as their superstructures (Be_5Au, $Li_{21}Si_5$, $Sm_{11}Cd_{45}$, and $Mg_{44}Ir_7$) which possess the perpendicular pseudo-fivefold axes

Figure 3.1: The cover of *Chemistry: A European Journal*, Volume 14, Issue 22 (July 28, 2008).

described earlier. The paper shows that an 8-D to 3-D projection method cleanly describes most (and in one case, all) of the atomic positions in these superstructures. This type of projection, which maps the E_8 lattice (a mathematically simple 8-D crystal) into 3-D space, combines the desired higher-dimensional point group's perpendicular fivefold rotations with 3-D translational symmetry—exactly what we see in the experimental crystal structures. The projection method successfully accounts for all heavy atom positions in the four superstructures, and at least 60-70% of the light atom positions. The results suggest that all of these structures, previously known to be connected only by qualitative similarities in their atomic "clusters", are approximants of a single, as-yet unknown, class of quasicrystal.

3.1 Introduction

To most physical scientists, the world of intermetallic phases is dominated by simple variants of a few familiar structures: face-centered cubic (fcc), hexagonal closest-packed (hcp), and body-centered cubic (bcc). Indeed, these structures can take our understanding a long way, as they account for most metallic elemental structures, as well as many atomically ordered intermetallic compounds and atomically disordered alloys. However, there are also extensive classes of much more complex intermetallic compounds. A deeper understanding of these more complicated phases is necessary if physical scientists are to become fully conversant with metallic structures, and, as metals make up more than $\frac{2}{3}$ of the periodic table, if we are to appreciate the intricacies of some half of all thermodynamically stable binary compounds.

In this paper, we concentrate on one important branch of these more complicated structures: cubic crystal compounds of purely metallic elements. *Pearson's Handbook of Crystallographic Data for Intermetallic Phases*[6] shows us that (limiting ourselves to structure types whose compounds often consist entirely of elements in the first twelve columns of the periodic table) the most common complex cubic structure types are quite varied. The $MgCu_2$[85] structure type is found in 807 compounds. In descending order of frequency are then the Cr_3Si[86] (260 compounds), Th_6Mn_{23}[87] (204 compounds), $NaZn_{13}$[88] (91 compounds), Be_5Au[89] (75 compounds), α-Mn[72] (73 compounds), Ti_2Ni[32] (62 compounds), β-Mn[90] (41 compounds), Cu_5Zn_8[10] (39 compounds), $Sm_{11}Cd_{45}$[15] (19 compounds), and YCd_6[91] (19 compounds) structures.

This paper focuses on six of the above eleven structure types: the $MgCu_2$ (the

cubic Laves phase), Be_5Au, α-Mn (the χ-phase), Ti_2Ni, Cu_5Zn_8 (γ-brass), and $Sm_{11}Cd_{45}$ structures.[a] We consider these six because either the structures themselves or more complex variants of them exhibit a common pseudo-fivefold symmetry. The common pseudo-fivefold axes lie along the $\langle 110 \rangle$ directions of the cubic unit cell, as opposed to the $\langle 1\tau 0 \rangle$ directions of other known cubic quasicrystal approximants ($\tau = \frac{1+\sqrt{5}}{2}$).[65] Interestingly, while there are 3-D point groups with fivefold axes along the $\langle 1\tau 0 \rangle$ directions (e.g., the I_h point group), there are no 3-D point groups with fivefold axes along the $\langle 110 \rangle$ directions.

Earlier work by Sadoc and Mosseri[69,70] has shown that the $MgCu_2$, γ-brass, and α-Mn structures can be understood in terms of a 4-D Platonic solid, the 600-cell. This finding helps rationalize the observed pseudo-fivefold symmetry in these structures. The 600-cell, along with its dual, the 120-cell, are the 4-D Platonic solids with the greatest number of symmetry elements (14,400 in total).[76] Among these symmetries are numerous fivefold rotations. One type of projection, the 4-D to 3-D cell-projection (we explain cell-projection later in this paper), places six of these fivefold operations closest to the center of the projection. By virtue of being closest to the center, these six fivefold operations best preserve their fivefold pseudosymmetry when projected into 3-D.[b] The six projected pseudo-fivefold axes lie exactly along the $\langle 110 \rangle$ directions of a cube. Thus, the symmetry of the 600-cell can be used to account for the pseudo-fivefold symmetry in the above structure types.[56]

One limitation of the above approach is that the 600-cell, for all its complexity, is still a finite polyhedroid,[c] while the structures of interest in this paper are

[a] Several of the remaining structure types (e.g., Cr_3Si and YCd_6) are known to be quasicrystal approximants of 3-D point group quasicrystals.[92,93]

[b] In 4-D, fivefold rotations occur around invariant planes. When projected into 3-D, they become pseudo-fivefold rotations, and occur around invariant axes.

[c] A polyhedroid[73,74] is the 4-D analog of a 3-D polyhedron. Just as a polygon is composed of

extended crystals and are hence infinite in size. One way around this difficulty has been the introduction of disclination lines.[77,78] In this paper, we adopt an alternate approach. Rather than consider the 600-cell itself, we consider a 4-D structure which has the same 4-D point group as the 600-cell but which, like the crystal structures of interest, is infinite in size. This 4-D object is the 4-D quasicrystal first proposed by Elser and Sloane[82] and later studied by Moody, Patera, Sadoc, and Mosseri.[94,95]

The Elser-Sloane 4-D quasicrystal, since its introduction in 1987, has lost favor to the now well-known 6-D crystal to 3-D quasicrystal model.[96–99] In the more widely used 6-D to 3-D model, as well as in all other quasicrystals and quasicrystal approximants of which we know, quasicrystals are rationalized by combining a 3-D point group with higher-dimensional translations. In this paper, by contrast, we find that rational approximants of the Elser-Sloane 4-D quasicrystal, with its fundamentally higher-dimensional point group, coupled with a 4-D to 3-D cell-projection can account for all the atomic positions of Be_5Au and all the *heavier* atom sites of $Li_{21}Si_5$,[17,18] $Sm_{11}Cd_{45}$,[15] and $Mg_{44}Ir_7$.[7,71] For the latter three structures, quasicrystal approximants of the Elser-Sloane quasicrystal account for respectively $\frac{10}{12}$, $\frac{9}{13}$, and $\frac{9}{11}$ of the lighter atom sites.

These results are of particular interest as Be_5Au and $Li_{21}Si_5$ are themselves exact superstructures of two of the title compounds of this article: $MgCu_2$ (the cubic Laves phase) and Cu_5Zn_8 (γ-brass), respectively. Furthermore, $Sm_{11}Cd_{45}$ is a superstructure built up from the α-Mn structure coupled with bcc. It has been recently shown that $Mg_{44}Ir_7$ is nicely rationalized as being composed of twinned Ti_2Ni-type domains.[2] Both $Sm_{11}Cd_{45}$ and $Mg_{44}Ir_7$ belong to a family of

vertices and edges and a polyhedron consists of vertices, edges, and faces, a 4-D polyhedroid has vertices, edges, faces, and polyhedra. These polyhedra are referred to as cells. The name 600-cell means that this polyhedroid contains 600 polyhedra.

superstructures (here termed $2\times2\times2$ superstructures for their usual description as arrays of "clusters" in large unit cells) first studied by Westman, Westin, and Samson.[7,8,12–26,28,71]

While it is superstructures (Be_5Au, $Li_{21}Si_5$, $Sm_{11}Cd_{45}$, and $Mg_{44}Ir_7$) which have the most enhanced pseudo-fivefold symmetry along the $\langle 110 \rangle$ directions, and which therefore connect best to the Elser-Sloane model, it seems fair to assume that their substructures ($MgCu_2$, Cu_5Zn_8, Ti_2Ni, and α-Mn) are also implicated in the Elser-Sloane model. With this ansatz, the results of this paper suggest that four of the most common complex cubic metallic structures ($MgCu_2$, Be_5Au, Cu_5Zn_8, and $Sm_{11}Cd_{45}$) are all related to rational cell-projections of the 4-D quasicrystal model. The results further tentatively suggest that an additional two common structure types (Ti_2Ni and α-Mn) are also so connected. We begin with the Laves phase $MgCu_2$ and its superstructure Be_5Au.

3.2 The Cubic Laves Structure: $MgCu_2$ and Be_5Au

The three most common binary intermetallic stoichiometries are $1:1$, $1:2$, and $1:3$. While the $1:1$ and $1:3$ stoichiometries are dominated by ordered variants of fcc, hcp, and bcc, the $1:2$ stoichiometry's most common structures are Laves phases.[6] In this paper, we consider the cubic Laves structure $MgCu_2$. In $MgCu_2$, the Mg atoms lie in a diamond network (Figure 3.2a), while the Cu atoms form a network of vertex-sharing tetrahedra (Figure 3.2b). The full $MgCu_2$ structure is illustrated in Figure 3.2c.

The most common $MgCu_2$ superstructure is the Be_5Au type. In this superstructure, the network of vertex-sharing tetrahedra remains all one atom type

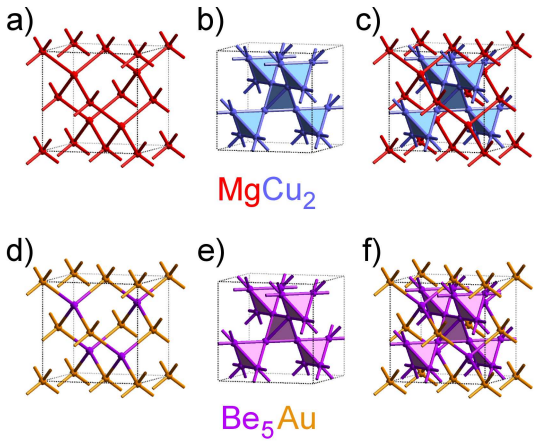

Figure 3.2: The cubic Laves structure $MgCu_2$ and its superstructure Be_5Au. a) A diamond network of Mg (red) atoms and b) a vertex-sharing tetrahedral network of Cu (blue) atoms combine to make c) the $MgCu_2$ structure. d) A diamond network of alternating Be (purple) and Au (orange) atoms and e) a vertex-sharing tetrahedral network of Be atoms combine to make f) Be_5Au.

(Be), but the original diamond network is replaced by an alternating network of the two atom types (Au and Be). The alternating network (Figure 3.2d) may be recognized as a sphalerite-like ordering of a diamond network. The vertex-sharing tetrahedra and the full Be_5Au structure are illustrated in Figure 3.2e,f.

While the $MgCu_2$ and Be_5Au structures differ only in the type of atom lying at individual sites, and may be thought of as having very similar structures, their diffraction patterns are noticeably different. Be_5Au has marked pseudo-tenfold diffraction symmetry (pseudo-fivefold structural symmetry coupled with Friedel's Law[57]) along the ⟨110⟩ directions; $MgCu_2$ does not. In Figure 3.3, we illustrate the calculated diffraction patterns[35] of both of these structures along [110]. The $MgCu_2$ diffraction pattern (Figure 3.3a) is a standard pattern with an immediately discernible rhomboid reciprocal lattice. By contrast, the

dominant diffraction peaks of the Be_5Au structure (Figure 3.3b) lie in two concentric rings, each composed of ten peaks. Given the constraint of the large reciprocal lattice (due to the relatively small direct lattice vectors), it is noteworthy how well these two tenfold rings parse themselves to give an overall pseudo-tenfold diffraction symmetry.

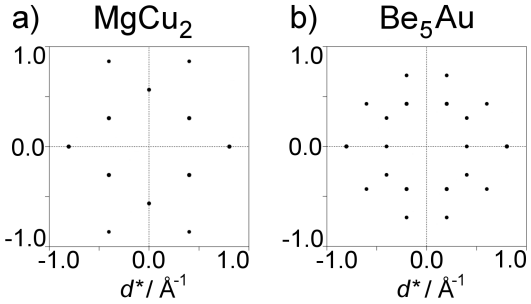

Figure 3.3: The strongest peaks in the [110] X-ray diffraction patterns of the a) $MgCu_2$ and b) Be_5Au structures. The site preferences in the Be_5Au structure give it a pseudo-tenfold diffraction symmetry that is absent in $MgCu_2$. The latter pattern was calculated using the isostructural compound UCu_5, a compound for which the pseudosymmetry is particularly vivid.

To understand the Be_5Au structure, we must rationalize its pseudo-tenfold diffraction symmetry. In our hands, such a rationalization is based on a higher-dimensional lattice, the E_8 lattice, which lies at the foundation of the Elser-Sloane quasicrystal model. Remarkably, this higher-dimensional crystal lattice lies in 8-D space; our interest will be in 3-D projections of it.

3.2.1 The E_8 Lattice and its Three-Dimensional Cell-Centered Projection

When it comes to using the 4-D 600-cell to generate 3-D projected crystal structures, there is a major complication: the 600-cell 4-D point group is not found in any 4-D space groups. In this, it is entirely akin to the 3-D I_h point group, which is not found in any 3-D space groups. Just as in the I_h case, where one needs to extend to a higher dimension (6-D is generally chosen[96–99]) to find a space group which contains I_h symmetry, we will extend into 8-D in the case of the 600-cell point group.[82,94,95,100] In the former case, projection from a 6-D crystalline lattice results in 3-D I_h quasicrystals. In the latter case, Elser and Sloane have found that projection from an 8-D crystalline lattice results in a 4-D quasicrystal with 600-cell point group symmetry.[82]

The 8-D lattice in question is the closest-packed E_8 lattice, with points of the types $(n_1, n_2, n_3, n_4, n_5, n_6, n_7, n_8)$ and $(n_1 + \frac{1}{2}, n_2 + \frac{1}{2}, n_3 + \frac{1}{2}, n_4 + \frac{1}{2}, n_5 + \frac{1}{2}, n_6 + \frac{1}{2}, n_7 + \frac{1}{2}, n_8 + \frac{1}{2},)$. In both cases, the n_i are all integers *and* their sum is even (i.e., $\sum_{i=1}^{8} n_i = 2N$).[101] As the crystal structures discussed in this paper are of T_d point group symmetry, our interest will be in 3-D projections of the E_8 lattice which preserve an overall 3-D T_d symmetry. We adapt a procedure from our previous paper.

In this earlier work, we required a projection of the 4-D 600-cell which placed a single tetrahedral cell at the center of the projection. In so doing, it preserved an overall T_d symmetry in the 3-D projected atomic cluster. This specification—that the four 4-D sites of a given 4-D tetrahedral cell project to the four sites of a 3-D tetrahedron—exactly determines all twelve matrix elements of the 3×4

projection matrix; it exactly determines what we term a cell-projection. Applying this same 3×4 matrix to the remaining sites of the 600-cell generates the full 3-D cell-projected 600-cell.[56]

Important to the current paper is that, just outside the central tetrahedron of the 3-D cell-projected 600-cell, there is a second tetrahedron roughly 1.6 times larger in size. This larger tetrahedron is termed the outer tetrahedron (OT), and the smaller one the inner tetrahedron (IT). The eight vertices that comprise IT and OT are collectively known as a stella quadrangula (Figure 3.4a).[33,34] One feature of the stella quadrangula that will be key to our later discussion is that each OT site, together with the triangular IT face nearest to it, forms a capping tetrahedron (Figure 3.4b). These capping tetrahedra are perfectly regular in shape if OT is exactly the golden mean times larger than IT ($\tau = \frac{1+\sqrt{5}}{2}$).

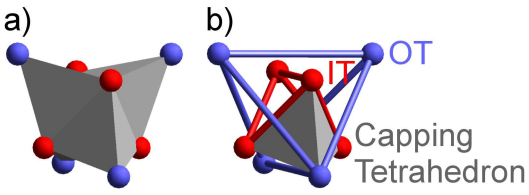

Figure 3.4: The eight-vertex formation known as a stella quadrangula. The vertices are shown as a) a single polyhedron, and b) an inner tetrahedron (IT, red) and an outer tetrahedron (OT, blue). Highlighted in gray in the latter view is a tetrahedron composed of three IT atoms and one OT atom, which caps the inner tetrahedron.

The stella quadrangula is vital to the desired 8-D to 3-D projection, for which a 3×8 matrix rather than the previous 3×4 matrix is required. For 8-D, we need to specify how eight, not four, sites project into 3-D. The natural choice for these eight sites are those comprising the stella quadrangula—the four IT sites and the four OT sites. In order to choose which 8-D points project

onto this 3-D stella quadrangula, we consider a stella quadrangula from the Elser-Sloane quasicrystal and determine the eight 8-D points which project onto it. We find the points $(1,0,0,0,1,0,0,0)$, $(1,0,0,0,0,1,0,0)$, $(1,0,0,0,0,0,1,0)$, and $(1,0,0,0,0,0,0,1)$ project onto the IT of the stella quadrangula, while the points $(\frac{1}{2},\frac{1}{2},\frac{1}{2},\frac{1}{2},\frac{1}{2},\frac{1}{2},\frac{1}{2},\frac{1}{2})$, $(\frac{1}{2},-\frac{1}{2},-\frac{1}{2},\frac{1}{2},\frac{1}{2},\frac{1}{2},\frac{1}{2},\frac{1}{2})$, $(\frac{1}{2},-\frac{1}{2},\frac{1}{2},-\frac{1}{2},\frac{1}{2},\frac{1}{2},\frac{1}{2},\frac{1}{2})$, and $(\frac{1}{2},\frac{1}{2},-\frac{1}{2},-\frac{1}{2},\frac{1}{2},\frac{1}{2},\frac{1}{2},\frac{1}{2})$ project onto the OT.

We therefore require that,

$$\begin{aligned}
(1,0,0,0,1,0,0,0) &\rightarrow (1,1,1)\\
(1,0,0,0,0,1,0,0) &\rightarrow (1,-1,-1)\\
(1,0,0,0,0,0,1,0) &\rightarrow (-1,1,-1)\\
(1,0,0,0,0,0,0,1) &\rightarrow (-1,-1,1)\\
(\tfrac{1}{2},\tfrac{1}{2},\tfrac{1}{2},\tfrac{1}{2},\tfrac{1}{2},\tfrac{1}{2},\tfrac{1}{2},\tfrac{1}{2}) &\rightarrow (-t,-t,-t)\\
(\tfrac{1}{2},-\tfrac{1}{2},-\tfrac{1}{2},\tfrac{1}{2},\tfrac{1}{2},\tfrac{1}{2},\tfrac{1}{2},\tfrac{1}{2}) &\rightarrow (t,-t,t)\\
(\tfrac{1}{2},-\tfrac{1}{2},\tfrac{1}{2},-\tfrac{1}{2},\tfrac{1}{2},\tfrac{1}{2},\tfrac{1}{2},\tfrac{1}{2}) &\rightarrow (-t,t,t)\\
(\tfrac{1}{2},\tfrac{1}{2},-\tfrac{1}{2},-\tfrac{1}{2},\tfrac{1}{2},\tfrac{1}{2},\tfrac{1}{2},\tfrac{1}{2}) &\rightarrow (t,t,-t).
\end{aligned}$$

Taking the above 8-D and 3-D points to be column vectors, the 3×8 matrix that performs these transformations is,

$$\begin{pmatrix}
0 & 0 & -2t & 0 & 1 & 1 & -1 & -1\\
0 & 0 & 0 & -2t & 1 & -1 & 1 & -1\\
0 & -2t & 0 & 0 & 1 & -1 & -1 & 1
\end{pmatrix}.$$

3.2.2 The $\frac{1}{1}$ Quasicrystal Approximant

Projection Matrix

Given a value of t, the above 3×8 matrix exactly defines the 8-D to 3-D projection. As we have noted above, if $t = \tau$, the resultant 3-D stella quadrangula will have perfectly regular capping tetrahedra. But, as we will find later, for this value and indeed for any irrational value of t, the resultant 3-D structure will be a quasicrystal. Rather than show this directly, we consider first several rational values of t.

We consider a sequence of rational numbers which converges to τ. The sequence chosen is composed of the ratios of consecutive members of the Fibonacci sequence $(1, 1, 2, 3, 5, 8, 13, \ldots)$. As can be seen by inspection, this sequence $(\frac{1}{1}, \frac{2}{1}, \frac{3}{2}, \frac{5}{3}, \frac{8}{5}, \frac{13}{8}, \ldots)$ converges rapidly to the desired value. We consider first $t = \frac{1}{1} = 1$. For this value, the 3×8 projection matrix reduces to,

$$\begin{pmatrix} 0 & 0 & -2 & 0 & 1 & 1 & -1 & -1 \\ 0 & 0 & 0 & -2 & 1 & -1 & 1 & -1 \\ 0 & -2 & 0 & 0 & 1 & -1 & -1 & 1 \end{pmatrix}.$$

We consider now the three column vectors,

$$\mathbf{a} = \begin{pmatrix} 0 \\ 0 \\ -2 \\ 0 \\ 1 \\ 1 \\ -1 \\ -1 \end{pmatrix} \qquad \mathbf{b} = \begin{pmatrix} 0 \\ 0 \\ 0 \\ -2 \\ 1 \\ -1 \\ 1 \\ -1 \end{pmatrix} \qquad \mathbf{c} = \begin{pmatrix} 0 \\ -2 \\ 0 \\ 0 \\ 1 \\ -1 \\ -1 \\ 1 \end{pmatrix}.$$

These three vectors are the transposed rows of the projection matrix. As can be directly verified, these three column vectors project onto respectively,

$$\vec{a} = \begin{pmatrix} 8 \\ 0 \\ 0 \end{pmatrix} \qquad \vec{b} = \begin{pmatrix} 0 \\ 8 \\ 0 \end{pmatrix} \qquad \vec{c} = \begin{pmatrix} 0 \\ 0 \\ 8 \end{pmatrix},$$

three orthogonal 3-D vectors. As their names suggest, these three orthogonal vectors can be seen as three ordinary 3-D unit cell axes.[d]

To cement this view, consider a given E_8 lattice point. Add to this 8-D vector a linear combination of integer multiples of the 8-D **a**, **b**, and **c** vectors. This addition will generate a new 8-D vector corresponding to a new E_8 lattice point. Under the 8-D to 3-D projection, this new E_8 lattice point will project onto a 3-D position related to the original projected 3-D position by the same combination of $\vec{a}$, $\vec{b}$, and $\vec{c}$ as the initially chosen combination of **a**, **b**, and **c**. Therefore, $\vec{a}$, $\vec{b}$, and $\vec{c}$ can be taken to be standard 3-D unit cell vectors.

[d] In this paper, we adopt the nomenclature that bold-font **a** is an 8-D vector, $\vec{a}$ is a 3-D vector, and a is a scalar, the length of $\vec{a}$.

Projected Distance

The 3×8 matrix with $t = \frac{1}{1} = 1$ projects E_8 onto a 3-D crystalline structure. However, this 3-D structure by itself is not of great interest; it is merely bcc. More useful projections will be ones in which only a portion of the E_8 lattice is projected into 3-D. To construct these, we require two additional concepts.

First is the concept of *projected distance*:[36] the distance between the original and projected coordinates. To explain what we mean by this, let us first illustrate projected distance in a simpler projection. In Figure 3.5a, we project a 2-D square lattice onto a 1-D line. This amounts to collapsing each lattice point perpendicularly onto the line (from the black circles to the cyan circles in the figure). The lengths of the red line segments are the projected distances of the points.

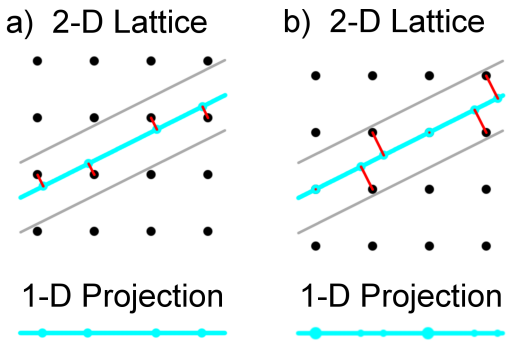

Figure 3.5: An illustration of projected distance and the effect of lattice translation, using the simpler projection of a 2-D square lattice onto to 1-D line. a) The points of a 2-D square lattice project onto a 1-D line (cyan) if they lie within a specified distance of that line (i.e., within the thinner gray lines). The lengths of the red line segments connecting the lattice points (black) to their projections (cyan) are what we define as projected distances. b) When the 2-D lattice is translated downward and the same rule is applied, the result is a qualitatively different projection that includes points with varying projected distances.

The concept of projected distance is the same for our 8-D to 3-D projection; it is the distance from an 8-D point to the 3-D "slice" onto which it is projected. This can be defined formally as the perpendicular distance from an 8-D point to the 3-D span of the rows of the projection matrix. We will assume, as is standard, that sites which project over a shorter distance count more heavily in the final structure than those which project over a longer distance. At the bottom of Figure 3.5, we represent points with shorter projected distances using larger circles. Points which lie beyond a specified projected distance, denoted by the gray lines, are not projected at all.

This standard concept enriches the possibilities of 3-D projected structures, in a way which we again illustrate using the simple 2-D to 1-D projection. In Figure 3.5b, the entire 2-D square lattice is translated downward with respect to the 1-D line of projection. This translation changes the projected distances of each point, moving some points closer to the line and others farther from it. The points that lie exactly on the line count more heavily in the projection than do the points farther from the line (and are consequently shown as larger circles at the bottom of Figure 3.5b). Thus, the translation of the lattice fundamentally alters the 1-D projected structure by changing which points count most heavily in the projection.

This type of translation can be extended to the E_8 lattice in our projections. The E_8 lattice can be translated by an 8-D vector $\mathbf{x}$, which will determine which lattice points have the shortest projected distances, and thus count most heavily. All of the structure types on which we focus in this paper—$MgCu_2$, Be_5Au, Cu_5Zn_8, $Li_{21}Si_5$, Ti_2Ni, α-Mn, $Sm_{11}Cd_{45}$, and $Mg_{44}Ir_7$—have centers of T_d point group symmetry. Our interest is therefore in vectors $\mathbf{x}$ which leave the T_d sym-

metry of the stella quadrangula unchanged. We must explore all **x** which maintain the equal projected distances of the four IT sites as well as the four OT sites. Some thought shows that vectors of the type $(x_1, 0, 0, 0, x_2, x_2, x_2, x_2)$ preserve the above equalities. There are therefore two free independent variables within the framework of $t = \frac{1}{1} = 1$ projection: x_1 and x_2.

3.2.3 Generating the Be_5Au Structure

We now apply the $t = \frac{1}{1} = 1$ model to the Be_5Au structure. Be_5Au is a fully ordered structure, with four Au atoms and twenty Be atoms in its cubic unit cell. This brings us to the second concept required to fully specify a projection. If we wish to replicate the Be_5Au structure through projection, we must make a rule deciding which E_8 lattice points project as Au and which as Be. Our rule is as follows: for a given projection (corresponding to a pair of values x_1 and x_2), we take the four lattice points with the shortest projected distances to be Au atoms (the heavier element), and the next twenty points to be Be atoms (the lighter element). All sites with projected distances longer than these twenty-four will remain unoccupied. In this way, we ensure that our projections have the desired population and stoichiometry.

Given this rule, we can now generate a 3-D crystal structure corresponding to any pair of values x_1 and x_2. Naturally, some of these structures will be more similar to the experimental Be_5Au structure than others. In Figure 3.6, we quantitatively assess how well each projection matches the Be_5Au structure. For given pairs of x_1 and x_2 parameters, we plot the total number of projected atoms that exactly correspond (including atom type) to the twenty-four exper-

imental atoms. That is, we plot the number of projected Au atoms that exactly correspond to the four experimental Au atoms *plus* the number of projected Be atoms that exactly correspond to the twenty experimental Be atoms.

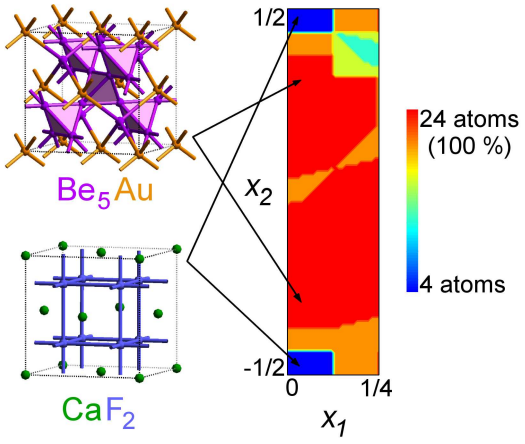

Figure 3.6: Correspondence between $\frac{1}{1}$ projected structures and the experimental Be_5Au structure as a function of x_1 and x_2, for a region containing all unique projected structures. The plot shows the number of atoms in the projected unit cell whose positions and elements exactly match those of experimental Be_5Au. There are substantial regions (shown in red) in which the match is perfect. In other regions, the projection perfectly matches the experimental CaF_2 structure.

The red regions in Figure 3.6 represent projections in which *all* four Au atoms and *all* twenty Be atoms exactly correspond to those in the experimental Be_5Au structure. As we can see, there are substantial regions in which the match between projected and experimental crystal structure is perfect. These results suggest that the Be_5Au structure can be profitably taken to be a rational projection of the E_8 lattice. And as Be_5Au is an exact superstructure of the cubic Laves phase $MgCu_2$ structure, the parent structure itself can also be so understood.

Before leaving our analysis of Figure 3.6, it is worth examining some of the values of x_1 and x_2 which lead to structures other than the Be_5Au structure.

As the blue regions of the figure suggest, a very different structure emerges near the values of $x_1 = 0$ and $x_2 = \frac{1}{2}$. This projected structure proves to be the CaF_2 structure type. As Figure 3.6 illustrates, it consists of an fcc lattice of the heavier element (the Ca site) which has all its tetrahedral holes filled by the lighter element (the F sites). An examination of known intermetallic CaF_2-type compounds confirms that the Ca and F sites are generally occupied by respectively the heavier and the lighter metallic elements.[6]

3.3 γ-Brass and the $Li_{21}Si_5$ Structure

The cubic unit cell of Cu_5Zn_8 (γ-brass), with fifty-two atoms, is roughly twice the size of those of the $MgCu_2$ and Be_5Au structures. It is composed of a body-centered arrangement of two identical 26-atom clusters, which are based on the stella quadrangula. As we show in Figure 3.7, the stella quadrangula has two types of edges—those which link IT atoms to each other, and those which link IT to OT atoms. Capping each of the IT-IT edges with an atom generates an octahedron, referred to as OH (Figure 3.7a). Similarly, capping the twelve IT-OT edges generates a distorted cubo-octahedron, referred to as CO (Figure 3.7b). The resulting edge-capped stella quadrangula (Figure 3.7c, left) has twenty-six vertices (4 IT +4 OT +6 OH +12 CO = 26), and is completely equivalent to the γ-brass cluster. On the right side of Figure 3.7c, we show a second view of the γ-brass cluster, which is more suggestive of the experimental site preferences in Cu_5Zn_8. The OT and OH sites, which are occupied by Cu atoms in Cu_5Zn_8, are connected as a black adamantane-like cage. The IT and CO sites, which are occupied by Zn, are connected as a light gray network of vertex-sharing tetrahedra. There are two of these 26-atom clusters in the 52-atom cubic unit

cell of Cu_5Zn_8, as shown in Figure 3.7d.

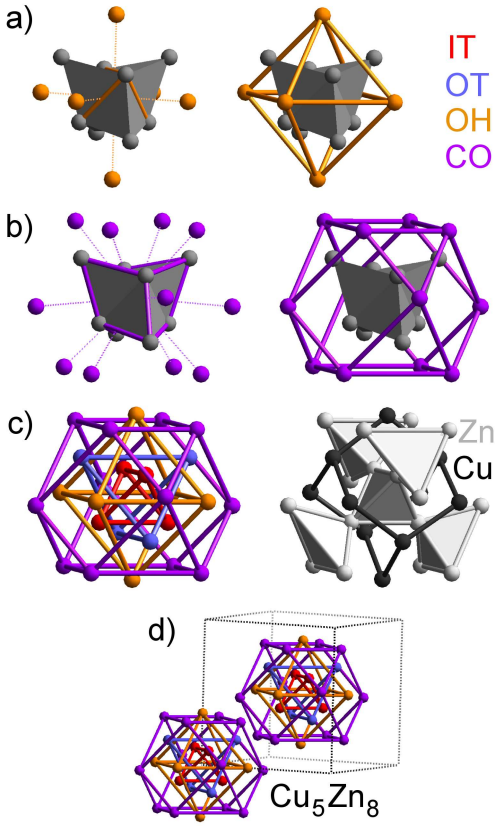

Figure 3.7: The construction of an edge-capped stella quadrangula, alternatively known as a γ-brass cluster. a) One type of edge of the stella quadrangula is capped with atoms (orange) that form an octahedron (OH), while b) the other type of edge is capped with atoms (purple) that form a distorted cubo-octahedron (CO). c) The full 26-atom edge-capped stella quadrangula can be seen as four nested polyhedra (left), or alternatively as an adamantane-like cage (right, black) and a network of vertex-sharing tetrahedra (right, light gray). d) The cubic unit cell of Cu_5Zn_8 contains two such identical clusters in a body-centered arrangement.

Our concern here will be with the γ-brass superstructure $Li_{21}Si_5$. This superstructure is significantly larger than the parent structure and has sixteen γ-brass clusters in its cubic unit cell. The unit cell has an a-axis length of 18.710 Å,

contains 416 atoms, and has a face-centered cubic Bravais lattice. The sixteen γ-brass clusters in this structure reduce to four crystallographically inequivalent clusters. It is convenient to consider the four clusters along the body diagonal of the cubic unit cell as representative examples of each crystallographically inequivalent cluster.

These four clusters are illustrated in Figure 3.8. For the sake of clarity, each is connected as an adamantane-like cage and a network of vertex-sharing tetrahedra (as illustrated on the right side of Figure 3.7c). Each cluster is given a specific name. The cluster centered at $(0, 0, 0)$ is labeled Z for zero. Similarly, clusters centered at $(\frac{1}{4}, \frac{1}{4}, \frac{1}{4})$, $(\frac{1}{2}, \frac{1}{2}, \frac{1}{2})$, $(\frac{3}{4}, \frac{3}{4}, \frac{3}{4})$ are respectively called Q, H, and T (for quarter, half, and three-quarters).

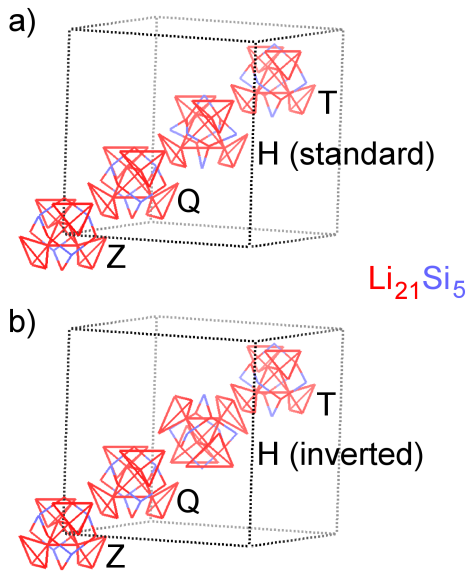

Figure 3.8: The four crystallographically inequivalent γ-brass clusters in the cubic unit cell of $Li_{21}Si_5$. The four Si (blue) sites are ZOT, QOT, HOH, and TOH, while the remaining twelve sites are Li (red). The H cluster is shown in a) the same orientation as the others, and in b) an inverted orientation. The latter picture is more indicative of experimental atomic positions.

$Li_{21}Si_5$ is a fully atomically ordered variant of the γ-brass structure. The OT sites of both the Z and Q clusters are occupied by Si atoms, as are the OH sites of the H and T clusters. We refer to the four Si sites as respectively ZOT, QOT, HOH, and TOH. The atomic ordering is illustrated in Figure 3.8. It is of interest that different sites are occupied by Si atoms: some are OT while others are OH.

Figure 3.8a shows a standard illustration of $Li_{21}Si_5$ with all four crystallographically inequivalent clusters oriented the same way. This standard view obfuscates one remarkable feature of the structure. While three of the four clusters in the $Li_{21}Si_5$ structure are typical γ-brass clusters, the inner tetrahedron of the H cluster is *larger* than the outer tetrahedron of the same cluster.

If we assume that inner tetrahedra should perforce be smaller than outer tetrahedra, we need to switch the atomic labels of these two sites. As shown in Figure 3.8b, it is possible to switch these labels and retain the overall edge-capped stella quadrangular geometry if we invert the entire H cluster. Thus, while one can describe $Li_{21}Si_5$ as a $2\times2\times2$ superstructure of γ-brass with all four γ-brass clusters oriented the same way, it is perhaps more atomically accurate to view this structure as a superstructure where three of the clusters have one orientation and the fourth cluster is inverted.

Just as in the case of Be_5Au and $MgCu_2$, the $Li_{21}Si_5$ superstructure has enhanced pseudo-tenfold diffraction symmetry along $\langle 110 \rangle$ compared to the Cu_5Zn_8 parent structure. The two diffraction patterns[35] are contrasted in Figure 3.9. As can be seen, the pseudo-tenfold diffraction of the $Li_{21}Si_5$ structure is quite marked. With its larger direct lattice cell and consequent smaller reciprocal lattice cell, the parsing of the ten concentric diffraction peaks is distinctly superior to what was found for Be_5Au.

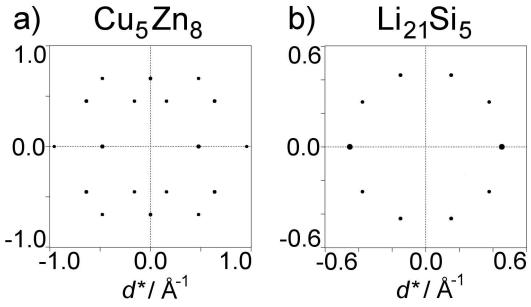

Figure 3.9: The strongest peaks in the [110] X-ray diffraction patterns of the a) Cu_5Zn_8 and b) $Li_{21}Si_5$ structures. The site preferences in $Li_{21}Si_5$ give it a pseudo-tenfold diffraction symmetry that is absent in Cu_5Zn_8.

3.3.1 The $\frac{2}{1}$ Quasicrystal Approximant

In an approach similar to that taken for the Be_5Au structure, we wish to show the connection between the $Li_{21}Si_5$ structure and the E_8 lattice. Its more complicated structure will require a few refinements to the overall procedure. In Be_5Au, all the atoms reside at positions of high symmetry, none of which contain any free atomic parameters. By contrast, in $Li_{21}Si_5$, there are four crystallographically inequivalent heavy atom sites and twelve inequivalent light atom sites with a combined twenty atomic parameters.

Our goal will be to project the E_8 lattice points near the experimentally observed atomic sites in $Li_{21}Si_5$. As we shall see, we will find a projection which locates all four inequivalent heavy atom sites and ten of the twelve inequivalent light atom sites. Moreover, this optimal structure will have three clusters with one orientation, and the H cluster correctly inverted.

For $Li_{21}Si_5$, we apply a 3×8 projection matrix where $t = \frac{2}{1} = 2$,

$$\begin{pmatrix} 0 & 0 & -4 & 0 & 1 & 1 & -1 & -1 \\ 0 & 0 & 0 & -4 & 1 & -1 & 1 & -1 \\ 0 & -4 & 0 & 0 & 1 & -1 & -1 & 1 \end{pmatrix}.$$

Similarly to the previous case, the three transposed rows of this matrix form the three 8-D vectors,

$$\mathbf{a} = \begin{pmatrix} 0 \\ 0 \\ -4 \\ 0 \\ 1 \\ 1 \\ -1 \\ -1 \end{pmatrix} \qquad \mathbf{b} = \begin{pmatrix} 0 \\ 0 \\ 0 \\ -4 \\ 1 \\ -1 \\ 1 \\ -1 \end{pmatrix} \qquad \mathbf{c} = \begin{pmatrix} 0 \\ -4 \\ 0 \\ 0 \\ 1 \\ -1 \\ -1 \\ 1 \end{pmatrix},$$

which project onto the three orthogonal 3-D cell axis vectors,

$$\vec{d} = \begin{pmatrix} 20 \\ 0 \\ 0 \end{pmatrix} \qquad \vec{b} = \begin{pmatrix} 0 \\ 20 \\ 0 \end{pmatrix} \qquad \vec{c} = \begin{pmatrix} 0 \\ 0 \\ 20 \end{pmatrix}.$$

Just as in the previous case, the E_8 lattice is subject to an 8-D translation by the vector **x**. In order to retain the T_d symmetry of the projection, **x** must again be of the form $(x_1, 0, 0, 0, x_2, x_2, x_2, x_2)$, with the two free parameters x_1 and x_2. In Figure 3.10, we plot the agreement between the projected structure and the experimental $Li_{21}Si_5$ structure as a function of these two parameters. Noting the

18.710 Å a-axis length of the experimental structure, we assume that projected atoms which lie within 1 Å of the actual atomic position are reasonably near the atomic position. As we shall see, most of the projected sites will lie significantly closer than the assumed 1 Å cut-off (with an average of 0.55 Å over the sixteen distinct sites in experimental $Li_{21}Si_5$).

As Figure 3.10 shows, when $x_1 = 0.81$ and $x_2 = 0.07$, all 80 Si atoms and 240 of the 336 Li atoms can be located. This corresponds to the correct determination of all four Si and ten of the twelve Li crystallographically inequivalent sites. In Table 3.1, all experimentally observed atomic sites are compared to their projected counterparts. Also given in this table are the projected distances of each of these sites for the optimal values of x_1 and x_2. A full account of this theoretical model is given in the Supporting Information (available online), which shows not only the sites that are found experimentally, but all sites in our theoretical projection.

Two features of the projected E_8 model are noteworthy. First, the projected model correctly finds that half the OT and half the OH sites are occupied by Si atoms. The ordering of the four clusters is the experimental one, with ZOT, QOT, HOH, and TOH being the four Si sites. Equally noteworthy is the success in generating the H cluster. All four crystallographically inequivalent H sites are contained in the optimal projected E_8 model (though one lies slightly beyond the 1 Å cut-off). These four sites belong to a cluster which is inverted with respect to the other three clusters. As we discussed above, this inversion is found experimentally.

While all the Si atoms are correctly determined, only 71% of the experimental Li atoms are correctly found. As Table 3.1 shows, one of the missing sites (HCO)

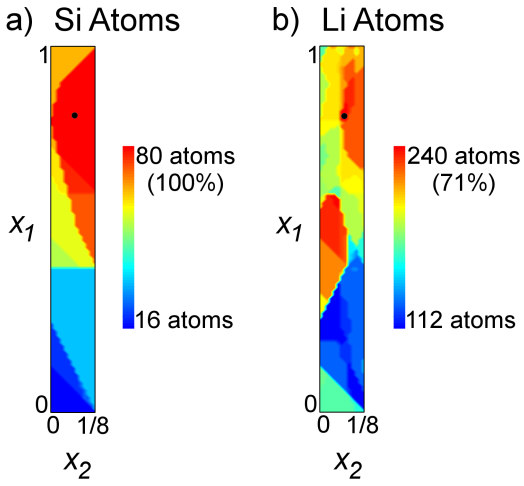

Figure 3.10: Correspondence between $\frac{2}{1}$ projected structures and the experimental $Li_{21}Si_5$ structure as a function of x_1 and x_2, for a region containing all unique projected structures. The plots show a) the number of projected Si atoms within 1 Å of experimental Si atoms, and b) the number of projected Li atoms within 1 Å of experimental Li atoms. The black dots indicate the optimal projection ($x_1 = 0.81$, $x_2 = 0.07$), for which 100% of the Si atoms and 71% of the Li atoms are correctly placed.

lies just beyond the established 1 Å cut-off (at 1.18 Å), while the other (QCO) lies just beyond the projected distance past which atoms do not project (1.03 vs. 1.02). A more complete understanding of the projected model of $Li_{21}Si_5$ can be obtained from the Supporting Information (available online). As this complete list of projected sites shows, there is a clear trend of shorter projected distances where atoms are found experimentally, and longer projected distances where atoms are not found. Of the twenty-two sites that are predicted theoretically by our optimal model of $Li_{21}Si_5$, fifteen are analogs of sites that are found experimentally. Of the thirty-four sites that lie beyond this optimal projection and are thus *not* predicted theoretically, thirty-three are *not* the analogs of experimental sites.

Table 3.1: Calculated atomic sites (in fractional coordinates of the cubic unit cell) in the $\frac{2}{1}$ projection centered at $(0.81, 0, 0, 0, 0.07, 0.07, 0.07, 0.07)$ which match the experimental sites in $Li_{21}Si_5$.

Theoretical coordinates	Theor. element	Proj. distance	Experimental coordinates	Exp. element	Exp. site name	Separation
(0.95, 0.75, 0.75)	Si	0.51	(0.928, 0.750, 0.750)	Si	TOH	0.41 Å
(0.35, 0.35, 0.35)	Si	0.52	(0.332, 0.332, 0.332)	Si	QOT	0.57 Å
(0.70, 0.50, 0.50)	Si	0.60	(0.681, 0.500, 0.500)	Si	HOH	0.36 Å
(0.10, 0.10, 0.10)	Si	0.61	(0.090, 0.090, 0.090)	Si	ZOT	0.31 Å
(0.20, 0.00, 0.00)	Li	0.80	(0.177, 0.000, 0.000)	Li	ZOH	0.43 Å
(0.55, 0.55, 0.55)	Li	0.81	(0.562, 0.562, 0.562)	Li	HIT	0.39 Å
(0.95, 0.95, 0.95)	Li	0.81	(0.946, 0.946, 0.946)	Li	ZIT	0.13 Å
(0.15, 0.15, 0.95)	Li	0.82	(0.158, 0.158, 0.988)	Li	ZCO	0.74 Å
(0.70, 0.70, 0.70)	Li	0.88	(0.691, 0.691, 0.691)	Li	TIT	0.29 Å
(0.90, 0.90, 0.70)	Li	0.88	(0.903, 0.903, 0.729)	Li	TCO	0.55 Å
(0.45, 0.25, 0.25)	Li	0.99	(0.424, 0.250, 0.250)	Li	QOH	0.49 Å
(0.85, 0.85, 0.85)	Li	0.99	(0.833, 0.833, 0.833)	Li	TOT	0.55 Å
(0.40, 0.40, 0.40)	Li	1.02	(0.421, 0.421, 0.421)	Li	HOT	0.68 Å
(0.20, 0.20, 0.20)	Li	1.02	(0.179, 0.179, 0.179)	Li	QIT	0.68 Å
(0.65, 0.65, 0.55)	$\frac{1}{2}$ Li	1.02	(0.662, 0.662, 0.489)	Li	HCO	1.18 Å
(0.40, 0.40, 0.20)	—	1.03	(0.414, 0.414, 0.250)	Li	QCO	1.01 Å

When looking at the discrepancies between the theoretical and experimental structures, it seems reasonable to assume that ordinary chemical constraints—atomic size, electronic structure, electronegativity, valence electron count, and quantum mechanics in general—should play a role in the structural energetics, and would thus modify the established "rules" for projection. We attribute the differences between the theoretical and experimental structures to such factors.

3.4 $Sm_{11}Cd_{45}$, $Mg_{44}Ir_7$, Ti_2Ni, and α-Mn

We turn now to the $Sm_{11}Cd_{45}$ and $Mg_{44}Ir_7$ structures. Both structures have excellent pseudo-tenfold diffraction symmetry[35] along ⟨110⟩, as shown in Figure 3.11. Both structures are ordered *F*-centered cubic structures with more than 400 atoms in their unit cells. Similarly to $Li_{21}Si_5$, their structures consist of four crystallographically inequivalent clusters centered at the Z, Q, H, and T positions. In $Sm_{11}Cd_{45}$, two clusters are based on the α-Mn structure, and two on bcc. In $Mg_{44}Ir_7$, clusters are derived from Ti_2Ni, γ-brass, and α-Mn.[27] We first turn to the new cluster types found in this pair of structures.

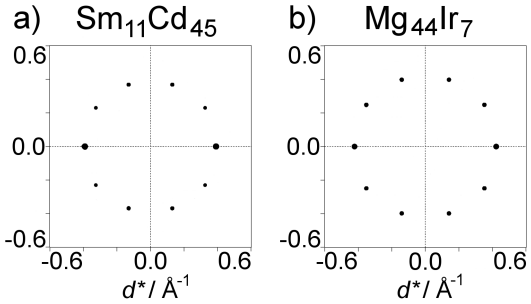

Figure 3.11: The strongest peaks in the [110] X-ray diffraction patterns of the a) $Sm_{11}Cd_{45}$ and b) $Mg_{44}Ir_7$ structures. Similarly to the structures we have already generated by projection, these two exhibit a pseudo-tenfold diffraction symmetry.

Three new cluster types need to be delineated: the α-Mn, Ti_2Ni, and bcc clusters. In Figure 3.12, we illustrate these three new cluster types. Site names used in describing γ-brass can also be used for the Ti_2Ni cluster (Figure 3.12a). For α-Mn and bcc (Figure 3.12b,c), however, in addition to the previously discussed site types, two new sites are also found: the cluster center (CC) and the truncated tetrahedron (TT). In Figure 3.13, we illustrate the crystallographically inequivalent clusters of $Sm_{11}Cd_{45}$ and $Mg_{44}Ir_7$ using the nomenclature derived

in Figure 3.8.

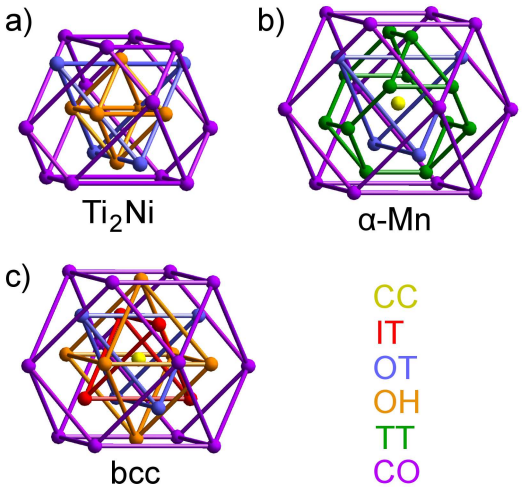

Figure 3.12: The a) Ti_2Ni, b) α-Mn, and c) body-centered cubic atomic clusters, connected as polyhedra according to their crystallographically inequivalent sites. In all, the clusters include six types of sites, which we abbreviate using two-letter names: CC (yellow), IT (red), OT (blue), OH (orange), TT (green), and CO (purple).

The heavy atoms of these two structures occupy a variety of site types. The Sm sites in $Sm_{11}Cd_{45}$ are ZCC, ZCO, QCC, HOT, and TOT, while the Ir sites in $Mg_{44}Ir_7$ are ZOT, QOT, and TOH. In all, four different site types—CC, OT, OH and CO—are occupied by heavier atoms.

We turn now to $t = \frac{2}{1} = 2$ models of the two structures. With the same approach as was previously used for $Li_{21}Si_5$, we plot the agreement between calculated and experimentally observed atomic sites for both the heavy and light atoms in $Sm_{11}Cd_{45}$ and $Mg_{44}Ir_7$ (Figure 3.14). For the former system and the values $x_1 = 0.36$ and $x_2 = 0.11$, all 88 Sm atoms (all five crystallographically inequivalent Sm sites) and 224 of the 360 Cd atoms (nine of thirteen Cd sites) are correctly located. For $Mg_{44}Ir_7$, optimal agreement occurs when $x_1 = 0.61$

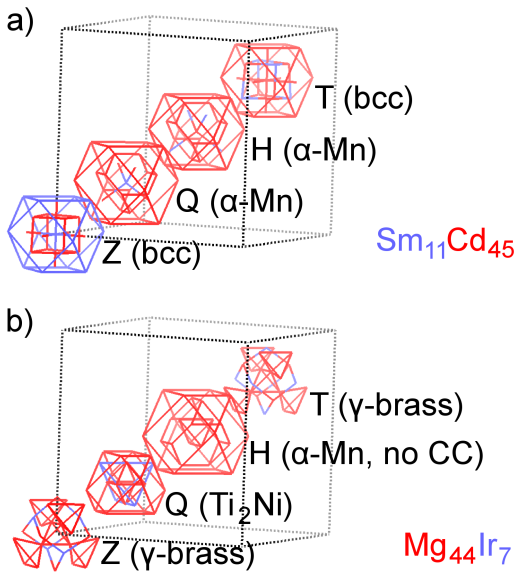

Figure 3.13: The four crystallographically inequivalent atomic clusters in the cubic unit cells of a) $Sm_{11}Cd_{45}$ and b) $Mg_{44}Ir_7$. In both cases, the heavier element is shown in blue, and the lighter element in red. The five Sm sites in $Sm_{11}Cd_{45}$ are ZCC, ZCO, QCC, HOT, and TOT, and the three Ir sites in $Mg_{44}Ir_7$ are ZOT, QOT, and TOH.

and $x_2 = 0.06$, when all 56 Ir atoms (all three crystallographically inequivalent Ir sites) and 232 of 352 Mg atoms (nine of eleven Mg sites) are successfully found. Tables 3.2 and 3.3 compare the projected and experimental atomic sites in $Sm_{11}Cd_{45}$ and $Mg_{44}Ir_7$, respectively.

The accuracy of these models is comparable to what was found for $Li_{21}Si_5$. All heavy atoms and 60-70% of light atoms are correctly located in the best projections for each structure. It is noteworthy that the projected E_8 models correctly account for the unusual mixture of CC, OT, OH, and CO sites occupied by the heavier elements.

Complete lists of the all the sites generated by our optimal $Sm_{11}Cd_{45}$ and

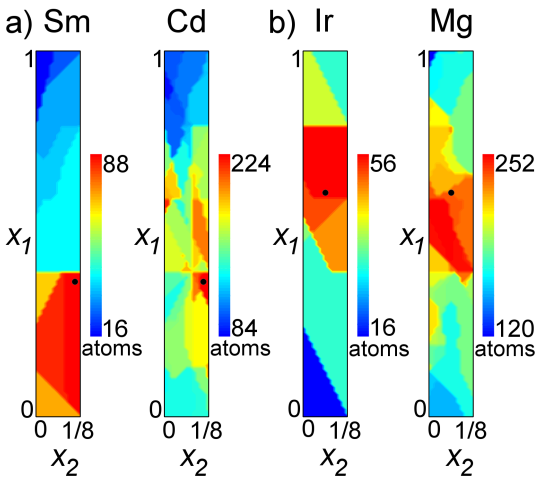

Figure 3.14: Correspondence between $\frac{2}{1}$ projected structures and the experimental a) $Sm_{11}Cd_{45}$ and b) $Mg_{44}Ir_7$ structures as functions of x_1 and x_2. In both panels, the plots show the number of projected heavy atoms within 1 Å of experimental heavy atoms (left), and the number of projected light atoms within 1 Å of experimental light atoms (right). The black dots indicate the optimal projection for each structure. For $Sm_{11}Cd_{45}$, the optimal point ($x_1 = 0.36$, $x_2 = 0.11$) correctly places 100% of the Sm atoms and 62% of the Cd atoms. For $Mg_{44}Ir_7$, the optimal point ($x_1 = 0.61$, $x_2 = 0.06$) correctly places 100% of the Ir atoms and 66% of the Mg atoms.

$Mg_{44}Ir_7$ projections are given in the Supporting Information (available online). As in the case of $Li_{21}Si_5$, these lists show a clear trend of shorter projected distances where atoms are found experimentally, and longer projected distances where atoms are not found. In the optimal theoretical models of both $Sm_{11}Cd_{45}$ and $Mg_{44}Ir_7$, thirty-seven sites lie beyond the projections and are thus *not* predicted theoretically. Comparing these two theoretical models to experiment, respectively thirty-three and thirty-five of those theoretically empty sites are correctly *not* the analogs of experimental atomic sites.

Table 3.2: Calculated atomic sites (in fractional coordinates of the cubic unit cell) in the $\frac{2}{1}$ projection centered at $(0.36, 0, 0, 0, 0.11, 0.11, 0.11, 0.11)$ which match the experimental sites in $Sm_{11}Cd_{45}$.

Theoretical coordinates	Theor. element	Proj. distance	Experimental coordinates	Exp. element	Exp. site name	Separation
(0.00, 0.00, 0.00)	Sm	0.42	(0.000, 0.000, 0.000)	Sm	ZCC	0.00 Å
(0.25, 0.25, 0.25)	Sm	0.46	(0.250, 0.250, 0.250)	Sm	QCC	0.00 Å
(0.40, 0.40, 0.40)	Sm	0.47	(0.406, 0.406, 0.406)	Sm	HOT	0.22 Å
(0.65, 0.65, 0.65)	Sm	0.50	(0.662, 0.662, 0.662)	Sm	TOT	0.44 Å
(0.20, 0.20, 0.00)	Sm	0.76	(0.174, 0.174, 0.014)	Sm	ZCO	0.87 Å
(0.45, 0.45, 0.25)	Cd	0.78	(0.438, 0.438, 0.263)	Cd	QCO	0.47 Å
(0.90, 0.90, 0.80)	Cd	0.79	(0.916, 0.916, 0.764)	Cd	TCO	0.93 Å
(0.75, 0.75, 0.75)	Cd	0.80	(0.750, 0.750, 0.750)	Cd	TCC	0.00 Å
(0.20, 0.00, 0.00)	Cd	0.81	(0.157, 0.000, 0.000)	Cd	ZOH	0.93 Å
(0.15, 0.15, 0.15)	Cd	0.83	(0.164, 0.164, 0.164)	Cd	QOT	0.51 Å
(0.50, 0.50, 0.50)	Cd	0.86	(0.500, 0.500, 0.500)	Cd	HCC	0.00 Å
(0.90, 0.90, 0.90)	Cd	0.88	(0.913, 0.913, 0.913)	Cd	ZOT	0.47 Å
(0.85, 0.85, 0.85)	Cd	0.98	(0.830, 0.830, 0.830)	Cd	TIT	0.76 Å
(0.30, 0.30, 0.40)	Cd	1.01	(0.296, 0.296, 0.390)	Cd	QTT	0.24 Å
(0.55, 0.55, 0.65)	—	1.02	(0.546, 0.546, 0.640)	Cd	HTT	0.25 Å
(0.05, 0.05, 0.05)	—	1.04	(0.083, 0.083, 0.083)	Cd	ZIT	1.26 Å
(0.95, 0.75, 0.75)	—	1.06	(0.910, 0.750, 0.750)	Cd	TOH	0.86 Å
(0.70, 0.70, 0.50)	—	1.07	(0.673, 0.673, 0.513)	Cd	HCO	0.88 Å

3.5 The Possibility of a New Quasicrystal

We have invoked many non-closest-packed cubic structures in this paper: $MgCu_2$ (the cubic Laves phase), Be_5Au, Cu_5Zn_8 (γ-brass), $Li_{21}Si_5$, Ti_2Ni, α-Mn, $Sm_{11}Cd_{45}$, and $Mg_{44}Ir_7$. All of these structures are connected to 3-D cell-projections of the E_8 lattice. If such quasicrystal approximants are so readily found, one might suppose that an actual cell-projected quasicrystal could also

Table 3.3: Calculated atomic sites (in fractional coordinates of the cubic unit cell) in the $\frac{2}{1}$ projection centered at $(0.61, 0, 0, 0, 0.06, 0.06, 0.06, 0.06)$ which match the experimental sites in $Mg_{44}Ir_7$.

Theoretical coordinates	Theor. element	Proj. distance	Experimental coordinates	Exp. element	Exp. site name	Separation
(0.35, 0.35, 0.35)	Ir	0.42	(0.348, 0.348, 0.348)	Ir	QOT	0.06 Å
(0.10, 0.10, 0.10)	Ir	0.55	(0.084, 0.084, 0.084)	Ir	ZOT	0.56 Å
(0.95, 0.75, 0.75)	Ir	0.61	(0.913, 0.750, 0.750)	Ir	TOH	0.74 Å
(0.15, 0.15, 0.95)	Mg	0.76	(0.156, 0.156, 0.980)	Mg	ZCO	0.62 Å
(0.90, 0.90, 0.70)	Mg	0.84	(0.902, 0.902, 0.719)	Mg	TCO	0.39 Å
(0.20, 0.00, 0.00)	Mg	0.86	(0.181, 0.000, 0.000)	Mg	ZOH	0.37 Å
(0.55, 0.55, 0.55)	Mg	0.88	(0.562, 0.562, 0.562)	Mg	HOT	0.43 Å
(0.95, 0.95, 0.95)	Mg	0.88	(0.948, 0.948, 0.948)	Mg	ZIT	0.06 Å
(0.70, 0.70, 0.70)	Mg	0.95	(0.697, 0.697, 0.697)	Mg	TIT	0.09 Å
(0.70, 0.70, 0.50)	Mg	0.96	(0.693, 0.693, 0.480)	Mg	HCO	0.45 Å
(0.85, 0.85, 0.85)	Mg	0.97	(0.834, 0.834, 0.834)	Mg	TOT	0.56 Å
(0.40, 0.40, 0.20)	$\frac{1}{12}$ Mg	0.97	(0.393, 0.393, 0.215)	Mg	QCO	0.35 Å
(0.55, 0.55, 0.35)	—	0.99	(0.552, 0.552, 0.338)	Mg	HTT	0.24 Å
(0.35, 0.25, 0.25)	—	1.09	(0.356, 0.250, 0.250)	Mg	QOH	0.12 Å

be eventually discovered. To aid in its potential search, let us detail what we may infer about such a quasicrystal.

By extension of the mathematics we considered above, such a quasicrystal will be based on the 3×8 matrix,

$$\begin{pmatrix} 0 & 0 & -2t & 0 & 1 & 1 & -1 & -1 \\ 0 & 0 & 0 & -2t & 1 & -1 & 1 & -1 \\ 0 & -2t & 0 & 0 & 1 & -1 & -1 & 1 \end{pmatrix}.$$

For all rational values of t, including those already considered, one finds quasicrystal approximants. Only if t is an irrational number does projection lead

to a non-crystal. The most interesting irrational value of t is τ. Here, each capping tetrahedron consisting of an OT atom and its three neighboring IT atoms is perfectly regular in shape. As the structures discussed above are all variants of tetrahedral packing, domains of such perfectly regular tetrahedra may be quite desirable.

The quasicrystal approximants discussed in this paper have elements vastly different in size. Let us assume that any potential quasicrystal will also contain at least two such dissimilar elements. In this paper, we have fared better in correctly locating the heavier of the elements. For the three $t = \frac{2}{1} = 2$ models discussed above, the heavier atoms were all correctly located, and had projected distances no longer than 0.61, 0.76, and 0.61 units of the E_8 lattice. Let us suppose that in an eventual quasicrystal, heavy atoms will be the E_8 vertices with projected distances shorter than 0.7.

What does such a structure look like? First, for a true quasicrystal, we no longer need consider the translation vector $\mathbf{x}$. The quasicrystal remains unchanged for different values of this vector. We therefore need only consider a single structure. Different approaches have been chosen in the literature for the graphical representation of quasicrystals. In this paper, we choose a highly local view. In Figure 3.15, we provide local views of the quasicrystal around three particularly pseudosymmetric positions. These views are directly compared with the heavy atom positions found in the various $t = \frac{2}{1} = 2$ quasicrystal approximants. Figure 3.15a shows one region of heavy atoms in this quasicrystalline projection. As shown, these sites match closely with those of the twenty-six Si atoms closest to $(\frac{1}{4}, \frac{1}{4}, \frac{1}{4})$ in $Li_{21}Si_5$, which represent all four symmetry-inequivalent Si sites in the structure. Not shown but equally true,

a subset of these projected heavy atoms in Figure 3.15a also match the fourteen Ir atoms closest to $(\frac{1}{4}, \frac{1}{4}, \frac{1}{4})$ in $Mg_{44}Ir_7$, which represent all three symmetry-inequivalent Ir sites. The configuration of heavy atoms in $Sm_{11}Cd_{45}$, which is quite different from that of $Li_{21}Si_5$ and $Mg_{44}Ir_7$, appears in another region of the proposed quasicrystal. This region of projected heavy atoms (Figure 3.15b) matches closely with the thirty-three Sm atoms closest to $(\frac{1}{4}, \frac{1}{4}, \frac{1}{4})$ in $Sm_{11}Cd_{45}$, which represent all five symmetry-inequivalent Sm sites. In still other regions of the proposed quasicrystal (of which Figure 3.15c is a representative example), the heavy atoms bear no obvious resemblance to the heavy atoms in $Li_{21}Si_5$, $Mg_{44}Ir_7$, or $Sm_{11}Cd_{45}$.

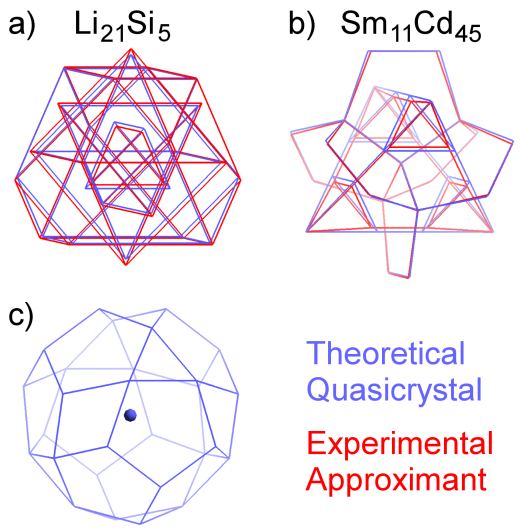

Figure 3.15: Correspondence between heavy atom positions in the proposed quasicrystal and its experimental approximants. a) Some regions in the quasicrystal resemble the pattern of heavy atoms in $Li_{21}Si_5$ (and $Mg_{44}Ir_7$), while b) others resemble the pattern of heavy atoms in $Sm_{11}Cd_{45}$. c) Still other regions in the proposed quasicrystal bear no such resemblance.

As Figure 3.15 shows, the quasicrystal can be thought of as containing domains which resemble all the quasicrystal approximants. At some locations, the

heavy atom structure resembles most that of $Sm_{11}Cd_{45}$, while in other places it is most like $Li_{21}Si_5$ and $Mg_{44}Ir_7$. Perhaps experimental quasicrystals will be found as intergrowths of two or more known quasicrystal approximant phases.

One more feature of this potential quasicrystal should be noted. In known quasicrystals, the quasicrystal belongs to a 3-D point group that is inaccessible in 3-D space groups (e.g., I_h). By contrast, for $t = \tau$, the resulting quasicrystal remains in 3-D T_d symmetry. It is only in the improvement of its pseudosymmetries that there is any additional symmetry in the cell-projected E_8 quasicrystal.

3.6 Conclusion

In the introduction to this paper, we catalogued all the metallic cubic structures which are not directly related to fcc, hcp, or bcc. In this paper, we have related roughly half of these structures to projections of the E_8 lattice. Of the remaining structures, some of them (e.g., Cr_3Si and YCd_6) are already known approximants related to 3-D quasicrystals of I_h symmetry.[92,93] Taken together, it appears the majority of the common non-closest-packed cubic structures are connected to quasicrystal approximants.

The limitation to cubic structures may be an arbitrary one. It seems plausible that the E_8 lattice is related to tetrahedral packing in general, and not just to tetrahedral packing in cubic unit cells. Perhaps structures belonging to non-cubic Bravais classes will also prove to be so connected. We save such explorations for future work.

3.7 Acknowledgment

This research was supported by the National Science Foundation through grant DMR-0504703. We thank Aaron Bloomfield and Julie Fichot for their separate work in our laboratory on the $Li_{21}Si_5$ structure. We thank Roald Hoffmann for his careful listening to our ideas.

CHAPTER 4

MIND THE PSEUDOGAP: THE DETERMINANTS OF STRUCTURE IN COMPLEX INTERMETALLICS

And all this science I don't understand
It's just my job five days a week.

—Sir Elton John, "Rocket Man"[102]

We come now to what may be considered the second section of this thesis. The first three chapters focused on a class of complex cubic intermetallic crystal structures, eventually simplifying and unifying them as projected slices of the E_8 lattice. This final chapter turns to electronic structure, focusing on the theoretical rationale for Hume-Rothery's electron-counting rules. While the link is not obvious, these two stories are closely connected through the common thread of X-ray diffraction. The diffraction pattern of an intermetallic compound is not only a manifestation of its crystal structure, but as this chapter discusses, also an indicator of its valence electron count. Our work therefore implies that the electronic factors driving the formation of complex intermetallics can productively be seen in higher dimensions. This will likely be a focal point of future research.

This chapter examines the electronic factors that lead compounds with certain numbers of valence electrons per atom to adopt certain intermetallic structures. The work is motivated by Hume-Rothery's empirically generated electron-counting rules, and Mott and Jones's subsequent theoretical explanation for them. Mott and Jones's rationale is based on the nearly free-electron model, crediting the stability of an electron count to the mixing and energy splitting of free-electron waves near Brillouin zone planes. This explanation at first

appears at odds with the way most chemists prefer to view electron-counting rules. But it need not be seen that way. In this work, we cast the traditional theoretical model of Hume-Rothery "electron phases" into the real-space language of linear combinations of atomic orbitals. In doing so, we develop an alternate understanding of the electron-counting rules in intermetallic crystals, more in keeping with the way chemists tend to rationalize molecular electron-counting rules.

4.1 Introduction

For a variety of intermetallic compounds, the per-atom valence electron count is seen as the primary determinant of ground-state crystal structure. The relationship between structure and electron count in these so-called "electron phases" has been elucidated through of a variety of empirical and theoretical insights. The key empirical observations were made by Hume-Rothery (whose name is often attached to electron phases) over several decades in the mid-1900s.[103,104] Hume-Rothery noted that in many cases, a crystal structure exists at the same electron count for various combinations of elements. Two prototypical examples of this, both discussed in detail later in this work, are the β-brass (bcc) and γ-brass (Cu_5Zn_8[10]) structures. In phase diagrams such as Cu–Zn, Cu–Ga, and Cu–Sn,[105] despite the changing number of valence electrons in the element paired with Cu, the β and γ structures exist in relatively narrow composition ranges surrounding $\frac{3}{2}$ and $\frac{21}{13}$ valence electrons per atom, respectively.

A theoretical rationale for the relationships between structural stability and valence electron count was first developed by Jones,[106] and later Mott and

Jones[107] (referred to from now on collectively as MJ). Their model argues that it is favorable for a compound to adopt a structure for which the Fermi surface cuts the boundaries of the first Brillouin zone or higher zones. This situation allows free-electron plane-wave states near the Fermi energy to mix, stabilizing filled states and destabilizing unfilled states. Concentrating mainly on γ-brass and employing a variety of approaches, subsequent work has repeatedly affirmed the basic principles of the MJ model. Much of that work focuses on band structures, and credits the γ-brass stability range to a pseudogap in the density of states at the Fermi energy[108–115]—a sign that MJ-type mixing of states has pushed filled states down in energy, and unfilled states up. Other work invokes productively the behavior of the dielectric function.[116–118] The same concepts used to rationalize γ-brass have also been applied to other families of metallic structures.[119–124]

A feature shared by the MJ model and nearly all subsequent work on Hume-Rothery electron phases is that they focus on reciprocal-space features to explain the electron counts of crystals. In molecules, however, some of our most successful qualitative explanations for electron-counting rules use real-space, rather than momentum-space, arguments. The octet rule for main-group elements, the 18-electron rule for transition-metal complexes, Hückel's rules for π-electrons in aromatics, and Wade's rules for electron-deficient clusters[125] all rest on real-space atomic orbital interactions. Even in crystals, there have been calculations showing that the Hückel method, which uses an atomic orbital basis set, can correctly reproduce the energy orderings that lead to various electron-counting rules.[126,127]

Since the MJ arguments attempt to rationalize the stability of electron phases,

it should be possible to cast them terms of real-space electronic states. There must be an analogous model that sees the relevant plane-wave electronic states as linear combinations of atomic orbitals, and the driving force for the stability range in electron phases as a gap between bands of these states. It is our goal in this work to develop such a bridging model. In doing so, we will show that Hume-Rothery's observations and the MJ approach to them can be understood in the same basic way that we understand all electron-counting rules. Just as the octet and 18-electron rules stem from the energy gap between one s/p or $s/p/d$ electronic shell and the next, the rules in Hume-Rothery electron phases arise from the mixing and splitting of an s-based band and a p-based band.

In this work, we must mix some concepts and arguments that are typically used by physicists with others that are part of the theoretical language of chemists. Therefore, in the next section, we introduce the basic concepts behind this paper using the simplest imaginable crystal, and prepare the reader (whether nominally a physicist or a chemist) for what is to come. Later on, we review the MJ model, cast it in the language of linear combinations of atomic orbitals (LCAOs), and discuss its validity and implications with respect to increasingly complex Hume-Rothery electron phases.

4.2 Reconciling the Nearly Free-Electron and LCAO Models

The hypothetical crystal on which this section focuses is the one-dimensional (1-D) chain of atoms of a main-group element. We simplify the system even further by looking only at its electronic states of σ-symmetry. If asked to sketch the band structure of this crystal, physicists and chemists would likely approach

the problem from very different directions—physicists in terms of the mixing of free-electron plane-wave states in the presence of a periodic potential, and chemists in terms of symmetry-adapted linear combinations of atomic orbitals whose energies are shaped by bonding and antibonding interactions. Even for a case as simple as this one, it takes a fair bit of thought to recognize the deep similarities between the results of these two approaches. We find it instructive to look briefly at each, and then compare and contrast the two.

First, we should make a brief note about our use of mathematical notation in this paper. As often as possible, our notation is intuitive and of minimal complexity, and is consistent with itself and with past work. A few conventions are worth mentioning. When employing a nearly free-electron model, we refer to free-electron plane waves by lowercase ψ, nearly free-electron wavefunctions (sums of plane waves) by capital Ψ, and the energies of either by ε. When using a LCAO model, we refer to atomic orbitals by lowercase ϕ, crystal orbitals (sums of atomic orbitals) by capital Φ, and the energies of either by ϵ. For continuity, we refer to energy by capital E in all figures. Other issues of notation are noted in the text as they arise.

4.2.1 Starting with Free Electrons: The Physical Viewpoint

The static energy levels of an electron are governed by the time-independent Schrödinger equation:

$$[-\frac{\hbar^2}{2m}(\frac{\partial^2}{\partial x^2}+\frac{\partial^2}{\partial y^2}+\frac{\partial^2}{\partial z^2})+V(\vec{r})]\Psi(\vec{r})=\varepsilon\Psi(\vec{r}).$$

For a free electron, one whose environment has no external potential, the equa-

tion is simpler:

$$-\frac{\hbar^2}{2m}\left(\frac{\partial^2}{\partial x^2}+\frac{\partial^2}{\partial y^2}+\frac{\partial^2}{\partial z^2}\right)\psi(\vec{r})=\varepsilon\psi(\vec{r}).$$

When treating a free electron, one traditionally enforces a periodic boundary condition such as the following, which assumes the eigenfunctions (electronic wavefunctions) repeat themselves outside of a cube of edge length $L = V^{\frac{1}{3}}$, a macroscopic quantity:

$$\psi(x,y,z)=\psi(x+L,y,z)=\psi(x,y+L,z)=\psi(x,y,z+L).^{a}$$

The set of periodic eigenfunctions of this equation are plane waves, each of which is associated with a wavevector $\vec{k}$ whose magnitude is inversely proportional to its wavelength:

$$\psi_{\vec{k}}(\vec{r})=\frac{1}{\sqrt{V}}e^{i\vec{k}\cdot\vec{r}}.$$

The corresponding eigenvalues (energies) are proportional to $\left|\vec{k}\right|^2$:

$$\varepsilon_{\vec{k}}=\frac{\hbar^2}{2m}\left|\vec{k}\right|^2.$$

The electrons of interest to this subsection are free to move not throughout a 3-D space, but along a 1-D string, which we define as the *x*-axis. The Schrödinger equation and its periodic boundary condition therefore become:

[a] In practice, one should use boundary conditions consistent with the symmetry of the problem at hand, to avoid introducing new degeneracies.

$$-\frac{\hbar^2}{2m}\frac{\partial^2}{\partial x^2}\psi(x) = \varepsilon\psi(x),$$

$$\psi(x) = \psi(x + L).$$

The wavefunctions and energies in this case are:

$$\psi_{k_x}(x) = \frac{1}{\sqrt{L}}e^{ik_x x},$$

$$\varepsilon_{k_x} = \frac{\hbar^2}{2m}k_x^2.$$

The energies of these plane-wave wavefunctions are proportional to k_x^2, resulting in a parabola when energy is plotted with respect to k_x (Fig. 4.1a).

In real crystal structures, electrons are of course not free. They are subject to a periodic potential $V(\vec{r})$ created by the ions. Still, the free-electron model often proves a useful starting point for understanding crystalline electronic structure. Provided the periodic potential is relatively weak on some scale, one can think of the valence electrons in many real crystals as "nearly free". That is, the actual electronic wavefunctions and energies resemble those of free electrons. For a 1-D crystal, we now begin with the empty-lattice limit (where the potential tends toward zero and the electrons tend toward free electrons), and "turn on" the potential.

Imagine that a periodic potential is imposed on an otherwise free electron, with repeat distance a along the x-axis. The result is a crystal of unit cell length a, whose band structure can be concisely plotted within the first Brillouin zone ($-\frac{\pi}{a} \leq k_x \leq \frac{\pi}{a}$). Electronic states lying outside the first Brillouin zone can be carried into it by subtracting a reciprocal lattice vector from k_x—in this case, an

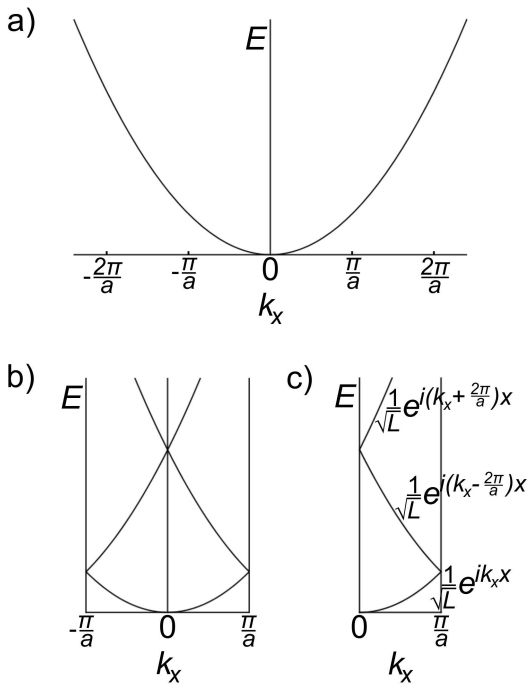

Figure 4.1: a) The energy of a free-electron plane wave with respect to k_x. b) The band structure of the empty-lattice limit of a 1-D chain of atoms, carried into the first Brillouin zone. c) Another view of the empty-lattice limit, confined to an irreducible piece of the first Brillouin zone, with the wavefunction of each branch labeled.

integral multiple of $\frac{2\pi}{a}$. In the empty-lattice limit, the resulting picture (Fig. 4.1b) approaches that of a free-electron parabola appearing to fold over onto itself indefinitely. An even more concise view of this band structure (Fig. 4.1c) uses an even smaller piece of reciprocal space, the irreducible region of the first Brillouin zone ($0 \leq k_x \leq \frac{\pi}{a}$). In the last panel of this figure, each branch of the band structure is shown along with the corresponding free-electron wavefunction.

The question we must now examine is how turning on the potential of a 1-D chain of ions perturbs the free-electron band structure shown in Fig. 4.1c. As the answer is derived in detail in most introductory solid-state physics text-books,[128,129] we only outline it here.

When an electron is subject to the periodic potential of an ion at every lattice point on the x-axis (i.e., every integral multiple of a), solutions to the Schrödinger equation are no longer pure plane waves. By Bloch's theorem, they can be written as functions of the form $\Psi_{k_x}(x) = e^{ik_x x}u_{k_x}(x)$, where $u_{k_x}(x)$ has the same periodicity as the potential $V(x)$ and can therefore be expressed as a Fourier series of plane waves. Depending on the function used to model the ionic potential, the exact form of the wavefunctions and electronic energies can vary. However, the qualitative picture (Fig. 4.2) is always the same. In large part, this nearly free-electron band structure remains similar to the empty-lattice limit (Fig. 4.1c). Far from the points $k_x = 0$ and $k_x = \frac{\pi}{a}$ (within the range of about $0.2\frac{\pi}{a} \leq k_x \leq 0.8\frac{\pi}{a}$), the bands resemble a parabola folding over onto itself. Likewise, each wavefunction within this range is dominated by the corresponding free-electron plane wave. That is, states in the bottom band resemble $\Psi_{k_x}(x) = \frac{1}{\sqrt{L}}e^{ik_x x}$, states in the second band resemble $\Psi_{k_x}(x) = \frac{1}{\sqrt{L}}e^{i(k_x - \frac{2\pi}{a})x}$, and states in the third band resemble $\Psi_{k_x}(x) = \frac{1}{\sqrt{L}}e^{i(k_x + \frac{2\pi}{a})x}$.

Near the points $k_x = 0$ and $k_x = \frac{\pi}{a}$, however, the nearly free-electron band structure looks quite different from the empty-lattice limit. Where the empty-lattice limit has pairs of plane-wave eigenstates whose energies approach degeneracy, the nearly free-electron case has eigenstates that are mixtures of those plane waves whose energies are split. Take the two lowest-energy eigenstates at $k_x = \frac{\pi}{a}$, for example. When a periodic potential of ion-centered wells is turned on, the eigenstates resemble a sum and a difference of two plane waves, $\Psi_{\frac{\pi}{a}}(x) = \frac{1}{\sqrt{2L}}(e^{i\frac{\pi}{a}x} + e^{-i\frac{\pi}{a}x}) = \sqrt{\frac{2}{L}}cos(\frac{\pi}{a}x)$ and $\Psi_{\frac{\pi}{a}}(x) = -\frac{i}{\sqrt{2L}}(e^{i\frac{\pi}{a}x} - e^{-i\frac{\pi}{a}x}) = \sqrt{\frac{2}{L}}sin(\frac{\pi}{a}x)$. While the size of the energy splitting between these standing-wave states depends on the strength of the ionic potential, the fundamental reason for the splitting can be seen in the visual representations of the two states on the right

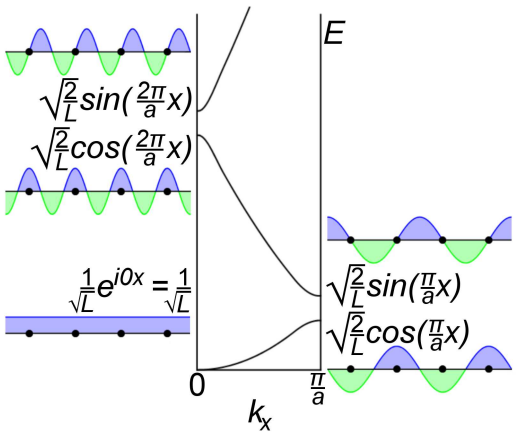

Figure 4.2: The nearly free-electron band structure of a 1-D chain of atoms. While the wavefunctions and energies resemble their empty-lattice analogs far from $k_x = 0$ and $k_x = \frac{\pi}{a}$, the wavefunctions and energies near $k_x = 0$ and $k_x = \frac{\pi}{a}$ reflect a mixing of plane-wave states and a consequent energy splitting. Ions are shown as black circles.

side of Fig. 4.2. An electron whose wavefunction is $\sqrt{\frac{2}{L}}cos(\frac{\pi}{a}x)$ resides mostly near the ions, while an electron whose wavefunction is $\sqrt{\frac{2}{L}}sin(\frac{\pi}{a}x)$ resides mostly between the ions. Provided the ions are taken to be positively charged, they have a stabilizing interaction with negatively charged valence electrons, and the former eigenstate is lower in energy than the latter.

A similar splitting occurs at $k_x = 0$. While the lowest-energy state remains relatively unaffected by a weak external potential, the two states above it mix. The free-electron plane waves $\psi_0(x) = \frac{1}{\sqrt{L}}e^{i\frac{2\pi}{a}x}$ and $\psi_0(x) = \frac{1}{\sqrt{L}}e^{-i\frac{2\pi}{a}x}$ mix to become a sum and a difference, the standing waves $\Psi_0(x) = \frac{1}{\sqrt{2L}}(e^{i\frac{2\pi}{a}x} + e^{-i\frac{2\pi}{a}x}) = \sqrt{\frac{2}{L}}cos(\frac{2\pi}{a}x)$ and $\Psi_0(x) = -\frac{i}{\sqrt{2L}}(e^{i\frac{2\pi}{a}x} - e^{-i\frac{2\pi}{a}x}) = \sqrt{\frac{2}{L}}sin(\frac{2\pi}{a}x)$. The former wavefunction is lower in energy than the latter, again because its magnitude is larger near the ions.

This familiar nearly free-electron band structure (Fig. 4.2) is a qualitative pic-

ture of the electronic σ-states in a 1-D chain of atoms, derived from the starting point of plane waves. We now derive the analogous picture from the starting point of localized atomic orbitals, and compare the two.

4.2.2 Starting with Atoms: The Chemical Viewpoint

In contrast to this physical viewpoint, which can approximate electronic states as perturbations of free-electron plane waves, the more chemical approach views them as linear combinations of atomic orbitals. One of the simplest and most transparent techniques utilizing this approach is the extended Hückel (eH) method.[130] The eH method was the first widely applied semi-empirical orbital procedure for molecules, and was later applied to extended structures.

The basis set in eH consists only of atomic valence orbitals (e.g., $1s$ for H, $2s/2p$ for C, $4s/4p/3d$ for Fe), expressed in the form $\phi(\vec{r}) = NR(r)Y(\theta,\varphi)$. Radial components of the basis s and p orbitals are chosen as nodeless Slater functions, $R(r) = r^{n-1}e^{-\zeta r}$, with exponents ζ chosen by Slater's rules or to match optimized atomic functions. So-called double-ζ functions, $R(r) = r^{n-1}(c_1e^{-\zeta_1 r} + c_2e^{-\zeta_2 r})$, are used for d orbitals. Angular components $Y(\theta,\varphi)$ are chosen as the real form of spherical harmonics. Constants N ensure that the functions satisfy the normalization condition, $\int_{\text{all space}} \phi(\vec{r})\phi^*(\vec{r})\,dV = 1$.

In a *molecular* calculation, the full molecular wavefunctions are taken to be LCAOs constructed from the atomic basis orbitals:

$$\Phi_j(\vec{r}) = \sum_i C_{ij}\phi_i(\vec{r}).$$

The columns of coefficients C_{ij} are eigenvectors of the following secular equation:

$$\mathbf{HC} = \epsilon\mathbf{SC}.$$

In this equation, **H** is an effective one-electron Hamiltonian, and **S** is the overlap matrix. Matrix elements $S_{ij} = \int_{\text{all space}} \phi_i(\vec{r})\phi_j^*(\vec{r})\, dV$ are the computed overlap integrals of the Slater-type basis functions. In contrast to the normal Hückel method, no overlap integrals are set to zero. The diagonal matrix elements H_{ii} are typically taken as valence-state ionization potentials. The off-diagonal elements H_{ij} are approximated by a Wolfsberg-Helmholtz formula:

$$H_{ij} = K(\frac{H_{ii} + H_{jj}}{2})S_{ij},$$

with a single parameter $K = 1.75$ for all interactions. The molecular wavefunctions are normalized, and the corresponding eigenvalues are the one-electron eH energies. In typical eH calculations, there is no self-consistency.

Given its simplicity (only a few parameters differentiate the various basis orbitals of distinct chemical elements), the eH method does remarkably well in getting the correct ordering of energy levels in molecules, and even the approximate energetics of angular deformations. To put it another way, eH gets the nodes in the right places in molecular orbitals. Extensive applications have shown the utility of the method for extended systems as well. The methodology is transparent, and it is uniquely well adapted to generating one-electron perturbation theory-based explanations. It comes also with a suite of analytical tools—overlap populations, fragments orbital analysis, etc.—that is, to this day, unmatched in utility.

The application to extended systems is straightforward. Basis orbitals are taken not as isolated Slater-type orbitals, but as Bloch functions of Slater-type orbitals. For a 1-D chain along the x-axis, with atomic spacing a and each atom labeled with an integral index n, these basis functions are (un-normalized) of the form $\sum_n e^{ik_x na}\phi_n(\vec{r})$. At a given k_x, there is a basis Bloch function for each valence atomic orbital in the unit cell. Therefore, when the secular equation is solved (with overlap calculations usually terminated at some long distance), the number of eigenfunctions is also equal to the number of valence atomic orbitals in the unit cell.

The qualitative features of the eH band structure of the 1-D chain are largely independent of which element comprises the chain. Here, the atoms are chosen to be carbon, with the following atomic parameters: H_{ii}(C 2s) = −21.4 eV, ζ_s = 1.625; H_{ii}(C 2p) = −11.4 eV, ζ_p = 1.625.[130] As in the previous subsection, our focus is only on σ-states. Thus, only 2s and 2p_x orbitals are used as a basis.

The band structures of two different 1-D carbon chains are shown in Fig. 4.3. While C–C bond lengths in diamond are 1.54 Å, nearest neighbors in these chains are placed at distances of 2.2 Å (Fig. 4.3a) and 1.9 Å (Fig. 4.3b). The large spacings are chosen to simulate relatively weak atomic orbital interactions. Each band structure has two bands reflecting the two basis orbitals (2s and 2p_x) on each atom, with the bottom band sloping upward and the top band sloping downward.[131] The bands in the 1.9 Å chain spread over a larger range of energies, because the shorter interatomic spacing leads to stronger bonding and antibonding interactions.

Also shown in Fig. 4.3 are cartoons of the crystal orbitals themselves, which

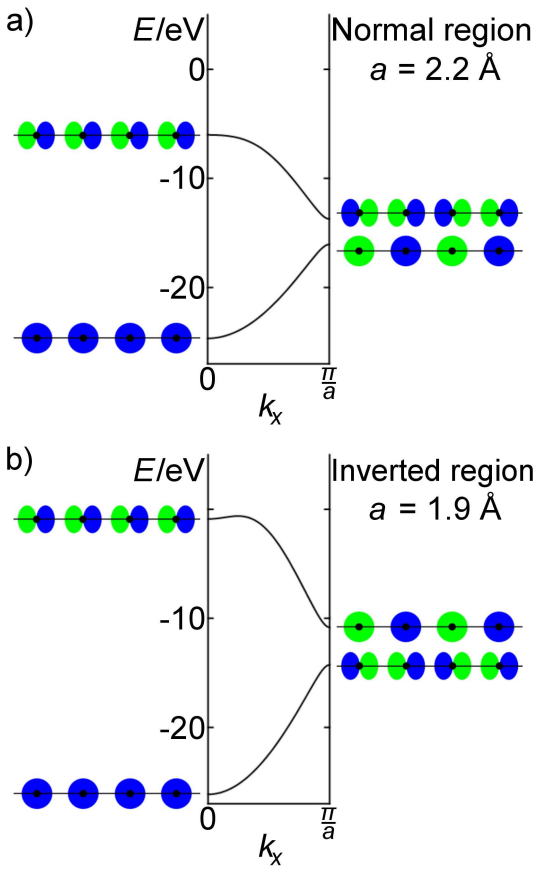

Figure 4.3: The extended Hückel band structure of a 1-D chain of carbon atoms separated by a) 2.2 Å and b) 1.9 Å. With the change in interatomic spacing, the energy ordering of the antibonding combination of 2*s* orbitals and the bonding combination of 2*p* orbitals at $k_x = \frac{\pi}{a}$ can lie in either the normal or inverted region (see text).

display *s* orbitals as isolated circles and *p* orbitals as pairs of ovals.[b] At $k_x = 0$, in both chains, the lower-energy orbital is the bonding combination of 2*s* orbitals, and the higher-energy orbital is the antibonding combination of $2p_x$ orbitals. At $k_x = \frac{\pi}{a}$, there is a significant difference between the electronic states of the two chains. In the 2.2 Å chain (Fig. 4.3a), the antibonding combination of 2*s*

[b]For ease of representation, we show the crystal orbitals only at $k_x = 0$ and $k_x = \frac{\pi}{a}$. At other values of k_x, the atomic orbitals have complex coefficients, and are therefore more difficult to represent.

orbitals is lower in energy than the bonding combination of $2p_x$ orbitals. We refer to this ordering (s antibonding below p σ-bonding) as the *normal region*, as it is what we are used to seeing in diatomic molecular orbital diagrams. In the 1.9 Å chain (Fig. 4.3b), we see the opposite ordering. We call this the *inverted region*. In other words, when the interatomic spacing is short enough, the strength of the bonding and antibonding interactions can overcome the inherent difference in energy of $2s$ and $2p$ orbitals. Both of these regions are seen in certain experimental crystal structures.[132] We discuss the importance of the distinction, along with similarities and differences between the eH band structures and their nearly free-electron counterpart, in the next subsection.

4.2.3 Different Viewpoints, Synergistic Conclusions

We have now examined the band structure of a 1-D chain of atoms using two very different approaches. It is reassuring to note that the band structures depicted in Figs. 4.2 and 4.3 bear striking similarities. In both cases, the lowest-energy band slopes upward and the second band slopes downward. Even the wavefunctions themselves look similar. The eH orbitals at $k_x = 0$, the most bonding combination of $2s$ and the most antibonding combination of $2p_x$, closely approximate the corresponding functions $\Psi_0(x) = \frac{1}{\sqrt{L}}$ and $\Psi_0(x) = \sqrt{\frac{2}{L}}sin(\frac{2\pi}{a}x)$ in the nearly free-electron picture. Similarly at $k_x = \frac{\pi}{a}$, the antibonding combination of $2s$ and the bonding combination of $2p_x$ resemble the nearly free-electron wavefunctions $\Psi_{\frac{\pi}{a}}(x) = \sqrt{\frac{2}{L}}cos(\frac{\pi}{a}x)$ and $\Psi_{\frac{\pi}{a}}(x) = \sqrt{\frac{2}{L}}sin(\frac{\pi}{a}x)$.

There are some differences between the band structures in Figs. 4.2 and 4.3 as well. While the nearly free-electron model predicts an infinite number of bands

of electronic states rising to infinitely high energies, the eH band structure is limited to the same number of bands as there are atomic valence orbitals in the unit cell. If the valence set were extended (say, to include 3s, 3p, and 3d), one would see more bands. The second difference, the one mentioned earlier, is in the ordering of states at $k_x = \frac{\pi}{a}$. While the nearly free-electron model produces a band structure in the normal region (provided the ions are taken to be positively charged), eH theory can produce a band structure in either the normal or inverted region, depending on the element and the interatomic spacing (which dictate overlap and thus band dispersion).

Despite the differences, the feature of these band structures that is most significant to the remainder of this paper is identical in both cases. In both the nearly free-electron and eH pictures (and in both the normal and inverted regions), there is an energy gap between the lowest-energy band and the second band, with no states lying between the two. Furthermore, in both cases, this gap is caused by the splitting of two states at $k_x = \frac{\pi}{a}$ that resemble standing waves whose wavelength is twice the interatomic spacing.

Based on this gap, one might predict that it would be energetically favorable for such a (hypothetical) 1-D chain to have two valence electrons per atom in states of σ-symmetry. If this were the case, all the lower-energy states below the gap would be filled, while all the higher-energy states above the gap would be empty. This assumption, that an energy gap is a favorable separator of filled states from empty states, is implicit in all electron-counting rules in molecules, from the octet and 18-electron rules to Hückel's rules and Wade's rules. The assumption is also implicit in Mott and Jones's (MJ) electronic justification of the Hume-Rothery rules in solids, which is the focus of the next section.

4.3 The MJ Model

The MJ model,[106,107] which was first developed in the 1930s, provides theoretical rationale for the valence electron counts in a number of Hume-Rothery electron phases. For those unfamiliar with the model, we introduce it by example, again using the σ-states of a 1-D chain of main-group atoms. As the model is generally presented from a nearly free-electron viewpoint, in terms of the mixing of plane-wave electronic states, we too begin by presenting it this way.

The arrangement of ions in a 1-D chain along the x-axis has two consequences that are important to MJ reasoning. One has already been discussed, and is reiterated in Fig. 4.4a, which employs the extended zone scheme so the bands resemble a free-electron parabola. The periodic potential causes free-electron plane-wave states of the form $\psi_{k_x}(x) = \frac{1}{\sqrt{L}} e^{ik_x x}$ to mix. This in turn creates energy gaps within the free-electron parabola by separating states whose electron density resides near the ions from states whose electron density resides between the ions. The lowest-energy splitting corresponds to the strong mixing of the $k_x \approx \frac{\pi}{a}$ states with the $k_x \approx -\frac{\pi}{a}$ states.[c]

Working under the assumption that a compound will adopt a structure for which the Fermi level resides in such an energy gap, this nearly free-electron reasoning allows one to predict how many σ-electrons are likely to be in such a chain (if it exists as a real crystal). In this case, the states $-\frac{\pi}{a} \leq k_x \leq \frac{\pi}{a}$ are likely to be filled, and the others empty. As this is 1 unit cell of the reciprocal lattice, it translates to 1 filled valence σ-orbital, or 2 valence σ-electrons, per unit cell. With just a single atom in the unit cell, the predicted valence σ-electron count

[c] In a periodic potential, the states that are allowed to mix are those whose k_x are separated by a reciprocal lattice vector (i.e., an integral multiple of $\frac{2\pi}{a}$). Therefore, the $k_x = 0.99\frac{\pi}{a}$ and $k_x = -1.01\frac{\pi}{a}$ states mix strongly, the $k_x = 1.01\frac{\pi}{a}$ and $k_x = -0.99\frac{\pi}{a}$ states mix strongly, etc.

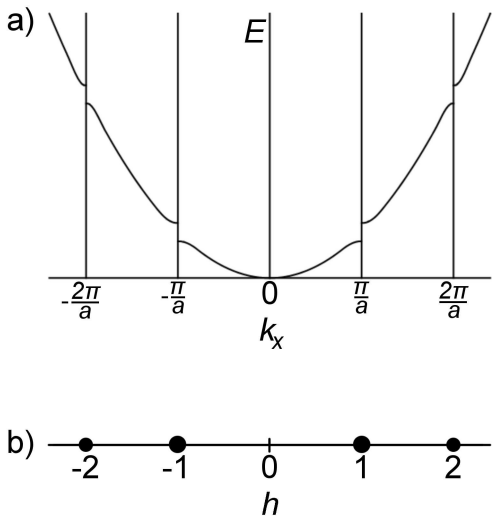

Figure 4.4: a) The nearly free-electron band structure of a 1-D chain of atoms, shown in the extended zone scheme. b) The X-ray diffraction pattern of the same chain, emphasizing the correspondence between energy splittings and diffraction peaks.

for this 1-D chain is 2 electrons per atom.

The second important consequence of the periodic arrangement of atoms relates not to the energies of electrons, but to their ability to scatter X-rays and thus create diffraction peaks. For a 3-D crystal, the relative intensities of X-ray peaks obey the proportionality:

$$I_{\Delta\vec{k}} \propto \left| \sum_j f_j(\Delta\vec{k}) e^{i\Delta\vec{k}\cdot\vec{r_j}} \right|^2 .$$

In this summation over every atom in the crystal, $f_j(\Delta\vec{k})$ are the atomic form factors of each atom, and $\vec{r_j}$ are the spatial coordinates of each atom. In order for constructive interference to occur, $\Delta\vec{k}$ must be a reciprocal lattice vector, traditionally expressed in the form $h\vec{a^*} + k\vec{b^*} + l\vec{c^*}$ (a sum of integer multiples of the reciprocal lattice basis vectors). In our 1-D crystal, because the scattering factor

of each atom is identical and all atoms lie on the x-axis, the proportionality can be simplified as follows:

$$I_{\Delta\vec{k}} \propto \left| f(\Delta\vec{k}) \sum_j e^{ih\frac{2\pi}{a}x_j} \right|^2 .$$

Knowing that the atoms in this chain are found at every integral multiple of a, one can verify that there are strong diffraction peaks corresponding to every integral value of h. The X-ray diffraction pattern of the 1-D chain, with the undiffracted beam (the $h = 0$ peak) omitted, is shown in Fig. 4.4b.

The importance of X-ray diffraction peaks to the MJ model lies in the deep connection between Figs. 4.4a and 4.4b. It is not a coincidence that each diffraction peak in Fig. 4.4b is shown directly below an energy splitting in Fig. 4.4a. The two phenomena arise for closely related reasons. X-ray diffraction peaks come about when the atoms in a crystal sync up with the crests of a diffraction plane wave. Because the atoms in this 1-D chain lie a units apart in x, they interfere constructively with diffraction plane waves of wavelength a ($h = \pm 1$), $\frac{a}{2}$ ($h = \pm 2$), $\frac{a}{3}$ ($h = \pm 3$), etc. Likewise, energy splitting in the nearly free-electron model arises when the atoms in a crystal sync up with the periodicity of free-electron plane waves (recall Fig. 4.2). With the atoms in this chain a units apart in x, there are energy splittings between free-electron states of wavelength $2a$ ($k_x = \pm\frac{\pi}{a}$), a ($k_x = \pm\frac{2\pi}{a}$), $\frac{2a}{3}$ ($k_x = \pm\frac{3\pi}{a}$), etc.

What this means is that the X-ray diffraction pattern of a crystal, which is generally used to determine atomic positions, also contains information about the electronic band structure and the especially favorable valence electron counts. Let us review the MJ logic for the 1-D chain. Because the atoms are spaced a units apart in x, the strongest diffraction peaks correspond to $h = \pm 1$.

The atomic spacing also results in the strong mixing of free-electron plane waves of wavelength $2a$ ($k_x = \pm\frac{\pi}{a}$), and consequently an energy splitting and a gap in the density of states. If a compound adopts this structure, it likely does so in order to place its Fermi level in this gap, which would mean the nearly free-electron states $\Psi_{k_x}(x)$ are filled for $-\frac{\pi}{a} \leq k_x \leq \frac{\pi}{a}$ and empty for all other k_x (see Fig. 4.4a). This region of filled states is $\frac{2\pi}{a}$ units of reciprocal space, or a single unit cell of the reciprocal lattice. It translates to 1 valence σ-orbital per unit cell, or 2 valence σ-electrons per unit cell, or 2 valence σ-electrons per atom.

The connection between X-ray diffraction patterns and conditions for stability has been consistently used in recent studies of structure under pressure by several groups, notably Degtyareva.[133–135] The thematic underpinnings of the method are explored in a recent paper by Feng et al.[136]

4.4 Moving Toward Complexity

As we will soon see, both the MJ model and our orbital interpretation of it hold even in much more complicated structures in 3-D space. For certain $\vec{k}$-vectors corresponding to strong X-ray diffraction peaks, there is an energy splitting between two electronic states caused by, depending on your viewpoint of choice, the mixing of two free-electron plane waves or the inherent difference between states of primarily *s*-antibonding and *p*-bonding character. For very complicated band structures, however, the trick is *finding* these two electronic states, which are hidden within a large number of bands. When there are on the order of 1,000 bands in a band structure, as there are for an eH calculation of the primitive unit cell of a γ-brass superstructure with the full complement of va-

lence orbitals, fishing out two hidden bands of interest sounds almost hopeless.

However, if we can devise a technique to cut through the tremendous amount of excess information in a complicated band structure, it becomes possible. Our goal is to do just that. From a huge number of bands, we will tease out the few features that actually drive these complex crystal structures to be stable at their experimentally observed electron counts. We first demonstrate our technique on a structure that, while still not very complicated, eases the transition into 3-D space.

4.4.1 CuZn and its Band Structure

The first 3-D phase we discuss is CuZn, an ordering of β-brass that forms at high temperatures.[137] CuZn has the well-known CsCl-type structure—a cubic unit cell of edge length a, with an atom of one type at $(0, 0, 0)$ and an atom of the other type at $(\frac{a}{2}, \frac{a}{2}, \frac{a}{2})$. CuZn ($\beta$-brass) will serve as a stepping stone to the more complex Cu_5Zn_8 (γ-brass) and its relatives.

Taking the Cu and Zn 3*d* states to be filled core orbitals, CuZn has a valence electron count of $\frac{3}{2}$ electrons per atom. This electron count is common among CsCl-type intermetallic phases,[d] shared by LiHg, BeCu, MgAg, MgAu, ZnAg, ZnAu, CdAg, CdAu, AlPd, AlPt, and GaNi.[6] We wish to explore the evidence for a MJ-type driving force behind this electronic trend.

The validity of the MJ model rests on the validity of the nearly free-electron model. We therefore expect that a crystal structure amenable to the MJ model

[d] Valence electron counts of 1 and 2 electrons per atom are also fairly common among intermetallic CsCl-type phases, such as ZnNi and AlAu, respectively.

must have electronic states and energies resembling those of free electrons. Indeed CuZn does. The shapes of the free-electron (Fig. 4.5a) and LDA-DFT[43–47] (Fig. 4.5b) electronic bands bear a striking resemblance. With the exception of the localized Zn and Cu 3*d* bands centered at −8 eV and −4 eV in Fig. 4.5b, each band in the LDA-DFT band structure has a free-electron analog.

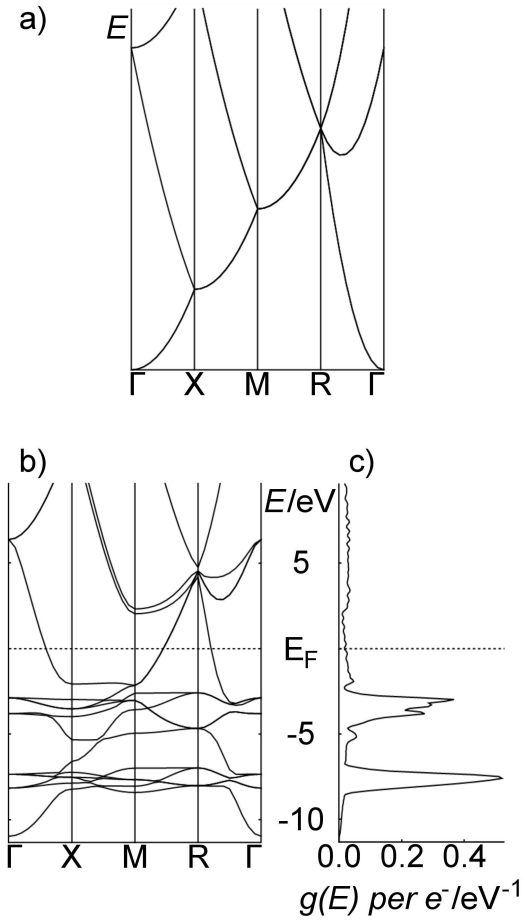

Figure 4.5: a) The free-electron band structure of CsCl-type CuZn, b) its LDA-DFT counterpart, and c) the LDA-DFT density of states. At *k*-point M, states that are degenerate in the free-electron picture become non-degenerate in LDA-DFT, which leads to a shallow pseudogap in the density of states near the Fermi energy. The *k*-points correspond to $\Gamma = (0,0,0)$, $X = (\frac{\pi}{a},0,0)$, $M = (\frac{\pi}{a},\frac{\pi}{a},0)$, and $R = (\frac{\pi}{a},\frac{\pi}{a},\frac{\pi}{a})$. On the energy axis of the LDA-DFT panels, the Fermi energy is defined as zero.

Of course, there are subtle differences between these two band structures. Most important to the discussion that follows is what occurs at k-point M = $(\frac{\pi}{a}, \frac{\pi}{a}, 0)$. In the free-electron band structure, the four lowest-energy electronic states at k-point M are degenerate. They correspond to four waves of equal wavelength: $\psi_{\mathrm{M}}(\vec{r}) = \frac{1}{\sqrt{V}} e^{i(\frac{\pi}{a}, \frac{\pi}{a}, 0)\cdot\vec{r}}$, $\psi_{\mathrm{M}}(\vec{r}) = \frac{1}{\sqrt{V}} e^{i(-\frac{\pi}{a}, -\frac{\pi}{a}, 0)\cdot\vec{r}}$, $\psi_{\mathrm{M}}(\vec{r}) = \frac{1}{\sqrt{V}} e^{i(-\frac{\pi}{a}, \frac{\pi}{a}, 0)\cdot\vec{r}}$, and $\psi_{\mathrm{M}}(\vec{r}) = \frac{1}{\sqrt{V}} e^{i(\frac{\pi}{a}, -\frac{\pi}{a}, 0)\cdot\vec{r}}$, where $\vec{r}$ is real-space position. In the LDA-DFT band structure, these states become two pairs, one degenerate and the other nearly degenerate. The pairs straddle the Fermi energy, and are separated by some 4 eV.

It is not a coincidence that the Fermi energy lies within this particular energy splitting. The splitting pushes states out of the energy region from about −2 eV to 2 eV, which translates to a shallow pseudogap in the density of states that reaches a minimum close to 2 eV (Fig. 4.5c). In the absence of a true energy gap, a compound is likely to adopt a structure that places its Fermi level in a pseudogap, as this one does. As we discuss in the next subsection, these observations of the CuZn band structure are consistent with the MJ model as traditionally implemented.

4.4.2 CuZn and the MJ Model

From our earlier discussion of the 1-D chain, recall that there are two related consequences of constructive interference between crystalline ions and plane waves. One is X-ray diffraction intensity, which emerges when atoms reside on parallel Miller planes. The other is the mixing and energy splitting of free-electron states. In Fig. 4.6, both phenomena are illustrated for CuZn.

The most intense X-ray diffraction peaks in CuZn are ⟨110⟩—the set of peaks

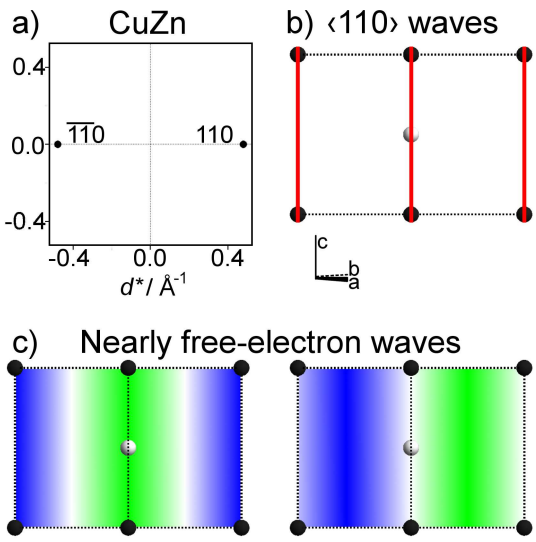

Figure 4.6: a) The strongest peaks in the $[1\bar{1}0]$ X-ray diffraction pattern of CuZn. b) Crests of the ⟨110⟩ diffraction plane waves (red), with all Cu (black) and Zn (gray) atoms lying on those crests. c) The nearly free-electron states whose periodicity syncs up with the ⟨110⟩ diffraction plane waves.

corresponding to waves that are symmetry-equivalent to $h = 1$, $k = 1$, $l = 0$ (Fig. 4.6a). The reason for the strength of these peaks can be seen pictorially in Fig. 4.6b, as all Cu (black) and Zn (gray) atoms in the structure lie on successive crests of the ⟨110⟩ diffraction plane waves (red). This arrangement of atoms on parallel planes has the additional consequence of causing free-electron states to mix (Fig. 4.6c). As shown, two free-electron states (with twice the wavelength of the ⟨110⟩ diffraction plane waves) mix to form one state whose electron density is near the ions (left), and a second state whose electron density is between the ions (right). Taking into account the potential of the ions, these two states split in energy.

To fully appreciate what the MJ model says about CuZn, consider where the states in Fig. 4.6c reside in the band structures in Fig. 4.5. These two states

are a mixture of the free-electron plane waves $\psi_{\mathrm{M}}(\vec{r}) = \frac{1}{\sqrt{V}} e^{i(\frac{\pi}{a},\frac{\pi}{a},0)\cdot\vec{r}} = \frac{1}{\sqrt{V}} e^{i\frac{\pi}{a}(x+y)}$ and $\psi_{\mathrm{M}}(\vec{r}) = \frac{1}{\sqrt{V}} e^{i(-\frac{\pi}{a},-\frac{\pi}{a},0)\cdot\vec{r}} = \frac{1}{\sqrt{V}} e^{-i\frac{\pi}{a}(x+y)}$, which are found at k-point M = $(\frac{\pi}{a}, \frac{\pi}{a}, 0)$ in the band structures. After mixing, these wavefunctions resemble $\Psi_{\mathrm{M}}(\vec{r}) = \frac{1}{\sqrt{2V}}(e^{i\frac{\pi}{a}(x+y)} + e^{-i\frac{\pi}{a}(x+y)}) = \sqrt{\frac{2}{V}} cos(\frac{\pi}{a}[x+y])$ (Fig. 4.6c, left) and $\Psi_{\mathrm{M}}(\vec{r}) = -\frac{i}{\sqrt{2V}}(e^{i\frac{\pi}{a}(x+y)} - e^{-i\frac{\pi}{a}(x+y)}) = \sqrt{\frac{2}{V}} sin(\frac{\pi}{a}[x+y])$ (Fig. 4.6c, right). Not shown in Fig. 4.6 are another pair of states, also at k-point M, corresponding to the $\bar{1}10$ diffraction plane wave. After mixing, they resemble the functions $\Psi_{\mathrm{M}}(\vec{r}) = \sqrt{\frac{2}{V}} cos(\frac{\pi}{a}[-x+y])$ and $\Psi_{\mathrm{M}}(\vec{r}) = \sqrt{\frac{2}{V}} sin(\frac{\pi}{a}[-x+y])$.

We can now rationalize our earlier observations of the band structure of CuZn (Fig. 4.5). At k-point M, four degenerate free-electron states ($\frac{1}{\sqrt{V}} e^{i\frac{\pi}{a}(x+y)}$, $\frac{1}{\sqrt{V}} e^{-i\frac{\pi}{a}(x+y)}$, $\frac{1}{\sqrt{V}} e^{i\frac{\pi}{a}(-x+y)}$, and $\frac{1}{\sqrt{V}} e^{-i\frac{\pi}{a}(-x+y)}$) mix to form four nearly free-electron states ($\sqrt{\frac{2}{V}} cos(\frac{\pi}{a}[x+y])$, $\sqrt{\frac{2}{V}} sin(\frac{\pi}{a}[x+y])$, $\sqrt{\frac{2}{V}} cos(\frac{\pi}{a}[-x+y])$, and $\sqrt{\frac{2}{V}} sin(\frac{\pi}{a}[-x+y])$). The latter four states come in two pairs, one of which has its electron density near the ions, and the other of which has its electron density between the ions. This leads to an energy splitting, made possible by the same arrangement of atoms on parallel planes that also results in strong ⟨110⟩ X-ray diffraction peaks. The energy splitting (Fig. 4.5b) in turn leads to the pseudogap (and stable valence electron count around $\frac{3}{2}$ electrons per atom) in Fig. 4.5c.

Before moving on, one more point should be clarified. In order to be formally correct about the mixing of these free-electron states ($\frac{1}{\sqrt{V}} e^{i\frac{\pi}{a}(x+y)}$, $\frac{1}{\sqrt{V}} e^{-i\frac{\pi}{a}(x+y)}$, $\frac{1}{\sqrt{V}} e^{i\frac{\pi}{a}(-x+y)}$, and $\frac{1}{\sqrt{V}} e^{-i\frac{\pi}{a}(-x+y)}$), one would have to consider all four to mix together, rather than pairwise. However, the pairwise mixing we have illustrated, in addition to being easier to visualize, is qualitatively accurate. Strong energy splitting of free-electron states can occur only when the states are separated by a reciprocal lattice vector corresponding to a significant Fourier component (i.e.,

a strong X-ray diffraction peak), as this creates states whose electron density is either near or between ions. Because CuZn has strong ⟨110⟩ peaks, the states corresponding to $(\frac{\pi}{a}, \frac{\pi}{a}, 0)$ and $(-\frac{\pi}{a}, -\frac{\pi}{a}, 0)$ mix strongly, as do those corresponding to $(-\frac{\pi}{a}, \frac{\pi}{a}, 0)$ and $(\frac{\pi}{a}, -\frac{\pi}{a}, 0)$. However, because the ⟨100⟩ peaks are nearly absent (they would be formally absent if Cu and Zn atoms were identical and/or randomly mixed in the structure), other pairs of these free-electron states do not mix strongly. Our pairwise picture is therefore qualitatively accurate for CuZn.

4.4.3 Ensuring the Applicability of the Extended Hückel Method to the CuZn Problem

The evidence in the previous subsection is all consistent with the MJ model for CuZn. However, all of the evidence is indirect. Without actually performing a calculation that allows us to look at the electronic states in CuZn, we cannot really prove that the splitting of free-electron waves is driving the stability of the valence electron count. The chemical reality of this system, as it turns out, is not quite as clean as the plane-wave story presented above.

In examining the electronic structure of CuZn more closely, we again employ eH theory. This method is both computationally cheap and chemically transparent, expressing crystalline electronic states as LCAOs whose energies are shaped by bonding and antibonding interactions. The drawback of eH is that, if one is not careful in choosing atomic parameters, the results of an eH calculation may bear little resemblance to more quantitatively reliable calculations. For this reason, we calibrate the eH parameters of Cu and Zn to match the LDA-DFT band structure of CuZn, using an automated optimization procedure

to find the best fit. This method has proven reliable in the past.[2,30,42,52–54]

The LDA-DFT and calibrated eH band structures of CuZn are superimposed in Fig. 4.7, with the Fermi energy defined as zero in both. For the bands that are filled, the calibrated eH bands (green) match their LDA-DFT counterparts (black) quite well. This suggests that these eH parameters represent the chemical reality of the system as accurately as possible. The calibrated atomic parameters for the Slater-type orbitals in this calculation are: H_{ii}(Cu 4s) = −11.63 eV, ζ_s = 1.80; H_{ii}(Cu 4p) = −5.72 eV, ζ_p = 1.625; H_{ii}(Cu 3d) = −11.94 eV, $\zeta_{1,d}$ = 6.93, $\zeta_{2,d}$ = 2.02, $c_{1,d}$ = 0.7234, $c_{2,d}$ = 0.7962; H_{ii}(Zn 4s) = −12.71 eV, ζ_s = 1.92; H_{ii}(Zn 4p) = −7.84 eV, ζ_p = 1.55; H_{ii}(Zn 3d) = −15.95 eV, $\zeta_{1,d}$ = 6.82, $\zeta_{2,d}$ = 2.26, $c_{1,d}$ = 0.7582, $c_{2,d}$ = 0.5730. These parameters will be used for the remainder of our discussion of CuZn.

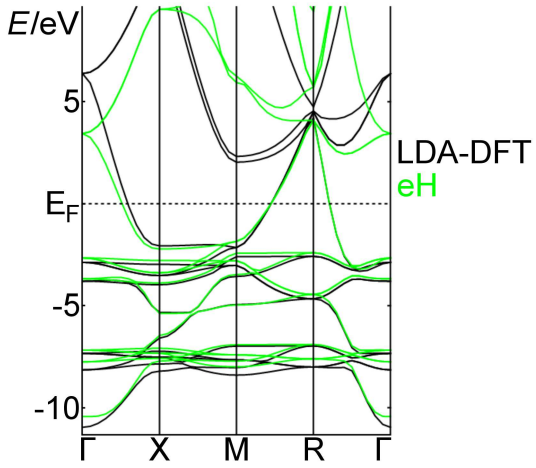

Figure 4.7: The band structure of CuZn, calculated using LDA-DFT methods (black) and eH methods with atomic parameters calibrated to the LDA-DFT band structure (green). For bands that are filled, the energies calculated by the two methods are quite close. For both methods, the Fermi energy is defined as zero.

4.4.4 Finding Hidden Plane Waves in CuZn

Armed with a quantitatively accurate band structure calculation that allows us to view the electronic states of CuZn as linear combinations of atomic orbitals, we are ready to search for the wavelike electronic states on which the MJ model focuses. In the earlier case of the 1-D chain, comparison between the nearly free-electron (Fig. 4.2) and eH (Fig. 4.3) band structures was straightforward because each individual eH crystal orbital had an obvious wave analog. The case is not quite so simple for real 3-D structures. Each nearly free-electron wavelike state, rather than having a single eH crystal orbital analog, is mixed into many eH states. If we wish to use an eH calculation to confirm, rather than simply infer, the validity of the MJ model for real chemical structures, we must develop a strategy to break down an eH band structure into its relevant plane waves. We do so in this subsection.

The difference between nearly free-electron and eH electronic states is largely a matter a basis set—the former are sums of plane waves, while the latter are sums of atomic valence orbitals. In principle, the two basis sets can be interconverted. That is, plane waves can be expressed as sums of valence orbitals, and vice versa. Our strategy is outlined as follows: (1) express the states in a nearly free-electron MJ band as sums of eH crystal orbitals, (2) assign energies to those nearly free-electron states as weighted averages of the eH energies, and (3) plot the energy of the MJ band hidden within the structure. In this way, we can start with a complicated eH band structure, and tease out the information relevant to the MJ model.

Free-electron plane-wave states have the form $\psi_{\vec{k}}(\vec{r}) = \frac{1}{\sqrt{V}} e^{i\vec{k}\cdot\vec{r}}$. Nearly free-electron states $\Psi_{\vec{k}}(\vec{r})$ are mixtures of these plane waves. The translational sym-

metry of a crystal dictates that mixing can only occur between waves separated by a reciprocal lattice vector $\vec{G}$:

$$\Psi_{\vec{k}}(\vec{r}) = \frac{1}{\sqrt{V}} \sum_{\vec{G}} c_{\vec{G},\vec{k}} e^{i(\vec{k}+\vec{G})\cdot\vec{r}}.$$

The $c_{\vec{G},\vec{k}}$ are complex coefficients of each component of the nearly free-electron state. As the nearly free-electron model requires that deviation from free-electron states is small, the dominant component of each state (i.e., the one with the largest magnitude $c_{\vec{G},\vec{k}}$) is the one corresponding to $\vec{G} = (0, 0, 0)$.

Each normalized nearly free-electron state $\Psi_{\vec{k}}(\vec{r})$ is then expressed, as accurately as possible,[e] as a linear combination of the full set of normalized eH wavefunctions $\Phi_{i,\vec{k}}(\vec{r})$ at the same *k*-point:

$$\Psi_{\vec{k}}(\vec{r}) = \sum_{i} p_{i,\vec{k}} \Phi_{i,\vec{k}}(\vec{r}).$$

The coefficients p_i in the above equation are projections of the nearly free-electron state onto each eH wavefunction:

$$p_{i,\vec{k}} = \int_{\text{unit cell}} \Psi_{\vec{k}}(\vec{r}) \Phi^{*}_{i,\vec{k}}(\vec{r})\, dV.$$

In the second step of the process, an energy $\varepsilon(\vec{k})$ is assigned to each nearly free-electron state $\Psi_{\vec{k}}(\vec{r})$. The energy is taken to be the weighted average of the energies $\epsilon_{i,\vec{k}}$ of the constituent eH crystal orbitals:

$$\varepsilon(\vec{k}) = \frac{\sum_i \epsilon_{i,\vec{k}} \left| p_{i,\vec{k}} \right|^2}{\sum_i \left| p_{i,\vec{k}} \right|^2}.$$

[e] Strictly speaking, sums of plane waves cannot be *exactly* expressed as sums of valence orbitals because a finite basis of valence orbitals does not span the function space.

The final step is to plot the energy of the projected MJ band. Recalling that the significant feature of this plot (an energy splitting that corresponds to the strong ⟨110⟩ X-ray diffraction peaks) is expected at k-point M $= (\frac{\pi}{a}, \frac{\pi}{a}, 0)$, this plot is constructed along a straight path from $\vec{k} = (0,0,0)$ through $\vec{k} = (\frac{\pi}{a}, \frac{\pi}{a}, 0)$. However, we must first take a brief step back and explain how the coefficients $c_{\vec{G},\vec{k}}$ are determined.

In principle, each nearly free-electron state $\Psi_{\vec{k}}(\vec{r})$ is the sum of an infinite number of plane-wave terms. Fortunately, very few of these terms make a significant contribution. A plane wave whose reciprocal lattice vector $\vec{G}$ corresponds to an intense X-ray diffraction peak mixes strongly into the sum only if its energy is similar to that of the dominant $\vec{G} = (0,0,0)$ term—that is, if $\left|\vec{k} + \vec{G}\right| \approx \left|\vec{k}\right|$. For most of our path through k-space—all but a small range close to $\vec{k} = (\frac{\pi}{a}, \frac{\pi}{a}, 0)$—there is no term close in energy to the $\vec{G} = (0,0,0)$ term. Thus, far from $\vec{k} = (\frac{\pi}{a}, \frac{\pi}{a}, 0)$, the nearly free-electron states approach $\Psi_{\vec{r}}(\vec{r}) = \frac{1}{\sqrt{V}} e^{i\vec{k}\cdot\vec{r}}$.

The situation is different close to $\vec{k} = (\frac{\pi}{a}, \frac{\pi}{a}, 0)$. The $\vec{G} = (0,0,0)$ and $\vec{G} = (-\frac{2\pi}{a}, -\frac{2\pi}{a}, 0)$ terms become close in energy, which means the nearly free-electron states must be expressed as $\Psi_{\vec{k}}(\vec{r}) = \frac{1}{\sqrt{V}}(c_1 e^{i\vec{k}\cdot\vec{r}} + c_2 e^{i(\vec{k}+(-\frac{2\pi}{a}, -\frac{2\pi}{a}, 0))\cdot\vec{r}})$. On the "near" side of $\vec{k} = (\frac{\pi}{a}, \frac{\pi}{a}, 0)$ (at $\vec{k} = (0.99\frac{\pi}{a}, 0.99\frac{\pi}{a}, 0)$, say), the $\vec{G} = (-\frac{2\pi}{a}, -\frac{2\pi}{a}, 0)$ term is higher in energy than the dominant term. We therefore expect this mixing to push the state to a lower energy, and we choose the c_1 and c_2 that result in the lowest energy. On the "far" side of $\vec{k} = (\frac{\pi}{a}, \frac{\pi}{a}, 0)$ (at $\vec{k} = (1.01\frac{\pi}{a}, 1.01\frac{\pi}{a}, 0)$, say), the reverse is true. The $\vec{G} = (-\frac{2\pi}{a}, -\frac{2\pi}{a}, 0)$ term is lower in energy than the dominant term, and pushes the state up in energy. We choose the c_1 and c_2 that result in the highest energy.

In Fig. 4.8a, the projected MJ band (red) is plotted on top of the calibrated

eH band structure (black), with a satisfying result. The MJ band resembles a nearly free-electron parabola, with an energy splitting of 2.74 eV at M = $(\frac{\pi}{a}, \frac{\pi}{a}, 0)$, the *k*-point corresponding to the strong ⟨110⟩ X-ray diffraction peaks. The two projected states at M (red circles at −1.80 eV and 0.94 eV) straddle the Fermi energy, further suggesting that the splitting does indeed help to stabilize CuZn at $\frac{3}{2}$ valence electrons per atom.

These two projected states at M are shown in Fig. 4.8b,c as contours of their component *s* and *p* atomic orbitals.[f] Both states resemble their nearly free-electron wave analogs, shown lightly in the background. The higher-energy state (Fig. 4.8b) is primarily a nonbonding combination of *s* orbitals, and the lower-energy state (Fig. 4.8c) a bonding combination of *p* orbitals. This ordering is representative of the inverted region as defined earlier. Though the ordering could have been reversed for different atomic or unit cell parameters, the energy splitting in the projected band would have been present regardless.

4.4.5 Energy Splitting at Other *k*-Points in CuZn

While the projected band, its energy splitting, and its wavelike eH states in Fig. 4.8 further support the MJ view of CuZn, they should still be met with a healthy dose of skepticism. One shortcoming of the argument presented in the previous subsection is that it examines the energy splitting of the projected MJ band at only one *k*-point, M = $(\frac{\pi}{a}, \frac{\pi}{a}, 0)$. If such splittings were found only at individual isolated *k*-points, then they would lead to a negligible pseudogap in the density of states. In order to argue that such splittings lead to a substantial

[f] Because the basis functions of an eH calculation are Slater-type atomic orbitals, they lack the radial nodes one would find in a true 4*s* or 4*p* state.

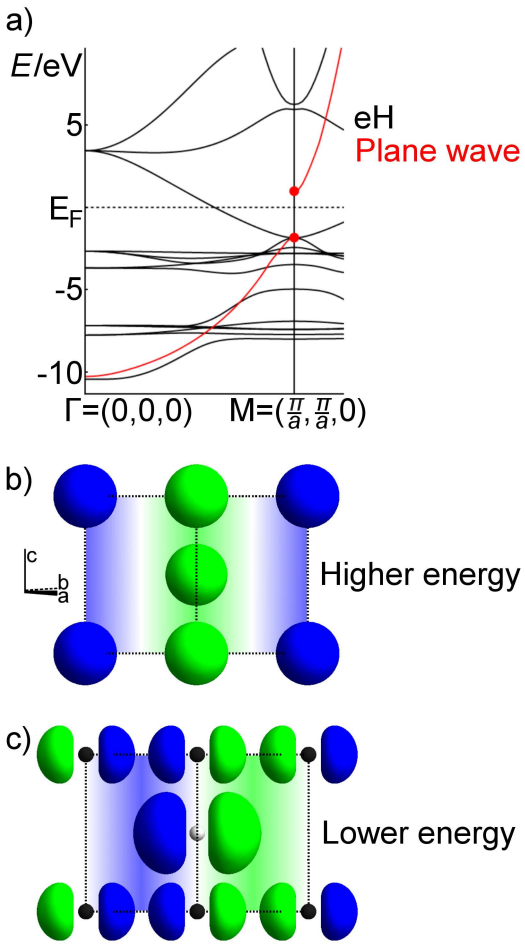

Figure 4.8: a) The calibrated eH band structure of CuZn (black) and the projected nearly free-electron MJ band (red), plotted along a straight path through k-space from $\Gamma = (0, 0, 0)$ through M = $(\frac{\pi}{a}, \frac{\pi}{a}, 0)$. b,c) The two projected crystal orbitals at M, expressed as contours of their component s and p atomic orbitals, with the corresponding nearly free-electron waves shown lightly in the background. The energies of these two states straddle the Fermi energy.

pseudogap, we must show that they occur at a continuum of k-points.

At which k-points should we expect to find these energy splittings? Recall that in order for two plane-wave electronic states $\psi_{\vec{k_1}}(\vec{r}) = \frac{1}{\sqrt{V}} e^{i\vec{k_1}\cdot\vec{r}}$ and $\psi_{\vec{k_2}}(\vec{r}) = \frac{1}{\sqrt{V}} e^{i\vec{k_2}\cdot\vec{r}}$ to mix and split, they must be separated by a reciprocal lattice vector $\vec{G}$ and be of equal energy. In symbols, these two conditions become:

$$\vec{k_1} + \vec{G} = \vec{k_2},$$

$$\left|\vec{k_1}\right| = \left|\vec{k_2}\right|.$$

In order for the resulting energy splitting to be large, there is the additional requirement that $\vec{G}$ correspond to a strong X-ray diffraction peak. As the strongest peaks for CuZn are $\langle 110 \rangle$, $\vec{G}$ can be any permutation of $\pm\frac{2\pi}{a}$, $\pm\frac{2\pi}{a}$, and 0. This ensures that once $\psi_{\vec{k_1}}(\vec{r})$ and $\psi_{\vec{k_2}}(\vec{r})$ mix, one wavefunction has its electron density concentrated near the ions, and the other between the ions.

Certainly, $\vec{k_1} = (\frac{\pi}{a}, \frac{\pi}{a}, 0)$ and $\vec{k_2} = (-\frac{\pi}{a}, -\frac{\pi}{a}, 0)$ satisfy these conditions. These vectors represent the two waves whose splitting is shown in Fig. 4.8. However, the coordinates of $\vec{k_1}$ and $\vec{k_2}$ need not be such round numbers. Consider the more general vectors $\vec{k_1} = (\frac{\pi}{a} + \alpha, \frac{\pi}{a} - \alpha, \beta)$ and $\vec{k_2} = (-\frac{\pi}{a} + \alpha, -\frac{\pi}{a} - \alpha, \beta)$, for any values of α and β. They too satisfy all of the above conditions for large energy splitting. The two degrees of freedom, α and β, indicate that *splitting occurs not just at isolated k-points, but on 2-D planes of k-points*.

In the reciprocal space of CuZn, there are twelve planes that satisfy the conditions for large energy splitting. These planes intersect to form the polyhedron in Fig. 4.9a. To a first approximation, this polyhedron can be used to estimate the likely electron count for β-brass alloys and CsCl-type intermetallics. The nearly

free-electron states $\Psi_{\vec{k}}(\vec{r})$ inside the polyhedron lie below the energy splitting and are filled, while those outside the polyhedron lie above the energy splitting and are empty. The reciprocal-space volume of the polyhedron thus represents the number of filled valence orbitals per unit cell. The volume in this case is $2(\frac{2\pi}{a})^3$, or 2 unit cells of the reciprocal lattice. This translates to 2 filled valence orbitals per unit cell, or 4 valence electrons per unit cell, or 2 valence electrons per atom.

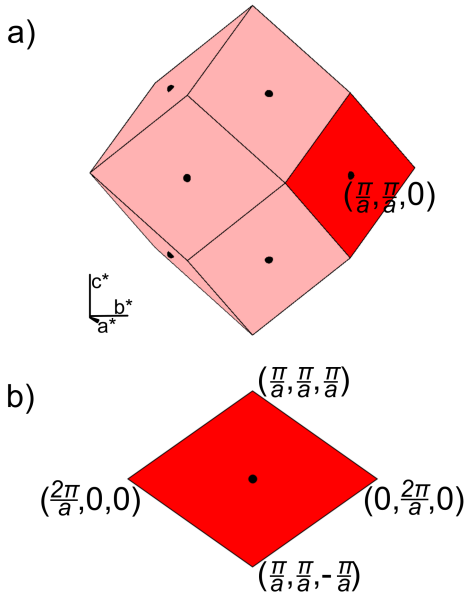

Figure 4.9: a) The reciprocal-space polyhedron that separates the CuZn nearly free-electron states that are above the energy splitting (outside the polyhedron) from those that are below it (inside the polyhedron). b) One face of the polyhedron, symmetry-equivalent to all the others.

While this estimate is in the right ballpark (though a bit higher than Hume-Rothery's observation of $\frac{3}{2}$ valence electrons per atom for β-brass), the argument used to derive it has a notable flaw. Namely, the surface in Fig. 4.9a is not a sphere. It has some points that jut out farther from the origin than others. Because the energy of a plane-wave electronic state is proportional to $\left|\vec{k}\right|^2$, splitting

occurs at a higher energy for those k-points that are farther out. It is therefore possible that the top of the splitting at (for example) $\vec{k} = (\frac{\pi}{a}, \frac{\pi}{a}, 0)$ is lower in energy than the bottom of the splitting at (for example) $\vec{k} = (\frac{2\pi}{a}, 0, 0)$. This possibility must be explored, as it would argue against the above assumption that states are filled if and only if they lie inside the polyhedron.

We therefore calculate the energies at the top and bottom of the splitting over the entire polyhedral surface. Only one of the twelve symmetry-equivalent faces (Fig. 4.9b) need be calculated. The result is shown in Fig. 4.10a. As expected, the energy curves of both the top (gray) and bottom (black) of the splitting resemble paraboloids with respect to $\vec{k}$. We see that our concern was justified—the top of the splitting at $\vec{k} = (\frac{\pi}{a}, \frac{\pi}{a}, 0)$ is indeed lower in energy than the bottom of the splitting at $\vec{k} = (\frac{2\pi}{a}, 0, 0)$. As a result, the Fermi energy (red) cannot lie within the gap for all k-points on the polyhedral surface simultaneously.

In the absence of a true energy gap between the top and bottom paraboloids in Fig. 4.10a, the Fermi energy is likely to be found in a pseudogap. One might reasonably guess that such a pseudogap would be centered at an energy that lies within the splitting for most of the polyhedral surface. Translated into the language of Fig. 4.10a, the "ideal" number of electrons for this system would place the Fermi energy (red plane) between the gray and black paraboloids for as much of the illustrated area of reciprocal space as possible. By inspection, this is accomplished when the Fermi energy just touches the bottom of the gray paraboloid, 0.94 eV above the actual Fermi energy. This estimate is confirmed in Fig. 4.10b. Integrating the density of states up to this energy predicts that the "ideal" electron count for CuZn is 1.77 valence electrons per atom.

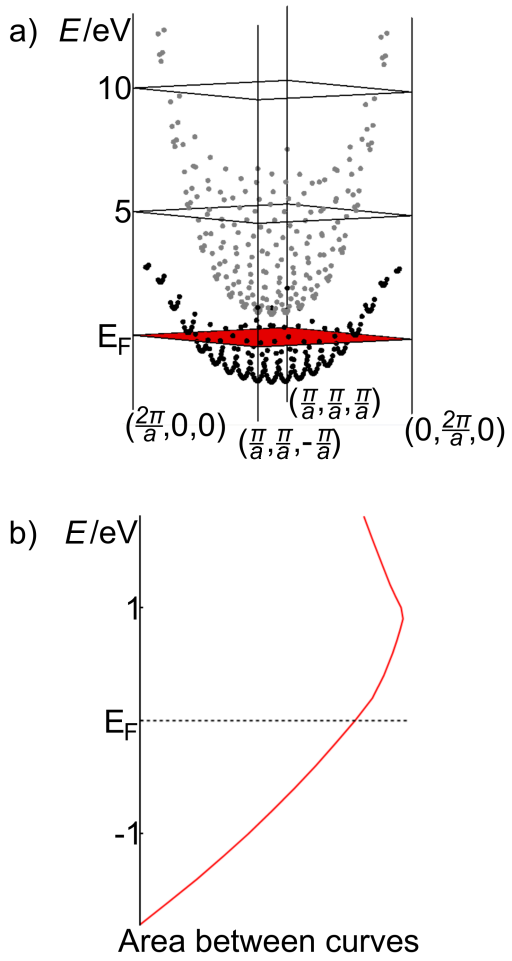

Figure 4.10: a) The energies at the top (gray) and bottom (black) of the splitting on one polyhedral face. b) The area on the polyhedral face for which a given energy lies between the two paraboloids. Area is plotted in arbitrary units.

Of course, there are several caveats to the electron count at which the previous paragraph arrives. The first is that our definition of "ideal" says little of how well the structure competes with others. Whether a structure forms at a given electron count depends not only on its own electronic properties, but on those of all competing structures. So even if CsCl-type CuZn has a pseudogap that favors 1.77 valence electrons per atom, it might have to compete with other possible structures that favor the same electron count. Second, the exact place-

ment of this "ideal" electron count is not general for CsCl-type compounds, and depends on the atomic and unit cell parameters. For example, if the energy splitting in Fig. 4.10a were wider, the "ideal" electron counts would move closer to 2. The third caveat is that the pseudogap in CuZn is not very deep. Because the reciprocal-space polyhedron (Fig. 4.9a) has vertices that jut out sharply, the top and bottom of the energy splitting (Fig. 4.10a) are not fully separated.

This concludes our discussion of CuZn, with reasonable results but an interesting and real ambiguity. We have adapted the MJ model to chemical ways of looking at the electronic structure of extended systems, and confirmed the observed range of stability between 1 and 2 valence electrons per atom in β-brass alloys and CsCl-type intermetallics. However, it emerges that for this particular structure, the "ideal" electron count is imprecise and element-dependent. As the remainder of this work will show, increasing complexity can actually sharpen an intermetallic structure's preference for a particular electron count.

4.5 Crystal Structures of the γ-Brasses

At a slightly higher Zn concentration than β-brass lies γ-brass. The γ-brass region of the Cu–Zn phase diagram includes the ordered intermetallic Cu_5Zn_8.[10] Taking the Cu and Zn 3*d* states to be filled core orbitals, Cu_5Zn_8 has a valence electron count of $\frac{21}{13}$ electrons per atom. Cu_5Zn_8 has a considerably more complex structure than CuZn. Crystallizing with $I\bar{4}3m$ symmetry, the cubic unit cell of Cu_5Zn_8 is traditionally seen as a body-centered arrangement of two identical 26-atom clusters. These clusters, termed γ-brass clusters, are in no way chemically isolated, and "exist" only as visual mnemonics.

A γ-brass cluster can be viewed in a number of ways. Perhaps the most common view (Fig. 4.11a) is of four nested polyhedra, one for each crystallographically inequivalent site. From the cluster center to the periphery, these polyhedra are an inner tetrahedron (IT), an outer tetrahedron (OT), an octahedron (OH), and a cubo-octahedron (CO). An alternative view (Fig. 4.11b), more suggestive of the experimental site preferences, connects the OT and OH sites (Cu atoms in Cu_5Zn_8) as an adamantane-like cage, and the IT and CO sites (Zn atoms in Cu_5Zn_8) as a tetrahedron of tetrahedra.[29,30] The full 52-atom cubic unit cell of Cu_5Zn_8 is shown in Fig. 4.11c.

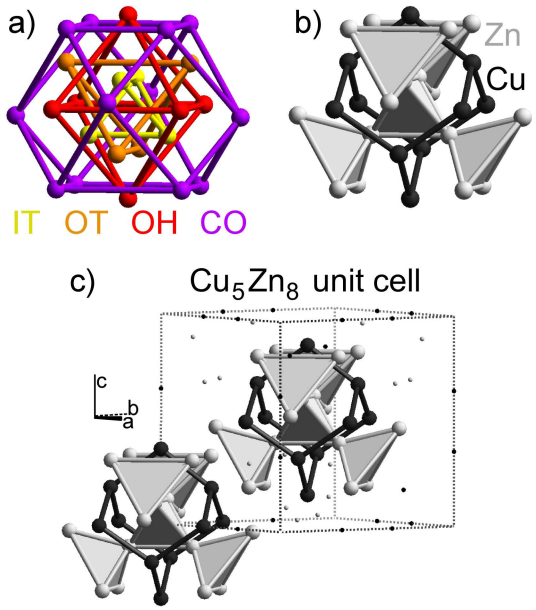

Figure 4.11: a) One view of a γ-brass cluster, showing an inner tetrahedron (IT, yellow), an outer tetrahedron (OT, orange), an octahedron (OH, red), and a cubo-octahedron (CO, purple). b) A second view, more suggestive of the site preferences in Cu_5Zn_8, showing an adamantane-like cage (Cu atoms, black) and a tetrahedron of tetrahedra (Zn atoms, gray). c) The cubic unit cell of Cu_5Zn_8, emphasizing its body-centered arrangement of γ-brass clusters.

Cu_5Zn_8 is the parent structure of a number of even more complicated

superstructures, which we call $2 \times 2 \times 2$ γ-brasses. As suggested by the name, these compounds have cubic unit cells that resemble the Cu_5Zn_8 unit cell doubled in all three dimensions. Each of these superstructures differs from Cu_5Zn_8 by some combination of distortions, colorings, vacancies, and interstitial atoms. Among the $2 \times 2 \times 2$ γ-brasses that have been solved using single crystal X-ray diffraction are $Zn_{21}Pt_5$,[23,24] $Li_{21}Si_5$,[17,18] $Mg_{44}Rh_7$,[7] $Mg_{44}Ir_7$,[71] Na_6Tl,[8] Mg_6Pd,[12] $Cu_{41}Sn_{11}$,[13,14] $Sm_{11}Cd_{45}$,[15] $Zn_{39}Fe_{11}$,[16] $Al_{69}Ta_{39}$,[20] $Zn_{13}(Fe, Ni)_2$,[19] $Mg_{29}Ir_4$,[21] $Zn_{20.44}Mo$,[22] $Zn_{91}Ir_{11}$,[28] and $Li_{13}Na_{29}Ba_{19}$.[26] All of these structures crystallize with $F\bar{4}3m$ symmetry. As the Cu_5Zn_8 unit cell contains two γ-brass clusters, and its superstructures represent a doubling of the unit cell in all three dimensions, each unit cell contains sixteen similar clusters, and roughly 400 atoms.

We wish to use MJ reasoning as the starting point for our analysis of the γ-brasses. This requires knowledge of which X-ray diffraction peaks are most intense. The strongest peaks in Cu_5Zn_8 are $\langle 330 \rangle$ and $\langle 114 \rangle$ (Fig. 4.12a). While the relative intensities vary from system to system, the strongest peaks in $2 \times 2 \times 2$ γ-brasses are generally $\langle 660 \rangle$, $\langle 228 \rangle$, and $\langle 555 \rangle$ (Fig. 4.12b). There is an interesting story to be told about the structural source of these strongest X-ray peaks. However, to avoid interrupting this work with a lengthy diversion, we simply take these diffraction patterns as given for now, and save the story for Appendix A of this thesis.

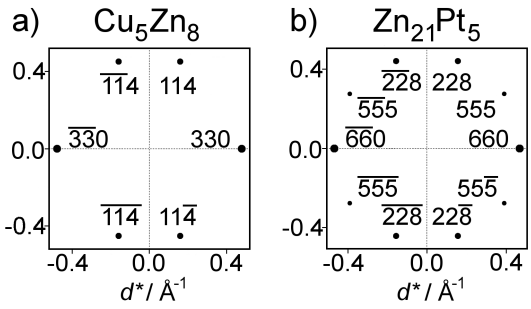

Figure 4.12: The strongest peaks in the $[1\bar{1}0]$ X-ray diffraction patterns of a) Cu_5Zn_8 and b) $Zn_{21}Pt_5$, a $2 \times 2 \times 2$ γ-brass.

4.6 Reinterpreting the MJ Model of Cu_5Zn_8

The MJ model has long been the dominant theoretical rationale for Hume-Rothery's empirical observations of the phase stability of γ-brass. According to the model, the alignment of atoms with $\langle 330 \rangle$ and $\langle 114 \rangle$ plane waves splits the energies of the corresponding nearly free-electron states. Together, the energy splittings create a pseudogap in the density of states, stabilizing the crystal structure for a narrow range surrounding the experimental electron count of Cu_5Zn_8, $\frac{21}{13}$ valence electrons per atom. To gain a more chemical understanding of this electron-counting rule, we now use the machinery developed in our earlier discussion of CuZn to reinterpret the MJ arguments for Cu_5Zn_8 in terms of LCAOs.

4.6.1 The Band Structure of Cu_5Zn_8

MJ reasoning rests on the nearly free-electron model. As Cu_5Zn_8 has proven amenable to the MJ model, we expect its band structure to resemble that of free electrons. The resemblance, however, is more difficult to confirm by inspection

for Cu_5Zn_8 (Fig. 4.13) than it was for CuZn (Fig. 4.5). The 26-atom primitive unit cell of Cu_5Zn_8 produces quite a complicated picture, in which it is somewhat difficult to pick out the individual parabolas. With some effort, though, one can see similarities in the shapes of the free-electron (Fig. 4.13a) and LDA-DFT[43–47] (Fig. 4.13b) bands, especially below the Fermi energy. Excluding the regions of localized Zn and Cu 3*d* bands centered at −8 eV and −4 eV, each band in the LDA-DFT band structure has a free-electron analog.

The density of states of Cu_5Zn_8 (Fig. 4.13c) shows the hallmark of an electron phase: a pseudogap very close to the Fermi energy. This pseudogap, centered just above the Fermi energy, is more pronounced than the corresponding pseudogap in CuZn (Fig. 4.5c).

In order to examine the source of this pseudogap and its relative sharpness, we again turn to eH theory. To ensure the quantitative accuracy of our eH calculation of Cu_5Zn_8, we calibrate the Cu and Zn atomic parameters to match LDA-DFT. These two band structures are superimposed in Fig. 4.14, with the Fermi energy defined as zero in both. The close match between calibrated eH (green) and LDA-DFT (black) suggests that these eH parameters accurately represent the chemical reality of the system. The calibrated atomic parameters for the Slater-type orbitals in this calculation are: H_{ii}(Cu 4*s*) = −11.47 eV, ζ_s = 1.75; H_{ii}(Cu 4*p*) = −5.55 eV, ζ_p = 1.69; H_{ii}(Cu 3*d*) = −11.95 eV, $\zeta_{1,d}$ = 6.09, $\zeta_{2,d}$ = 2.00, $c_{1,d}$ = 0.6006, $c_{2,d}$ = 0.6873; H_{ii}(Zn 4*s*) = −12.57 eV, ζ_s = 1.88; H_{ii}(Zn 4*p*) = −7.53 eV, ζ_p = 1.48; H_{ii}(Zn 3*d*) = −16.02 eV, $\zeta_{1,d}$ = 6.04, $\zeta_{2,d}$ = 2.21, $c_{1,d}$ = 0.6161, $c_{2,d}$ = 0.5730. Not surprisingly, these parameters, which will be used for the remainder of our discussion of Cu_5Zn_8, are very similar to those used for CuZn.

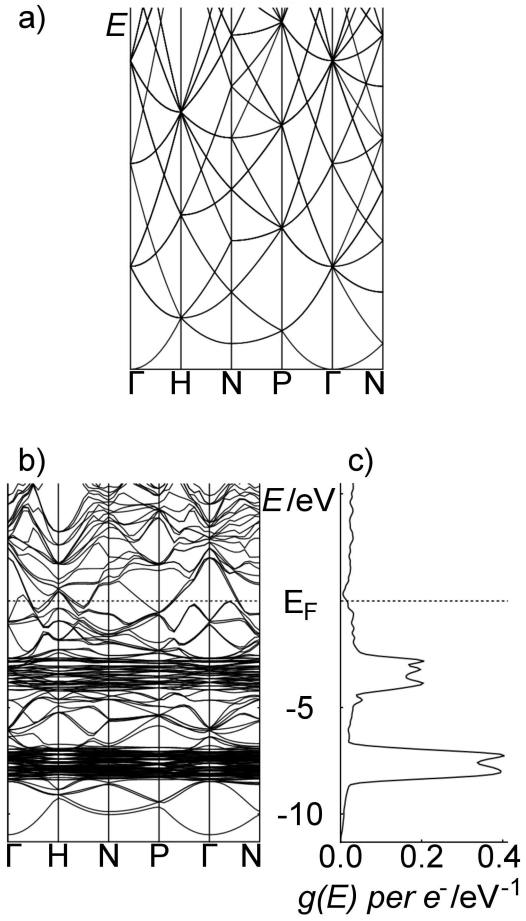

Figure 4.13: a) The free-electron band structure of Cu_5Zn_8, b) its LDA-DFT counterpart, and c) the LDA-DFT density of states. Note the pseudogap in the density of states near the Fermi energy. The *k*-points with respect to the cubic cell correspond to $\Gamma = (0,0,0)$, $H = (\frac{2\pi}{a},0,0)$, $N = (\frac{\pi}{a},\frac{\pi}{a},0)$, and $P = (\frac{\pi}{a},\frac{\pi}{a},\frac{\pi}{a})$. On the energy axis of the LDA-DFT panels, the Fermi energy is defined as zero.

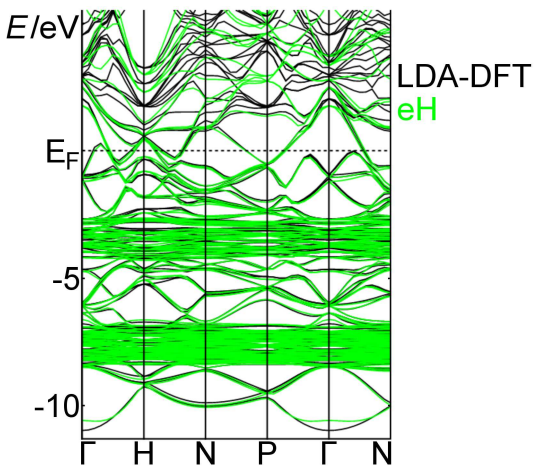

Figure 4.14: The band structure of Cu_5Zn_8, calculated using LDA-DFT methods (black) and eH methods with atomic parameters calibrated to the LDA-DFT band structure (green). For bands that are filled, the energies calculated by the two methods are quite close. For both methods, the Fermi energy is defined as zero.

4.6.2 Finding Hidden Plane Waves in Cu_5Zn_8

The strength of the ⟨330⟩ and ⟨114⟩ X-ray diffraction peaks indicates that the atoms in Cu_5Zn_8 sync up with the corresponding sets of Miller planes. According to the MJ model, this periodic arrangement of ions causes free-electron plane-wave electronic states (with twice the wavelength of the diffraction plane waves) to mix and split in energy. The result, as we saw in our earlier discussion of CuZn, is pairs of nearly free-electron states in which one has its electron density near the ions, and the other between the ions.

Though the atoms in Cu_5Zn_8 are not as neatly aligned on diffraction planes as those in CuZn, the expected wavelike states (Fig. 4.15) are qualitatively the same. Fig. 4.15a shows a mixing representative of the ⟨330⟩ X-ray diffraction peaks. These two states are a mixture of the plane waves $\psi_N(\vec{r}) = \frac{1}{\sqrt{V}} e^{i(\frac{3\pi}{a}, \frac{3\pi}{a}, 0)\cdot\vec{r}} =$

$\frac{1}{\sqrt{V}}e^{i\frac{3\pi}{a}(x+y)}$ and $\psi_N(\vec{r}) = \frac{1}{\sqrt{V}}e^{i(-\frac{3\pi}{a},-\frac{3\pi}{a},0)\cdot\vec{r}} = e^{-i\frac{3\pi}{a}(x+y)}$, which are found at k-point N = $(\frac{\pi}{a}, \frac{\pi}{a}, 0)$ with respect to the cubic unit cell. After mixing, these wavefunctions resemble $\Psi_N(\vec{r}) = \frac{1}{\sqrt{2V}}(e^{i\frac{3\pi}{a}(x+y)} + e^{-i\frac{3\pi}{a}(x+y)}) = \sqrt{\frac{2}{V}}cos(\frac{3\pi}{a}[x+y])$ (Fig. 4.15a, left) and $\Psi_N(\vec{r}) = -\frac{i}{\sqrt{2V}}(e^{i\frac{3\pi}{a}(x+y)} - e^{-i\frac{3\pi}{a}(x+y)}) = \sqrt{\frac{2}{V}}sin(\frac{3\pi}{a}[x+y])$ (Fig. 4.15a, right). The former has its electron density near most of the ions, the latter between most of the ions. Corresponding to each pair of peaks in the ⟨330⟩ set is a similar pair of states.

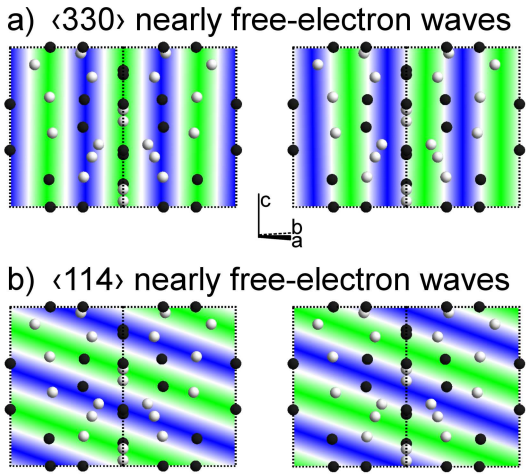

Figure 4.15: The nearly free-electron states whose periodicity syncs up with the a) ⟨330⟩ and b) ⟨114⟩ diffraction plane waves of Cu_5Zn_8. Cu (black) and Zn (gray) atoms are shown.

A mixing representative of the ⟨114⟩ diffraction peaks is shown in Fig. 4.15b. The pair of free-electron states that mix to produce these pictures are $\psi_N(\vec{r}) = \frac{1}{\sqrt{V}}e^{i(\frac{\pi}{a},\frac{\pi}{a},\frac{4\pi}{a})\cdot\vec{r}} = \frac{1}{\sqrt{V}}e^{i\frac{\pi}{a}(x+y+4z)}$ and $\psi_N(\vec{r}) = \frac{1}{\sqrt{V}}e^{i(-\frac{\pi}{a},-\frac{\pi}{a},-\frac{4\pi}{a})\cdot\vec{r}} = \frac{1}{\sqrt{V}}e^{-i\frac{\pi}{a}(x+y+4z)}$, which are again found at k-point N = $(\frac{\pi}{a}, \frac{\pi}{a}, 0)$. There is a subtle difference between the mixing shown in Fig. 4.15b and the previous cases. Namely, the resulting cosine and sine waves are not aligned with the origin of the unit cell. That is, these mixed states resemble $\Psi_N(\vec{r}) = \sqrt{\frac{2}{V}}cos(\frac{\pi}{a}[x+y+4z]+\alpha)$ and $\psi_N(\vec{r}) = \sqrt{\frac{2}{V}}sin(\frac{\pi}{a}[x+y+4z]+\alpha)$ with some phase factor α. This phase factor is needed to produce the same qualitative picture as before: one state whose electron density is near

most of the ions (Fig. 4.15b, left), and a second whose electron density is between most of the ions (Fig. 4.15b, right).

Before proceeding to find these nearly free-electron states within the eH band structure of Cu_5Zn_8, we should make one more point about these states. The reader might notice that all waves in Fig. 4.15, whether they correspond to the $\langle 330 \rangle$ or $\langle 114 \rangle$ diffraction peaks, appear to have the same wavelength. This is indeed true, for the basic reason that $\left|\vec{k}\right|$ is inversely proportional to wavelength, and $|(3,3,0)| = |(1,1,4)|$. Because the energy of a plane-wave electronic state is proportional to $\left|\vec{k}\right|^2$, equal wavelengths translate to equal energies. It is vital to the MJ model that all waves that mix to produce Fig. 4.15 have the same energy. In this way, when mixing causes their energies to split, they contribute to a pseudogap at a single energy.

While the premise and implementation of the MJ model for the γ-brasses are beautiful, we ask this: Does the model alone confirm, to the satisfaction of a typical chemist, that the nearly free-electron states in Fig. 4.15 drive the stability of the Cu_5Zn_8 valence electron count? Probably not. To most chemists, it is important to see how this theoretical framework plays out within a quantum calculation of Cu_5Zn_8. For this, we employ the same procedure we used earlier for CuZn to extract the relevant MJ states and energies from the complex tangle that is the eH band structure of Cu_5Zn_8.

Fig. 4.16 summarizes our LCAO interpretation of the MJ model as it relates to the $\langle 330 \rangle$ X-ray diffraction peaks in Cu_5Zn_8. In Fig. 4.16a, the projected MJ band (red) is plotted on top of the calibrated eH band structure (black) along a straight path from $\vec{k} = (0,0,0)$ through $\vec{k} = (\frac{3\pi}{a}, \frac{3\pi}{a}, 0)$. The MJ band resembles a nearly free-electron parabola. Due to the mixing of plane waves, the band

has energy splittings at N = $(\frac{\pi}{a}, \frac{\pi}{a}, 0)$, Γ = $(\frac{2\pi}{a}, \frac{2\pi}{a}, 0)$, and N = $(\frac{3\pi}{a}, \frac{3\pi}{a}, 0)$ (the waves corresponding to the ⟨110⟩, ⟨220⟩, and ⟨330⟩ peaks). However, because the atoms in Cu_5Zn_8 do not interfere particularly constructively with the ⟨110⟩ or ⟨220⟩ diffraction plane waves, the energy splittings at N = $(\frac{\pi}{a}, \frac{\pi}{a}, 0)$ (0.15 eV) and Γ = $(\frac{2\pi}{a}, \frac{2\pi}{a}, 0)$ (0.21 eV) are quite small. Due to the strong constructive interference of the atoms with the ⟨330⟩ diffraction plane waves, the splitting at N = $(\frac{3\pi}{a}, \frac{3\pi}{a}, 0)$ (2.37 eV) is much larger. Also encouraging is that fact that the two projected states at this last *k*-point (red circles at −1.76 eV and 0.60 eV) straddle the Fermi energy, and thus help stabilize Cu_5Zn_8 at $\frac{21}{13}$ valence electrons per atom.

The two projected states at N = $(\frac{3\pi}{a}, \frac{3\pi}{a}, 0)$ are displayed in Fig. 4.16b,c. For ease of plotting, they are shown in a slightly different way than were the projected states in CuZn (Fig. 4.8b,c). The component *s* and *p* orbitals on each atom that make up the projected states are shown not as contours of constant value of the wavefunction, but as pairs of spheres whose volumes scale with the coefficients of the atomic orbitals. If the orbital on a given atom is purely *s*, it appears as a single sphere. If it is purely *p*, it appears as two spheres of equal size and opposite sign. If it is a mixture of *s* and *p*, is appears as two spheres of unequal size and opposite sign, skewed toward the sign of the *s* orbital. These two states resemble their nearly free-electron wave analogs, shown lightly in the background. As was the case for CuZn, the higher-energy state (Fig. 4.16b) is primarily a combination of *s* orbitals, and the lower-energy state (Fig. 4.16c) a combination of *p* orbitals. This ordering is again representative of the inverted region.

In Fig. 4.17, we move on to the states corresponding to the ⟨114⟩ diffraction peaks in Cu_5Zn_8. The story here is more or less the same as it was for the ⟨330⟩

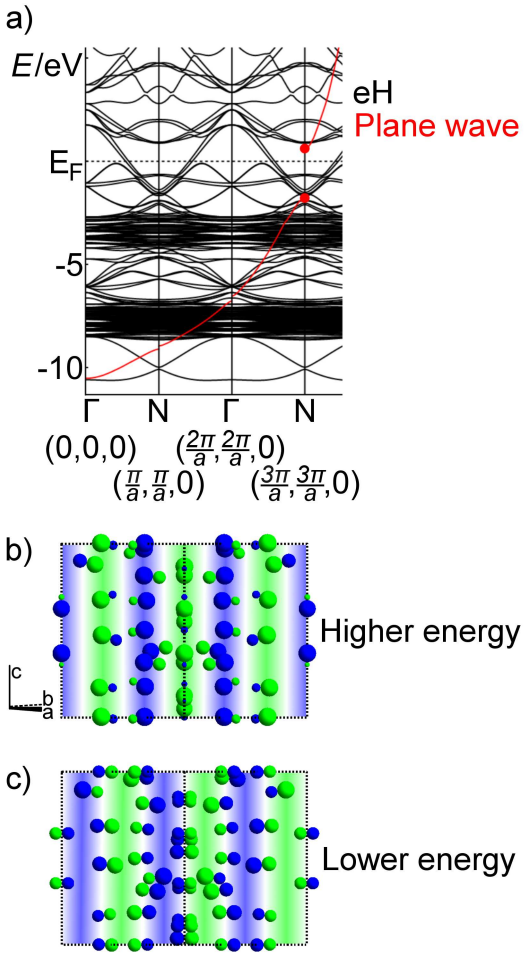

Figure 4.16: a) The calibrated eH band structure of Cu_5Zn_8 (black) and the projected nearly free-electron MJ band (red), plotted along a straight path through *k*-space from $\Gamma = (0,0,0)$ through $N = (\frac{3\pi}{a}, \frac{3\pi}{a}, 0)$. b,c) The two projected crystal orbitals at $N = (\frac{3\pi}{a}, \frac{3\pi}{a}, 0)$, expressed as spheres which represent their component *s* and *p* atomic orbitals (see text), with the corresponding nearly free-electron waves shown lightly in the background. The energies of these two states straddle the Fermi energy.

peaks. The projected MJ band (Fig. 4.17a), when plotted along a straight path from $\vec{k} = (0, 0, 0)$ through $\vec{k} = (\frac{\pi}{a}, \frac{\pi}{a}, \frac{4\pi}{a})$, resembles a nearly free-electron parabola. The band splits by 1.03 eV at N = $(\frac{\pi}{a}, \frac{\pi}{a}, \frac{4\pi}{a})$, only about half the size of the splitting corresponding to the ⟨330⟩ peaks. This is to be expected, as the ⟨114⟩ peaks in Cu_5Zn_8 are less intense than ⟨330⟩. The two projected states at the top and bottom of this splitting are shown in Fig. 4.17b,c. They again resemble their free-electron wave analogs, with the higher-energy state (Fig. 4.17b) consisting primarily of *s*, and the lower-energy state (Fig. 4.17c) consisting primarily of *p*. This ordering is again in the inverted region.

However, there is one significant way in which Fig. 4.17 differs from Fig. 4.16. Namely, the two projected states at N = $(\frac{\pi}{a}, \frac{\pi}{a}, \frac{4\pi}{a})$ (red circles in Fig. 4.17a at −1.59 eV and −0.56 eV) both lie below the Fermi energy. This seems at first to be a strike against the MJ model or our interpretation of it, as it suggests that the energy splitting at this *k*-point does not stabilize Cu_5Zn_8 at its experimental electron count. But as the next subsection explains, this result need not be seen as problematic at all.

4.6.3 Energy Splitting at Other *k*-Points in Cu_5Zn_8

We showed earlier that MJ-type energy splitting occurs not just at isolated *k*-points, but on the surface of a reciprocal-space polyhedron. Because CuZn had only the strong ⟨110⟩ diffraction peaks corresponding to states near the Fermi energy, its polyhedron in Fig. 4.9a had only one type of face. Cu_5Zn_8, however, has strong ⟨330⟩ and strong ⟨114⟩ peaks. Its reciprocal-space polyhedron is therefore bounded by two symmetry-inequivalent types of faces.

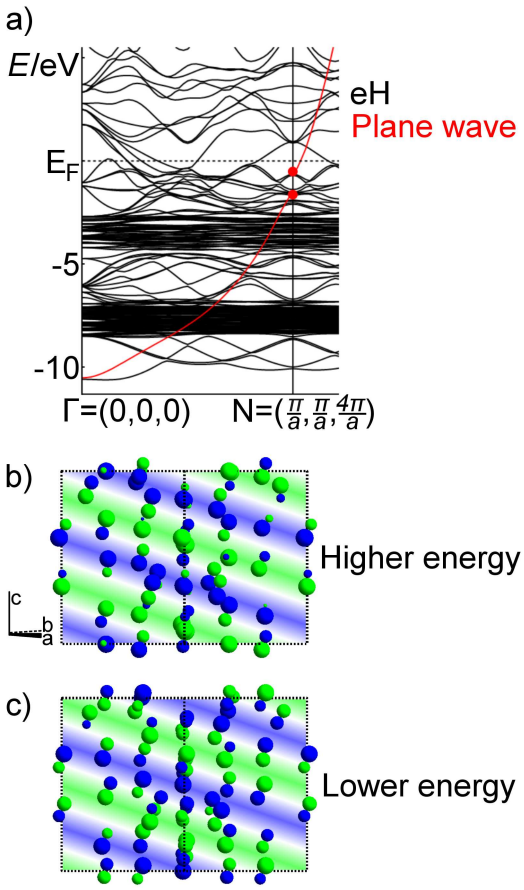

Figure 4.17: a) The calibrated eH band structure of Cu_5Zn_8 (black) and the projected nearly free-electron MJ band (red), plotted along a straight path through k-space from $\Gamma = (0,0,0)$ through $N = (\frac{\pi}{a}, \frac{\pi}{a}, \frac{4\pi}{a})$. b,c) The two projected crystal orbitals at $N = (\frac{\pi}{a}, \frac{\pi}{a}, \frac{4\pi}{a})$, expressed as spheres which represent their component s and p atomic orbitals (see text), with the corresponding nearly free-electron waves shown lightly in the background. The energies of both states lie below the Fermi energy.

The Cu_5Zn_8 polyhedron (Fig. 4.18a) is shown with one of each type of face emphasized (Fig. 4.18b). The twelve red faces correspond to the ⟨330⟩ reflections, while the twenty-four blue faces correspond to ⟨114⟩. One notable qualitative feature of this Cu_5Zn_8 polyhedron is that it is much closer to spherical that its CuZn counterpart. Due to its larger number of faces, the vertices of the Cu_5Zn_8 polyhedron do not jut out as much. The result is that the energy splitting on the surface of the polyhedron occurs over a narrower range of energies for Cu_5Zn_8 than for CuZn. This can be seen in the respective densities of states, in which the pseudogap is sharper and more pronounced for Cu_5Zn_8 (Fig. 4.13c) than for CuZn (Fig. 4.5c).

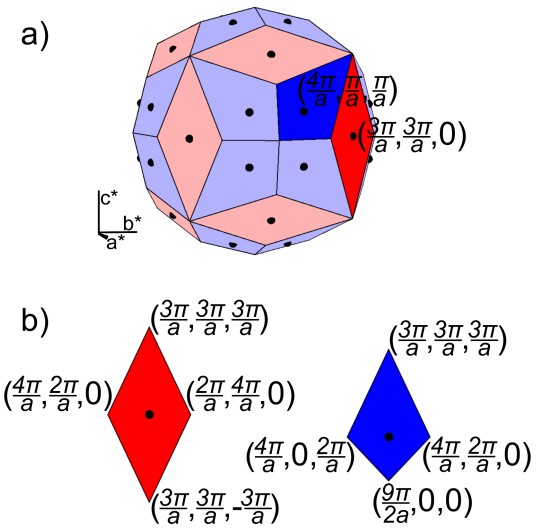

Figure 4.18: a) The reciprocal-space polyhedron that separates the Cu_5Zn_8 nearly free-electron states that are above the energy splitting (outside the polyhedron) from those that are below it (inside the polyhedron). b) One of each type of face of the polyhedron, corresponding to the ⟨330⟩ (left, red) and ⟨114⟩ (right, blue) X-ray diffraction peaks.

In order to estimate the number of valence electrons this system is likely to hold, one might first assume that all states inside the polyhedron (below the

energy splitting) are filled, and all those outside the polyhedron (above the energy splitting) are empty. If this is true, then the reciprocal-space volume of the polyhedron represents the number of filled valence orbitals per unit cell. The volume of this polyhedron is $45(\frac{2\pi}{a})^3$, or 45 unit cells of the reciprocal lattice. This translates to 90 valence electrons per unit cell, or 1.73 per atom—slightly higher than Hume-Rothery's empirical observations of the γ-brasses.

Once again, the assumption that all states at the bottom of the splitting are of lower energy than all states at the top of the splitting proves faulty. This is clear in Fig. 4.19, in which we plot the top (gray) and bottom (black) of the energy splitting over the polyhedral faces corresponding to the ⟨330⟩ (Fig. 4.19a) and ⟨114⟩ (Fig. 4.19b) reflections. Even with a reciprocal-space polyhedron that better approximates a sphere, there is still nowhere the Fermi energy can be placed such that it lies between the two paraboloids for all *k*-points simultaneously.

Because there is no true energy gap in the density of states of Cu_5Zn_8, the Fermi energy is likely to be found at a pseudogap. We expect such a pseudogap to be centered at an energy that lies within the splitting for most of the polyhedral surface. Inspection of the two different polyhedral surfaces individually would lead one to arrive at two different estimates of the Fermi energy. For the surface corresponding to ⟨330⟩ (Fig. 4.19a), it would be optimal to have the Fermi energy just touch the bottom of the gray paraboloid, 0.60 eV above the actual Fermi energy. For the surface corresponding to ⟨114⟩ (Fig. 4.19b), the bottom of the gray paraboloid is 0.56 eV below the actual Fermi energy. These estimates are confirmed in Fig. 4.20a, which shows the area on each polyhedral face for which a given energy lies between the upper and lower curves. Taking both types of faces into account, we expect the actual Fermi energy to lie between

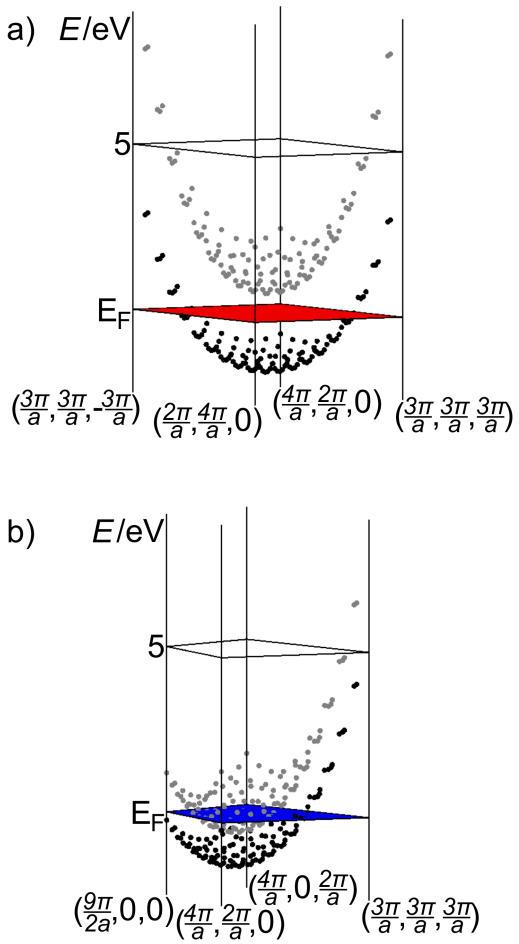

Figure 4.19: The energies at the top (gray) and bottom (black) of the splitting on the polyhedral faces of Cu_5Zn_8 corresponding to the a) ⟨330⟩ and b) ⟨114⟩ X-ray diffraction peaks. The Fermi energy (red and blue) lies between the paraboloids over much of the surfaces.

0.60 eV and −0.56 eV (1.68 and 1.49 valence electrons per atom, respectively)—a reassuring result.

It is difficult to pin down exactly where is this range the Fermi energy "should" lie for Cu_5Zn_8. One might make an estimate by finding the energy that maximizes the *total* polyhedral surface area that lies within the energy splitting. However, this estimate of the Fermi energy (Fig. 4.20b) does not differ sig-

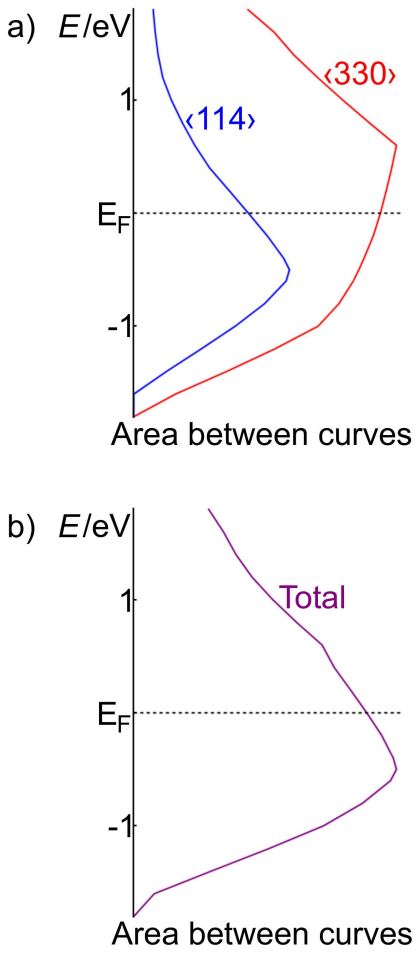

Figure 4.20: a) The area on the Cu_5Zn_8 polyhedral faces corresponding to ⟨330⟩ and ⟨114⟩ for which a given energy lies within the splitting. b) The area on the entire polyhedral surface for which a given energy lies within the splitting. Area is plotted in arbitrary units.

nificantly from the estimate obtained by considering only the ⟨114⟩ faces, and comes out on the low side of experimental reality. There are a number of ways in which this estimate is perhaps too simplistic, which are possible reasons for the discrepancy.

One possible oversimplification is in the way the energies on the polyhedral surface are calculated. As described earlier, the energies at the top and bottom

of the gap reflect a mixing of two plane waves found on opposite faces of the polyhedron. While these pairs of waves are indeed the primary contributors to MJ-type energy splitting, the splitting could be made more accurate by including the contributions of other terms as well. This could mean including waves that correspond to weaker, but still significant, X-ray diffraction peaks. It could also mean including extra terms for points near the edges and vertices of the polyhedron, corresponding to the neighboring faces that approach each other. By considering only the pairwise mixing of plane waves, we likely underestimate the energy splitting, especially near edges and vertices of the polyhedral surface.

A second possible oversimplification is in our use of polyhedral surface area to estimate the pseudogap energy. This method, to look for the energy at which the largest amount of surface area lies within the splitting, neglects a key fact. When plane-wave states mix and split in energy, they do not simply disappear. Rather, they are pushed to an energy outside the splitting—likely *just* outside the splitting. So in considering whether a given energy would be an energetically stable Fermi energy, we must not only consider it favorable for the energy to lie within the splitting, but also unfavorable for that energy to lie *just* outside the splitting.

One can imagine how our methods could be modified to account for each of these issues. To more accurately calculate the energies at the top and bottom of the gap, we could include more plane-wave terms in our mixing equations. To more correctly estimate the energy of the pseudogap, we could develop a slightly different method of counting surface area, in which area just outside the energy gap is disfavored. These (and possibly other) adjustments would

likely allow us to estimate valence electron counts and Fermi energies to greater numerical accuracy.

4.7 A Note About $2 \times 2 \times 2$ γ-Brasses

We hope the previous sections of this account have convinced the reader that there is chemical importance to the electronic states on which the MJ model focuses. Even if the model and our LCAO interpretation of it cannot yet predict stable electron counts as precisely or as unambiguously as we would hope, they appear to be meaningful and qualitatively correct.

We therefore have certain expectations of how the same line of reasoning is likely to turn out for the $2\times2\times2$ γ-brass superstructures. In the X-ray diffraction patterns of these compounds (Fig. 4.12b), we saw that in addition to the strong $\langle 660 \rangle$ and $\langle 228 \rangle$ peaks derived from γ-brass itself, there are strong $\langle 555 \rangle$ peaks. These new peaks indicate more opportunities for MJ-type mixing, each of which contributes to the pseudogap that stabilizes the compounds at a given valence electron count. Fig. 4.21 shows the reciprocal-space polyhedron that marks the energy gap in the $2 \times 2 \times 2$ γ-brasses (Fig. 4.21a). It consists of three symmetry-inequivalent types of faces (Fig. 4.21b): twelve faces corresponding to the $\langle 660 \rangle$ peaks (red), twenty-four faces corresponding to the $\langle 228 \rangle$ peaks (blue), and eight faces corresponding to the $\langle 555 \rangle$ peaks (green).

With its relatively large number of faces, the polyhedron representing the $2 \times 2 \times 2$ γ-brasses is quite nearly spherical. This should mean that the energy splitting occurs over a narrow range of energies, and that the pseudogap in the density of states is quite sharp and pronounced. One would expect the

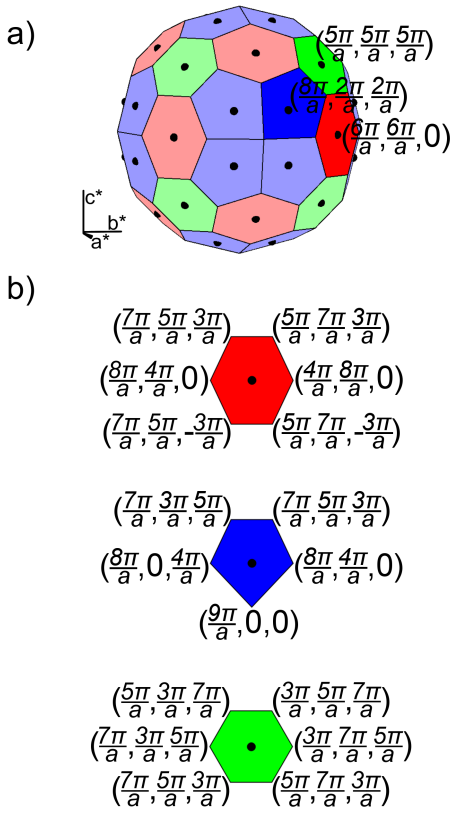

Figure 4.21: a) The reciprocal-space polyhedron that separates the $2\times2\times2$ γ-brass nearly free-electron states that are above the energy splitting (outside the polyhedron) from those that are below it (inside the polyhedron). b) One of each type of face of the polyhedron, corresponding to the $\langle 660\rangle$ (top, red), $\langle 228\rangle$ (middle, blue), and $\langle 555\rangle$ (bottom, green) X-ray diffraction peaks.

number of valence orbitals per unit cell with energies lower than this pseudogap to be roughly equal to the polyhedral volume. The volume of the polyhedron is $348(\frac{2\pi}{a})^3$, meaning the unit cell of 2×2×2 γ-brass holds 696 valence electrons. This is a reasonable estimate of the actual valence electron counts in many of the $2\times$ 2×2 γ-brasses: $Zn_{21}Pt_5$ (672 per unit cell, 1.62 per atom), $Li_{21}Si_5$ (656 per unit cell, 1.58 per atom), $Mg_{44}Rh_7$ (648 per unit cell, 1.59 per atom), $Mg_{44}Ir_7$ (648 per unit cell, 1.59 per atom), Mg_6Pd (679 per unit cell, 1.71 per atom), $Cu_{41}Sn_{11}$ (680 per unit cell, 1.63 per atom), $Mg_{29}Ir_4$ (648 per unit cell, 1.64 per atom), $Zn_{91}Ir_{11}$ (684

per unit cell, 1.68 per atom), and $Li_{13}Na_{29}Ba_{19}$ (640 per unit cell, 1.31 per atom). For technical reasons, it has proven difficult to extract precise information about the $2 \times 2 \times 2$ γ-brasses from a calibrated eH calculation. For now, our suggestion that the electron counts of these compounds are driven by the same factors that guide CuZn and Cu_5Zn_8 therefore remains an inference.

4.8 Conclusion

In this work, we have reviewed Mott and Jones's theoretical model for Hume-Rothery electron phases, casting it into real-space LCAO language. In doing so, we have shown that the hallmark of an electron phase—a pseudogap in the density of states at the Fermi energy—can be seen not only in terms of the mixing and splitting of plane-wave electronic states, but also in terms of the energy difference between an *s*-based band and a *p*-based band. This latter interpretation highlights the fundamental similarity between the Hume-Rothery rules in solids and the molecular electron-counting rules that are ingrained in the language and logic of chemists.

However, neither Mott and Jones's traditional model nor our LCAO interpretation of it does everything it sets out to do. That is to say, neither reproduces Hume-Rothery's electron-counting rules unambiguously or with much numerical precision. The likely reason for this is that both models focus on *pseudogap* energies of crystal structures, rather than their *total* energies. While related, it is only through a total energy comparison that one can determine which structure is favored over others at a given electron count.

We hope to achieve this goal—a rationale that accounts for the stability

ranges of the Hume-Rothery electron phases—in our future work. Our LCAO interpretation of Mott and Jones's arguments will likely be an integral part of such a rationale, as it has already been shown that Hückel theory is capable of correctly ordering the total energies of these structures.[126,127]

We do not wish to suggest that either the nearly free-electron or the LCAO viewpoint is superior. The two complement each other nicely, with the former focusing on the wavelike nature of the electronic states, and the latter on the bonding and antibonding interactions between atomic orbitals. The two viewpoints arrive at similar conclusions, and clash only in subtle ways. Each has its advantages, and each allows one to understand certain aspects of the electronic structure of these compounds more clearly.

4.9 Acknowledgment

Because the work in this chapter has not yet been published as of the printing of this thesis, it should be noted that the list of authors on any papers containing this work would include Robert F. Berger, Peter Walters, Stephen Lee, and Roald Hoffmann. In addition, we thank Prof. Neil Ashcroft for his careful reading of our work.

APPENDIX A

STRONG X-RAY DIFFRACTION PEAKS IN THE γ-BRASSES

This was a triumph
I'm making a note here: HUGE SUCCESS
It's hard to overstate my satisfaction.

—GLaDOS, "Still Alive" (Theme from *Portal*)[138]

The work described in this thesis aims to make sense of the crystal and electronic structures of complex intermetallic phases—in particular, γ-brass and its so-called $2 \times 2 \times 2$ superstructures. Throughout, single crystal X-ray diffraction proves a valuable tool, through its connections to both structural symmetry and valence electron count. The sets of strong X-ray diffraction peaks in these crystals are, in fact, invoked in every chapter of this thesis (Figs. 1.15, 2.3, 3.9, 4.12). For γ-brass, the dominant peaks are $\langle 330 \rangle$ and $\langle 114 \rangle$; for the $2 \times 2 \times 2$ superstructures, the are $\langle 660 \rangle$, $\langle 228 \rangle$, and $\langle 555 \rangle$. But we have yet to explore *why* this is so. We would like to identify, from a qualitative real-space standpoint, the source of these strong peaks.

These sets of strong diffraction peaks are similar to each other in that the γ-brass $\langle 330 \rangle$ and $\langle 114 \rangle$ peaks become $\langle 660 \rangle$ and $\langle 228 \rangle$ when the unit cell is doubled in all three dimensions. However, they differ in that the $\langle 555 \rangle$ peaks in the $2 \times 2 \times 2$ superstructures have no analog in γ-brass. In this Appendix, we therefore address two questions. First, what is the source of the strong $\langle 330 \rangle$ and $\langle 114 \rangle$ peaks in γ-brass? Second, what features of the transformation from γ-brass to the $2 \times 2 \times 2$ γ-brasses bring about the intense $\langle 555 \rangle$ peaks?

A.1 The ⟨330⟩ and ⟨114⟩ Peaks in γ-Brass

With practice, the human eye is quite good at judging which X-ray diffraction peaks are strong for a given crystal structure. A strong peak is one for which most of the atomic positions lie near the crests of the plane wave corresponding to that peak. So in order to find the strong peaks in the ordered γ-brass phase Cu_5Zn_8, we must identify the directions in which the atoms lie on parallel planes. While this task is not so simple for a unit cell with many atoms, it can certainly be done.

Recall that the Cu_5Zn_8 structure has a cubic unit cell with a body-centered arrangement of two 26-atom γ-brass clusters. One γ-brass cluster is shown in Fig. A.1a, as four nested polyhedra. In anticipation of the discussion that follows, the cluster is shown from a slightly different viewpoint in Fig. A.1b. When γ-brass clusters are placed in unit cells, the viewpoint in Fig. A.1b is generally oriented along a face diagonal of the cell. From now on, we will consider this view (i.e., the direction normal to the page in Fig. A.1b) to be along the $[1\bar{1}0]$ direction. In Fig. A.1c, the cluster is connected in a way that illustrates an approximate tenfold symmetry.[a] When shown with the viewpoint and connectivity of Fig. A.1c, the γ-brass cluster looks like a group of central atoms surrounded by a decagon and half of a second decagon.

The last five panels of this figure (Fig. A.1d-h) suggest five possible plane waves for which the cluster atoms lie mostly near the crests. In keeping with the approximate tenfold symmetry of the cluster, the directions of these plane waves differ by 36°. These waves, along with all other symmetry-equivalent

[a] While we do not dwell on it here, this pseudosymmetry is remarkable in its own right, and we have studied it in greater depth in the past.[56]

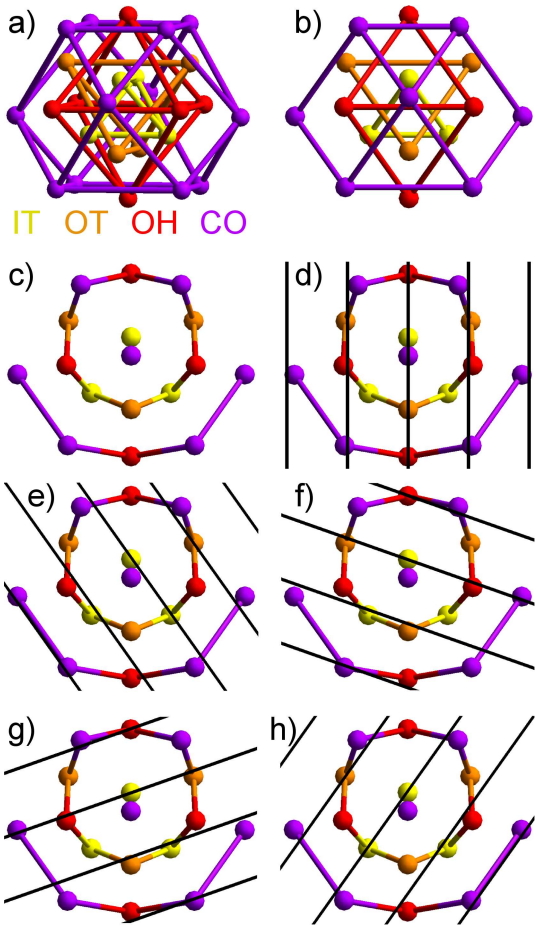

Figure A.1: a,b) Two views of a 26-atom γ-brass cluster, depicted as an inner tetrahedron (IT), an outer tetrahedron (OT), an octahedron (OH), and a cubo-octahedron (CO). c) An alternative connectivity of the cluster, highlighting its approximate tenfold symmetry. d-h) Five plane waves for which most of the cluster atoms lie near the crests.

ones, could potentially correspond to strong diffraction peaks in a crystal structure with γ-brass clusters. However, this figure alone cannot identify the strong X-ray peaks for Cu_5Zn_8. Because diffraction is measured not for a single cluster but for an entire crystal, we must observe how these plane waves interact with all clusters in the unit cell.

In keeping with its body-centered translational symmetry, the Cu_5Zn_8 struc-

ture has two γ-brass clusters centered at $(0,0,0)$ and $(\frac{a}{2},\frac{a}{2},\frac{a}{2})$ in the cubic unit cell (Fig. A.2a). For the five plane waves that sync up with the atoms of a single γ-brass cluster (Fig. A.1d-h), let us see how each wave interacts with the pair of clusters within a unit cell. In Fig. A.2b, the wave from Fig. A.1d is shown interacting with two clusters. The important result is that the wave's interactions with the two clusters are in phase with each other. That is, when the wave is positioned to have its crests aligned with the atoms in one cluster, its crests are consequently aligned with the atoms in the other cluster. Therefore, all γ-brass clusters in the Cu_5Zn_8 structure interfere constructively with this plane wave, resulting in a strong X-ray diffraction peak. As our view is in the $[1\bar{1}0]$ direction, this plane wave and this diffraction peak have Miller indices 330. By symmetry, the structure must have an entire set of twelve equally strong $\langle 330 \rangle$ peaks (all permutations of ± 3, ± 3, and 0).

By symmetry of the γ-brass clusters, the plane waves in Fig. A.1f,g are equivalent. We therefore show only one of them interacting with two clusters (Fig. A.2c). Once again, this wave's interactions with the two clusters are in phase, as the wave crests are aligned with the atoms in both clusters. Therefore, this plane wave, whose Miller indices are 114, corresponds to a strong X-ray diffraction peak. The entire set of twenty-four equivalent $\langle 114 \rangle$ peaks (all permutations of ± 1, ± 1, and ± 4) must be equally strong.

Lastly, we come to the two symmetry-equivalent plane waves in Fig. A.1e,h, one of which we show interacting with two clusters (Fig. A.2d). In contrast to the previous cases, this wave's interactions with the two clusters are not in phase. When the wave is positioned to have its crests aligned with the atoms in one cluster, its crests are not aligned with the atoms in the other. In other

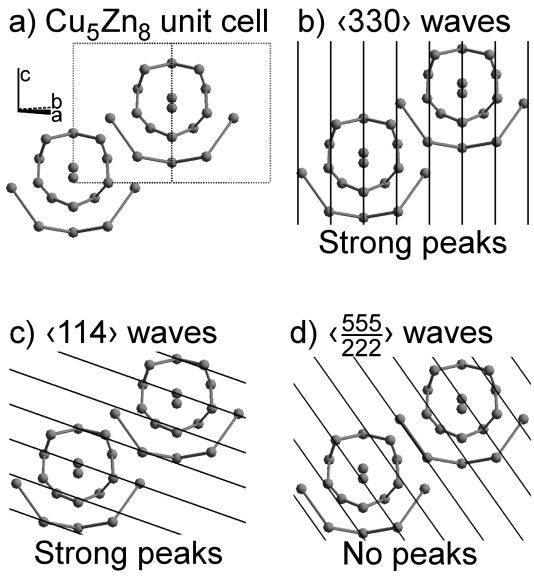

Figure A.2: a) The two γ-brass clusters in a cubic unit cell of Cu_5Zn_8. Representatives of the three unique sets of plane waves with constructive intracluster interference: b) $\langle 330 \rangle$, c) $\langle 114 \rangle$, and d) $\langle \frac{5}{2}\frac{5}{2}\frac{5}{2} \rangle$. Of the three, $\langle 330 \rangle$ and $\langle 114 \rangle$ also have constructive intercluster interference, and therefore strong X-ray diffraction peaks. However, $\langle \frac{5}{2}\frac{5}{2}\frac{5}{2} \rangle$ has destructive intercluster interference, and therefore no diffraction intensity.

words, while the wave's intracluster interference is constructive, its intercluster interference is destructive. Consequently, this plane wave, whose Miller indices are $\frac{5}{2}\frac{5}{2}\frac{5}{2}$, has no corresponding X-ray diffraction peak.[b]

Despite the relative complexity of the Cu_5Zn_8 structure, we have accounted for the dominant peaks in its X-ray diffraction pattern using real-space pictures. We now move on to the diffraction peaks of the significantly more complicated $2 \times 2 \times 2$ γ-brasses.

[b]Those familiar with diffraction theory will recognize that such a plane wave, with non-integer Miller indices, cannot have any diffraction intensity regardless of whether or not the cell is body-centered. No matter which way one thinks about it, the underlying reason for this lack of a diffraction peak is the same—this plane wave cannot simultaneously sync up with all γ-brass clusters in the Cu_5Zn_8 structure.

A.2 Cluster Inversion and the $\langle 555 \rangle$ Peaks in $2 \times 2 \times 2$ γ-Brasses

Of the $2 \times 2 \times 2$ γ-brass structures that have been solved by single crystal X-ray diffraction, $Zn_{21}Pt_5$[23,24] and $Li_{21}Si_5$[17,18] can be compared most easily to Cu_5Zn_8, as they are built entirely of γ-brass clusters. We therefore focus our attention on $Zn_{21}Pt_5$ and $Li_{21}Si_5$, though any discussion of these structures for the remainder of this Appendix relates to other superstructures as well.

$Zn_{21}Pt_5$ and $Li_{21}Si_5$, very nearly identical to each other with the exception of the elemental identities, crystallize with $F\bar{4}3m$ symmetry. As the Cu_5Zn_8 unit cell contains two γ-brass clusters, those of the $2 \times 2 \times 2$ γ-brasses contain sixteen such clusters, a total of 416 atoms. By face-centered translational symmetry, these sixteen clusters represent four crystallographically unique sets. One representative of each set in the unit cell of $Zn_{21}Pt_5$ is displayed in Fig. A.3. Using conventions we introduced in a previous paper,[2] we show the clusters centered at $(0, 0, 0)$, $(\frac{a}{4}, \frac{a}{4}, \frac{a}{4})$, $(\frac{a}{2}, \frac{a}{2}, \frac{a}{2})$, and $(\frac{3a}{4}, \frac{3a}{4}, \frac{3a}{4})$, and refer to them as Z (*z*ero), Q (*q*uarter), H (*h*alf), and T (*t*hree quarters).

$Zn_{21}Pt_5$ and $Li_{21}Si_5$ share two key structural features which distinguish them from Cu_5Zn_8. The first one, and the focus of this section, is that the H cluster distorts to the point that it is more accurately shown as inverted with respect to the other clusters. In Fig. A.4, the clusters of $2 \times 2 \times 2$ γ-brass are shown in two ways. Fig. A.4a is a simple doubling of the Cu_5Zn_8 unit cell in all three dimensions, with all clusters oriented exactly as they are in Cu_5Zn_8. The second panel (Fig. A.4b), which more accurately reflects the crystal structures of $Zn_{21}Pt_5$ and $Li_{21}Si_5$, shows the H cluster inverted with respect to the other three.

This H cluster inversion seems at first surprising and mysterious. Why

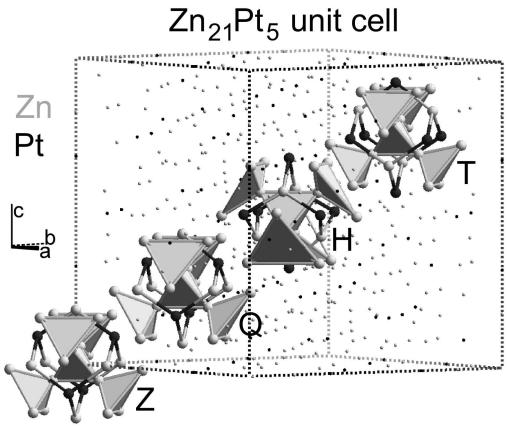

Figure A.3: The cubic unit cell of $Zn_{21}Pt_5$, emphasizing four crystallographically inequivalent γ-brass clusters centered at Z = $(0,0,0)$, Q = $(\frac{a}{4},\frac{a}{4},\frac{a}{4})$, H = $(\frac{a}{2},\frac{a}{2},\frac{a}{2})$, and T = $(\frac{3a}{4},\frac{3a}{4},\frac{3a}{4})$. The strongly distorted H cluster is shown in its more accurate inverted form. Pt atoms (black) occupy the ZOT, QOT, HOH, and TOH sites, while Zn atoms (gray) occupy the rest.

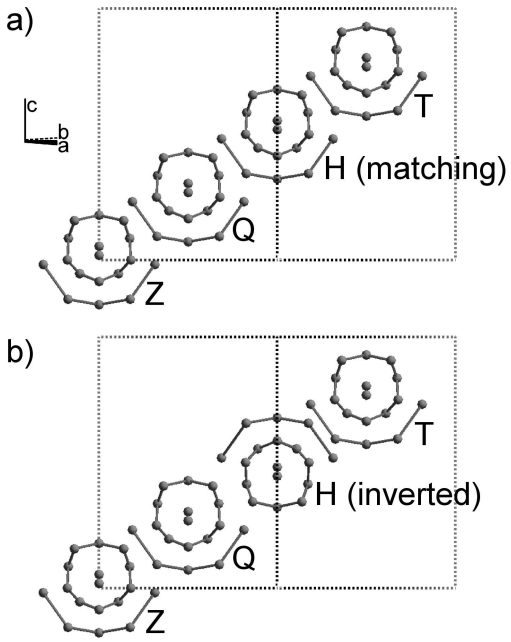

Figure A.4: The four crystallographically inequivalent clusters in a cubic unit cell of $2 \times 2 \times 2$ γ-brass, a) with all four clusters oriented identically and b) with the H cluster inverted with respect to the others.

would it stabilize the structures electronically? For the answer, we turn to the X-ray diffraction patterns. As the Mott and Jones model (see Chapter 4) dictates, the stability of electron phases is closely related to the strength of their diffraction peaks. Let us therefore examine the role inversion of the H cluster in creating strong ⟨660⟩, ⟨228⟩, and ⟨555⟩ peaks in the X-ray diffraction patterns of $Zn_{21}Pt_5$ and $Li_{21}Si_5$.

For Cu_5Zn_8, we have seen that the strongest peaks are ⟨330⟩ and ⟨114⟩. When the unit cell of Cu_5Zn_8 is doubled in all three dimensions without changing the atomic positions (Fig. A.4a), the diffraction intensities cannot change. Without inversion of the H cluster, we therefore expect $2 \times 2 \times 2$ γ-brass to have the same strong peaks as γ-brass itself. The labels of these peaks change, however, taking on the Miller indices ⟨660⟩ and ⟨228⟩ in the new unit cell. By recognizing that ⟨660⟩ and ⟨228⟩ are simply the strong peaks of Cu_5Zn_8, we are well on our way to understanding the diffraction patterns of $Zn_{21}Pt_5$ and $Li_{21}Si_5$. What remains is to explain how inversion of the H cluster allows the ⟨660⟩ and ⟨228⟩ to remain strong while also creating strong ⟨555⟩ peaks. We illustrate this in a series of three figures.

The first of these figures (Fig. A.5) deals with the ⟨660⟩ peaks. Regardless of whether all four γ-brass clusters have the same orientation (Fig. A.5a) or the H cluster is inverted (Fig. A.5b), all clusters interfere constructively with the ⟨660⟩ plane waves, resulting in strong ⟨660⟩ peaks. The same is true of the ⟨228⟩ peaks (Fig. A.6). When all four γ-brass clusters have the same orientation (Fig. A.6a), they all interfere constructively with the ⟨228⟩ plane waves. When the H cluster is inverted (Fig. A.6b), its atoms still sync up almost as well with the wave crests, allowing the ⟨228⟩ peaks to remain strong.

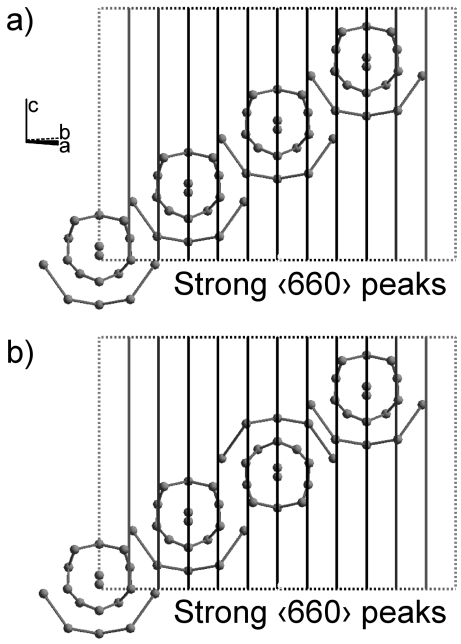

Figure A.5: Interaction between the four clusters in $2 \times 2 \times 2$ γ-brass and the $\langle 660 \rangle$ plane waves, a) with all four clusters oriented identically and b) with the H cluster inverted. In both cases, intra- and intercluster interference are constructive, leading to strong diffraction peaks.

Finally we come to the $\langle 555 \rangle$ peaks (Fig. A.7), the major distinguishing feature of $2 \times 2 \times 2$ γ-brass X-ray diffraction patterns as compared to γ-brass. When all four clusters are identical (Fig. A.7a), the $\langle 555 \rangle$ peaks have no intensity. This can be seen in the destructive intercluster interference with the $\langle 555 \rangle$ plane waves.[c] Take special note of the fact that the Z and H clusters cancel each other out by having most of the Z atoms near wave crests and most of the H atoms near wave troughs. Now, consider what happens when the H cluster is inverted (Fig. A.7b). The H cluster atoms now reside near wave crests, making the previously nonexistent $\langle 555 \rangle$ peaks relatively intense. The emergence of strong $\langle 555 \rangle$ peaks in $Zn_{21}Pt_5$ and $Li_{21}Si_5$ can thus be rationalized using the inversion of the

[c]For a more convincing argument that $\langle 555 \rangle$ can have no diffraction intensity when all clusters are identical, recall that Cu_5Zn_8 cannot have $\langle \frac{5}{2}\frac{5}{2}\frac{5}{2} \rangle$ peaks.

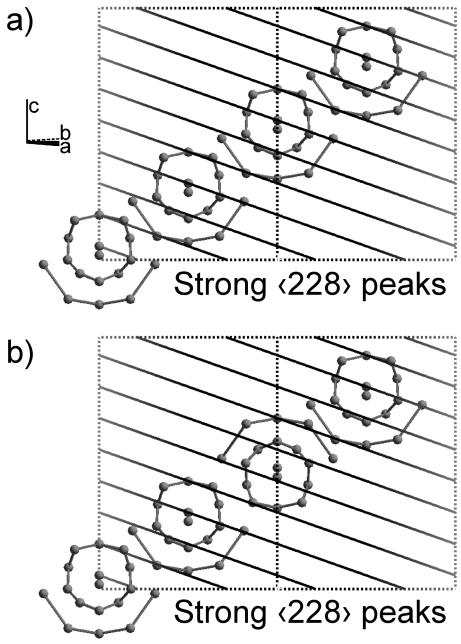

Figure A.6: Interaction between the four clusters in $2 \times 2 \times 2$ γ-brass and the $\langle 228 \rangle$ plane waves, a) with all four clusters oriented identically and b) with the H cluster inverted. In both cases, intra- and intercluster interference are constructive, leading to strong diffraction peaks.

H cluster.

A.3 The Role of Coloring in the Diffraction Patterns of $2 \times 2 \times 2$ γ-Brasses

So far, we have been concerned only with atomic positions, and not with which elements lie at which sites. We have implicitly assumed that all atoms scatter X-rays equally, which is of course not true. An atom's scattering factor is related to its number of electrons. So when a compound has two elements of very different numbers of electrons, as do $Zn_{21}Pt_5$ and $Li_{21}Si_5$, its X-ray diffraction

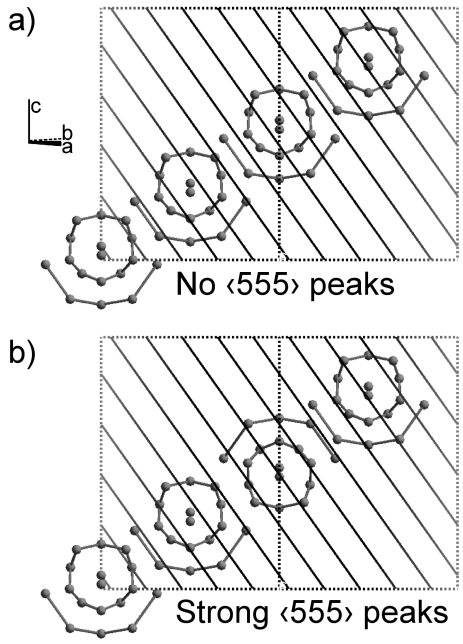

Figure A.7: Interaction between the four clusters in $2 \times 2 \times 2$ γ-brass and the $\langle 555 \rangle$ plane waves, a) with all four clusters oriented identically and b) with the H cluster inverted. While both pictures have good intracluster interference, only the second has the constructive intercluster interference required to create strong diffraction peaks.

pattern is strongly influenced by the site preferences of the constituent elements. Specifically, when one determines the strength of an X-ray peak by observing how well the atoms sync up with the peaks of a plane wave, one must consider the placement of heavier atoms to be more important.

This brings us to the second feature that distingishes $Zn_{21}Pt_5$ and $Li_{21}Si_5$ from Cu_5Zn_8. In both superstructures, the heavy element (i.e., Pt or Si) occupies four crytsallographic sites: the outer tetrahedron of the Z cluster (ZOT), the outer tetrahedron of the Q cluster (QOT), the octahedron of the H cluster (HOH), and the octahedron of the T cluster (TOH) (Fig. A.8a). As we will now see, these heavy atoms are positioned in such a way that they strengthen the

already strong ⟨660⟩, ⟨228⟩, and ⟨555⟩ diffraction peaks.

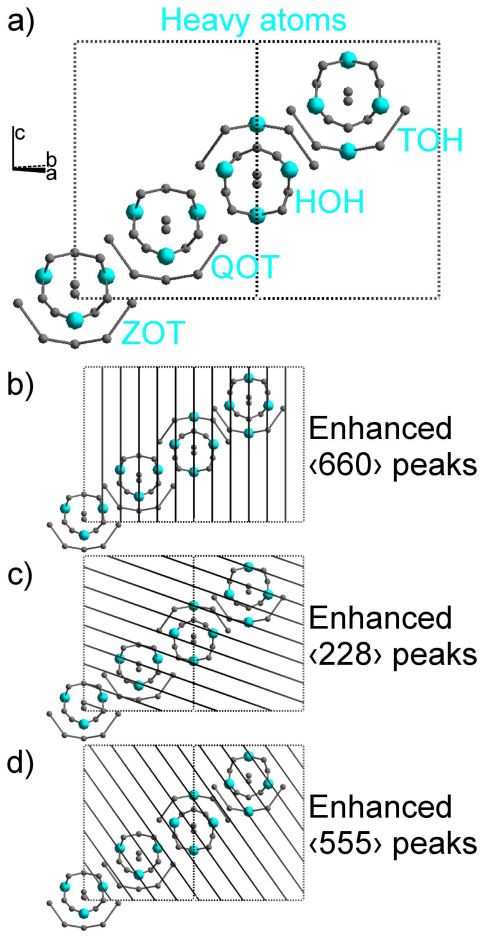

Figure A.8: a) The experimentally observed site positions of the heavier element in $Zn_{21}Pt_5$ and $Li_{21}Si_5$, shown in cyan. These four sites (ZOT, QOT, HOH, and TOH) align particularly well with the crests of the b) ⟨660⟩, c) ⟨228⟩, and d) ⟨555⟩ plane waves, strengthening the intensities of the corresponding X-ray diffraction peaks.

As Fig. A.8b shows, these four heavy atom sites are exceptionally in phase with the ⟨660⟩ plane waves, with every heavy atom lying almost exactly on a crest. Because heavy atoms have extra importance in determining the strength of diffraction peaks, we expect this pattern of site occupancy to strengthen the ⟨660⟩ peaks of $Zn_{21}Pt_5$ and $Li_{21}Si_5$. There is, however, a caveat to this conclu-

sion. Because the ⟨660⟩ plane waves interact equivalently with all four clusters, the peaks would be similarly enhanced if the heavy atoms were found on any combination of OT and OH sites. All the ⟨660⟩ peaks can tell us is that they are enhanced when the heavy atoms are found on OT and OH sites.

A similar story can be told of the ⟨228⟩ peaks (Fig. A.8c). As nearly all the heavy atoms in $Zn_{21}Pt_5$ and $Li_{21}Si_5$ are found very close to the crests of the ⟨228⟩ plane waves, we expect the ⟨228⟩ peaks to be strengthened. But once again, we should not read too much into this conclusion. Except for the H cluster (which is inverted), the ⟨228⟩ plane waves interact equivalently with all clusters. This means the ⟨228⟩ peaks would be enhanced by the placement of heavy atoms on any combination of OT and OH sites. The lone exception is that, due to the inversion of the H cluster, the placement of heavy atoms on HOT would interfere destructively with these waves. Indeed, heavy atoms are not found on HOT in $Zn_{21}Pt_5$ or $Li_{21}Si_5$.

As was the case for inversion of the H cluster, the strongest argument for the ZOT-QOT-HOH-TOH heavy atom occupancy pattern is in the ⟨555⟩ diffraction peaks. As Fig. A.8d shows, the heavy atoms line up well with the crests of the ⟨555⟩ plane waves, enhancing the ⟨555⟩ peaks. What is important here is that the ⟨555⟩ waves are in a slightly different phase with respect to each of the four clusters. While the OT atoms of the Z and Q clusters line up with the ⟨555⟩ wave crests, the OH atoms do not. And while the OH atoms of the H and T clusters line up with the ⟨555⟩ wave crests, the OT atoms do not. Therefore, the experimentally observed ZOT-QOT-HOH-TOH heavy atom occupancy pattern is the optimal one for enhancing the ⟨555⟩ peaks in $Zn_{21}Pt_5$ and $Li_{21}Si_5$.

We have shown in this Appendix, using real-space pictures, that the crystal

structures of γ-brasses are optimized to bring out the intensities of certain X-ray diffraction peaks. It might seem odd that crystal structures such as Cu_5Zn_8, $Zn_{21}Pt_5$, and $Li_{21}Si_5$, which are dictated by energetic stability, would go to such great lengths to create sets of intense diffraction peaks. The reasons for this are explored in the preceding chapters of this thesis.

REFERENCES

[1] A.C. Doyle. *The Adventures and Memoirs of Sherlock Holmes*. Modern Library, New York, NY, 2001.

[2] R.F. Berger, S. Lee, and R. Hoffmann. "A quantum mechanically guided view of $Mg_{44}Rh_7$". *Chem. Eur. J.*, 13:7852–7863, 2007.

[3] S. Samson. "Crystal structure of $NaCd_2$". *Nature*, 195:259–262, 1962.

[4] S. Samson. "The crystal structure of the phase β-Mg_2Al_3". *Acta Crystallogr.*, 19:401–413, 1965.

[5] S. Samson. "The crystal structure of the intermetallic compound Cu_4Cd_3". *Acta Crystallogr.*, 23:586–600, 1967.

[6] P. Villars and L.D. Calvert. *Pearson's Handbook of Crystallographic Data for Intermetallic Phases, 2nd Edition*. ASM International, Materials Park, OH, 1991.

[7] L. Westin. "Crystal structure of Rh_7Mg_{44}". *Chemica Scripta*, 1:127–135, 1971.

[8] S. Samson and D.A. Hansen. "Complex cubic A_6B compounds. I. The crystal structure of Na_6Tl". *Acta Crystallogr.*, B28:930–935, 1972.

[9] S. Andersson. "An alternative description of the structures of Rh_7Mg_{44} and Mg_6Pd". *Acta Crystallogr.*, A34:833–835, 1978.

[10] A. Bradley and P. Jones. "An X-ray investigation of the copper-aluminium alloys". *J. Inst. Met.*, 51:131–162, 1933.

[11] A. Zalkin and W.J. Ramsey. "Intermetallic compounds between lithium and lead. IV. The crystal structure of $Li_{22}Pb_5$". *J. Phys. Chem.*, 62:689–693, 1958.

[12] S. Samson. "Complex cubic A_6B compounds. II. The crystal structure of Mg_6Pd". *Acta Crystallogr.*, B28:936–945, 1972.

[13] L. Arnberg, A. Jonsson, and S. Westman. "The structure of the γ-phase in the Cu-Sn system. A phase of γ-brass type with an 18 Å superstructure". *Acta Chem. Scand. A*, 30:187–192, 1976.

[14] M.H. Booth, J.K. Brandon, R.Y. Brizard, C. Chieh, and W.B. Pearson. "γ-Brasses with *F* cells". *Acta Crystallogr.*, B33:30–36, 1977.

[15] M.L. Fornasini, B. Chabot, and E. Parthé. "The crystal structure of $Sm_{11}Cd_{45}$ with γ-brass and α-Mn clusters". *Acta Crystallogr.*, B34:2093–2099, 1978.

[16] A.S. Koster and J.C. Schoone. "Structure of the cubic iron-zinc phase $Fe_{22}Zn_{78}$". *Acta Crystallogr.*, B37:1905–1907, 1981.

[17] R. Ramirez, R. Nesper, H.-G. von Schnering, and M.C. Böhm. "The electronic structure of crystalline $Li_{21}Si_5$. A cluster approach to a γ-brass structure". *Z. Naturforsch. A: Phys. Sci.*, 41a:1267–1282, 1986.

[18] R. Nesper and H.-G. von Schnering. "$Li_{21}Si_5$, a Zintl phase as well as a Hume-Rothery phase". *J. Solid State Chem.*, 70:48–57, 1987.

[19] S. Lidin, M. Jacob, and A.-K. Larsson. "(Fe,Ni)$Zn_{6.5}$, a superstructure of γ-brass". *Acta Crystallogr.*, C50:340–342, 1994.

[20] S. Mahne and B. Harbrecht. "$Al_{69}Ta_{39}$, a new variant of a face-centered cubic giant cell structure". *J. Alloys Compd.*, 203:271–279, 1994.

[21] F. Bonhomme and K. Yvon. "Cubic $Mg_{29}Ir_4$ crystallizing with an ordered variant of the Mg_6Pd-type structure". *J. Alloys Compd.*, 227:L1–L3, 1995.

[22] T. Nasch and W. Jeitschko. "Niobium and molybdenum compounds with high zinc content: $NbZn_3$, $NbZn_{16}$, and $MoZn_{20.44}$". *J. Solid State Chem.*, 143:95–103, 1999.

[23] A. Johansson and S. Westman. "Determination of the structure of cubic γ-Pt,Zn: A phase of γ-brass type with an 18 Å superstructure". *Acta Chem. Scand.*, 24:3471–3479, 1970.

[24] B. Harbrecht, S. Thimmaiah, M. Armbrüster, C. Pietzonka, and S. Lee. "Structure and properties of γ-brass-type $Pt_2Zn_{11-\delta}$ ($0.2 < \delta < 0.3$)". *Z. Anorg. Allg. Chem.*, 628:2744–2749, 2002.

[25] S. Thimmaiah, K.W. Richter, S. Lee, and B. Harbrecht. "γ_1-Pt_5Zn_{21}: A reappraisal of a γ-brass type complex alloy phase". *Solid State Sci.*, 5:1309–1317, 2003.

[26] V. Smetana, V. Babizhetskyy, G.V. Vajenine, and A. Simon. "Li_{26} clusters in the compound $Li_{13}Na_{29}Ba_{19}$". *Angew. Chem., Int. Ed. Engl.*, 45:6051–6053, 2006.

[27] B. Chabot, K. Cenzual, and E. Parthé. "Nested polyhedra units: A geometrical concept for describing complicated cubic structures". *Acta Crystallogr.*, A37:6–11, 1981.

[28] W. Hornfeck, S. Thimmaiah, S. Lee, and B. Harbrecht. "Structure-composition relations for the partly disordered Hume-Rothery phase $Ir_{7+7\delta}Zn_{97-11\delta}$ $(0.31 \leq \delta \leq 0.58)$". *Chem. Eur. J.*, 10:4616–4626, 2004.

[29] O. von Heidenstam, A. Johansson, and S. Westman. "A redetermination of the distribution of atoms in Cu_5Zn_8, Cu_5Cd_8, and Cu_9Al_4". *Acta Chem. Scand.*, 22:653–661, 1968.

[30] J.T. Schmidt, S. Lee, D.C. Fredrickson, Matthias Conrad, Junliang Sun, and Bernd Harbrecht. "$Pd_{0.213}Cd_{0.787}$ and $Pd_{0.235}Cd_{0.765}$ structures: Their long *c* axis and composite crystals, chemical twinning, and atomic site preferences". *Chem. Eur. J.*, 13:1394–1410, 2007.

[31] M. O'Keeffe and B.G. Hyde. *Crystal Structures. I. Patterns and Symmetry*. Mineralogical Society of America, Washington, DC, 1996.

[32] G.A. Yurko, J.W. Barton, and J.G. Parr. "The crystal structure of Ti_2Ni". *Acta Crystallogr.*, 12:909–911, 1959.

[33] H. Nyman and S. Andersson. "On the structure of Mn_5Si_3, Th_6Mn_{23}, and γ-brass". *Acta Crystallogr.*, A35:580–583, 1979.

[34] H. Nyman and S. Andersson. "The *stella quadrangula* as a structural building unit". *Acta Crystallogr.*, A35:934–937, 1979.

[35] *Cerius2, v. 3.8*. Molecular Simulations Inc., San Diego, CA, 1998.

[36] C. Janot. *Quasicrystals: A Primer, 2nd Edition*. Clarendon Press, Oxford, UK, 1994.

[37] H.-G. von Schnering. "Homoatomic bonding of main group elements". *Angew. Chem., Int. Ed. Engl.*, 20:33–51, 1981.

[38] J.K. Burdett, S. Lee, and T.J. McLarnan. "The coloring problem". *J. Am. Chem. Soc.*, 107:3083–3089, 1985.

[39] J.K. Burdett, E. Canadell, and T. Hughbanks. "Symmetry control of the coloring problem: The electronic structure of MB_2C_2 (M = Ca, La, ...)". *J. Am. Chem. Soc.*, 108:3971–3976, 1986.

[40] G.J. Miller. "The 'coloring problem' in solids: How it affects structure, composition, and properties". *Eur. J. Inorg. Chem.*, 5:523–536, 1998.

[41] C.-S. Lee and G.J. Miller. "Experimental and theoretical studies of elemental site preferences in quasicrystalline approximants (R-phases) within the Li-Mg-Zn-Al system". *Inorg. Chem.*, 40:338–345, 2001.

[42] D.C. Fredrickson, S. Lee, and R. Hoffmann. "Interpenetrating polar and nonpolar sublattices in intermetallics: The $NaCd_2$ structure". *Angew. Chem., Int. Ed. Engl.*, 46:1958–1976, 2007.

[43] G. Kresse and J. Hafner. "*Ab initio* molecular dynamics for liquid metals". *Phys. Rev. B*, 47:558–561, 1993.

[44] G. Kresse and J. Hafner. "*Ab initio* molecular-dynamics simulation of the liquid-metal–amorphous-semiconductor transition in germanium". *Phys. Rev. B*, 49:14251–14269, 1994.

[45] G. Kresse and J. Furthmüller. "Efficiency of *ab initio* total-energy calculations for metals and semiconductors using a plane-wave basis set". *Comput. Mater. Sci.*, 6:15–50, 1995.

[46] G. Kresse and J. Furthmüller. "Efficient iterative schemes for *ab initio* total-energy calculations using a plane-wave basis set". *Phys. Rev. B*, 54:11169–11186, 1996.

[47] D. Vanderbilt. "Soft self-consistent pseudopotentials in a generalized eigenvalue formalism". *Phys. Rev. B*, 41:7892–7895, 1990.

[48] R. Ferro. "Ricerche sulle leghe dei metalli nobili con gli elementi piu elettropositivi. IV. Le fasi gamma dei sistemi magnesio-rodio e magnesio-palladio". *Atti Accad. Naz. Lincei Cl. Sci. Fis. Mat. Nat. Rend.*, 29:70–73, 1960.

[49] H.J. Monkhorst and J. Pack. "Special points for Brillouin-zone integrations". *Phys. Rev. B*, 13:5188–5182, 1976.

[50] G.A. Landrum. *YAeHMOP: Yet Another extended Hückel Molecular Orbital Package, v. 2.0b*, 1997. Freely available on the WWW at URL http://sourceforge.net/projects/yaehmop/.

[51] P. Alemany and S. Alvarez. Unpublished work cited in an unpublished table of eH parameters compiled by S. Alvarez, 1976.

[52] D.C. Fredrickson, S. Lee, R. Hoffmann, and J. Lin. "The Nowotny chimney ladder phases: Following the c_{pseudo} clue toward an explanation of the 14 electron rule". *Inorg. Chem.*, 43:6151–6158, 2004.

[53] D.C. Fredrickson, S. Lee, and R. Hoffmann. "The Nowotny chimney ladder phases: Whence the 14 electron rule?". *Inorg. Chem.*, 43:6159–6167, 2004.

[54] P.M. Clark, S. Lee, and D.C. Fredrickson. "Transition metal AB_3 intermetallics: Structure maps based on quantum mechanical stability". *J. Solid State Chem.*, 178:1269–1283, 2005.

[55] L. Carroll. *Through the Looking-Glass, and What Alice Found There*. Bloomsbury, New York, NY, 2001.

[56] R.F. Berger, S. Lee, J. Johnson, B. Nebgen, F. Sha, and J. Xu. "The mystery of perpendicular fivefold axes and the fourth dimension in intermetallic structures". *Chem. Eur. J.*, 14:3908–3930, 2008.

[57] G. Friedel. "General law of the diffraction of Röntgen rays by crystals". *C. R. Acad. Sci. Paris*, 156:1676–1679, 1913.

[58] J.S. Kasper. *Theory of Alloy Phases*. American Society of Metals, Cleveland, OH, 1956.

[59] F.C. Frank and J.S. Kasper. "Complex alloy structures regarded as sphere packings. I. Definitions and basic principles". *Acta Crystallogr.*, 11:184–190, 1958.

[60] F.C. Frank and J.S. Kasper. "Complex alloy structures regarded as sphere packings. II. Analysis and classification of representative structures". *Acta Crystallogr.*, 12:483–499, 1959.

[61] W.B. Pearson and C.B. Shoemaker. "A system for the coding and generating of layered, tetrahedrally close-packed structures". *Acta Crystallogr.*, B25:1178–1183, 1969.

[62] C.B. Shoemaker and D.P. Shoemaker. "Concerning systems for the generating and coding of layered, tetrahedrally close-packed structures of intermetallic compounds". *Acta Crystallogr.*, B28:2957–2965, 1972.

[63] Ya.P. Yarmolyuk and P.I. Kripyakevich. "Weighted mean coordination numbers and genesis of structures with the closest packing of atoms of different dimensions and normal coordination polyhedra". *Kristallografiya*, 19:539–545, 1974.

[64] D.P. Shoemaker and C.B. Shoemaker. "Concerning the relative numbers of atomic coordination types in tetrahedrally close-packed metal structures". *Acta Crystallogr.*, B42:3–11, 1986.

[65] V. Khare, N. Lalla, R. Tiwari, and O. Srivastava. "On the new structural phases in $Al_{65}Cu_{20}Cr_{15}$ quasicrystalline alloy". *J. Mater. Res.*, 10:1905–1912, 1995.

[66] C. Dong. "The δ-Al_4Cu_9 phase as an approximant of quasicrystals". *Philos. Mag. A*, 73:1519–1528, 1996.

[67] V. Demange, J. Ghanbaja, F. Machizaud, and J.M. Dubois. "About γ-brass phases in the Al-Cr-Fe system and their relationships to quasicrystals and approximants". *Philos. Mag.*, 85:1261–1272, 2005.

[68] B.G. Hyde and S. Andersson. *Inorganic Crystal Structures*. John Wiley & Sons, New York, NY, 1989.

[69] J.-F. Sadoc. "Periodic networks of disclination lines: Application to metal structures". *J. Phys. Let.*, 44:L707–L715, 1983.

[70] J.-F. Sadoc and R. Mosseri. *Geometrical Frustration*. Cambridge University Press, Cambridge, UK, 1999.

[71] L. Westin and L.-E. Erdshammar. "Crystal structure of iridium-magnesium (Ir_7Mg_{44})". *Acta Chem. Scand.*, 26:3619–3626, 1972.

[72] C.P. Gazzara, R.M. Middleton, R.J. Weiss, and E.O. Hall. "A refinement of the parameters of α-manganese". *Acta Crystallogr.*, 22:859–862, 1967.

[73] H.P. Manning. *Geometry of Four Dimensions*. The Macmillan Company, New York, NY, 1914.

[74] E. Jouffret. *Traité Elémentaire de Géométrie à Quatre Dimensions et Introduction à la Géométrie à n-Dimensions*. Gauthier-Villars, Paris, FRA, 1903.

[75] I. Stringham. "Regular figures in n-dimensional space". *Am. J. Math.*, 3:1–14, 1880.

[76] H.S.M. Coxeter. *Regular Polytopes, 3rd Edition*. Dover Publications Inc., New York, NY, 1973.

[77] M. Kléman and J.-F. Sadoc. "A tentative description of the crystallography of amorphous solids". *J. Phys. Let.*, 40:L569–L574, 1979.

[78] D.R. Nelson and M. Widom. "Symmetry, Landau theory, and polytope models of glass". *Nucl. Phys.*, B240:113–139, 1984.

[79] T.F. Banchoff. *Beyond the Third Dimension*. Scientific American Library, New York, NY, 1990.

[80] M.F.C. Ladd and R.A. Palmer. *Structure Determination by X-Ray Crystallography, 2nd Edition*. Plenum Press, New York, NY, 1985.

[81] M. Feuerbacher et al. "The Samson phase, β-Mg_2Al_3, revisited". *Z. Kristallogr.*, 222:259–288, 2007.

[82] V. Elser and N.J.A. Sloane. "A highly symmetric four-dimensional quasicrystal". *J. Phys. A: Math. Gen.*, 20:6161–6168, 1987.

[83] "Treehouse of Horror VI". *The Simpsons*, 1995.

[84] R.F. Berger, S. Lee, J. Johnson, B. Nebgen, and A.C.-Y. So. "Laves phases, γ-brass, and $2 \times 2 \times 2$ superstructures: A new class of quasicrystal approximants and the suggestion of a new quasicrystal". *Chem. Eur. J.*, 14:6627–6639, 2008.

[85] K.H. Lieser and H. Witte. "The ternary systems Mg-Cu-Zn; Mg-Ni-Zn; Mg-Cu-Ni". *Z. Metallk.*, 43:396–401, 1952.

[86] Y.A. Chang. "Phase relations in the system chromium-silicon". *Trans. AIME*, 242:1509–1515, 1968.

[87] J.V. Florio, R.E. Rundle, and A.I. Snow. "Compounds of thorium with transition metals. I. The thorium-manganese system". *Acta Crystallogr.*, 5:449–457, 1952.

[88] E. Zintl and W. Haucke. "Metals and alloys. XXV. Constitution of the intermetallic phases, $NaZn_{13}$, KZn_{13}, KCd_{13}, $RbCd_{13}$, and $CsCd_{13}$". *Z. Elektrochem. Angew. Phys. Chem.*, 44:104–111, 1938.

[89] L. Misch. "Crystal structure of $AuBe_5$ and $PdBe_5$ and its relation to the cubic AB_2 structure". *Metallwirt. Metallwissen. Metalltech.*, 14:897–899, 1935.

[90] C.B. Shoemaker, D.P. Shoemaker, T.E. Hopkins, and S. Yindepit. "Refinement of the structure of β-manganese and of a related phase in the Mn-Ni-Si system". *Acta Crystallogr.*, B34:3573–3576, 1978.

[91] A.C. Larson and D.T. Cromer. "The crystal structure of YCd_6". *Acta Crystallogr.*, B27:1875–1879, 1971.

[92] Z.M. Wang, Q.B. Yang, and K.H. Kuo. "Description of hexagonal Frank-Kasper phases by a projection method". *Acta Crystallogr.*, A45:268–274, 1989.

[93] H. Takakura, J. Guo, and A.P. Tsai. "Crystal and quasicrystal structures in Cd-Yb and Cd-Ca binary alloys". *Philos. Mag. Let.*, 81:411–418, 2001.

[94] R.V. Moody and J. Patera. "Quasicrystals and icosians". *J. Phys. A: Math. Gen.*, 26:2829–2853, 1993.

[95] J.-F. Sadoc and R. Mosseri. "The E_8 lattice and quasicrystals: Geometry, number theory, and quasicrystals". *J. Phys. A: Math. Gen.*, 26:1789–1809, 1993.

[96] P. Kramer and R. Neri. "On periodic and non-periodic space fillings of E^m obtained by projection". *Acta Crystallogr.*, A40:580–587, 1984.

[97] M. Duneau and A. Katz. "Quasiperiodic patterns". *Phys. Rev. Let.*, 54:2688–2691, 1985.

[98] P.A. Kalugin, A.Y. Kitaev, and L.C. Levitov. "Aluminum-manganese ($Al_{0.86}Mn_{0.14}$), a six-dimensional crystal". *Pis'ma Zh. Eksp. Teor. Fiz.*, 41:119–121, 1985.

[99] V. Elser and C.L. Henley. "Crystal and quasicrystal structures in Al-Mn-Si alloys". *Phys. Rev. Let.*, 55:2883–2886, 1985.

[100] M. Koca, R. Koç, and M. Al-Barwani. "Noncrystallographic Coxeter group H_4 in E_8". *J. Phys. A: Math. Gen.*, 34:11201–11213, 2001.

[101] J.H. Conway and N.J.A. Sloane. *Sphere Packings, Lattices, and Groups, 3rd Edition*. Springer-Verlag, New York, NY, 1999.

[102] E. John and B. Taupin. "Rocket Man (I Think It's Going to Be a Long, Long Time)". *Honky Château*, 1972.

[103] W. Hume-Rothery. *The Metallic State*. Clarendon Press, Oxford, UK, 1931.

[104] W. Hume-Rothery. *Electrons, Atoms, Metals, and Alloys*. Dover, New York, NY, 1963.

[105] M. Hansen. *Constitution of Binary Alloys*. McGraw-Hill, New York, NY, 1958.

[106] H. Jones. "The theory of alloys in the γ-phase". *Proc. R. Soc. A*, 144:225–234, 1934.

[107] N.F. Mott and H. Jones. *The Theory of the Properties of Metals and Alloys*. Clarendon Press, Oxford, UK, 1936.

[108] A.T. Paxton, M. Methfessel, and D.G. Pettifor. "A bandstructure view of the Hume-Rothery electron phases". *Proc. R. Soc. A*, 453:1493–1514, 1997.

[109] T. Takeuchi, H. Sato, and U. Mizutani. "Investigation of the Hume-Rothery stabilization mechanism from *ab initio* band calculations for different electron compounds: Cu_5Zn_8 and Al-Mg-Zn, Al-Cu-Ru-Si approximants". *J. Alloys Compd.*, 342:355–359, 2002.

[110] U. Mizutani, T. Takeuchi, and H. Sato. "Interpretation of the Hume-Rothery rule in complex electron compounds: γ-Phase Cu_5Zn_8 alloy, FK-type $Al_{30}Mg_{40}Zn_{30}$, and MI-type $Al_{68}Cu_7Ru_{17}Si_8$ 1/1-1/1-1/1 approximants". *Prog. Mat. Sci.*, 49:227–261, 2004.

[111] U. Mizutani, T. Takeuchi, and H. Sato. "Interpretation of the Hume-Rothery rule in quasicrystals and their approximants". *J. Non-Cryst. Solids*, 334-335:331–335, 2004.

[112] R. Asahi, H. Sato, T. Takeuchi, and U. Mizutani. "Verification of Hume-Rothery electron concentration rule in Cu_5Zn_8 and Cu_9Al_4 γ-brasses by *ab initio* FLAPW band calculations". *Phys. Rev. B*, 71:165103, 2005.

[113] R. Asahi, H. Sato, T. Takeuchi, and U. Mizutani. "Interpretation of the Hume-Rothery electron concentration rule in the T_2Zn_{11} (T = Ni, Pd, Co, and Fe) γ-brasses based on first-principles FLAPW calculations". *Phys. Rev. B*, 72:125102, 2005.

[114] U. Mizutani, R. Asahi, H. Sato, and T. Takeuchi. "The Hume-Rothery electron concentration rule for a series of γ-brasses studied by full-potential linearized augmented plane wave (FLAPW) band calculations". *Philos. Mag.*, 86:645–654, 2006.

[115] O. Gourdon, D. Gout, D.J. Williams, T. Proffen, S. Hobbs, and G.J. Miller. "Atomic distributions in the γ-brass structure of the Cu-Zn system: A structural and theoretical study". *Inorg. Chem.*, 46:251–260, 2007.

[116] A. Blandin. "Theoretical considerations of the Hume-Rothery rules". In P.S. Rudman, J. Stringer, and R.I. Jaffee (Eds.). *Phase Stability in Metals and Alloys*. McGraw-Hill, New York, NY, 1967.

[117] V. Heine. "Pseudopotentials applied to stability of structures". In P.S. Rudman, J. Stringer, and R.I. Jaffee (Eds.). *Phase Stability in Metals and Alloys*. McGraw-Hill, New York, NY, 1967.

[118] D. Stroud and N.W. Ashcroft. "Phase stability in binary alloys". *J. Phys. F: Metal Phys.*, 1:113–124, 1971.

[119] N.W. Ashcroft. "Fermi surfaces of potassium and rubidium". *Phys. Rev.*, 140:A935–A940, 1965.

[120] J. Hafner, S.S. Jaswal, M. Tegze, A. Pflugi, J. Krieg, P. Oelhafen, and H.J. Güntherodt. "The atomic and electronic structure of metallic glasses: Search for a structure-induced minimum in the density of states". *J. Phys. F: Metal Phys.*, 18:2583–2604, 1988.

[121] N.W. Ashcroft. "Quantum-solid behavior and the electronic structure of the light alkali metals". *Phys. Rev. B*, 39:10552–10559, 1989.

[122] R.D. Werkman, P.J. Schurer, I. Vincze, and F. van der Woude. "Are quasicrystals Hume-Rothery alloys?". *Hyperfine Interact.*, 45:409–414, 1989.

[123] P.M. Ossi and D.C. Kothari. "Quasicrystals: An electron phase". *J. Less-Common Met.*, 171:221–230, 1991.

[124] Q. Jiang, B.Q. Chi, and J.C. Li. "A valence electron concentration criterion for glass-formation ability of metallic liquids". *Appl. Phys. Lett.*, 82:2984–2986, 2003.

[125] T.A. Albright, J.K. Burdett, and M.-H. Whangbo. *Orbital Interactions in Chemistry*. John Wiley & Sons, New York, NY, 1985.

[126] L. Hoistad and S. Lee. "The Hume-Rothery electron concentration rules and second moment scaling". *J. Am. Chem. Soc.*, 113:8216–8220, 1991.

[127] S. Lee and L. Hoistad. "Second moment scaling, metallic and covalent structure rationalization, and electron counting rules". *J. Alloys Compd.*, 229:66–79, 1995.

[128] N.W. Ashcroft and N.D. Mermin. *Solid State Physics*. Saunders College Publishing, New York, NY, 1976.

[129] C. Kittel. *Introduction to Solid State Physics, 8^{th} Edition*. John Wiley & Sons, New York, NY, 2005.

[130] R. Hoffmann. "An extended Hückel theory. I. Hydrocarbons". *J. Chem. Phys*, 39:1397–1412, 1963.

[131] R. Hoffmann. *Solids and Surfaces: A Chemist's View of Bonding in Extended Structures*. VCH, New York, NY, 1988.

[132] T.D. Brennan and J.K. Burdett. "Electronic structure of elemental calcium and zinc". *Inorg. Chem.*, 32:746–749, 1993.

[133] G.J. Ackland and I.R. Macleod. "Origin of the complex crystal structures of elements at intermediate pressure". *New J. Phys.*, 6:138, 2004.

[134] V.F. Degtyareva. "Simple metals at high pressures: The Fermi sphere-Brillouin zone interaction model". *Phys.-Uspekhi*, 49:369–388, 2006.

[135] J. Feng, R.G. Hennig, N.W. Ashcroft, and R. Hoffmann. "Emergent reduction of electronic state dimensionality in dense ordered Li-Be alloys". *Nature*, 451:445–448, 2008.

[136] J. Feng, R. Hoffmann, and N.W. Ashcroft. "The double-diamond structure for Na-Al: Pressure-induced Jones zone activation". Unpublished manuscript, 2009.

[137] L.H. Beck and C.S. Smith. "Copper-zinc constitution diagram, redetermined in the vicinity of the β-phase by means of quantitative metallography". *Trans. AIME*, 194:1079–1083, 1952.

[138] J. Coulton. "Still Alive". *The Orange Box (Original Soundtrack)*, 2007.